

Gary L. Cloud · Eann Patterson · David Backman *Editors*

Joining Technologies for Composites and Dissimilar Materials, Volume 10

Proceedings of the 2016 Annual Conference on
Experimental and Applied Mechanics



Conference Proceedings of the Society for Experimental Mechanics Series

Series Editor

Kristin B. Zimmerman, Ph.D.
Society for Experimental Mechanics, Inc
Bethel, CT, USA

More information about this series at <http://www.springer.com/series/8922>

Gary L. Cloud • Eann Patterson • David Backman
Editors

Joining Technologies for Composites and Dissimilar Materials, Volume 10

Proceedings of the 2016 Annual Conference
on Experimental and Applied Mechanics

Editors

Gary L. Cloud
Composite Vehicle Research Center
Michigan State University
Lansing, MI, USA

Eann Patterson
University of Liverpool
Liverpool, UK

David Backman
National Research Council Canada
Ottawa, ON, Canada

ISSN 2191-5644 ISSN 2191-5652 (electronic)
Conference Proceedings of the Society for Experimental Mechanics Series
ISBN 978-3-319-42425-5 ISBN 978-3-319-42426-2 (eBook)
DOI 10.1007/978-3-319-42426-2

Library of Congress Control Number: 2012943040

© The Society for Experimental Mechanics, Inc. 2017

This work is subject to copyright. All rights are reserved by the Publisher, whether the whole or part of the material is concerned, specifically the rights of translation, reprinting, reuse of illustrations, recitation, broadcasting, reproduction on microfilms or in any other physical way, and transmission or information storage and retrieval, electronic adaptation, computer software, or by similar or dissimilar methodology now known or hereafter developed.

The use of general descriptive names, registered names, trademarks, service marks, etc. in this publication does not imply, even in the absence of a specific statement, that such names are exempt from the relevant protective laws and regulations and therefore free for general use.

The publisher, the authors and the editors are safe to assume that the advice and information in this book are believed to be true and accurate at the date of publication. Neither the publisher nor the authors or the editors give a warranty, express or implied, with respect to the material contained herein or for any errors or omissions that may have been made.

Printed on acid-free paper

This Springer imprint is published by Springer Nature
The registered company is Springer International Publishing AG Switzerland

Preface

Joining Technologies for Composites and Dissimilar Materials represents one of ten volumes of technical papers presented at the 2016 SEM Annual Conference & Exposition on Experimental and Applied Mechanics organized by the Society for Experimental Mechanics and held in Orlando, FL, on June 6–9, 2016. The complete Proceedings also includes volumes on *Dynamic Behavior of Materials; Challenges in Mechanics of Time-Dependent Materials; Advancement of Optical Methods in Experimental Mechanics; Experimental and Applied Mechanics; Micro and Nanomechanics; Mechanics of Biological Systems and Materials; Fracture, Fatigue, Failure and Damage Evolution; and Residual Stress, Thermomechanics & Infrared Imaging, Hybrid Techniques and Inverse Problems.*

Composite materials are being increasingly utilized at multiple levels in application areas including automotive, aerospace, marine, biomechanical, and civil infrastructure, so the need for improved joining of these materials has become critical. While the design of the composite laminate is important, it is the ability to join sections of composite to one another or to components made of dissimilar materials that is the enabling technology for creating structures that approach optimum in function, weight, durability, and cost.

Composite joining technologies have been routinely classified in the past as either mechanical or adhesive. Increasingly, joint optimization requires combinations of the two types as well as the introduction of innovative new methods, such as composite welding, that provide high strength and light weight. Hybrid composite joints that allow the joining of composites to monolithic or other classes of material comprise another important technology that will facilitate the use of composites in many new application areas. Today, developments in composite joining technologies are progressing at a rapid rate, driven by both technology and user requirements.

This symposium addresses pertinent issues relating to design, analysis, fabrication, testing, optimization, reliability, and applications of composite joints, especially as these issues relate to experimental mechanics of macroscale and microscale structures.

East Lansing, MI, USA
Liverpool, UK
Ottawa, ON, Canada

Gary L. Cloud
Eann A. Patterson
David Backman

Contents

1	How to Join Fiber-Reinforced Composite Parts: An Experimental Investigation.....	1
	Yaomin Dong, Arnaldo Mazzei, Javad Baqersad, and Azadeh Sheidaei	
2	Analysis of a Composite Pi/T-Joint Using an FE Model and DIC.....	11
	Chris Sebastian, Mahmoodul Haq, and Eann Patterson	
3	5xxx Aluminum Sensitization and Application of Laminated Composite Patch Repairs.....	21
	Daniel C. Hart	
4	Investigation and Improvement of Composite T-Joints with Metallic Arrow-Pin Reinforcement.....	33
	Sebastian Heimbs, Michael Jürgens, Christoph Breu, Georg Ganzenmüller, and Johannes Wolfrum	
5	Review of Natural Joints and Bio-Inspired CFRP to Steel joints.....	41
	Evangelos I. Avgoulas and Michael P.F. Sutcliffe	
6	Fabrication of 3D Thermoplastic Sandwich Structures Utilizing Ultrasonic Spot Welding.....	49
	Cassandra M. Degen and Navaraj Gurung	
7	Impact and Lap Shear Properties of Ultrasonically Spot Welded Composite Lap Joints.....	59
	Cassandra M. Degen, Lidvin Kjerengtroen, Eirik Valseth, and Joseph R. Newkirk	
8	Numerical and Experimental Characterization of Hybrid Fastening System in Composite Joints.....	71
	Ermias G. Koricho, Mahmoodul Haq, and Gary L. Cloud	
9	Application of Digital Image Correlation to the Thick Adherend Shear Test.....	81
	Jared Van Blitterswyk, David Backman, Jeremy Laliberté, and Richard Cole	
10	Interfacial Strength of Thin Film Measurement by Laser-Spallation.....	91
	Leila Seyed Faraji, Dale Teeters, and Michel W. Keller	
11	Joining of UHTC Composites Using Metallic Interlayer.....	99
	Noritaka Saito, Laura Esposito, Toshio Yoneima, Koichi Hayashi, and Kunihiko Nakashima	
12	Metal-to-Composite Structural Joining for Drivetrain Applications.....	107
	Peter J. Fritz, Kelly A. Williams, and Javed A. Mapkar	
13	Short-term Preload Relaxation in Composite Bolted Joints Monitored with Reusable Optical Sensors.....	115
	Anton Khomenko, Ermias G. Koricho, Mahmoodul Haq, and Gary L. Cloud	

Chapter 1

How to Join Fiber-Reinforced Composite Parts: An Experimental Investigation

Yaomin Dong, Arnaldo Mazzei, Javad Baqersad, and Azadeh Sheidaei

Abstract A coupler has been developed to prevent windshield wiper systems from being damaged by excessive loads that can occur when the normal wiping pattern is restricted. Unlike the traditional steel coupler used in wiper systems, the composite coupler will buckle at a prescribed compressive load threshold and become extremely compliant. As a result, the peak loading of the coupler and the entire wiper system can be greatly reduced. The coupler is composed of a pultruded composite rod with injection-molded plastic spherical sockets attached at either end. The sockets are used to attach the coupler to the crank and rocker of the windshield wiper linkage. Because the loads exerted on a coupler vary in magnitude and direction during a wiping cycle, the joint between the sockets and the pultruded composite rod must be robust. The paradigm for attaching sockets to steel couplers (i.e. over-molding the sockets around holes stamped into the ends of traditional steel couplers) was tested and found to produce inadequate joint strength. This paper details the methodology that was employed to produce and optimize an acceptable means to join the injection-molded sockets to the fiber glass pultruded rods. Specifically, a designed experiment based on the Robust Design Strategy of Taguchi was used to identify the process, processing parameters, and materials that yield a sufficiently strong joint at a reasonable manufacturing cost without damaging the integrity of the underlying composite structure.

Keywords Composite materials • Buckling • Wiper systems • Durability • Joint strength

1.1 Introduction

Automotive windshield wiper systems, in conjunction with washer systems, are used in vehicles to remove contaminants such as rain, sleet, snow, and dirt from the windshield. As shown in Fig. 1.1, a typical wiper system consists of an electric motor, a linkage to transform the rotational motion from the motor to oscillatory motion, and a pair of wiper arms and blades. The areas of the windshield that must be wiped by the wiper system are mandated by the federal motor vehicle safety standards FMVSS 104 [1].

Figure 1.2 shows that snow has accumulated above the cowl screen and caused the normal wiping pattern of the system to be restricted. Under such conditions, the loads in the wiper system have been observed to be approximately four times greater than those encountered under normal wiping conditions for a particular application. The elevated loads are due to two factors: (1) As the arm(s) and/or blade(s) come into contact with the restriction, the speed of the wiper system decreases and the output torque of the motor increases. (2) This factor is aggravated by the very large mechanical advantage of the wiper linkage near the reversal positions.

In extreme cases, the loads that result from restricting the wipe pattern can cause failures. For example, Fig. 1.3 depicts a 5-mm thick hardened steel rocker arm that has fractured as a result of such a loading. Clearly, such a damage is unacceptable from both safety and warranty standpoints.

Penrod and Dong [2] reviewed various methods that have been developed to solve this problem. One such solution is to use a coupler fabricated from a thermoset polyester/glass fiber pultruded composite material [3–6]. This coupler—referred to as the composite link—has the advantage of being sufficiently stiff during normal operation providing very good pattern control. However, in the event that elevated loads occur, the coupler is designed to buckle at a prescribed load level (i.e. the critical load). Once buckled, the coupler becomes extremely compliant. As a result, the peak loading of the coupler and, moreover, the entire system, can be limited and greatly reduced when compared to the same system without the composite link.

Y. Dong, Ph.D. (✉) • A. Mazzei, Ph.D. • J. Baqersad, Ph.D., P.E. • A. Sheidaei, Ph.D.
Department of Mechanical Engineering, Kettering University, 1700 University Avenue, Flint, MI 48504-4898, USA
e-mail: ydong@kettering.edu

Fig. 1.1 A typical wiper system consists of wipers, motor, and a linkage, and wiper arms

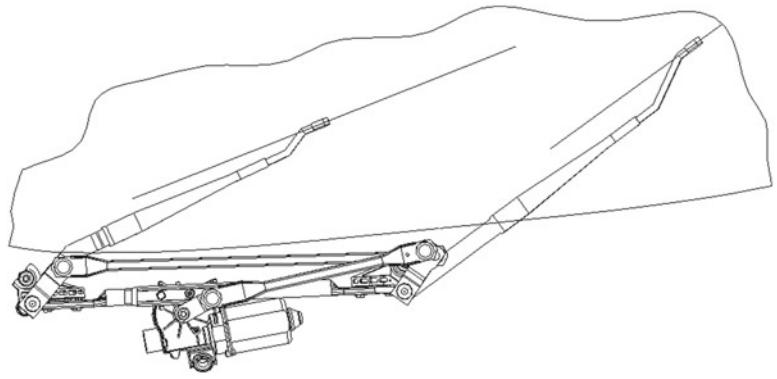


Fig. 1.2 Restricted wiping pattern due to snow accumulation



Fig. 1.3 Fractured rocker arm resulting from snow accumulation



Figure 1.4 shows the operating principle of the composite link. In the illustration the wiper arms have encountered snow/ice accumulation (depicted by the hatched pattern) above the cowl screen that blocks the normal wiping pattern of the system. As a result, the wiper system loads have increased sufficiently to buckle the composite link (depicted by the arcuate member

Fig. 1.4 Operating principle of the composite link

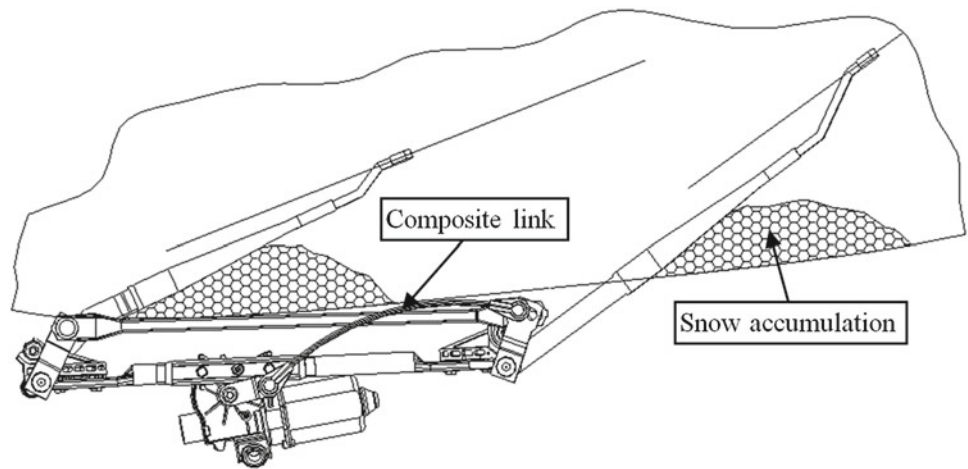
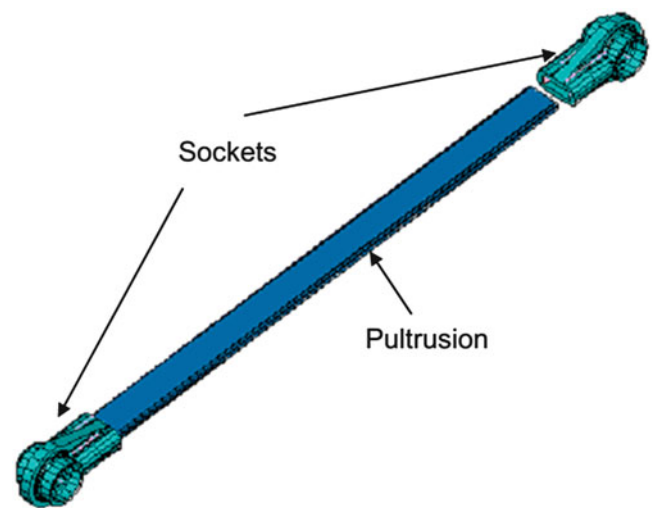


Fig. 1.5 Composite link assembly



of the wiper linkage). Once buckled, the composite link behaves nearly perfectly-plastic. As a result, the chord length of the composite link decreases significantly without a corresponding appreciable increase in axial load. Thus the crank is able to continue rotating and the wiper system is enabled to wiper at a reduced area above the restriction.

The composite link is an assembly of a 16.7 mm×5.2 mm rectangular cross-section pultrusion and glass-filled plastic sockets attached at either end, as shown in Fig. 1.5. The design methodology, material selection, validation testing, and application guidelines for the composite link are discussed in detail by Penrod, Dong, and Buchanan [3]. Because the loads exerted on the coupler vary in magnitude and direction during each wiping cycle, the joint between the sockets and the pultrusion is critical and must be robust.

Initially, it was planned to attach the sockets to the pultrusion rod using the same approach that sockets have been traditionally joined to steel couplers (i.e. over-molding the sockets around holes stamped into the ends of the traditional steel coupler). In the case of the composite link, holes were drilled into the ends of the pultrusion and the sockets were over-molded onto the pultrusions. Unfortunately, this joining method performed dismally as it was characterized by bearing stress failures of the pultrusion at relatively low tensile loads. In retrospect, this failure mode was no surprise. The pultrusions consist of longitudinally oriented continuous glass fibers bound together by a thermosetting polyester matrix. Drilling holes on the pultruded rod cuts the continuous fibers and weakens the composite structure. As such, the material has little strength on short-transverse planes where the bearing failure was observed to occur.

Since the paradigm for attaching sockets to steel links did not work, a Greenfield approach to attaching sockets to the pultrusions was embarked upon. This paper details the approach that was employed to generate, evaluate, and optimize an acceptable means of attaching the injection-molded plastic sockets to the pultrusions.

1.2 Designed Experiment for Joining Socket to Pultrusion

How can the plastic sockets be attached to the pultruded composite rod? The traditional approach of over-molding the sockets to steel links proved inadequate as was discussed previously. In order to answer this question, a set of design specifications were generated to assess design concepts against. Qualitatively, the specifications of paramount importance were that the attachment method.

- Provide adequate joint strength in tension and compression when subjected to monotonic and cyclic loads.
- Avoid damaging the integrity of the glass fibers to the extent that the pultrusion would no longer be capable of providing a predictable critical load and adequate post-buckled axial compressive deflection.
- Be cost-effective.

Once the aforementioned specifications were established, three phases of the development were sequentially undertaken. Specifically,

- *System Design*: the first phase of the development where a variety of state-of-the-art candidate processes were generated using input from a cross-functional team of material, manufacturing, and product specialists. Once identified, the candidate processes were then narrowed to the most promising approaches via conceptual evaluation by the cross-functional team. Additionally, some ad hoc testing was completed in this phase of the development that suggested adding grooves to the ends of the pultrusion so that the over-molded socket could form a positive lock was the most viable approach.
- *Parameter Design*: the second phase of the development where a series of designed experiments were used to quantitatively ascertain the optimal combination of design and processing parameters.
- *Tolerance Design*: the third and final phase of the development where the allowable tolerance range on the critical dimensions and processing parameters were determined.

The focus of this paper is on the series of designed experiments that were used to identify the optimal combination of designs, materials, and processes during the parameter design phase of the development.

1.2.1 Parameter Selection Stage 1: Screening

The Robust Design Strategy of G. Taguchi [7] has gained broad acceptance in Japan, the United States, and elsewhere for use in product design and development. Taguchi's approach to parameter design provides a systematic and efficient method for determining near-optimum design parameters. The Taguchi method allows for the sensitivity of the design to a large number of parameters to be evaluated using a relatively small number of sample parts by utilizing orthogonal arrays from design of experiments theory. The conclusions drawn from such small scale experiments are valid over the entire experimental range spanned by the control factors and control factor levels.

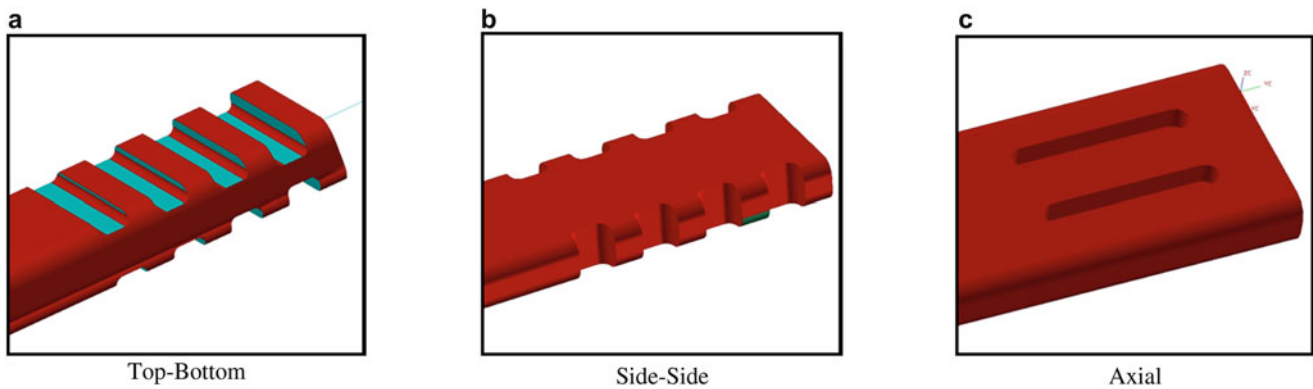
As mentioned previously, adding grooves to the pultrusion ends so that the over-molded socket would be positively locked to the pultrusion was deemed the most viable approach. However, the influence of other factors on the joint strength was still unknown. Specifically, what is the influence of the surface finish of the pultrusion on joint strength? What role does the location of the grooves play? Does the socket material significantly impact the joint strength? What benefit might be derived from the use of adhesives? What is the influence of glass content in the pultrusion on joint strength? To answer these questions, an experiment was designed to screen these factors for relative importance and identify where the various factors might interact—both in a positive and negative sense.

Table 1.1 depicts the L18 Orthogonal Array that was used to screen the design candidates. Notice that the five aforementioned design parameters (A~F) are chosen as control factors, with each factor having three levels. Descriptions of the control levels indicated in the array are as follows.

- **Surface Finish**: Smooth denotes the surface finish of the pultrusion without any additional processing. Abrasive-fine, and abrasive-coarse denote that the ends of the pultrusion have been grit blast with a fine and coarse medium, respectively. Chemical etched refers to the resin-rich surface of the pultrusion ends being removed using an acidic solution. Laser etches #1 and #2 denote two power levels used to remove the resin-rich surface of the pultrusion via the use of a laser.
- **Machined Grooves**: Smooth denotes no grooves, top-bottom denotes grooves machined into the top and bottom surfaces of the pultrusions. Side-side denotes grooves machined into the edges of the pultrusions. Ultimately, axial grooves which

Table 1.1 L18 Orthogonal array for stage 1 (screening)

	1&2	3	4	5	6
	A	B	D	E	F
	Surface finish	Machined grooves	Socket material	Attachment/adhesives	Pultrusions
1	Smooth	Smooth	Nylon	Insert mold/hot curing	Low modulus
2	Smooth	Top-bottom	Acetal #1	Mech attach/chem. cure	Moderate modulus
3	Smooth	Side-side	Acetal #2	Insert mold/no adhesive	High modulus
4	Abrasive-fine	Smooth	Nylon	Mech attach/chem. cure	Moderate modulus
5	Abrasive-fine	Top-bottom	Acetal #1	Insert mold/no adhesive	High modulus
6	Abrasive-fine	Side-side	Acetal #2	Insert mold/hot curing	Low modulus
7	Abrasive-coarse	Smooth	Acetal #1	Insert mold/hot curing	High modulus
8	Abrasive-coarse	Top-bottom	Acetal #2	Mech attach/chem. cure	Low modulus
9	Abrasive-coarse	Side-side	Nylon	Insert mold/no adhesive	Moderate modulus
10	Chemical etch	Smooth	Acetal #2	Insert mold/no adhesive	Moderate modulus
11	Chemical etch	Top-bottom	Nylon	Insert mold/hot curing	High modulus
12	Chemical etch	Side-side	Acetal #1	Mech attach/chem. cure	Low modulus
13	Laser etch #1	Smooth	Acetal #1	Insert mold/no adhesive	Low modulus
14	Laser etch #1	Top-bottom	Acetal #2	Insert mold/hot curing	Moderate modulus
15	laser etch #1	Side-side	Nylon	Mech attach/chem. cure	High modulus
16	Laser etch #2	Smooth	Acetal #2	Mech attach/chem. cure	High modulus
17	Laser etch #2	Top-bottom	Nylon	Insert mold/no adhesive	Low modulus
18	Laser etch #2	Side-side	Acetal #1	Insert mold/hot curing	Moderate modulus

**Fig. 1.6** Groove configurations

are oriented longitudinally were also considered. (Please see Sect. 2.3 for details.) All grooves were full-filletted as indicated in Fig. 1.6 and were machined by grinding.

- **Socket Material:** Nylon denotes a glass-filled nylon 6/6. Acetal #1 refers to 20% glass-filled acetal, whereas acetal #2 refers to 30% glass-filled acetal.
- **Attachment/adhesives:** Three possibilities were considered. Insert molding the sockets over the ends of the pultrusion was done both without adhesives (i.e. insert mold/no adhesive) and with adhesives (i.e. insert mold/hot curing). Hot curing refers to the heat available from the injection molded material promoting rapid curing of the adhesive.) Mechanical attachment of the socket to the pultrusion was also considered and used an adhesive to bond the sockets to the pultrusions. In this case an accelerant was used to promote curing of the adhesive. Thus, this approach is denoted by mech attach/chem cure in Table 1.1. In all cases, the adhesive used was a commercially available cyanoacrylate.
- **Pultrusions:** Low-, moderate-, and high-modulus refer to elastic modulus of the pultrusions resulting from three different glass content levels being used. The higher the glass content, the higher the modulus.

It should be noted that a full-factorial experiment would require evaluating the performance of $(6 \times 3 \times 3 \times 3 \times 3 =)$ 486 combinations of control factors and control levels. Using the Taguchi approach, only 18 combinations need to be considered with the 18 specific combinations of control factors and control levels dictated by the method.

Fig. 1.7 Strip test used to determine the ultimate strength of the joint

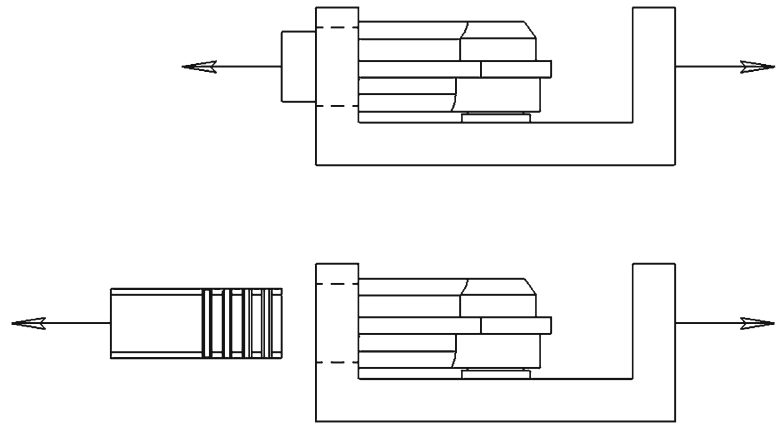


Table 1.2 L9 Orthogonal array for stage 2 (groove design)

	1	2	3
	A	B	C
	Groove size	Groove spacing	Number of grooves
1	Small	#1	Few
2	Small	#2	Moderate
3	Small	#3	Many
4	Medium	#1	Moderate
5	Medium	#2	Many
6	Medium	#3	Few
7	Large	#1	Many
8	Large	#2	Few
9	Large	#3	Moderate

Once the 18 combinations were prototyped, a strip test was run on each configuration to determine the ultimate strength of each joint in tension. Figure 1.7 depicts the test. The assembled composite link was placed in a specially designed fixture that captured the socket only. The tensile load was increased until the assembly of the socket and pultrusion separated. Analyzing the data collected from the testing using the Taguchi approach allowed for the contribution to the joint strength of each control factor and control level, and interactions of the control factors and control levels to be quantified. From this analysis, it was found that grooves added to the top and bottom faces of the pultrusion were the single greatest contributor to joint strength. The use of adhesives to produce bonding between the socket and pultrusion was found to be the second largest contributor to strength, but was ruled out due to processing difficulties. Additionally, altering the surface finish of the pultrusion provided little benefit and was quite costly. As such, it was also disqualified from further consideration.

1.2.2 Parameter Selection Stage 2: Groove Design

Based on the results of the screening designed experiment, a second designed experiment was constructed to further optimize the groove design. Table 1.2 depicts the L9 Orthogonal Array that was constructed for this purpose. In this experiment three control factors (i.e. groove size, groove spacing, and number of grooves) were considered at three different control levels. Once again it is noteworthy that the number of configurations to be tested is only nine and that a full factorial experiment would require 27 (i.e. $3 \times 3 \times 3$) configurations.

The control levels indicated in Table 1.2 are described as follows.

- Groove Size: Small denotes 0.5 mm depth, while medium corresponds to 1.0 mm depth, and large denotes a 1.5 mm depth.
- Groove Spacing: The spacing between adjacent grooves with level #1 corresponding to 2 mm spacing, level #2 corresponding to 3 mm spacing, and level #3 corresponding to 4 mm spacing.
- Number of Grooves: Few denotes two grooves per face, moderate denotes four grooves per face; and many corresponding to six grooves per face.

Prototype parts of each configuration were fabricated and evaluated against two criteria. The first criterion was simply evaluating the tensile strength of the joint as was performed in the screening experiment. The second criterion involved examining the performance of the composite links in compression after being buckled and axially compressed to a preset deflection. Doing so revealed that under certain circumstances, the pultruded material tends to delaminate on long-transverse planes with the delamination initiating at the root of the groove.

Analyzing the data using the Taguchi approach once again allowed for the contribution to the joint strength of each control factor and control level, and interactions of the control factors and control levels to be determined. From this analysis and delamination considerations, it was found that numerous small, closely-spaced grooves provided the optimal combination of joint strength in tension and delamination resistance after buckling.

1.2.3 Parameter Selection Stage 3: Final Design

Once the groove optimization designed experiment was completed, a third and final designed experiment was constructed to examine various processing methods to produce the grooves. Additionally, surface finish was once again considered and the use of adhesives was revisited. An additional six configurations were added to the experiment for checking purposes.

Table 1.3 depicts the L18 Orthogonal Array that was constructed for this final investigation. Table 1.4 contains six additional configurations of interest that were included in the experiment. Prototype parts representing the 24 configurations specified in Tables 1.3 and 1.4 were fabricated and evaluated for tensile strength per the procedure used in the previous experiments. Notice that four different processes were considered to produce the grooves both across the grain (cross grooves) and axially—machining (i.e. cutting), grinding, grit blasting, and laser ablation, as well as, a control case of no grooves.

Table 1.3 L18 Orthogonal array for stage 3 (final design)

	1&2	3	4
	A	C	D
	Grooves	Surface finish	Attachment method
1	Smooth	Smooth	Insert mold
2	Smooth	Ground axial fiber exposure	Adhesive assy W/o surface primer
3	Smooth	Laser axial fiber exposure	Adhesive assy W/surface primer
4	Ground axial grooves	Smooth	Insert mold
5	Ground axial grooves	Ground axial fiber exposure	Adhesive assy w/o surface primer
6	Ground axial grooves	Laser axial fiber exposure	Adhesive assy W/ surface primer
7	Ground top-bottom grooves	Smooth	Adhesive assy W/o surface primer
8	Ground top-bottom grooves	Ground axial fiber exposure	Adhesive assy W/ surface primer
9	Ground top-bottom grooves	Laser axial fiber exposure	Insert mold
10	Ground side-side grooves	Smooth	Adhesive assy W/surface primer
11	Ground side-side grooves	Ground axial fiber exposure	Insert mold
12	Ground side-side grooves	Laser axial fiber exposure	Adhesive assy W/o surface primer
13	Laser axial grooves	Smooth	Adhesive assy W/o surface primer
14	Laser axial grooves	Ground axial fiber exposure	Adhesive assy W/ surface primer
15	Laser axial grooves	Laser axial fiber exposure	Insert mold
16	Cut top-bottom grooves	Smooth	Adhesive assy W/ surface primer
17	Cut top-bottom grooves	Ground axial fiber exposure	Insert mold
18	Cut top-bottom grooves	Laser axial fiber exposure	Adhesive assy W/o surface primer

Table 1.4 Six additional configurations of interest

19	Ground cross grooves	Plasma axial fiber exposure	Insert mold
20	Ground cross grooves	Plasma axial fiber exposure	Adhesive assy W/o surface primer
21	Grit blast cross grooves	Smooth	Adhesive assy W/o surface primer
22	Grit blast cross grooves	Laser axial fiber exposure	Insert mold
23	Laser cross grooves	Smooth	Adhesive assy W/o surface primer
24	Laser cross grooves	Laser axial fiber exposure	Insert mold

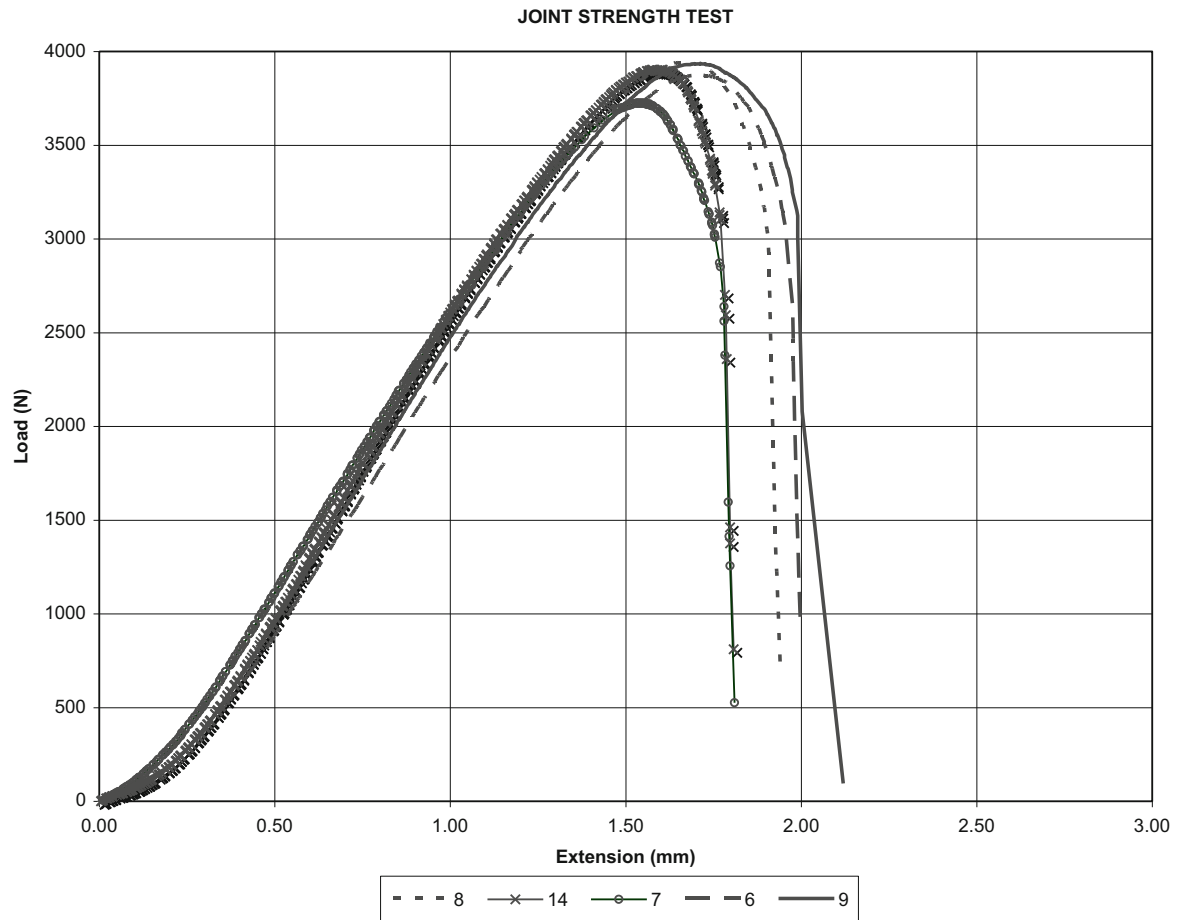


Fig. 1.8 Joint strength of the top five performing configurations

Three surface treatments were considered—grinding, laser ablation, and plasma cutting, as well as, untreated (smooth) finish. Additionally, insert-molding the sockets was compared to attaching the sockets using adhesives with and without a surface primer. It is again worth noting that a full factorial experiment would require 54 (i.e. $6 \times 3 \times 3$) configurations, whereas the designed experiment requires only 18 configurations.

Figure 1.8 depicts the test results for the top five performing configurations. In all five cases, the joint strength requirement was exceeded by a factor of two. Once again the strip test method depicted in Fig. 1.7 was used to obtain these results. The non-linear portion of the curves near the origin is attributable to the small amount of “play” in the joint due to shrinkage of the injection-molded socket material. Then, the loading noted to increase linearly with respect to deflection until the peak load-carrying capability of the joint is reached. At this point, either the socket material filling the grooves sheared off or the pultruded sheared off on a transverse plane.

1.3 Conclusions

Based on the aforementioned testing, and considering cost and quality control, the results of the investigation can be summarized as follows:

- When machining grooves into the pultrusions, grinding is superior to cutting due to the nature of the glass-filled composite structure.
- Avoid attaching parts to pultrusions via through holes as the transverse planes of the pultrusion which are sheared by tensile loading have little strength.

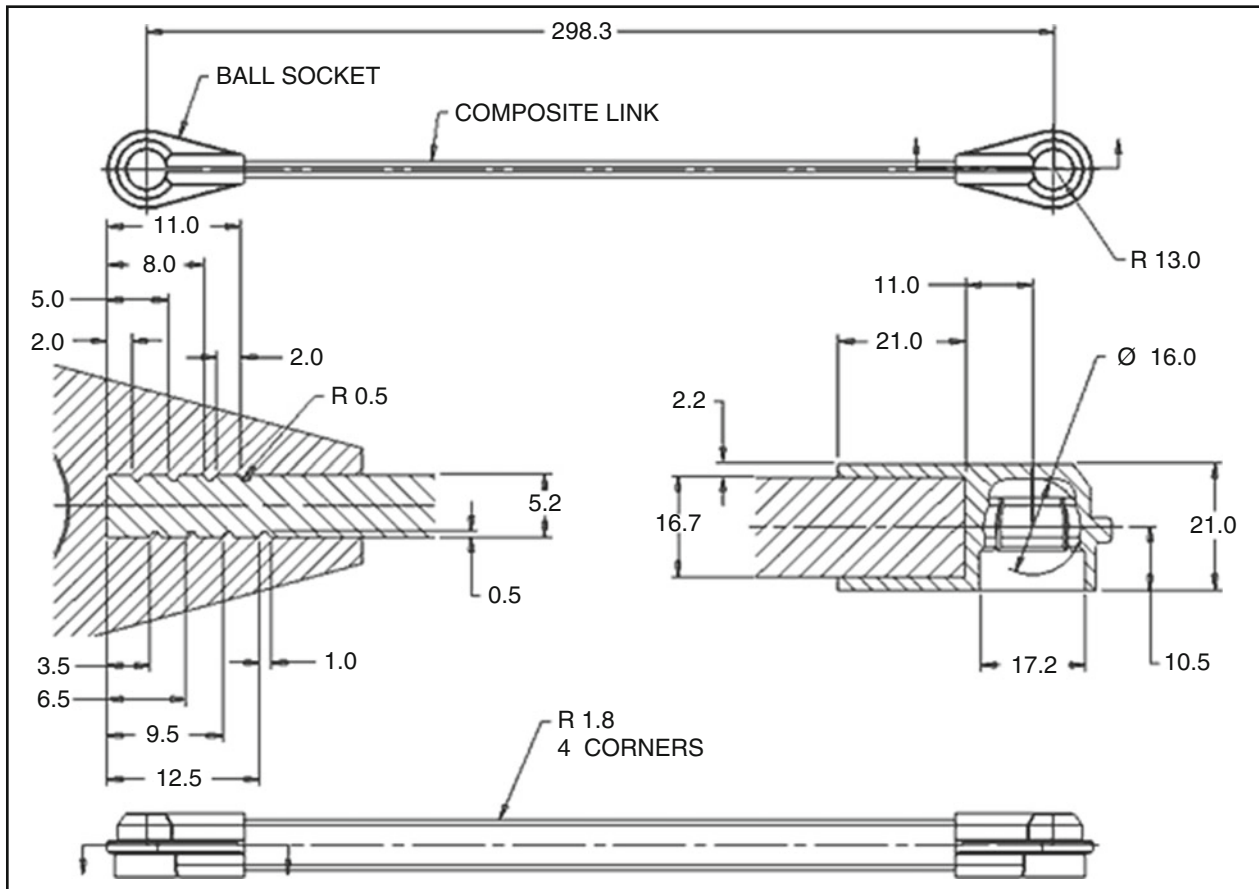


Fig. 1.9 Composite link socket attachment

- Grooves should be on the faces of the pultrusion having the greatest surface area (e.g. the top and bottom in the present design). Offsetting the grooves has been observed to make the design less susceptible to delamination.
- Numerous fine grooves are superior to a fewer coarse grooves.
- Adhesives can be used to significantly improve joint strength, but are noted to be difficult to process since they are very time-sensitive and difficult to control during the molding process.
- Surface roughness has minimal impact on joint strength. Due to the extra cost associated with this processing, it should only be considered when the load requirement cannot be satisfied otherwise.

In lieu of these assertions, the final, optimized groove configuration and dimensions of the joint between the sockets and the pultrusion is depicted in Fig. 1.9.

References

1. FMVSS 571-104, 49 CFR. Federal Motor Vehicle Safety Standards; Windshield Wiping and Washing Systems. National Highway Traffic Safety Administration, DOT, Washington, DC
2. Penrod, J., Dong, Y.: An Application Flexible Method to Limit the Loads in Windshield Wiper System. SAE Technical Paper Series, 2005-01-1835 (2005)
3. Penrod, J., Dong, Y., Buchanan, H. C.: A Novel Use of a Composite Material to Limit the Loads in Windshield Wiper System, SAE Technical Paper Series, SP-1575, 2001-01-0104 (2001)
4. Buchanan, H.C., Dong, Y.: Windshield wiping system, US Patent US 6,148,470, Valeo Electrical Systems (2000)
5. Buchanan, H.C., Dong, Y.: Windshield wiping system, US Patent US 6,381,800 B1, Valeo Electrical Systems (2002)
6. Bryson, B.A., Buchanan, H.C., Dong, Y., Penrod, J.P.: Windshield wiping system manufacturing method, US Patent US 068 81 373, Valeo Electrical Systems (2005)
7. Peace, G.: Taguchi Methods: A hands-On Approach to Quality Engineering. Addison, Reading, MA (1993)

Chapter 2

Analysis of a Composite Pi/T-Joint Using an FE Model and DIC

Chris Sebastian, Mahmoodul Haq, and Eann Patterson

Abstract An analysis of composite Pi/T-joint was performed through the comparison of a finite element simulation and experimental results obtained using digital image correlation. The finite element simulation was performed in ABAQUS using a realistically modeled adhesive layer consisting of cohesive zone elements. The composite Pi/T-joints were manufactured using vacuum assisted resin transfer molding (VARTM). The resulting Pi/T-joints were loaded in out-of-plane (web pull-out) until failure, during which three-dimensional digital image correlation (3D-DIC) was used to measure the in-plane displacements and strains.

From the experiments, it was found that the average peak pull-out force was 12.56 ± 0.82 kN, which was 10% less than that from the FE simulation at 13.77 kN. However, this does not give much information about whether the stress and strain distribution has been accurately predicted by the simulation. To better understand this, the experimental data obtained using DIC was compared to that from the FE simulation using image decomposition. The image decomposition process reduces the large, full-field data maps to a feature vector of 130 or so elements which can be compared much more easily. In this case, there was good agreement between the experiment and simulation, when taking into account the experimental uncertainty.

Keywords Composite joint • VARTM • Digital image correlation • Numerical simulation

2.1 Introduction

Composite Pi-joints are being extensively used in the marine and aerospace industries and are called T-joints, or Tee joints in some sectors. ‘T’ refers to the parts being joined while ‘Pi’ describes the shape of the preform used to form the joint. These joints are of special importance due to their complex geometry and criticality to overall structural integrity. T-joints are found at composite bulkhead-to-skin, rib-to-skin and spar-to-skin interfaces [1]. T-shaped stiffeners are extensively used in aircraft wings [1]. Additionally, the requirement for reduced structural weight and the ever-increasing demand for efficient aerospace structures has driven the development of adhesively bonded T-joints. However, these joints have been found to be sensitive to peel and, or delamination and through-the-thickness stresses. It has been reported that composite T-joints often fail near the web/skin interface [2].

Various configurations of composite T-joints have been studied extensively, mostly in the context of marine structures [3–18], including tee-joints made of sandwich panels [9–12]. The damage and failure analysis of such marine composite joints has also been studied [13–18]. A good overview on adhesively bonded composite joints is provided by Banea and Silva [19]. Moreover most of the aforementioned T-joints were manufactured by connecting the horizontal (flange) and vertical (web) laminates with a hand-layup laminate/skin (overlaminated). Similarly, literature on T-joints using a pi-preform (hence a Pi-joint) is relatively limited [20]. The use of Pi-preforms compared to hand-layup skins offers ease of manufacturing and speedy construction. Researchers from the Wright Patterson Air Force Research Laboratory (AFRL), Ohio, US, have studied adhesively bonded Pi-preform T-joints and also incorporated them in an aircraft wing and reported enhanced performance relative to a similar wing manufactured by conventional methods [2, 21, 22]. In addition, they tested the wings with T-joints

C. Sebastian (✉) • E. Patterson
School of Engineering, University of Liverpool, Liverpool L69 3GH, UK
e-mail: c.sebastian@liverpool.ac.uk

M. Haq
Composite Vehicle Research Center, Department of Civil and Environmental Engineering, Michigan State University, Lansing,
MI 48910, USA

in fatigue and found no failure in the joints [21, 22]. They reported considerable savings in manufacturing time (days instead of weeks) and up to 75 % reduction in costs. Apart from the AFRL study [2, 21, 22], the literature on pre-form Pi-joints is relatively limited. Hence, this work focuses on evaluating the pull-out performance using both structural tests to destruction and integrated experimental and simulation approach to analyzing the strain fields in structural Pi-preform composite T—joints.

In this work, the out-of-plane behavior or pull-out performance behavior of the composite Pi-joints was experimentally studied by using three-dimensional Digital Image Correlation (3D DIC). To the best of author's knowledge, the use of DIC to study the composite Pi-joints is unique and no other work has been reported, except the preliminary results reported earlier by the authors [23, 24]. The following sections provide brief details on the manufacturing process, materials used, and the experimental and numerical results.

2.2 Experimental Method

2.2.1 Manufacture of the Pi-joints

The Pi-joints of dimensions shown in Fig. 2.1 were manufactured by connecting flange and web plates with a Pi-preform and infusing the resin (adhesive) using vacuum assisted resin transfer molding (VARTM). The VARTM technique was also used to manufacture the glass fiber composite adherends (base and web plates) for the Pi-joints. The reinforcement used for the adherends was Owens Corning ShieldStrand S, S2-glass plain weave fabric with areal weight of 818 g/m². The base and web plates had 16 and eight layers of plain weave glass fabric respectively resulting in cured thicknesses of 9.53 mm (3/8 in.) and 4.76 mm (3/16 in.), respectively. The resin used was a two part toughened epoxy (SC-15, Applied Poleramic). The base and web plates were then connected with the Pi-preform and infused with SC-15 adhesive. The Pi-preform used was a carbon-fiber 3D woven preform (Albany Engineered Composites, Inc., Rochester, NH, USA.).

A constant adhesive bond-line thickness in Pi-joints was maintained by placing steel wires of 0.127 mm (0.005 in.) diameter in the bond-line. These spacers were placed strategically such that they did not influence the resulting performance. The tensile properties of the adhesive were obtained from experimental tests following the ASTM D638 standard. The fracture properties of the resin were obtained experimentally from Mode-I and Mode-II tests. The properties of the flange and web plates were also obtained experimentally. A summary of the material properties is provided in Table 2.1.

All bonded surfaces were grit-blasted and then cleaned with acetone. Figure 2.2 provides a step-by-step overview of the Pi-joint manufacturing process. Figure 2.2b shows the aluminum mold used to obtain the desired pi-preform dimensions. The aluminum mold has inlet and outlet pipe-fittings that attach to the vacuum pump and the resin-bath, respectively. The inlet

Fig. 2.1 Pi-joint dimensions (in mm) with the adhesive thickness omitted. Not to scale

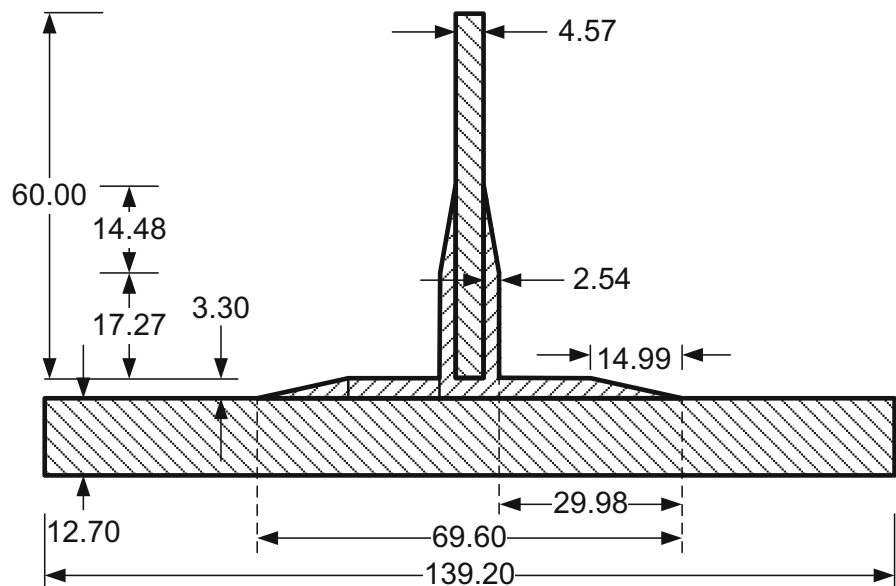
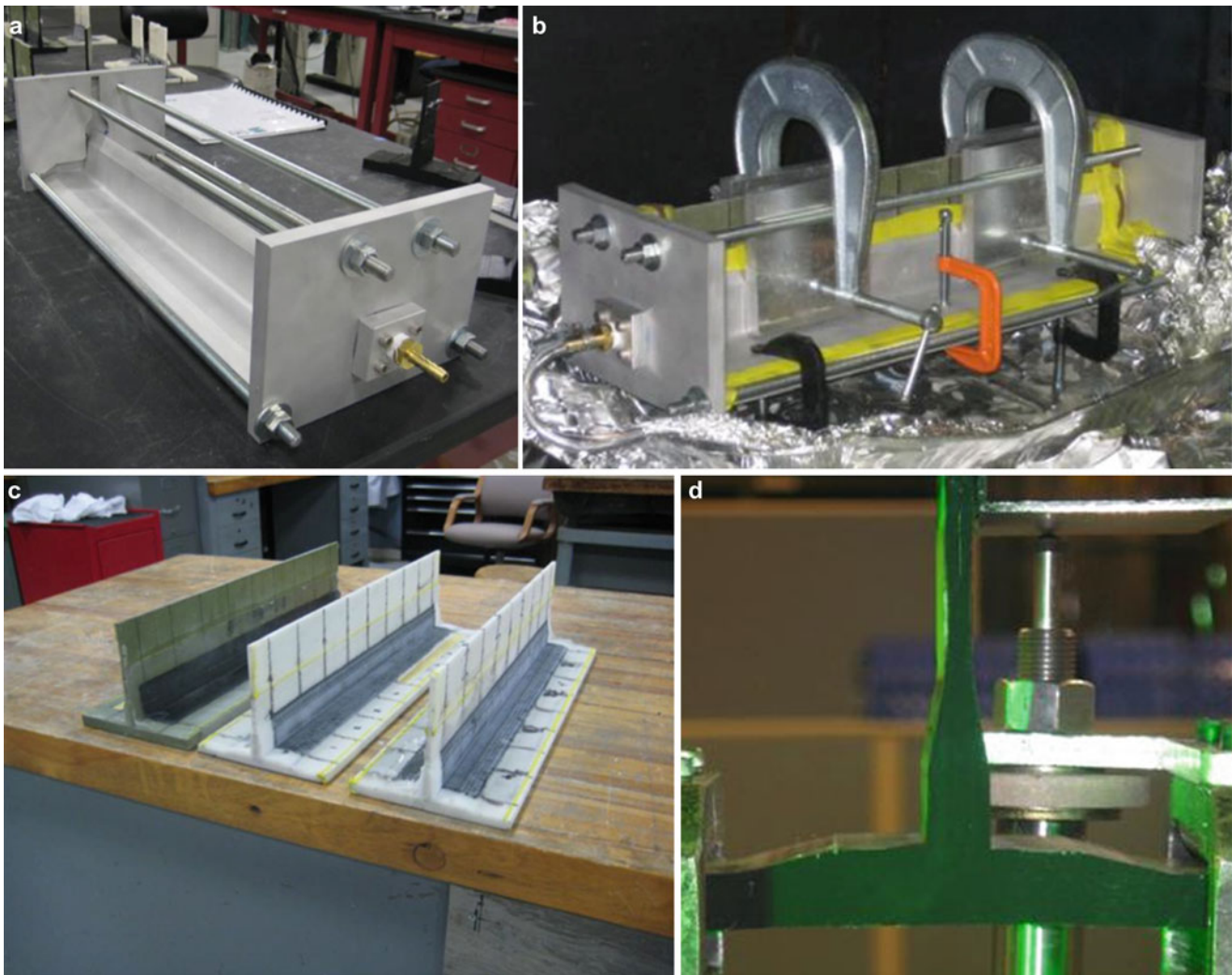


Table 2.1 Material properties used in the numerical simulation

(a) Adhesive tensile properties (experimental)	
Modulus (GPa)	2.69 ± 0.19
Tensile strength (MPa)	58.10 ± 3.94
Tensile failure elongations (%)	3.45 ± 0.37
(b) Adhesive fracture toughness [29]	
GI_c (N/m)	0.132
GII_c (N/m)	0.146
(c) Plates—GFRP (experimental)	
Web, tensile modulus (GPa)	17.25
Base, flexural modulus (GPa)	7.00
Poisson's ratio [5]	0.17
(d) 3D-Preform—CFRP [30]	
Elastic, isotropic modulus (GPa)	32.8
Poisson's ratio	0.17

**Fig. 2.2** Manufacturing of the Pi-joint using VARTM: (a) aluminum mold, (b) assembled pi-joint during VARTM, (c) completed pi-joints, and (d) a 50 mm wide section of pi-joint during a tensile pull-out test

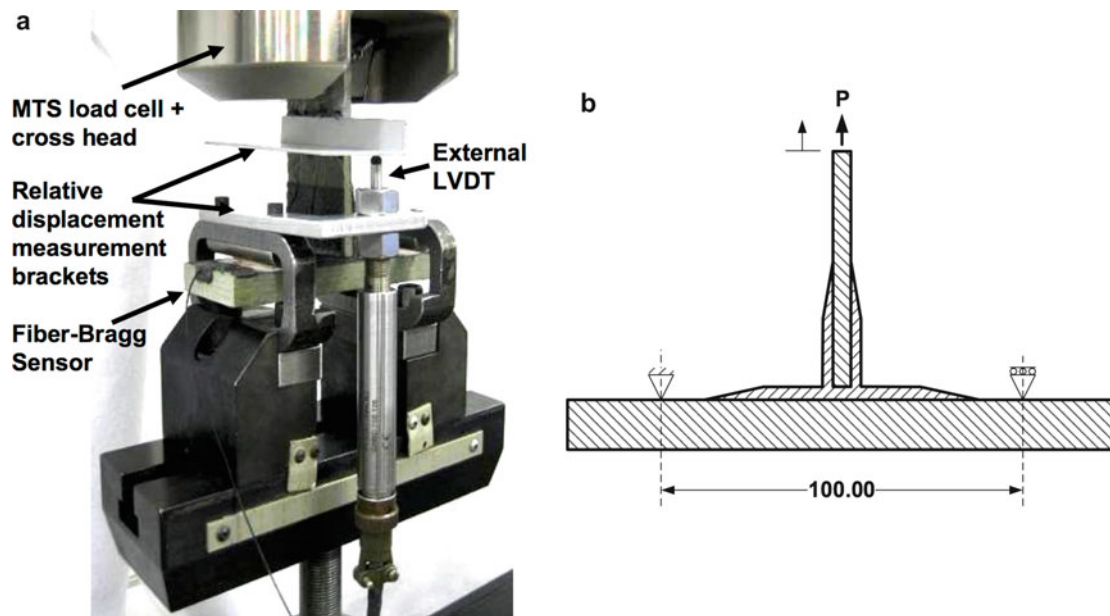


Fig. 2.3 Picture of a typical pull-out test setup (a); schematic of the experimental test setup (b)

and outlet are located just above the web-location of the Pi-preform. The permeability of the preform was found to be sufficient for successful manufacture of the Pi-joints, and hence, a distribution media was not required. The aluminum mold was fitted with end-plates and enclosed with vacuum tape prior to infusion as shown in Fig. 2.2c. The resin-infused joint was cured in a convection oven at 60 °C for 2 h and post cured at 94 °C for 4 h. The completed joints, which are shown in Fig. 2.2c, were then cut into sections of 50 mm wide using a water jet prior to being subjected to experimental testing as shown in Fig. 2.2d.

2.2.2 Pull-Out and Damage Resistance (DIC)

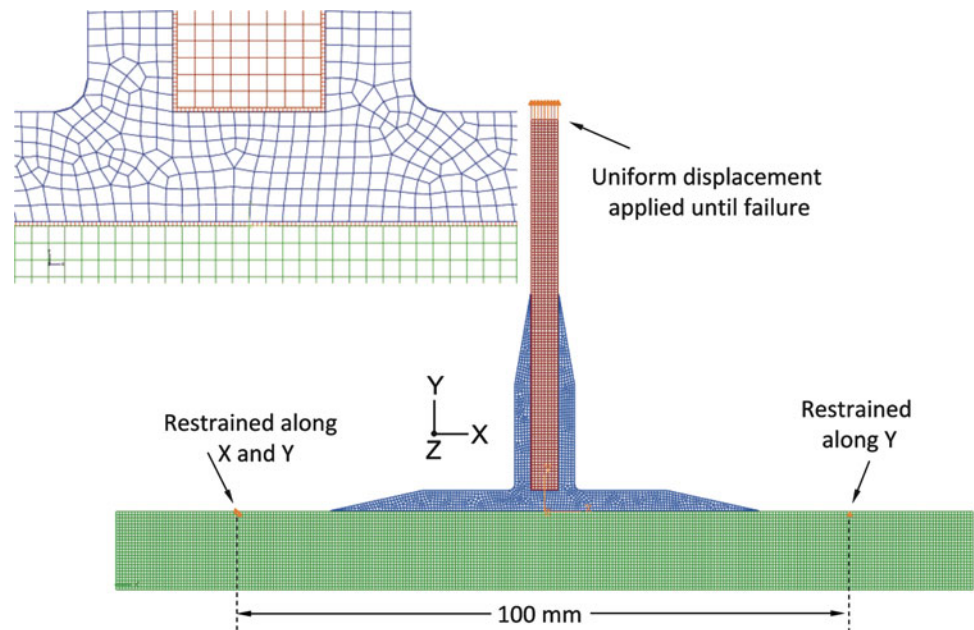
The out-of-plane behavior of the Pi-joints was evaluated by performing pull-out tests on the manufactured Pi-joints using a specially designed rig in a servo-hydraulic test machine, as shown in Fig. 2.3a. The specimens were tested at a loading rate of 1 mm/min until failure. The load and displacement from the test machine cross-head was recorded. Additionally, an external LVDT (linear voltage displacement transducer) was used to measure the relative displacement of the web with respect to the support.

In addition to the load and displacement values measured during the pull-out tests, a 3-D Digital Image Correlation system was employed to measure the full-field displacement and strains on the cut surface of the pi-joint. This was a commercially available DIC system (Dantec Dynamics Q-400) which consisted of a pair of cameras (AVT F-125B) along with a matched pair of lenses with a 12 mm focal length. Illumination was provided using a small panel of green LEDs. The cut surface of the Pi-joint was prepared by painting it first with a coat of matte white spray paint (Krylon matte white) and then misting with matte black (Krylon matte black) to provide the contrasting speckle pattern. Reference images for the correlation process were captured with a small pre-load applied to the joint, in order to remove any slack from the experimental setup. Images were then captured in 500 N increments up until failure of the joint occurred.

2.3 Numerical Simulations

An integrated approach to numerical simulations and experiments was taken with the intention of using simulations to facilitate the design of the experiments, sensor placement and also to support the interpretation of the experimental data, as well as creating a validated numerical model that could be used in future design work with a high-level of confidence. In this work, simulations of Pi-joint pull-out behavior were performed using a commercially-available finite element package, ABAQUS® [25].

Fig. 2.4 Details of the FE model showing the boundary conditions and applied loading. The *inset* shows a more detailed view of the mesh with the quadrilateral elements and the adhesive elements



A two-dimensional plane-stress model of the Pi-joint was created in ABAQUS®. The web, flange and the pre-form were created as separate parts for ease of defining the properties and also the meshing. The adhesive was also created as a separate part but with a much finer mesh using cohesive elements. The adhesive surfaces were appropriately connected with respective surfaces of the web, flange and pre-form to assemble the model. Models that reproduced the three cases studied in the experiments were analyzed.

2.3.1 Mesh, Gap Creation and Material Models

Four-node quadrilateral plane-stress elements were used to mesh all the parts of the model in ABAQUS®. All parts were given an out-of-plane thickness of 50 mm corresponding to the width of the Pi-joint in the experiment. The flange, web and Pi-preform were modeled as linear elastic materials. An element size of 0.5 mm was used for all parts except the adhesive layers. A meshed finite element model for a Pi-joint is shown in Fig. 2.4. For adhesive layers, cohesive elements, the mesh was more refined as illustrated in the inset of Fig. 2.4. The element size of cohesive elements was equal to bond-line thickness (0.005 in., 0.127 mm), and an aspect ratio of 1 (unity) prior to load application. The adhesive was modeled in greater detail using cohesive elements and the delamination was simulated using a traction-separation material model [25]. The damage evolution was modeled in ABAQUS by defining the fracture energy as a function of the mixed modes using the analytical power law fracture criterion. The material properties used in the simulations are provided in Table 2.1.

2.3.2 Boundary Conditions and Loading

The loading pattern and boundary conditions used in the experiments were replicated in the finite element models. A schematic of the FE model is provided in Fig. 2.4. It has been reported that the number of degrees of freedom at the constraints and the angle of loading play a vital role in the accuracy of the results [6]. Kesavan et al. [6] simulated marine composite T-joints and applied the loading at an angle of 0.55° to the positive Y-axis in Fig. 2.4, to take into account manufacturing inconsistencies, and found good agreement with their experimental results. In this work, the web was assumed to be perfectly perpendicular and the angle of loading was not considered. The applied load was distributed along the top nodes in the web. The model was constrained symmetrically at two points on the flange simulating a simply-supported condition with a total span of 100 mm. The left-hand side support constraint does not permit translation in either the X- or Y-direction while the right-hand support constraint does not permit translation in the Y-direction. All simulations were performed on an eight-core 3.16 GHz machine with 64 gigabytes of RAM.

2.4 Results and Discussion

2.4.1 Experimental Pull-Out Results

Figure 2.5 provides the pull-out performance of the Pi-joints from the experiments. The general failure mode in the experiments for the Pi-joints consisted of an increasing load until failure, which led to the separation of the Pi-preform from the base. The failure was instantaneous and the direction of failure propagation could not be seen with the naked eye. A high-frame rate camera would be required to confirm the propagation path of failure. Since symmetric failure initiation was observed, the delamination propagation was also expected to be symmetric. Instead an asymmetric failure was observed. Such a discrepancy may be caused by a combination of eccentricity in load application and manufacturing flaws. The use of a brittle adhesive, like the one used in this work, makes the joint highly susceptible to manufacturing flaws and less tolerant to damage.

2.4.2 Digital Image Correlation Results

Digital Image Correlation was used to capture the displacement and strain on the cut surface of the Pi-joint as it was loaded in the tensile test. The images were processed using commercial software (Dantec Dynamics Istra 4D) to calculate the displacements and strains in the Pi-joint. A facet (or subset) size of 25 pixels was used, with an offset (or shift) of 15 pixels. The measured surface strain in the x-direction is shown in Fig. 2.7 at an applied load of 3 kN. The two red boxes indicate the areas for comparison with the FE results.

2.4.3 Numerical Simulation Results

The finite element (FE) simulations successfully modeled the complete pull-out response of the damaged and undamaged Pi-joints and the results are shown in Fig. 2.5. Figure 2.6 shows the failure mechanisms observed in the FE simulation. The initial onset of failure occurs in the web/Pi region (see inset in Fig. 2.6) and continues asymmetrically on one side of the web. This onset of failure does not reduce the load carrying capacity as the load transfer continues mostly across the other bonded

Fig. 2.5 Comparison of the complete pull-out response of the experiment and the FE simulation

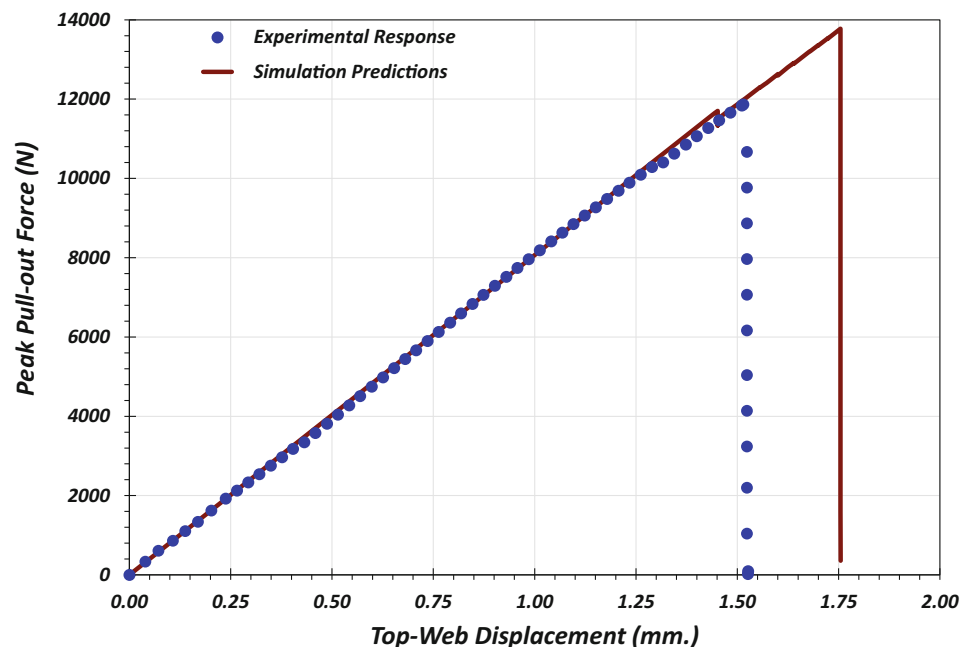


Fig. 2.6 Failure mechanism for the pi-joint in the simulation

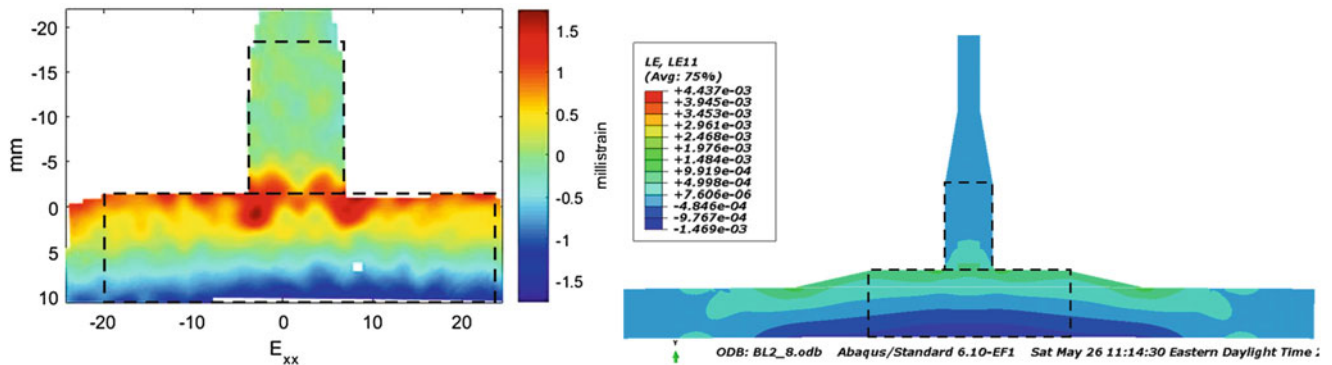
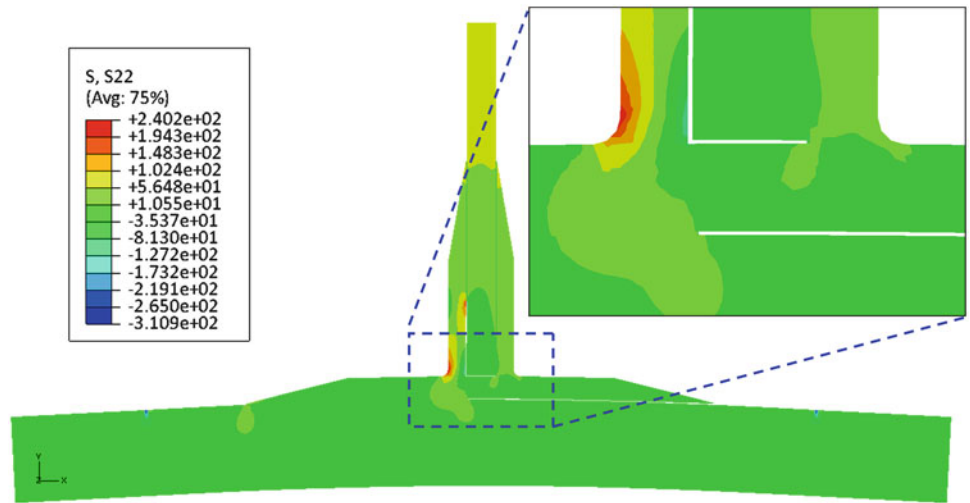


Fig. 2.7 Comparison of the principal strain from DIC (*left*) and FE (*right*). The highlighted boxes indicates where there the image decomposition comparison was performed

side of the web/Pi. As the applied load increases, the subsequent onset of failure occurs in the adhesive/bond between the preform and the base. This failure initiated from the termination of the preform with the base and continues until separation of the Pi-preform from the base.

The peak pull-out loads from the simulations agreed very well with the average experimental data as shown in Fig. 2.5. Similar load eccentricity and mis-alignment issues have been reported by Kesavan et al. [6] who applied the pull-out load at an angle of 0.55° counterclockwise to the vertical axis (web) in order to obtain better agreement between experimentation and computational results. Such modifications were not considered made in this study and all loads were applied to the web.

Additionally, the experimental data provided in Fig. 2.5 shows the standard deviation (as error bars) for each Pi-joint studied. The variation in experimental data may be due to many factors including manufacturing inconsistencies, variation in material properties of constituents, errors induced in experimental test-setup, instruments etc., Similarly, the numerical simulations assume average material properties and ideal test configurations.

2.4.4 Comparison of DIC and FE Using Image Decomposition

Although the pull-out force data matched well between the experiments and the simulation, it was desired to perform a more thorough validation of the simulation. Figure 2.7 shows the measured strain in the x-direction from the DIC experiment (left) compared to the x-strain found from the FE simulation (right). A recently published CEN document [26] recommends the use of image decomposition using Tchebichef polynomials to make quantitative comparisons of measured and predicted strain fields as part of a model validation process, This approach, which has been used previously to validate models of a

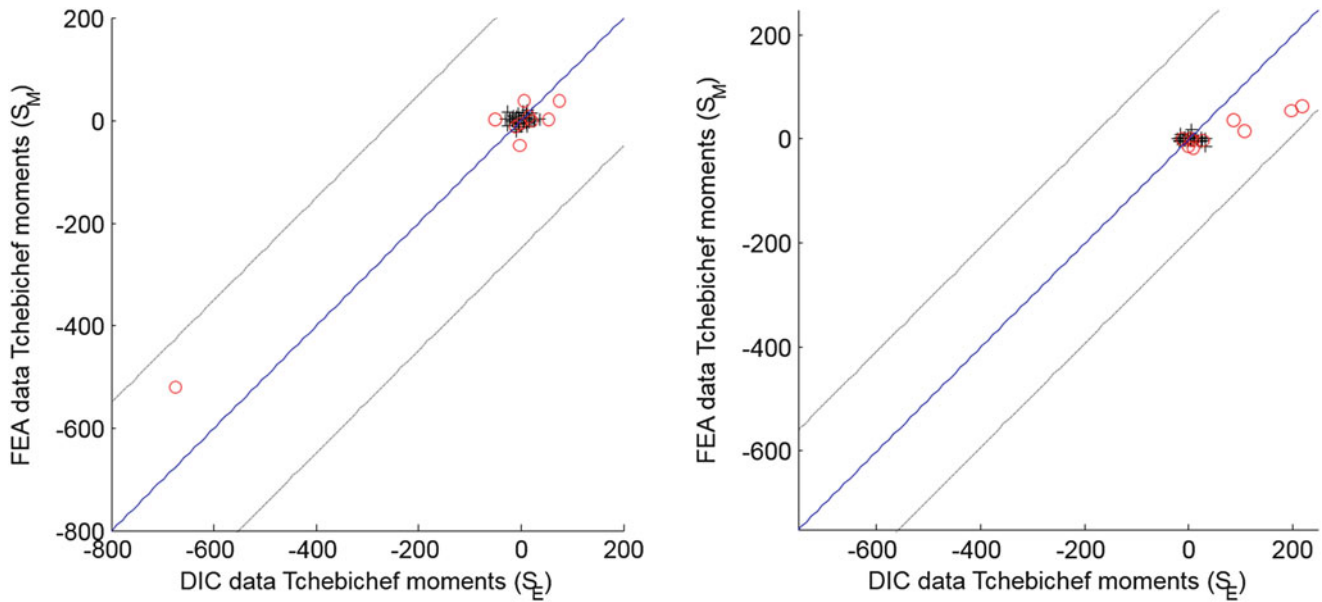


Fig. 2.8 Comparison plots of the most significant moments from the experiment and the simulation for the horizontal section (*left*) and the vertical section (*right*). If the data were in perfect agreement, all points would fall on a line with a gradient of unity (*solid line*) the dashed lines represent confidence bands equal to twice the uncertainty in the data from the experiments

vibrating plate [27] and a composite protective panel [28], was adopted here. The image decomposition using the discrete Tchebichef moments can only be performed over a rectangular domain, so the pi-joint was divided into two sections for analysis. One rectangular patch was taken from the vertical section, and another from the horizontal section.

The Tchebichef polynomials were used to represent the strain component in the x-direction from both the experiment and the simulation following the procedure described in [28]. A reconstruction of the original strain image was performed from the Tchebichef coefficients to ensure that they were an accurate representation of the original data. In this fashion, 136 coefficients were used to represent the strain data from the vertical section and 176 coefficients from the horizontal section. The larger number of coefficients required to describe the horizontal section would indicate that the strain distribution was more complicated in this region.

The decomposition was performed on both the experimental and simulation data sets, producing a set of coefficients representing each strain field. These coefficients were then plotted against each other for the horizontal and vertical sections, as shown in Fig. 2.8. The experimental coefficients were plotted along the x-axis, and the simulation coefficients along the y-axis. If there were perfect agreement between the two sets of coefficients, the points would all lie along the line with gradient of unity (solid line in the figure).

Deviation from this line indicates differences between the experimental and simulation data sets. In reality, uncertainty in both the experiment and the simulation will cause deviations, and so it is unrealistic to expect all the points to fall on this line. For that reason, Fig. 2.8 has been plotted along with confidence bounds (dashed lines) which relate to the experimental uncertainty. The bands are defined by combining of the uncertainty from the experiment and from the image decomposition reconstruction process. For the case shown here, all of the moments fell within the confidence bounds. The points are primarily concentrated along the solid line, but there are a few moments close to the dashed lines, particularly in the comparison of the vertical section.

2.5 Conclusions

The performance of adhesively bonded structural composite Pi/T-joints was evaluated by experimental pull-out tests and numerical simulations. The values of the peak pull-out force recorded experimentally matched well with those from the numerical simulation (~10% difference). The vacuum assisted resin transfer molding (VARTM) technique was found to be a successful technique to produce Pi/T-joints. 3-D digital image correlation was used to capture the displacements and strains in the pi-joint during the pull-out tests. The CEN procedure for making quantitative comparisons of measured and predicted

strain fields was applied using image decomposition. The simulation was found to produce acceptable results within the confidence bounds provided by the uncertainty in the experiment. Experimentally validated simulations can be used to further understand the behavior of Pi-joints with other joint configurations and also to understand damage-induced behaviors beyond the case explored in this work, and such validated simulations have great potential in use as a design tool.

Acknowledgements This work was supported by the U.S. Army and ONR under TACOM/MSU Cooperative Agreement No. W56HZV-07-2-0001 and in collaboration with US Army TARDEC. The authors are thankful to Albany Engineered Composites Inc., NH, USA, for supplying the 3D-woven Pi-preforms. EAP was the recipient of a Royal Society Wolfson Research Merit Award.

References

- Stickler, P.B., Ramulu, M.: Investigation of mechanical behavior of transverse stitched T-joints with PR520 resin in flexure and tension. *Compos. Struct.* **52**, 307–314 (2001)
- Flansburg, B.D., Engelstad, S.P.: Robust design of composite bonded Pi joints. 50th AIAA/ASME/ASCE/AHS/ASC Structures, Structural Dynamics, and Materials Conference. Palm Springs, CA (2009)
- Dulieu-Smith, J.M., Quinn, S., Sheno, R.A., Read, P.J.C.L., Moy, S.S.J.: Thermoelastic stress analysis of a GRP Tee Joint. *Appl. Compos. Mater.* **4**, 283–303 (1997)
- Marcadon, V., Nadot, Y., Roy, A., Gacougnolle, J.L.: Fatigue behavior of T-joints for marine applications. *Int. J. Adhes. Adhes.* **26**, 481–489 (2006)
- Li, H.C.H., Dharmawan, F., Herszberg, I., John, S.: Fracture behavior of composite maritime T-joints. *Compos. Struct.* **75**, 339–350 (2006)
- Kesavan, A., Deivasigamani, M., John, S., Herszberg, I.: Damage detection in T-joint composite structures. *Compos. Struct.* **75**, 313–320 (2006)
- Sheno, R.A., Violette, F.L.M.: A study of structural composite tee joints in small boats. *J. Compos. Mater.* **24**, 644–666 (1990)
- Sheno, R.A., Hawkins, G.L.: Influence of material and geometry variations on the behaviour of bonded tee connections in FRP ships. *Composites* **23**, 335–345 (1992)
- Hicks, I.A., Read, P.J.C.L., Sheno, R.A.: Tensile compressive and flexural characteristics of tee-joints in foam-cored sandwich structures. *Proc. 3rd Int. Conf. Sandwich Construction*, 579–590 (1996)
- Sheno, R.A., Read, P., Jackson, C.L.: Influence of joint geometry and load regimes on sandwich tee joint behaviour. *J. Reinf. Plast. Compos.* **17**, 725–740 (1998)
- Dulieu-Barton, J.M., Earl, J.S., Sheno, R.A.: Determination of the stress distribution in foam-cored sandwich construction composite tee joints. *J. Strain Anal. Eng. Des.* **36**, 545–560 (2001)
- Toftgaard, H., Lystrup, A.: Design and test of lightweight sandwich T-joint for naval ships. *Compos. Part A: Appl. Sci. Manuf.* **36**, 1055–1065 (2005)
- Theotokoglou, E.E., Moan, T.: Experimental and numerical study of composite T-joints. *J. Compos. Mater.* **30**, 190–209 (1996)
- Theotokoglou, E.E.: Study of the numerical fracture mechanics analysis of composite T-joints. *J. Reinf. Plast. Compos.* **18**, 215–223 (1999)
- Dodkins, A.R., Sheno, R.A., Hawkins, G.L.: Design of joints and attachments in FRP ships' structures. *Mar. Struct.* **7**, 365–398 (1994)
- Theotokoglou, E.E.: Strength of composite T-joints under pull-out loads. *J. Reinf. Plast. Compos.* **16**, 503–518 (1997)
- Rispler, A.R., Steven, G.P., Tong, L.: Failure analysis of composite T-joints including inserts. *J. Reinf. Plast. Compos.* **16**, 1642–1658 (1997)
- Phillips, H.J., Sheno, R.A.: Damage tolerance of laminated tee joints in FRP structures. *Compos. Part A: Appl. Sci. Manuf.* **29**, 465–478 (1998)
- Banea, M.D., da Silva, L.F.M.: Adhesively bonded joints in composite materials: an overview. *J. Mater. Des. Appl.* **223**, 1–18 (2009)
- Haq, M., Patterson, E.A., Drzal, L.T.: Pull-out behavior of adhesively bonded composite Pi-joints: damage modeling and comparison with experiments. *Proceedings of the 25th Annual Technical Conference, American Society of Composites*, Dayton, OH (2010)
- Online: Air Force Print News. http://www.wpafb.af.mil/news/story_print.asp?id=123035046 (2009). Accessed 16 Sept 2009
- Russell, J.D.: Composites affordability initiatives. *Adv. Mater. Process.* **165**, 29–32 (2007)
- Haq, M., Conway, A., Patterson, E.A.: A study on damage-induced behavior of bonded Pi-/T-joints using digital image correlation (DIC) and FE modeling, 2012 SEM XII, International Congress and Exposition on Experimental and Applied Mechanics, Costa Mesa, CA (2012)
- Sebastian, C., Haq, M., Conway, A., Patterson, E.A.: Comparison of FE and DIC measurements of a Pi-joint using feature vectors, 2012 SEM XII, International Congress and Exposition on Experimental and Applied Mechanics, Costa Mesa, CA (2012)
- Simulia, I.: Abaqus/CAE Version 6.8-2 (2008)
- CWA16799. Validation of Computational Solid Mechanics Models. Comité Européen de Normalisation, Brussels (2014)
- Wang, W., Mottershead, J.E., Ihle, A., Siebert, T., Reinhard Schubach, H.: Finite element model updating from full-field vibration measurement using digital image correlation. *J. Sound Vib.* **330**(8), 1599–1620 (2011)
- Sebastian, C.M., Patterson, E.A., Ostberg, D.: Comparison of numerical and experimental strain measurements of a composite protective panel using image decomposition. *Appl. Mech. Mater.* **70**, 63–68 (2011)
- Bucinell, R.B.: *Composite materials fatigue and fracture*, vol. 7. STP-1330 ASTM, PA (1998)
- Truong, T.C., Vettori, M., Lomov, S., Verpoest, I.: Carbon composites based on multi-axial multi-ply stitched preforms: part 4, mechanical properties and damage observation. *Compos. Part A: Appl. Sci. Manuf.* **36**, 1207–1221 (2005)

Chapter 3

5xxx Aluminum Sensitization and Application of Laminated Composite Patch Repairs

Daniel C. Hart

Abstract Sensitization can occur in 5xxx aluminum alloy utilized in welded ship structures. Cumulative exposure of plating to elevated temperatures causes magnesium in the aluminum to migrate to the grain boundaries and develop a corrosion cell. As a result, the sensitized plate is susceptible to intergranular corrosion, which when exposed to salt water and stress leads to stress-corrosion cracking (SCC), typically at stress levels below nominal plate strength. SCC typically occurs at a level of sensitization that renders welded repairs impractical, requiring an alternative methodology. One alternative to traditional welded repair of marine structures is the application of a composite patch. Composite patch repairs have seen significant use by the aerospace community on thin aluminum aircraft skins to address stress related cracking while only limited use on thicker marine structures. Patches for marine structures have demonstrated their ability to mitigate crack growth, inhibit water ingress, and reinforce damaged or degraded structure for commercial and military vessels. The use of composite patches for repair of SCC onboard U.S. Navy ships began in December of 2010. Patch design and installation are supported by ASTM material testing, environmental conditioning, large center crack tension fracture mechanics specimens, and experience with a full scale plate ductile tearing test. Patch repairs patches are installed in-situ with vacuum consolidated hand laminations and have demonstrated the ability to increase static plate strength, fatigue life, large displacement capacity of the crack plate, and durability for in-service applications.

Keywords Composite • Sensitization • Aluminum • Fatigue • Stress corrosion cracking

3.1 Background

Aluminum became a common material for use in ship structures in the 1960s with destroyers for the Netherlands Navy, frigates of the British Royal Navy, and U.S. Navy vessels from patrol boats to frigates. Early issues included galvanic corrosion of plating resulting in exfoliation and fatigue cracking of aluminum superstructures on steel hulls. These issues were corrected by updating the temper of the alloys. Recent times have seen an increasing number of Navy and maritime ships constructed of welded aluminum, either hull or topside, or in the case of high speed catamarans and the independence class of littoral combat ships (LCS) both the hulls and topside structures. Marine grade 5xxx aluminum alloys are used because of their corrosion resistant and residual weld strength characteristics. These enhanced characteristics are developed in part by the magnesium content of the alloy, which is typically greater than 3%.

Ships and superstructures constructed of welded aluminum have generally proven to be rugged while in service, and easily modified for alterations and modernizations. Damage to these structures occurs in service from accidental causes, battle damage, fatigue fracture, corrosion, or sensitization of aluminum structure. The primary method for repair of aluminum structure requires welding and material replacement, though decreasing maintenance budgets and increased operational requirements are increasing the demand and frequency of lower cost alternatives. An additional driver for alternative repair methods is the fact that high magnesium content 5xxx alloys are susceptible to sensitization in months to years when subjected to elevated temperatures [1]. Then, starting in the early 2000s sensitization was identified as a significant issue for high speed aluminum marine vessels [2] and for the U.S. Navy's CG-47 class ship superstructures [3]. A high degree of sensitization makes welding impractical or infeasible. This is where repairs such as composite patches and bonded aluminum repairs have filled the gap to support fleet needs.

D.C. Hart (✉)

Naval Surface Warfare Center, Carderock Division, 9500 MacArthur Blvd., West Bethesda, MD 20817, USA

e-mail: daniel.c.hart@navy.mil

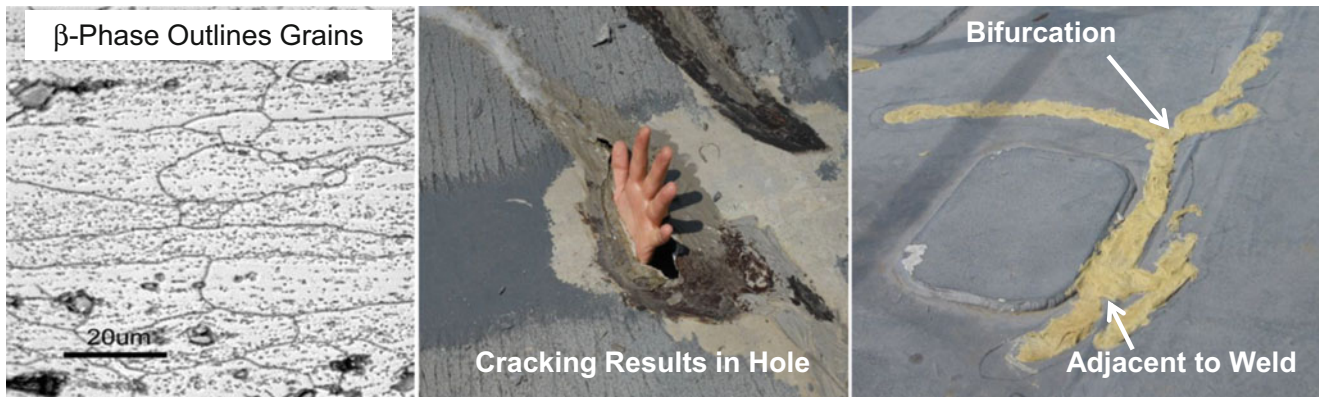


Fig. 3.1 Sensitized grain structure and the results of stress corrosion cracking

Sensitization is the cumulative exposure of 5xxx aluminum to elevated temperatures causing the magnesium in the alloy to migrate to the grain boundaries. This migration eventually develops a corrosion cell when the magnesium precipitate forms a continuous network around the grains considered intergranular corrosion. Exposing the intergranular corrosion to salt water and stress, levels typically well below nominal plates strength, results in stress-corrosion cracking (SCC). SCC typically occurs when plate becomes highly sensitized, and in some cases the level of sensitization makes welding not possible. In the most severe cases SCC resulted in loss of a small section of deck plating or large bifurcating cracks adjacent to recent weld repairs as shown in Fig. 3.1.

The level of sensitization currently governs the repair method used to address damage or cracking. Several methods exist to determine the level of sensitization in the material. Detection of the sensitization level can be performed using a destructive test such as the ASTM G67 mass loss [4], or with non-destructive means such as detailed visual inspection or the Degree of Sensitization (DoS) probe, the later measures electric current due to a localized chemical reaction [5]. All methods produce a value comparable to the G67 mass loss. Aluminum repair guidance exists for three ranges of mass loss values as shown in Fig. 3.3. Starting on a plate where simple welding can be performed, as the sensitization increases pre-welding cold working of the material must be performed, and finally component replacement when the sensitization has progressed far enough welding is not permitted [5, 6]. Additionally, alternative methods are needed when welding is not permitted due to time or safety concerns, such as proximity to combustible liquid or gas or other ignitable material.

One alternative to traditional welded repair of marine structures is the application of a composite patch. Composite patch repairs of metallic aircraft structures were pioneered in the 1970s and 1980s with work in both Australia and the US [7–11]. Development of aircraft patch repairs continued through mechanical testing, design method development, and analysis efforts [12–16]. Typical repairs were performed on thin aluminum aircraft skins to address stress related cracking. Composite patch repairs of marine structures have seen increasing use, demonstrated their ability to mitigate crack growth, inhibit water ingress, and reinforce damaged or degraded structure. Allan and Clark examined the strength of carbon-epoxy patches applied to the fatigue or over stressed areas of the aluminum superstructure on British Royal Navy Type 21 Frigates. Repair performance was backed up with fatigue testing of butt-joints and welded aluminum joints with and without double sided composite patches. Cracks were weld repaired followed by application of a carbon epoxy patch for six ships in the class; patch repairs were in service for 10 years prior to sale [17]. The Royal Australian Navy experimented with carbon fiber vinyl ester composite patches on FFG-7 class frigates to address an overstressed region of the deckhouse [18, 19]. Composite patches were large, 5 m × 1 m × 1.25 cm thick, and were designed to carry longitudinal seaway loads at the top level of the deckhouse at the midship dog-bone section. Fiber, resin, and, surface preparation procedure selections were made following material characterization, environmental conditioning, Boeing wedge testing, and lap shear testing efforts. After 15 years of service, maintenance, and repairs the composite patches were considered a success [20]. Carbon composite patches designed with cross sectional stiffness matching that of the base metal were applied to the UK's Royal Navy Type 42 Destroyers, and also commercial off-shore oil platforms. Patch repairs of steel food tray lift shafts onboard the Type 42 destroyers offered a cost and time efficient repair method to address the cracking. Seven ships and 35 patches were applied using hand layup, infusion, and pre-preg installation methods performed successfully in restricted spaces [21]. Following these successes, QinetiQ installed composite patch repairs to floating production storage and offloading (FPSO) oil ship platforms, especially since a weld repair or “hot-work” is dangerous and restricted onboard FPSO's. Performing hot-work requires gas free environment and oil free tanks for a minimum of two bulkheads in any direction, which is a costly endeavor. In contrast,



Fig. 3.2 U.S. Navy composite patch repair examples

composite patch repairs do not require hot-work, and in 2002 QinetiQ repaired the steel structure of an FPSO ballast tank with an adhesively bonded pre-preg repair [21]. In the early 2000s, Det Norske Veritas (DNV) researched composite patch repairs of FPSO structure to address corrosion and fatigue cracking. This resulted in current DNV recommended practice for design, fabrication, operation, and qualification of bonded repairs on steel structure [22–24]. More recently, as shown in Fig. 3.2, U.S. Navy patches have been installed and in service on aluminum superstructure of 11 ships starting in December of 2010 [5, 25].

3.2 Sensitization and Detection

Magnesium content has been identified as the root cause of 5xxx aluminum being susceptible to sensitization. Marine grade alloys have magnesium contents that range from 2.2 to 5.5%, those that have greater than 3% magnesium content are super saturated and allow small amounts of magnesium to precipitate to the grain boundaries as temperature exceeds 40–65 °C [1, 5]. From a simple sail plane study reported by Greene, solar heating combined with ambient temperature and surface color can drive surface temperatures beyond 50 °C [26]. Ship structure operating in tropical environments consistently achieve surface temperatures at which sensitization begins. Enough time at temperature leads to the formation of a continuous film of beta phase (Mg_2Al_3) at the grain boundaries. Beta phase is anodic, and when exposed to moisture a corrosion cell leads to intergranular corrosion, and the plate becomes brittle [6]. Applying stress to the degraded plate results in SCC at stress levels below design limits and when subjected to fatigue stresses the crack growth rate increases [27]. Stress can be from solar or thermal loads, longitudinal bending from sea way motion, local equipment or systems, and welding. Performing a weld repair of SCC requires knowledge of the level of sensitization.

Detection of plate sensitization level can be performed using a destructive test or with non-destructive means such as detailed visual inspection or the Degree of Sensitization (DoS) probe. The primary destructive method for measuring the DoS is ASTM G67 nitric acid mass loss test (NAMLT), which measures the amount of specimen mass lost in mg/cm^2 [4]. Mass loss is measured using nitric acid to dissolve the beta phase from a 50 mm by 6 mm specimen. Specimens are typically extracted from shipboard material using a hole saw leaving 75 mm diameter or larger hole in the structure that must now be repaired. Visual techniques are being developed to optically measure the amount of beta phase particles at the plate surface, and estimate a mass loss value. Initial efforts successfully matched probabilistically processed digital image analysis results of laboratory prepared specimens to ASTM G67 measurements [28]. One of the non-destructive methods requires etching and polishing a 25–50 mm square area to a 0.5 μm finish, and utilizing an image magnification in the $\times 400$ –600 range to show clear contrast between grain and beta-phase material. Without the ability to digitally analyze the image onboard the ship, a catalog of images with known sensitization levels is being compiled for in-situ identification of the sensitization level [5]. Lastly, another non-destructive method that is being employed at the RMC's uses a portable non-destructive degree of sensitization (DoS) probe. This method requires removal of surface coatings and abrasion of a 100×100 mm area of the surface with 1200 grit abrasive. The DoS probe measures the electric current due to a localized chemical reaction as nitric acid dissolves the surface beta-phase [29]. The results have been calibrated for 5456 aluminum and are currently used by repair and maintenance center (RMC) personnel to determine the degree of sensitization. Continued development is underway to calibrate the results from the DoS probe for 5083 aluminum [5].

3.3 Mitigation and Repair of Sensitized Aluminum

Knowledge of the DoS governs the scope and methodology for repairing the affected structure. Typical repair methods implemented on marine structures utilize metal inert gas (MIG) welding techniques. Repair scope ranges from direct welding of a small crack to large scale crop out and complete replacement with new material. For some repairs cold working of the surrounding material prior to welding can improve residual strength of the repair. When welding is not an option, an alternative repair method such as mechanically fastened or adhesively bonded reinforcement is needed. Limitations and guidance on repair methods (Fig. 3.3) are based on the DoS from G67 test data, or alternative equivalent to mass loss testing. G67 material mass loss values below 30 mg/cm² are considered weldable, from 30 to 60 mg/cm² are weldable but require cold working, and above 60 mg/cm² indicates the material is not weldable and requires an alternative repair method [5].

Repair methods include cold working the aluminum, advanced welding processes to reduce the heat imparted on the plating, and adhesively bonding metallic or composite reinforcements to the affected structure. Finally, new and updated aluminum materials have been developed to reduce or eliminate sensitization such as the H128 temper.

3.3.1 Weld Repair

Sensitization levels below 30 mg/cm² can be repaired with welding. Basic repair of cracks can be performed by grinding the crack and re-welding. Often the search for weldable material requires cropping areas of highly sensitized plate and replacing the removed material with new plate and welding that to the existing structure. Repair material typically matches the existing alloy and is either the same thickness or thicker to mitigate sensitization. New or advanced materials developed to resist sensitization can be substituted as replacement plate.

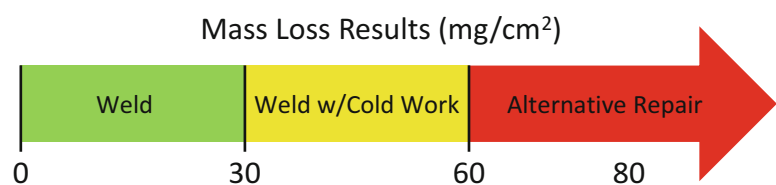
Research into sensitization and material processing has led to the development of a new temper, H128, registered with the Aluminum Association for 5083 alloys but can also be produced as 5456 alloys [5]. The H128 temper was developed to extend the new ASTM B928 specification, which only sets requirements for “as delivered” plate, and does not include requirements related to sensitization rates. Bushfield et al. discussed the background of establishing the ASTM B928 specification [2]. Cracking and corrosion that occurred on high speed aluminum vessels was directly linked to the use of plate manufactured to ASTM B209 specifications but delivered in a sensitized condition. The new standard, B928, requires as delivered plate to pass both ASTM G66 and G67 tests. This, however, only qualifies the as-delivered plate and does not specify sensitization rate during service. The updated temper, H128, extends ASTM B928 requirements to include a 7 day 100 °C treatment prior to the ASTM testing and also meets all of the H116 temper requirements [5]. Designing the temper to meet these strict requirements should limit the rate of sensitization under normal ship operating conditions.

Another alternative material to prevent sensitization is the recently developed Novelis Fusion plate produced by Novelis Inc. using their patented casting method (US Patent 7,472,740). The patented process produces a single cast aluminum ingot sandwich with outer layers of low magnesium content alloy and high magnesium content 5456 alloy core. This ingot can then be rolled to produce plate of the desired thickness. Using a sandwich structure isolates any beta phase that forms in the core material from the corrosive marine environment. Both the Novelis Fusion and the H128 temper plate can be welded to existing plate with existing welding methods.

3.3.2 Cold Worked Welded Repair

Mass loss measurements between 30 and 60 mg/cm² require cold working of the material prior to accomplishing a weld repair. One cold working method currently employed is ultrasonic peening, which uses ultrasonic impulses to drive an indenter onto the aluminum surface resulting in a refined micro structure and imparting residual compressive stress in the plate.

Fig. 3.3 5xxx repair recommendations based on G67 mass loss test results



Though this is typically performed only on one side of the plate, residual stress has been measured at depths from the surface of up to 10 mils. The improved micro structure and the altered stress state near the weld reduce the residual stress present after the weld cools and have been shown to prevent re-cracking [5]. From experience, this method requires careful planning and can induce cracking when not performed correctly or in locations where bending loads can reverse the stress state of the surface where cold worked stresses can add to the stress state.

3.3.3 *Un-Weldable Material*

Guidance for 5xxx aluminum defines the mass loss welding limit as 60 mg/cm². At or above this limit welding is not permitted, though through experience is often attempted and results in cracking at or in close proximity to the weld. When shipboard plating is not weldable the currently approved alternative methods are application of an E-Glass epoxy patch or a temporary adhesively bonded aluminum repair (BAR) kit applied by ship's force. Both methods are designed to reinforce the region ahead of the crack tip, carry loads across the crack plane, and restore weather tight integrity of the plate.

3.4 Alternative Repair Methods

Two primary alternative repair methods developed for U.S. Navy use since 2010 are the composite patch and bonded aluminum repair (BAR) kit. Composite patch repairs are the primary method for repairing non-weldable aluminum. Application requires trained and qualified personnel, the developed technique requires detailed surface preparation procedures, and advanced lamination techniques involving vacuum consolidation of the hand laminated composite. As experience grows there are composite patches that have seen over 5 years of service, continue to pass inspections, and receive approval for continued use. In parallel with composite patch research and implementation, BAR kits were developed to address emergent cracking while underway and can be applied by Navy sailors. These patches have been applied to areas experiencing low stresses during typical operation.

3.4.1 *Bonded Aluminum Repair*

The current surface preparation and lamination procedures associated with composite patch repairs are not suitable for shipboard personnel, this is due to the level of training and experience required to achieve a consistent repair quality, and the expense of hazardous material handling and storage requirements. As a result, a Bonded Aluminum Repair (BAR) kit was developed to provide a temporary repair method that effectively mitigates crack growth, restores weather-tight integrity, and allows ship's personnel to apply the repair while underway. BAR kits consist of malleable 11 gauge 5052 O-temper plates, methyl-methacrylate (MMA) adhesive cartridges with dispensing equipment, abrasive surface preparation tools, and disposables required for repair application. The steps required to install the kit are shown in Fig. 3.4. First, basic surface abrasion

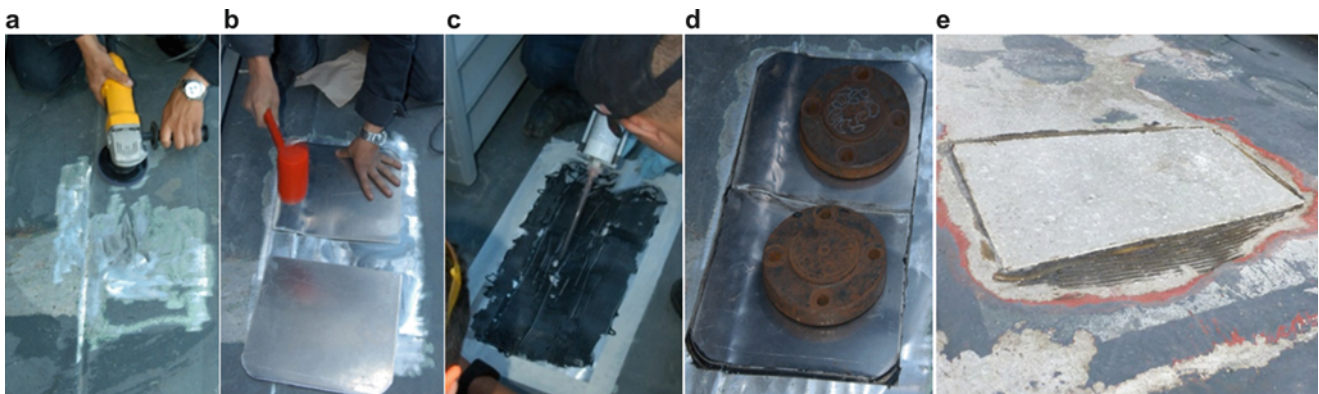


Fig. 3.4 BAR installation process: surface preparation (a), initial plate forming (b), adhesive application (c), final BAR repair step using weights to apply pressure (d), and BAR after 6 months in service (e)

is performed to remove paint and coatings (a). The O-temper plates are easily formed to the shape of the deck (b) and the MMA adhesive is applied to the deck (c) and then cures with simple fixturing methods (d). The MMA achieves a durable bond with minimal surface preparation. The BAR method achieved similar fatigue performance benefits to the composite repairs; However upon base plate failure, the BAR plate immediately cracked and did not carry additional load. As will be discussed below, the composite patches remained intact after the base structure aluminum failure, and continued to carry load. Though BAR is meant to be temporary, there are several repairs that have been in service for over 3 years (e).

3.4.2 Composite Patch Repair

In cases where welded repairs are not practical for immediate accomplishment such as fuel tank repairs, which must be first emptied and gas-freed, or the case of highly sensitized plate, alternative repair methods are necessary. Other potentially dangerous conditions which would preclude immediate welded repairs include ammunition spaces, locations with equipment that must be temporarily removed to permit access to the back side of the structure, or the lack of trained personnel. Deck repair using a composite patch offers a significant repair cost and safety benefit from the fact that applying the patch does not require “hot work”, and can be applied from one side. Hot work refers to torch cutting and welding tasks that require a fire watch and a clear area on both sides of the repair, and when in the vicinity of a flammable substance requires the spaces to be gas free.

Strength and fatigue life benefits of the composite patch repair method have been well documented. Static testing of edge notch panels repaired with a composite patch demonstrated a significant increase in panel strength with a thin composite patch across the crack tip. Testing results showed that a single layer of unidirectional E-Glass increased ultimate strength of 6.35 mm thick specimens by 33 and 37% for 3.18 mm thick aluminum plate [30]. Testing 6.35 mm thick aluminum center crack tension specimens with stiffness-matched bonded unidirectional boron patches to study effects of a composite patch dimensions on the aluminum plate fatigue life. Results showed no benefit of increased patch length perpendicular to the crack plane. A critical finding was that an elliptical crack front was developed during fatigue loading which lagged by up to 10 mm from the patched to un-patched surfaces [13]. Fatigue performance benefits were also demonstrated for three configurations of 3-ply unidirectional boron-patched, stiffened 1 mm. thick aluminum plates were tested to study the tension-tension fatigue crack growth rate: cracked plate, cracked stiffened plate with 101.6 mm spacing, and cracked stiffened plate with 152.4 spacing. FEA was utilized to calculate the Stress Intensity Factor (K) and modeled the crack growth using Paris Law coefficients for the underlying plate. Test and analysis results showed that the composite patches decreased the crack growth rate and increased the fatigue life of the repaired panels [12]. Over the past 5 years, the Navy has utilized thin low modulus E-glass epoxy composite patch repairs on 12 ships. Patches have demonstrated their ability to mitigate crack growth, inhibit water ingress, and maintain a weather tight compartment. These patches were installed in-situ with vacuum consolidated hand laminations [5, 25]. Laminate design and installation procedures were supported by laboratory lamination trials, ASTM standard material testing, environmental conditioning, large center crack tension fracture mechanics specimens, and experience with a full scale plate ductile tearing test. Patch repairs increased the fatigue life of the center crack tension (CCT) plates 4 \times , 6 \times , and 10 \times for three far-field stress levels [31]. Additional performance capability was demonstrated on a full scale ductile tearing specimen subjected to high stress and durability was demonstrated on patched aluminum plates subjected to dynamic impact.

3.5 Composite Patch Strength and Durability

Surface preparation, lamination procedure, and material selection were supported by laboratory lamination trials and material testing. The surface preparation method that achieved the highest lap shear strength involves mechanical abrasion of the surface followed by a phosphoric acid scrub and application of an acetic acid based coupling agent. Vacuum schedule, peel ply, perforated film, and bleeder cloth selection were based on post lamination quality assurance testing, such as fiber volume fraction and void content, and limited in-plane mechanical testing. Additionally, resin gel time studies were performed to understand behavior at various temperatures experienced at repair facilities around the world. ASTM standard tests, performed on material coupons pictured in Fig. 3.5, were used to measure elastic-plastic resin behavior, lamina and laminate in-plane mechanical properties, interface ply fracture behavior, and long term durability of environmentally exposed samples. Baseline composite patch laminates are nominally 6.44 kg/m² (1.32 lbs/ft²) with a fiber volume fraction (FVF) of 32.5%, an elastic modulus of 11.7 GPa, tensile strength of 181.3 MPa, and compressive strength of 214.4 MPa.

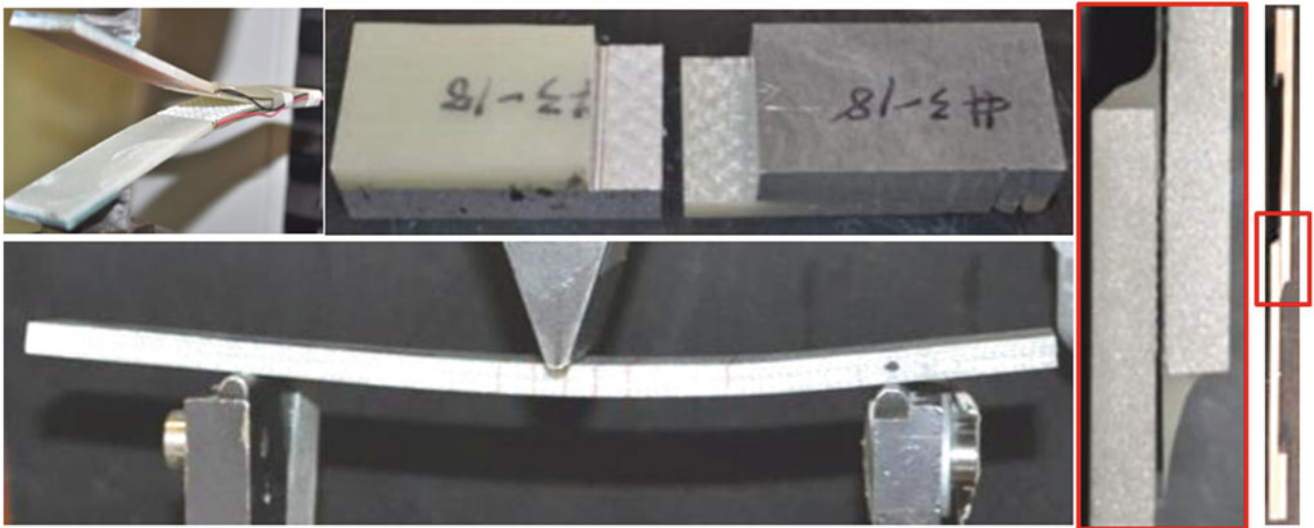


Fig. 3.5 Material testing specimens. Clockwise from upper right: mode I fracture, compressive notch shear, lap shear, and mode II fracture

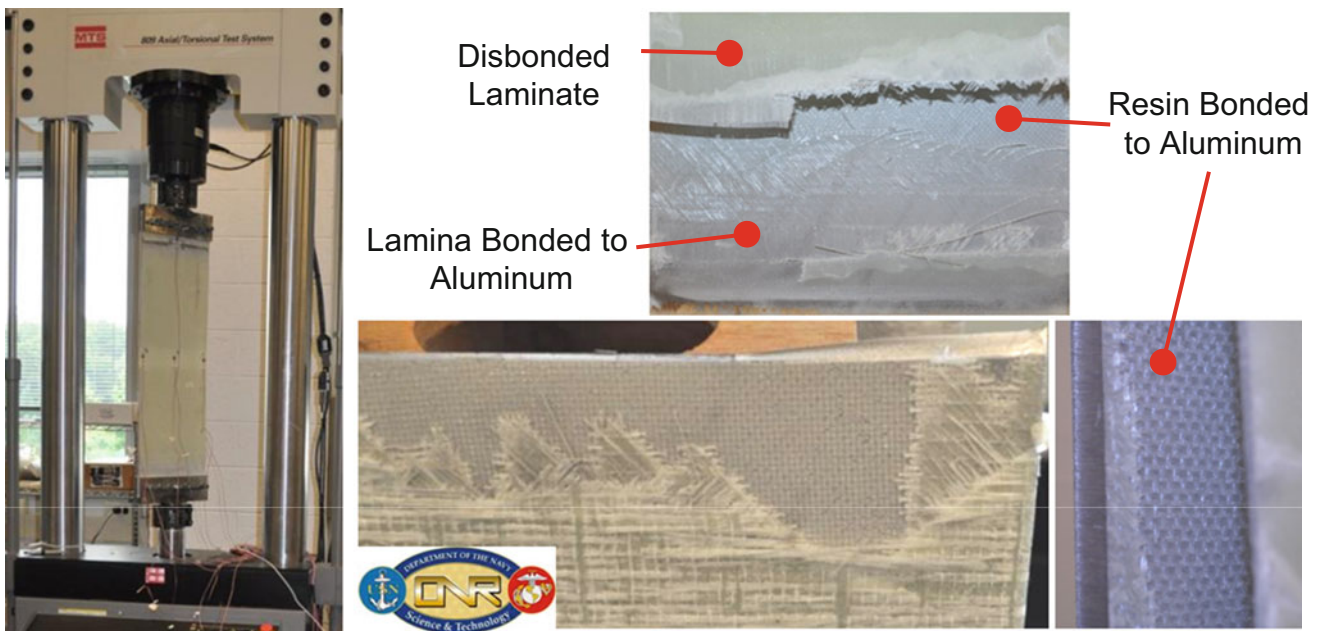


Fig. 3.6 Load frame with CCT test specimen (*left*). Failure surfaces typical of the 100.3 MPa far-field stress (*right*)

Center crack tension (CCT) tests were used to demonstrate the design method and resulting laminate configuration for the thin E-glass epoxy patch repairs performed on U.S. Navy ships. Though reinforcement length relative to the crack plane does not affect crack growth, initial CCT specimens had composite patches that extended 15 in. from the crack plane in each direction to represent the configuration of repair patches installed on ship structure. Minimum recommended patch length perpendicular to the crack is 40 cm for sensitized plate and often extend further past the nearest structural detail, such as a stiffener or frame below the deck being repaired. The CCT configuration shown in Fig. 3.6 was tested for three far-field stress levels; working stress, above the Eurocode 9 fatigue design stress limit, and a stress level resulting in plastic deformation at the crack tip. For two of three applied stress levels tested, 34.5 and 75.2 MPa, the composite patch continued to carry the applied load with only minor delamination adjacent to the crack, even after the aluminum crack extended the full width of the plate. Composite patch disbond failures, when they occurred, were limited to a small area adjacent to the crack plane and extended less than 12 mm beyond the crack tip. When the load was increased to 100.3 MPa the composite patch disbonded and delaminated from the base panel as shown in Fig. 3.6. Typical failure surfaces showed resin bonded to the aluminum with fiber tearing and inter-laminar delamination between various plies through the thickness of the composite patch.

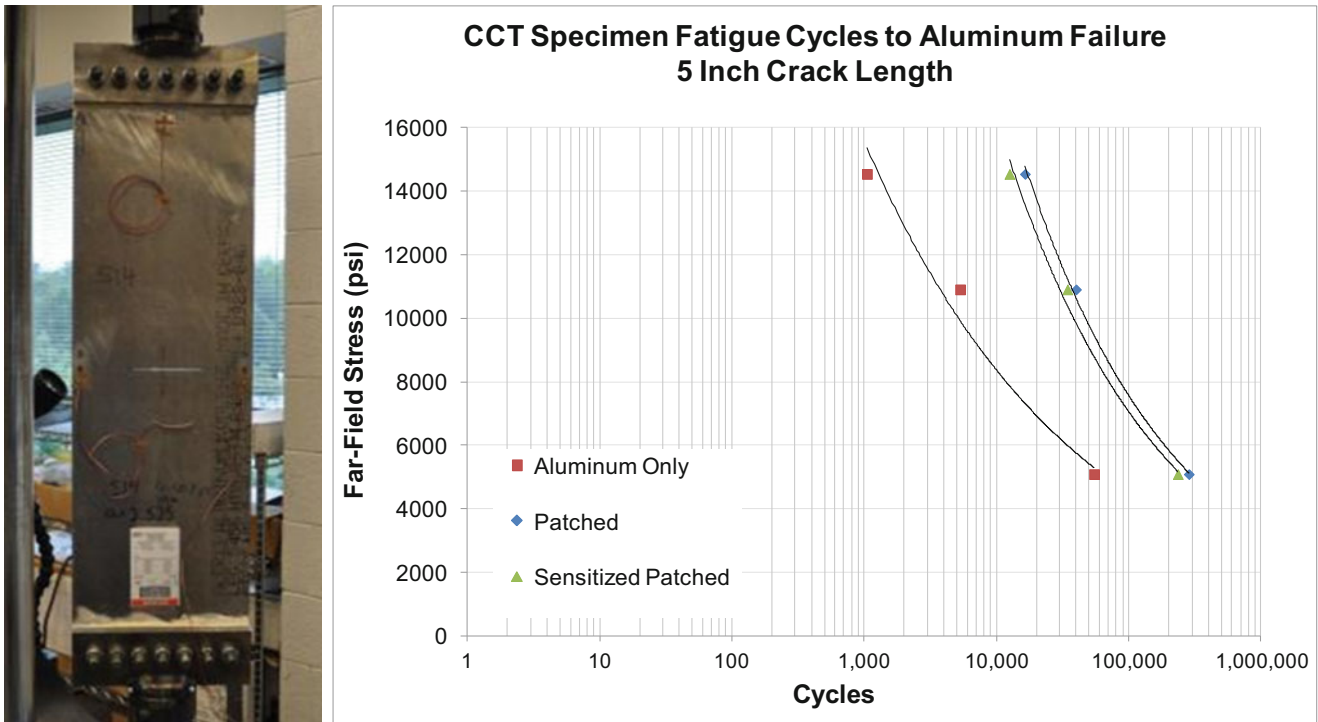


Fig. 3.7 Aluminum specimen and series far-field stress level versus cycles to failure for $2a_0=5$ in. fatigue testing

Stress level as a function of failure cycle for the un-patched aluminum, composite patch repaired aluminum, and the oven sensitized composite patch aluminum for the three stress levels are shown in Fig. 3.7. Sensitized plate was “as-delivered” aluminum conditioned at 121 °C for 10 h, which resulted in a DoS of 47.3 mg/cm² as measured by the G67 test method. The data points for each plate condition are fit with a power law to highlight the general trend of the data and to show the difference between the plate condition groups. Each data point represents one specimen. Application of a composite patch repair to a cracked aluminum plate subjected to a cyclic tensile load increased the cycle count to failure for the three stress levels tested. The benefit of the composite patch repair system increased with the level of applied stress. When subjected to a far-field tensile stress level of 34.5 MPa the number of load cycles increased by four to five times for the sensitized and as-delivered plate condition. Similarly, for the 75.2 MPa stress level the cycle counts increased 6.5 to 7.5 times. When the stress level was increased to 100.3 MPa the cycle count increased between 12 and 15.7 times the baseline cracked plates [31].

Composite patch repairs increase static plate strength, fatigue life, and large displacement capacity of the crack plate. Additionally, to demonstrate performance under high stress, a large composite patch reinforced aluminum edge notch test specimen (0.8×1.0 m) was tested in the custom designed fixture shown in Fig. 3.8. The fixture consists of four floating load arms and two compression struts. With load applied to the arms a large region of high stress forms ahead of the blunt notch that typically produces highly controlled ductile fracture of the aluminum plate [32]. The reinforced specimen consisted of a 28 ply E-Glass epoxy laminate with a nominal thickness of 15 mm and an axial elastic modulus of 18.6 GPa bonded to a 5083-H116 aluminum plate 6.35 mm thick. Uni-directional reinforcement was inserted between plies of the typical quasi isotropic laminate to increase patch modulus and strength across the crack plane. Initial quasi static analysis of the specimen indicated grip failure prior to laminate failure. Mitigation of this risk involved extending the 50.8 mm V-notch into a 127 mm blunt notch and removal of 152 mm of composite at the notch tip as shown in Fig. 3.8. Dominant failure modes observed during testing are shown along with the test fixture in Fig. 3.8. Aluminum fracture and laminate failure were observed, however disbonding of the composite did not occur. Visible aluminum bonding surfaces include multiple composite plies starting with the interface ply, which indicates the composite to aluminum bondline remained intact. Laminate failure propagated through the bottom half of the laminate until testing was terminated but the patch above the crack remained intact and securely bonded to the aluminum.

The load-deflection response of the composite reinforced plate is compared with baseline aluminum and welded aluminum plates in Fig. 3.9 [32]. Under load the aluminum crack propagated approximately 30° to the crack plane and then arrested 2 cm from the composite, which is the location where the crack direction changes in Fig. 3.8. Loading increased until aluminum plate failure, shown in Fig. 3.9, occurred within the grips. Loading continued to increase until composite

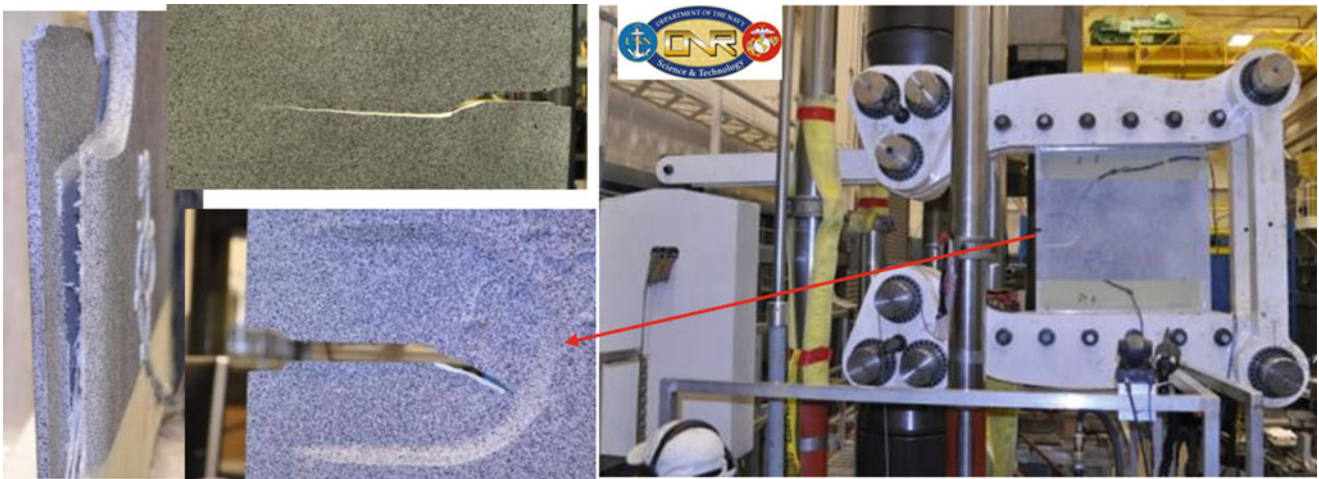


Fig. 3.8 Ductile tearing specimen failure (*left*) and test fixture (*right*)

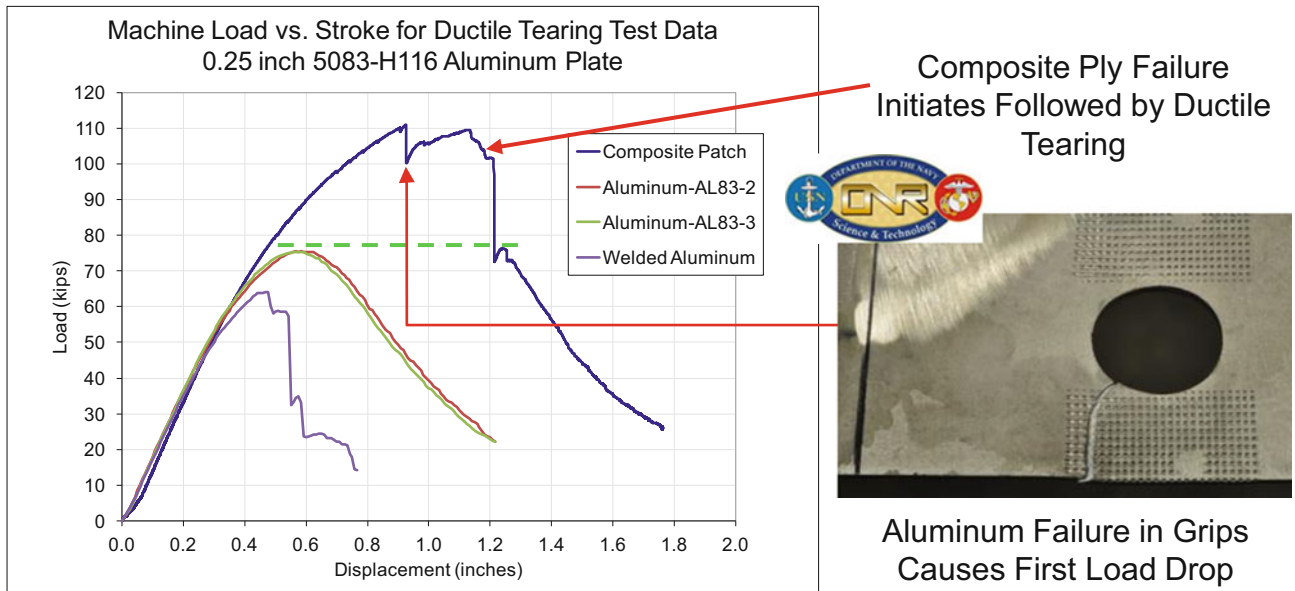


Fig. 3.9 Ductile tearing test machine load versus cross head displacement results with failure notes

failure initiated. After the load drop associated with composite failure, the aluminum plate fracture propagated following the same unloading measured for the baseline aluminum plate. The demonstrated benefit of the composite patch was additional in-plane load and displacement capacity of the plate. Though compared below, the baseline aluminum plate performance cannot be directly compared to that of the reinforced specimen. Baseline plates had electrical discharge machined (EDM) V-notches while the composite reinforced plate tested had a 76 mm crack extension cut with a bandsaw, resulting in a blunt notch. The more than 45 % of additional load capacity of the composite reinforced specimen matched that achieved with the 9.53 mm aluminum plate with the added benefit of an additional 100 % of displacement capacity. The peak load and the work (area under the curve) to fracture the hybrid panel was greater than the equivalent aluminum plate. Optimization of the composite patch could conservatively reduce composite patch weight by 15 % and still achieve equivalent performance.

Demonstration of composite patch repair durability was performed with 40.6 cm², and 6.35 mm thick aluminum plates, reinforced with composite patches subjected to dynamic impact. Impact energies were designed to represent tools or equipment being dropped during service or maintenance. Testing was performed using the U.S. Naval Academy’s Instron Dynatup model 9250HV spring assisted drop tower with a 50 mm diameter steel cylinder and a 76 mm diameter spherical impact TUP pictured in Fig. 3.10. Two impact energies, 400 and 815 J, were used with a consistent 7.62 m/s impact velocity to impart

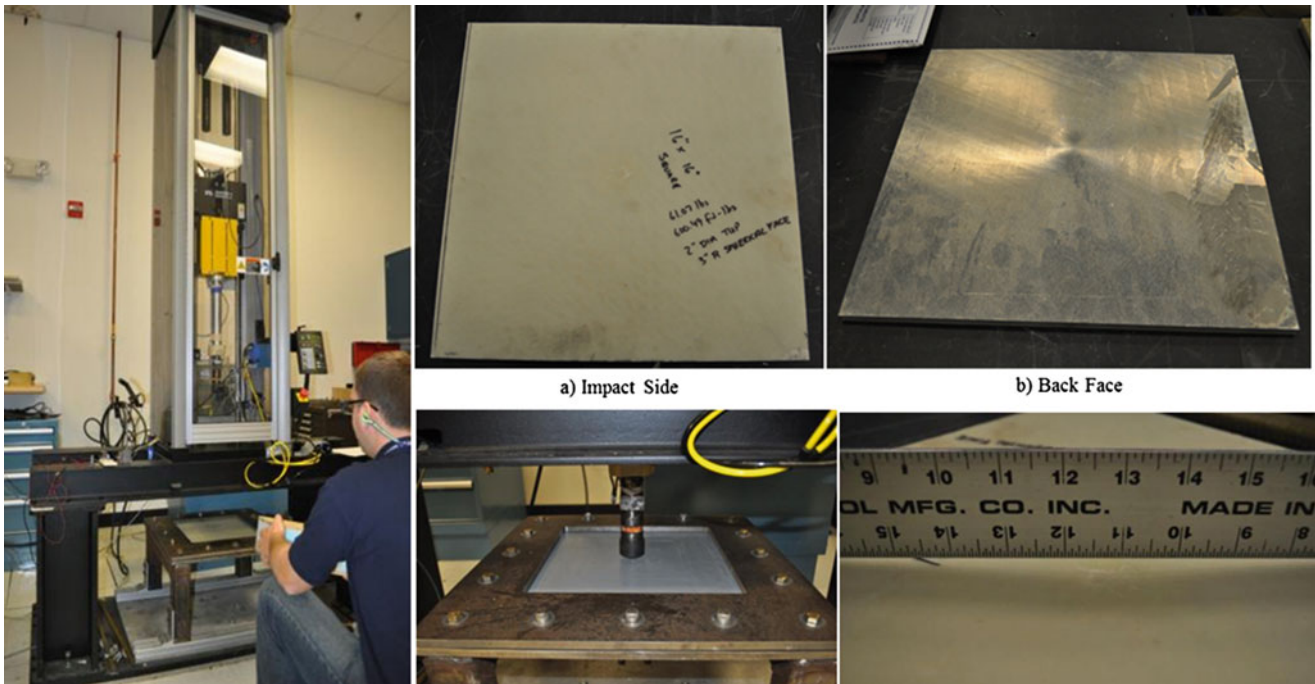


Fig. 3.10 Impact testing and residual panel deflection after 600 ft/lb impact

damage on reinforced panels with a 35.6 cm unsupported span and clamped edges. Impact produced permanent deflection of the aluminum plate, as shown in Fig. 3.10. Ultrasonic testing (UT) C-scan results showed matrix damage in the region of impact but did not include delamination of the composite from the aluminum. The area of damage for the quasi-isotropic laminate was elliptical with an area proportional to the impact energy. At 400 J the impact damage was no larger than the diameter of the impactor TUP but increased to twice the area of the TUP when impacted with 815 J.

3.6 Summary

High magnesium content 5xxx marine aluminum alloys used for welded structures are susceptible to sensitization when operating in moderate to hot marine environments. Cumulative exposure of plate to elevated temperatures causes magnesium in the aluminum to migrate to grain boundaries making the plate susceptible to intergranular corrosion and stress-corrosion cracking (SCC), which is a failure mechanism that can occur at stress levels well below nominal plate strength. Determining the repair method for sensitized plate requires knowledge of the degree of sensitization (DoS). The three methods for DoS detection used by the U.S. Navy are the ASTM G67 NAMLT, the DoS Probe, and visual analysis techniques. ASTM G67 is a destructive mass loss test, while the DoS Probe and visual analysis offer non-destructive alternatives. The resulting level of sensitization governs whether a standard weld repair, weld repair in combination with cold working, or an alternative repair method is required. Two alternative repair methods are currently approved for use, the composite patch repair and the bonded aluminum repair (BAR) kit. Though the BAR kit has demonstrated fatigue performance, the strength and durability of the composite patch repair exceeds that of the BAR. In fatigue, thin low modulus composite patches increased the cycles to failure more than four times. In addition to the cycle count increase, composite patches carried tensile load beyond aluminum plate failure for stresses up to 72.5 MPa. Under high stress associated with ductile tearing, composite reinforcement significantly increased the work required to fracture the panel by increasing the peak load and displacement achieved during testing. For in-service applications, testing up to an impact energy of 815 J, which represents a dropped toolbox or tool during maintenance, demonstrated the durability of composite patch repairs. In addition to the testing, composite patch repair of SCC onboard U.S. Navy ships began in December of 2010, with repairs that have achieved over 5 years of service, continue service, and are subject to annual inspections. Patches for marine structures have demonstrated their ability to mitigate crack growth, inhibit water ingress, and reinforce damaged or degraded aluminum structure. The U.S. Navy is continuing composite patch development with the goal of designing and implementing structural reinforcement for load carrying applications and survivability.

Acknowledgements Work described was performed by the Naval Surface Warfare Center Carderock Division's Survivability, Structures, Materials, and Environmental Department with impact testing performed at the U.S. Naval Academy in the Mechanical Engineering department's impact testing lab. Financial and technical support was provided by Dr. Paul Hess of the Office of Naval Research Code 331, the Naval Sea Systems Command Surface (NAVSEA) Surface Warfare Directorate (SEA 21), and the NAVSEA Engineering Directorate (SEA 05).

References

- O'Shaughnessy, T.G.: ALCOA 5000-Series Alloys Suitable for Welded Structural Applications. Aluminum Company of America, Application Engineering Division, ALCOA Laboratories, ALCOA Center, Pennsylvania (1985)
- Bushfield, H., Cruder, M., Farley, R., Towers, J.: Marine Aluminum Plate—ASTM Standard Specification B 928 and the Events Leading to its Adoption, in Society of Naval Architects and Marine Engineers, World Maritime Technology Conference and Exposition, San Francisco, CA, 2003
- Cavas, C.P.: Cracks Plague Ticonderoga-Class Cruisers, Navy Times, 9 Dec 2010
- ASTM G67-13: Standard Test Method for Determining the Susceptibility to Intergranular Corrosion of 5xxx Series Aluminum Alloys by Mass Loss After Exposure to Nitric Acid (NAMLT) Test. ASTM International, Conshohocken, PA (2013)
- Golubfskie, W.J., Tran, K.T., Noland, J.M., Park, R., Stiles, D.J., Grogan, G., Wong, C.: Survey of detection, mitigation, and repair technologies to address problems caused by sensitization of Al-Mg alloys on navy ships. *Corrosion* **72**(2), 314–328 (2016)
- Golubfskie, W.J.: Aluminum sensitization and the Navy. In: The Minerals, Metals, and Materials Society 143rd Annual Meeting and Exhibition, San Diego, CA, 2014
- Baker, A.A.: Repair of cracked or defective metallic aircraft components with advanced fibre composites—an overview of Australian work. *Compos. Struct.* **2**, 153–181 (1984)
- Baker, A.A., Rose, L.R.F., Jones, R.: In: *Advances in the Bonded Composite Repair of Metallic Aircraft Structures*, vol. 1. Elsevier, Amsterdam (2002)
- Baker, A.A., Rose, L.R.F., Walker, K.E., Wilson, E.S.: Repair substantiation for a bonded composite repair to F111 lower wing skin. *Appl. Compos. Mater.* **6**, 251–267 (1999)
- Christian Jr., T.F., Hammond, D.O., Cochran, J.B.: Composite material repairs to metallic airframe components. *J. Aircraft* **29**(3), 470–476 (1992)
- Guyt, C.B.: Design and Installation of Bonded Repairs to Cracked Fuselage Skins on C-5A T/N 69-021, SPC 94-4050, USAF European Office of Aerospace Research and Development and the Fatigue and Fracture Group, Flight Dynamics Directorate, 1995
- Sabelkin, V., Mall, S., Avram, J.B.: Fatigue crack growth analysis of stiffened cracked panel repaired with bonded composite patch. *Eng. Fract. Mech.* **73**, 1553–1567 (2006)
- Schubbe, J.J., Mall, S.: Investigation of a cracked thick aluminum panel repaired with a bonded composite patch. *Eng. Fract. Mech.* **63**, 305–323 (1999)
- Tsai, G.-C., Shen, S.B.: Fatigue analysis of cracked thick aluminum plate bonded with composite patches. *Compos. Struct.* **64**, 79–90 (2004)
- Jones, R., Chiu, W.K.: Composite repairs to cracks in thick metallic components. *Compos. Struct.* **44**, 17–29 (1999)
- Duong, C.N.: Design and validation of composite patch repairs to cracked metallic structures. *Compos. Part A: Appl. Sci. Manuf.* **40**, 1320–1330 (2009)
- Allan, R.C., Bird, J., Clarke, J.D.: Use of adhesives in repair of cracks in ship structures. *Mater. Sci. Technol.* **4**, 853–859 (1988)
- Grabovac, I., Pearce, P., Camilleri, J.A., Challis, K., Lingard, J.: Are composites suitable for reinforcement of ship structures? In: 12th International Conference on Composite Materials, Paris, 1999
- Grabovac, I.: Bonded composite solution to ship reinforcement. *Compos. Part A: Appl. Sci. Manuf.* **34**, 847–854 (2003)
- Grabovac, I., Whittaker, D.: Application of bonded composites in the repair of ships structures—a 15-year service experience. *Compos. Part A: Appl. Sci. Manuf.* **40**, 1381–1398 (2009)
- Turton, T.J.D.-J., Livingstone, F.: Oil platforms, destroyers, and frigates—case studies in QinetiQ's marine composite patch repairs. *Compos. Part A: Appl. Sci. Manuf.* **36**, 1066–1072 (2005)
- McGeorge, D., Echtermeyer, A.T., Leong, K.H., Melve, B., Robinson, M., Fischer, K.P.: Repair of floating offshore units using bonded fibre composite materials. *Compos. Part A: Appl. Sci. Manuf.* **40**(9), 1364–1380 (2009)
- Weitzenbock, J.R., McGeorge, D.: A cold repair method for FPSOs. In: Offshore Technology Conference, Houston, TX, 2012
- Recommended Practice DNV-RP-C301: Design, Fabrication, Operation and Qualification of Bonded Repair of Steel Structures. Det Norske Veritas, 2012
- Noland, J.M., Hart, D.C., Udinski, E.P., Sielski, R.A.: Initiatives in bonded ship structural repairs. In: ASNE Fleet Maintenance and Modernization Symposium, American Society of Naval Engineers, San Diego, 2013
- Greene, J.P.: *Why is White So Sacred? Soaring* (1975)
- Brosi, J.K., Lewandowski, J.J.: Delamination of a sensitized commercial Al-Mg alloy during fatigue crack growth. *Scr. Mater.* **63**, 799–802 (2010)
- LaMontagne, K., Stiles, D.J.: Aluminum alloy sensitization data visualization and analysis. In: Department of Defense Corrosion Conference, Gaylord National Resort and Convention Center, Washington, DC, 2009
- Bumiller, E., Shedd, M., Kazerooni, B., Adedeji, W., Kelly, R.G.: The electrochemistry of intergranular corrosion and sensitization in 5XXX aluminum alloys. In: Department of Defense Corrosion Conference, Gaylord National Resort and Convention Center, Washington, DC, 2009
- Bone, J.S., Karr, D., Waas, A.M.: Testing of composite patches for ship plating fracture repair. In: Naval Architecture and Marine Engineering, University of Michigan, 2003

31. Hart, D.C., Udinski, E.P., Hayden, M.J., Liu, X.: Fatigue performance and analysis of composite patch repaired cracked aluminum plates. In: Sustainability and Stewardship, Vessel Safety and Longevity Through Research, Conference, Ship Structures Committee, Linthicum Heights, 2014
32. Nahshon, K., Hoffman, W.A., Ullagaddi, C.B.: Characterization of structural scale ductile fracture of aluminum panels using digital image correlation. In: Proceedings of the 2014 Annual Conference on Experimental and Applied Mechanics, Conference, 2014

Chapter 4

Investigation and Improvement of Composite T-Joints with Metallic Arrow-Pin Reinforcement

Sebastian Heimbs, Michael Jürgens, Christoph Breu, Georg Ganzenmüller, and Johannes Wolfrum

Abstract Aiming at an increase in failure resistance and damage tolerance of composite T-joints, a novel reinforcement technique in through-thickness direction using metallic arrow-pins has been proposed by the authors in previous studies. In a recent investigation, different options for further improvement of the T-pull performance have been assessed. These include optimized arrow-pin configurations, filler and ply materials and thermoplastic interleaf layers. T-specimens have been manufactured and tested under quasi-static and high-rate dynamic loading conditions to quantify the influence of these measures. Additionally, FE models have been developed in LS-Dyna to predict the performance numerically. Model validation was conducted step by step using material coupon test data, dedicated single-pin pull-out tests and T-pull tests.

Keywords T-joint • Composite material • Metal pin reinforcement • T-pull testing • Numerical simulation

4.1 Introduction

T-joints can be found in many box-like or stringer-stiffened composite structures and they can be the weakest link for structural failure under severe loading. Hence, lots of past and current research activities are related to the assessment and improvement of the strength of composite T-joints by advanced designs [1, 2] or reinforcement techniques [3–5]. The load case in the focus of the current study is the hydrodynamic ram loading of a fluid-filled composite tank structure. The structural performance of the T-joints for this kind of load case shall not only provide maximized static strength at failure initiation but also maximized post-damage energy absorption until complete separation to ensure structural integrity.

The authors of this study have proposed a novel reinforcement technique of composite T-joints in through-thickness direction using metallic arrow-pins, which has shown good potential for damage resistance and energy absorption in first T-pull test series (Fig. 4.1) [6–9]. This type of hybrid joint makes use of the metallic plasticity of the reinforcing pins, which is beneficial for high energy absorption targets, and of the mechanical interlocking effect of the arrow-head under pull-out loads. The principle of this patented technique is to use a thin metallic sheet, in this case a 0.4 mm DC4 steel sheet, where the pin geometry is cut and bent on a special bending machine in order to obtain a reinforcement sheet with pins of various length on both sides. This sheet is intended to be placed between two laminates, in this case between skin and vertical spar of the T-joint (Fig. 4.2).

Now, the previous studies were extended in order to further improve the T-pull performance by new design solutions of the arrow-pin reinforcement architecture and by new material solutions for filler, plies and ply interfaces. The basis for these

S. Heimbs (✉) • M. Jürgens • C. Breu
Airbus Group Innovations, 81663 Munich, Germany
e-mail: sebastian.heimbs@airbus.com

G. Ganzenmüller
Fraunhofer Institute for High-Speed Dynamics (EMI), 79104 Freiburg, Germany

J. Wolfrum
Bundeswehr Research Institute for Materials, Fuels and Lubricants (WIWeB), 85435 Erding, Germany

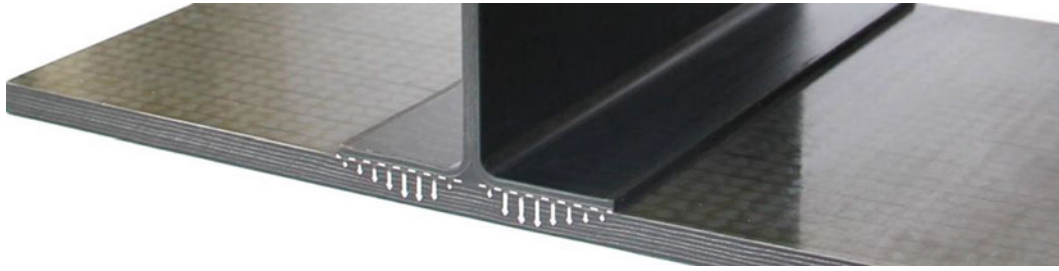


Fig. 4.1 Composite T-joint with metallic arrow-pin reinforcement

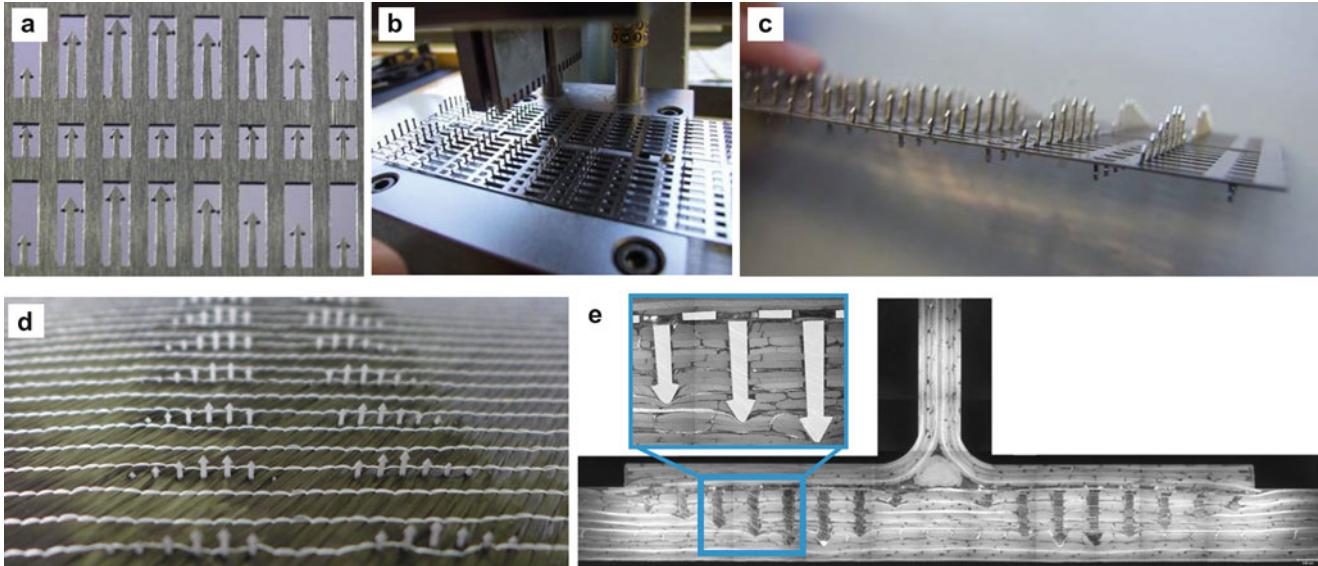


Fig. 4.2 Arrow-pin reinforcement of composite T-joint: (a) laser-cut steel sheet, (b) bending of pins, (c) final pin-reinforcement sheet, (d) pins inserted into dry carbon fiber textile, (e) micrograph of cured composite T-joint

considerations was a numerical T-pull simulation study with LS-Dyna, which was performed to identify the influence and optimum of different design and material parameters like the T-joint radius, the spar feet length, the filler material stiffness and the interlaminar fracture toughness [10]. The results of this study led to the decisions for the new T-specimen manufacturing and T-pull testing campaign described below.

The aim of this investigation is to assess the potential performance improvements by advanced design and material solutions using quasi-static and high-rate dynamic T-pull tests and numerical T-pull simulations with LS-Dyna.

4.2 T-Joint Design Specification

Seven different composite T-joint designs are compared in this study (Fig. 4.3). The first two designs D1 and D2 have already been investigated in a past study [6, 9] and form the basis for further improvements.

Design D1 is a conventional monolithic composite T-joint without through-thickness reinforcement acting as a reference or as a state-of-the-art in-service solution. It is made of Tenax HTS carbon fibers (CF) and Hexcel HexFlow® RTM6 epoxy resin. The stacking sequence of the 7 mm thick skin ($[0^\circ/+45^\circ/90^\circ/-45^\circ/0^\circ/-45^\circ/90^\circ/+45^\circ/0^\circ/+45^\circ/90^\circ/-45^\circ/0^\circ/90^\circ]_S$) and of the 4 mm thick spar ($[+45^\circ/0^\circ/-45^\circ/+45^\circ/-45^\circ/+45^\circ/0^\circ/-45^\circ]_S$) is similar for all seven T-joint designs.

Design D2 is made of the same material but has metallic arrow-pins of 2 mm length on the top side and varying length on the bottom side as through-thickness reinforcement.

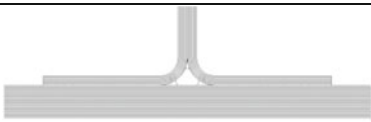
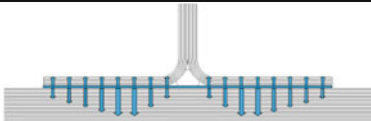
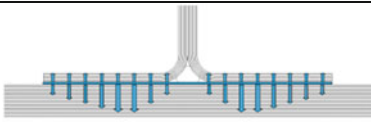
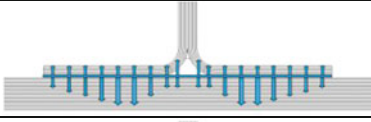
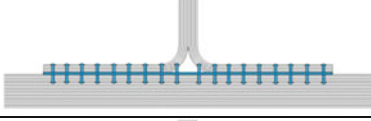
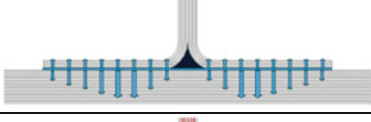
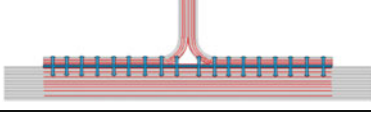
Design	Illustration	Details
D1		HTS-CF/RTM6; no metal pins
D2		HTS-CF/RTM6; metal pins
D3		HTS-CF/EP2400; metal pins
D4		HTS-CF/EP2400; metal pins + additional center pins
D5		HTS-CF/EP2400; metal pins of maximum density
D6		HTS-CF/EP2400; metal pins + thermoplastic filler
D7		HTS-CF/EP2400; metal pins of max. density + thermoplastic binder

Fig. 4.3 Overview of composite T-joint designs investigated in this study

Design D3 has the same arrow-head reinforcement but instead of the un-toughened RTM6 the toughened epoxy resin system Cytec Prism® EP2400 was used in order to improve the fracture toughness. This toughened epoxy resin is used for all further specimens D4–D7, too.

Design D4 is comparable to D3 but has additional pins in the center region in order to investigate their influence on failure initiation and energy absorption.

An optimization of the reinforcement architecture or pin lay-out was attempted in **design D5**. This optimized design is characterized by a maximum pin density in order to investigate, if more shorter pins are superior to fewer longer pins. All pins have an equal length of 2 mm and cannot be positioned any closer than in the selected design in order to prevent undulation problems and excessive resin-rich zones.

Design D6 is similar to D3 but uses a different filler material in the T-joint center. Instead of a carbon fiber braid like in all other designs, a milled thermoplastic filler made of polyetherimide (PEI) was used, which enables higher elasticity and a more precise ply path of the spar laminate plies and avoids resin-rich zones at the corners.

In **design D7** the influence of additional thermoplastic co-polyamide (PA) binder fleece layers between all skin and spar plies was assessed, which is supposed to further increase the fracture toughness and damage resistance. The pin reinforcement pattern is similar to design D5 with the high pin density.

4.3 Experimental Characterization

The experimental test series was divided into three categories. First of all, standard coupon tests with the composite laminate and steel material of the pin sheets were performed in order to obtain mechanical properties for the numerical material modeling. These involved tensile, compression and shear tests as well as double cantilever beam (DCB) and end-notched flexure (ENF) tests for delamination properties characterization.



Fig. 4.4 Single-pin pull-out tests: (a) test set-up, (b) single-pin specimen (post-test), (c) 5×5 pins specimen (post-test)

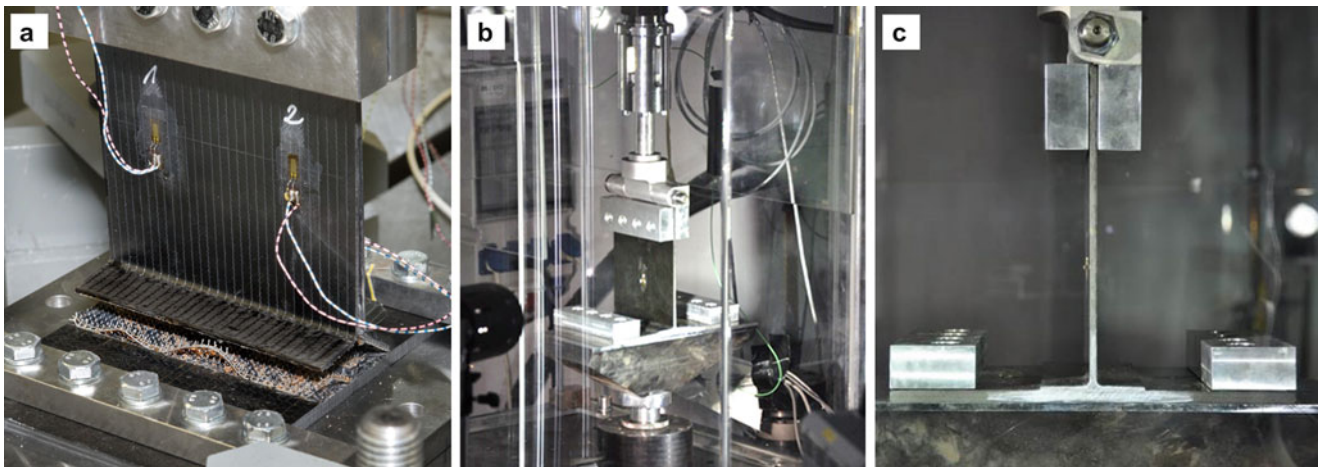


Fig. 4.5 T-pull tests: (a) quasi-static test set-up, (b) high-rate dynamic test set-up, (c) specimen fixation

The second test campaign was dedicated to characterizing the metal pin-to-laminate bonding strength and pin pull-out behavior in detail. For this purpose, single-pin pull-out tests were performed by manufacturing and testing specimens with just one pin in normal tension mode (Fig. 4.4). A Teflon foil was used to decouple the upper laminate from the steel sheet in order to let only the pin carry the tensile load. However, high scatter of test results and dependence of specimen quality led to the decision to go for 5×5 pins specimens, which turned out to be more robust and reproducible. The test results, which are documented in detail in a separate publication [11], gave valuable information on bonding strength and pin bending, detachment and pull-out behavior, which are helpful for later comparisons of simulation and test.

Finally, the third test campaign involved the T-pull testing under quasi-static and high-rate dynamic loading conditions. The latter are more representative of the transient hydrodynamic ram loading as the realistic target load case (Fig. 4.5). The specimen geometry was similar to previous test series [6, 9] with a width of 240 mm, depth of 150 mm and height of 188 mm. The T-specimens were clamped with metallic blocks through boreholes in the specimen and pulled in 90° direction. Digital image correlation technique was used for optical displacement and strain measurement. Additional strain gauges on both sides of the vertical spar laminate were used to identify asymmetric loading or spar bending. The strain gauge signal was also used to calculate the tensile force in the dynamic tests, as this signal was less affected by oscillations than the load cell signal itself. The high-rate dynamic tensile tests were performed on a servo-hydraulic testing machine at a loading velocity of 5 m/s and revealed an increase in stiffness and failure load, which is discussed in further detail in [6, 7]. This paper will focus on the quasi-static test results only, as these curves are less influenced by complex dynamic effects and can more easily be interpreted.

An overview of all quasi-static force–displacement curves of all seven T-joint designs is given in Fig. 4.6. Just one representative curve of each design is shown, although each test was repeated with 4–6 specimens. In order to make comparisons easier and to visualize the influence of the different design improvement options, Fig. 4.7 shows the same curves as a one to one comparison. It can be seen that the reference specimen D1 without reinforcement in through-thickness direction shows

Fig. 4.6 T-pull test results: force–displacement diagram of all seven T-joint designs

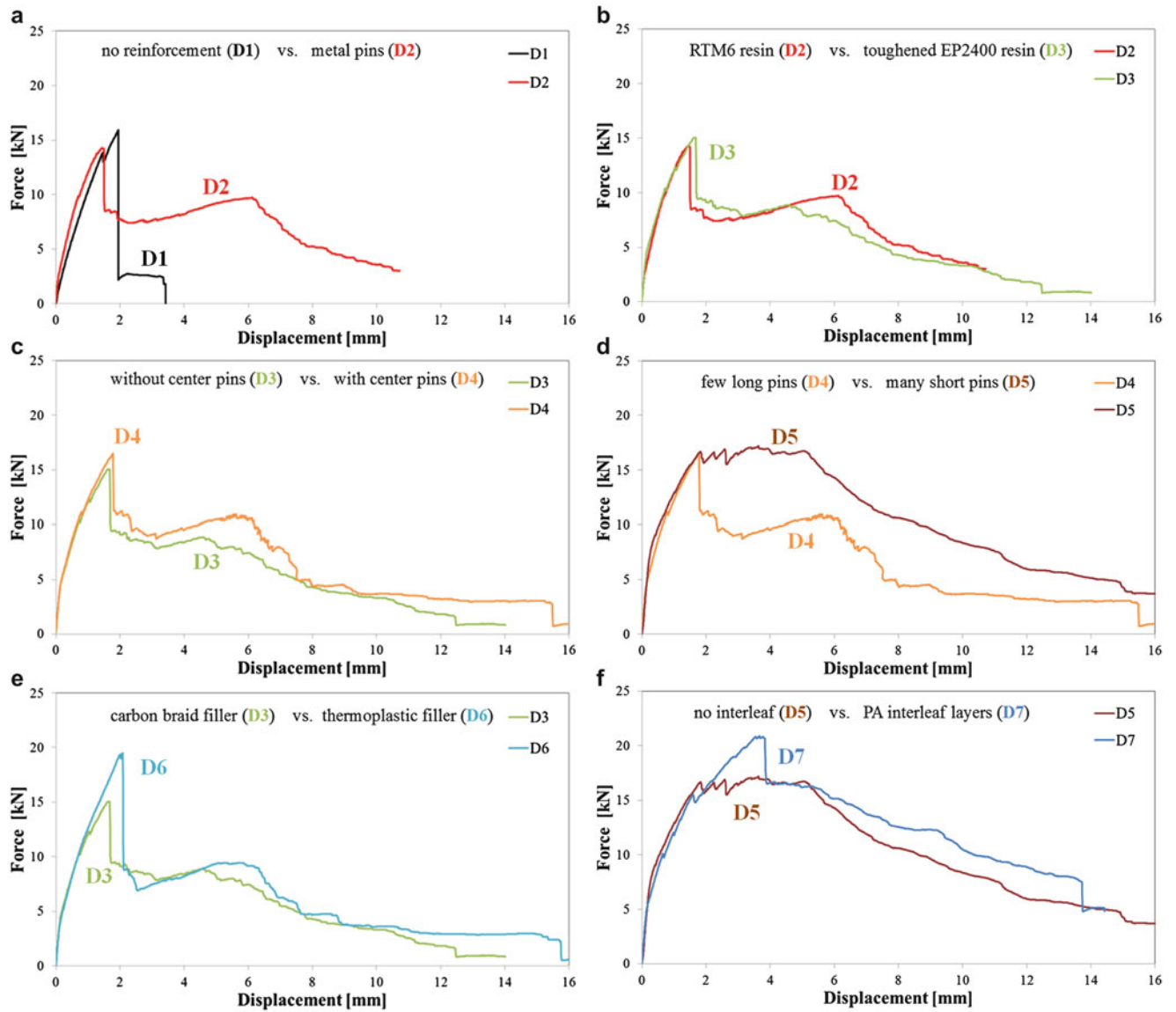
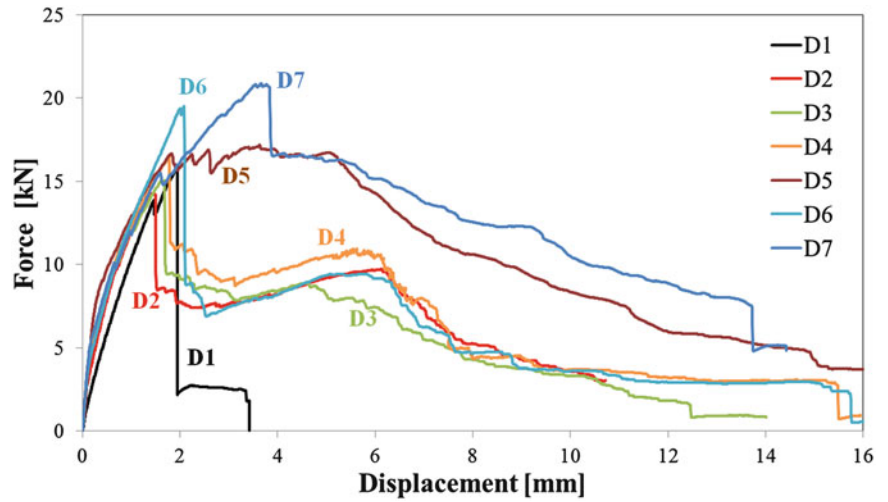


Fig. 4.7 T-pull test results: comparison of force–displacement curves

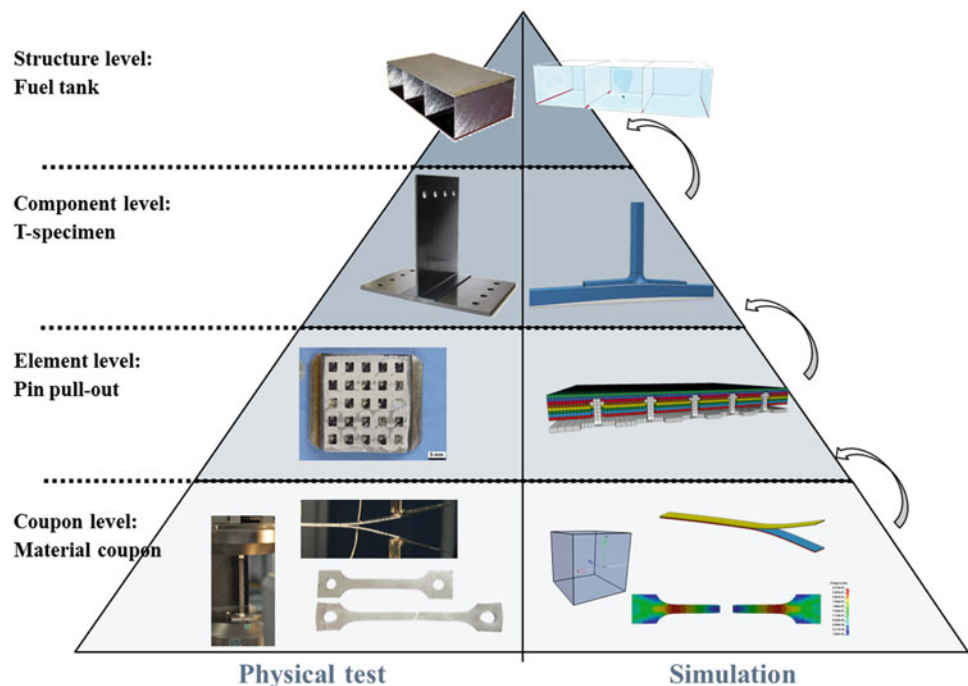
a very brittle behavior with a sudden drop of the force curve when spar-skin detachment occurs. The absorbed energy for T-joint separation was calculated as the integral of the force–displacement curve and has the lowest value for the D1 specimens with 22 J. The implementation of metallic arrow-pin-reinforcements in D2 slightly reduces the failure initiation load due to induced imperfections that enable crack initiation, but the residual post-damage force level is much higher than for specimens D1 (Fig. 4.7a). The energy absorption increases by 250 % to 78 J. Using the toughened epoxy resin EP2400 in D3 compared to un-toughened RTM6 in D2 leads to a slight increase in failure initiation load and a comparable total energy absorption of 79 J (Fig. 4.7b). The addition of further pins in the specimen center in design D4 leads to a significant improvement of failure initiation load and residual force level (Fig. 4.7c). The total absorbed energy of 109 J increases by 37 % compared to design D3.

Even more impressive is the improvement with design D5, which uses a maximized pin density with many short pins instead of fewer longer pins (Fig. 4.7d). The energy absorption increases to 170 J, which is 56 % higher than design D4 or 114 % higher than design D3. The influence of the milled thermoplastic PEI filler in design D6 compared to the carbon braid filler in design D3 with a similar pin-reinforcement is shown in Fig. 4.7e. Also this measure leads to a significant improvement with 23 % higher energy absorption of 98 J. Most obvious is the strong increase of failure initiation load. This is mainly ascribed to the ideal filler geometry without any resin-rich zones or other imperfections, which can lead to an earlier crack initiation in design D3. Finally, the influence of the PA binder fleece in design D7 is shown in Fig. 4.7f in a direct comparison to design D5 with the same reinforcement pattern. The absorbed energy rises by further 7 % to 181 J and the initial failure load is significantly increased due to the higher fracture toughness provided by the thermoplastic interleaf layers. This design shows the best performance of this whole study with an impressive improvement in energy absorption of 720 % compared to the state-of-the-art reference design D1.

4.4 Modeling and Simulation

Parallel to the specimen manufacturing and experimental testing activities, numerical simulation studies with the commercial finite element (FE) solver LS-Dyna were performed to predict the structural performance and failure behavior of the different T-joint designs. In order to increase the accuracy of the numerical predictions, the building block approach along the test pyramid was used to support the model build-up and to validate the models step by step from coupon level up to the T-specimen and even fuel tank structure level (Fig. 4.8).

Fig. 4.8 Building block approach for T-joint FE model generation and validation



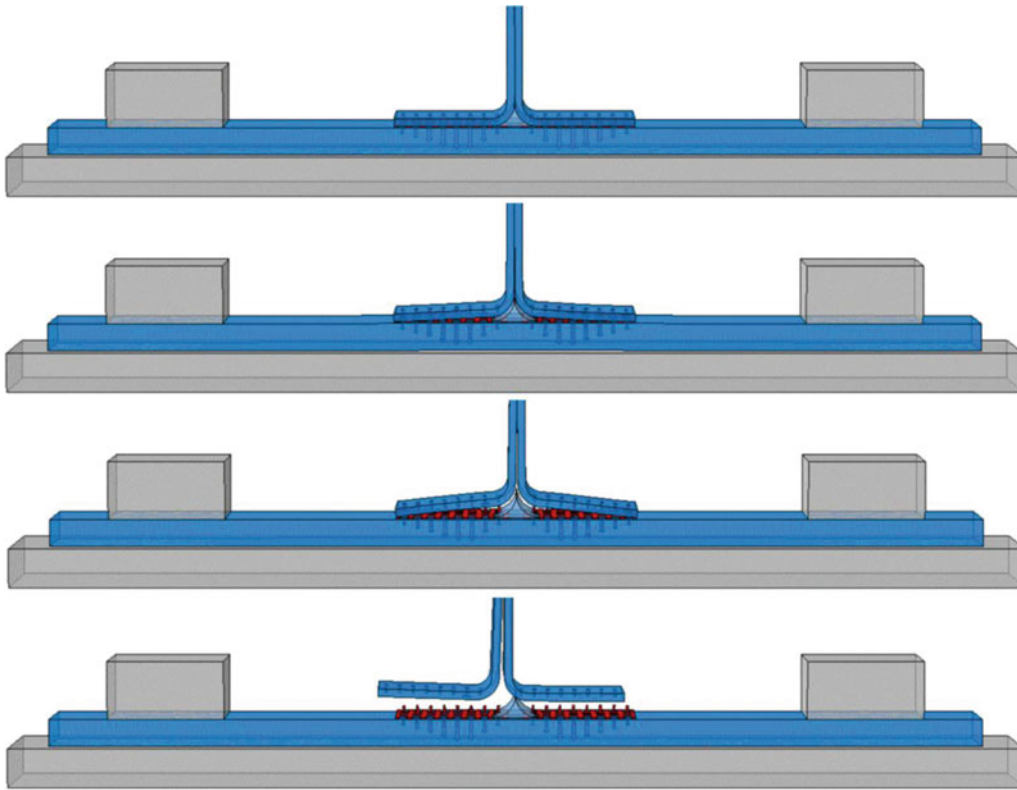


Fig. 4.9 FE simulation of T-pull loading of design D6 specimen

On coupon level, the tensile tests of the steel material were simulated to validate the metallic material law and plasticity behavior. Material model MAT24 with the tabular input of the plasticity curve in combination with solid elements was used for the metallic pin modeling. Also the composite coupon tests were simulated to validate the material model MAT59 for the modeling of each individual ply with solid elements. Special focus was also put on the simulation of the delamination tests in order to enable an accurate interlaminar failure representation and parameter calibration for the surface-based delamination tiebreak contact formulation between each ply.

The same tiebreak contact type was also used to connect the metal pins to the composite material in the T-joint model. The parameters of this metal-to-composite tiebreak contact were defined and validated in dedicated simulations of the single pin pull-out tests and 5×5 pin pull-out tests as the second level of the test pyramid (Fig. 4.8).

Finally, the T-joint models were built up using the aforementioned techniques. The model size was similar to the tested T-specimens in terms of specimen width and height, but the depth was reduced from 150 mm to just one repeating pattern of upper and lower pins with periodic boundary conditions. The realistic elasticity of the metallic clamping blocks was also covered in the models, as this has shown to have a significant influence on the slope of the force–displacement curve. With a mesh size of 0.25 mm and element numbers of 200,000–900,000—depending on the design—and tiebreak contact interfaces between each individual part and ply, the final calculation clock times in double precision mode were between 24 and 48 h on a 14 CPU workstation. An image sequence of such a T-pull simulation is shown in Fig. 4.9.

In the validation phase of the T-pull simulation models, it turned out that the models are very sensitive to parameter changes, especially with respect to the tiebreak contact parameters of the metal pin-to-composite interface. Although the initial stiffness in the resulting T-pull force–displacement diagrams could be predicted with very high accuracy compared to the test results, and the failure initiation load could be predicted with acceptable accuracy, the discrepancy between test and simulation was larger for the post-damage pin pull-out behavior. One explanation was found in the too simplified modeling of the arrow-pins and especially their pin root geometry, which leads to a different pin upward bending behavior between test and simulation. Furthermore, certain imperfections like resin-rich zones around the pin roots and pin heads as well as fiber undulations are not represented in the model. Including these details would make the already very complex models even more complex and reduce mesh size and computational efficiency.

4.5 Conclusion

The reinforcement concept in through-thickness direction of composite T-joints using metallic arrow-pin sheets was further elaborated in this study both on experimental and numerical side. More precisely, new material and design improvement options were assessed, which could further increase the damage resistance and total energy absorption for joint separation. All these options, i.e. toughened epoxy resin, additional center pins, increased pin density, milled thermoplastic filler and additional thermoplastic binder fleece layers, showed beneficial effects. Design D7, which incorporates almost all of these measures, could increase the total energy absorption by impressive 720 % compared to the state-of-the-art design D1.

The numerical studies using detailed meso-models indicated the high complexity of these arrow-pin-reinforced structures and their failure behavior. Although the models were built and validated step by step along the test pyramid, the overall predictive quality of local failure modes and overall energy absorption can still be improved by more realistic modeling of the pin sheet geometry and local imperfections.

As a next step of this study, these improved T-joint designs will be used for fuel-filled tank structures in order to verify the performance enhancements under hydrodynamic ram loads.

Acknowledgement Sincere thanks are given to Jose Luis Sandoval Murillo and Florian Troeltsch for their contributions to the numerical studies and to Christian Metzner for the support in the thermoplastic interleaf technology.

References

1. Burns, L., Mouritz, A.P., Pook, D., Feih, S.: Bio-inspired hierarchical design of composite T-joints with improved structural properties. *Compos. Part B-Eng.* **69**, 222–231 (2015)
2. Burns, L., Mouritz, A.P., Pook, D., Feih, S.: Strengthening of composite T-joints using novel ply design approaches. *Compos. Part B-Eng.* **88**, 73–84 (2016)
3. Motsch, N., Magin, M.: Influence of structural stitching on composite T-joint strength. In: 20th International Conference on Composite Materials (ICCM-20), Copenhagen, Denmark, 19–24 July 2015
4. Yan, S., Long, A., Zeng, X.: Experimental assessment and numerical analysis of 3D woven composite T-joints under tensile loading. In: 20th International Conference on Composite Materials (ICCM-20), Copenhagen, Denmark, 19–24 July 2015
5. Bianchi, F., Koh, T.M., Zhang, X., Partridge, I.K., Mouritz, A.P.: Finite element modelling of z-pinned composite T-joints. *Compos. Sci. Technol.* **73**, 48–56 (2012)
6. Heimbs, S., Nogueira, A.C., Hombergsmeier, E., May, M., Wolfrum, J.: Failure behaviour of composite T-joints with novel metallic arrow-pin reinforcement. *Compos. Struct.* **110**, 16–28 (2014)
7. May, M., Ganzenmüller, G., Wolfrum, J., Heimbs, S.: Analysis of composite T-joint designs for enhanced resistance to hydrodynamic ram. *Compos. Struct.* **125**, 188–194 (2015)
8. Heimbs, S., Duwensee, T., Nogueira, A.C., Wolfrum, J.: Hydrodynamic ram analysis of aircraft fuel tanks with different composite T-joint designs. In: 13th International Conference on Structures Under Shock and Impact (SUSI 2014), New Forest, UK, 3–5 June 2014
9. Heimbs, S., Mierzwa, A., Duwensee, T., Nogueira, A.C., Breu, C., May, M., Less, C., Wolfrum, J.: Investigation of static and dynamic failure behaviour of composite T-joints. In: 4th ECCOMAS Thematic Conference on the Mechanical Response of Composites (Composites 2013), Azores, Portugal, 25–27 September 2013
10. Sandoval Murillo, J.L., Ganzenmüller, G.C., Heimbs, S., May, M.: Design parameter study of a CFRP T-joint under overpressure conditions due to ballistic impact. In: 17th European Conference on Composite Materials (ECCM17), Munich, 26–30 June 2016
11. Juergens, M., Von Hafe Perez Ferreira Da Silva, M.T., Heimbs, S., Lang, H., Ladstaetter, E., Hombergsmeier, E.: Pull-out testing of multiscale structured metallic z-reinforcements for CFRP laminates. *Compos. Struct.* submitted for publication (2016)

Chapter 5

Review of Natural Joints and Bio-Inspired CFRP to Steel joints

Evangelos I. Avgoulas and Michael P.F. Sutcliffe

Abstract There is a great variety of joint types used in nature, from jaws, bones and tendons to root systems and tree branches. To understand how to optimise biomimetic-inspired engineering joints, first it is important to understand how biological joints work. In this paper, a review based on the functions of natural joint systems is presented. Emphasis was given to understanding natural joints from a mechanical point of view, so as to inspire engineers to find innovative methods of joining man-made structures. Nature has found many ingenious ways of joining dissimilar materials, with a transitional zone of stiffness at the insertion site commonly used. In engineering joints, one way to reduce the material stiffness mismatch is to gradually decrease the effective stiffness of the steel part of the joint by perforating it with holes. This paper investigates joining of flat perforated steel plates to a CFRP part by a co-infusion resin transfer moulding process. The joints are tested under static tensile loading. The perforated steel joints show a 175% increase of joint strength comparing to non-perforated ones. Finite element analyses are used to interpret the experimental results.

Keywords Biomimetics • Nature • Joints/joining • CFRP • Perforated steel • Resin transfer moulding (RTM)

5.1 Introduction

Joining of composites parts, together with their damage tolerance and inserts, are of paramount importance in mechanical design because they cause structural discontinuities that are often the Achilles heel of a structural design. Adhesive bonding is a popular method for joining dissimilar materials because produces joints with higher structural efficiency, excellent fatigue life, a particularly small weight penalty and more uniform stress fields than alternatives such as fastening or riveting. Additionally, corrosion between the dissimilar materials is prevented [1–5]. However, joining composite with metal parts leads to high stress concentrations, and thus weak joints, due to the material property mismatch. Since joining of dissimilar materials, such as CFRP to steel, is widely used in high performance structures, an innovative approach is needed to meet this challenge. This paper uses the biomimetic approach to inspire a new joint design. Biomimetics is the imitation of nature's design principles applied to engineering/man-made structures. Nature has the advantage of 3.8 billions of years of research and development programme to produce an amazing range of design solutions. There is an abundance of natural world examples where two components of differing material properties are joined together [6]. The aim is to understand and analyse the functions of natural joints from a mechanical perspective and, thus, to identify characteristics that can be transferred from natural to engineering joints between metal and composite. A common solution found in nature when joining dissimilar materials is to use a transitional zone of stiffness in the insertion site [6]. One way to apply this design to engineering joints is to gradually decrease the stiffness of the joint metal part by perforating it. The concept of reducing the stiffness of a steel plate using perforations was firstly proposed and patented by Unden and Ridder [7]. Related studies have been conducted in GFRP to perforated steel joints [8] and in a sandwich structure with GFRP skins joined to a perforated steel structure [9].

In the present paper, co-infused CFRP to perforated steel joints were numerically and experimentally investigated under static mechanical testing. The structure of this paper is as follows. A brief review of natural joint systems is presented in Sect. 5.2. Section 5.3 introduces the finite element modelling and experimental methodology of the bio-inspired CFRP to perforated steel joints. The results and discussion of the outputs are analysed in Sect. 5.4, with the conclusions presented in Sect. 5.5.

E.I. Avgoulas (✉) • M.P.F. Sutcliffe
Department of Engineering, University of Cambridge, Trumpington Street, Cambridge CB2 1PZ, UK
e-mail: eia21@cam.ac.uk; mpfs@eng.cam.ac.uk

5.2 Review of Natural Joint Systems

A literature review of natural joint systems has been carried out [6], where natural joints were classified into five different categories, based on the different joining method used by nature to create the joint. These are network structures, stiffness transitional zone, mechanisms, hooks and adhesive. In the present paper, the first two categories will be briefly mentioned as they have already inspired researchers to develop biomimetic engineering joint design concepts. An in depth review of natural joint systems from a mechanical perspective can be found in [6].

5.2.1 Joining Method—Network Structures

The study of the joints between tree branches and trunks has provided a source of inspiration for the design of biomimetic aerospace composite T-joints with increased damage tolerance [10]. In a study of the tree species *Pinus Radiata*, the branch-trunk connection was found to exhibit a ductile failure response, despite the relatively brittle nature of the underlying cellulose constituent material comprising the natural wood composite. This ductile response and high structural efficiency was achieved in nature using an efficient and complex hierarchical structure to the joint. Such a hierarchical design is common in biological structures, where the nano-, micro-, meso- and macro-length scales can interact so as to achieve a uniform strain distribution associated with high structural efficiency [11]. Burns et al. [10] applied the embedded tree-joint design to a composite T-joint and demonstrated that the ductility and the damage tolerance of the joint were increased. However, the joints showed a reduction in the load at which damage started because of the higher interlaminar stresses induced in the embedded design at the radius bend. By optimising the stacking sequence of the plies of the composite laminate at the joint this study showed that the interlaminar tension and shear stresses in the radius could be reduced [12]. This change in the local stresses led to an increase in the load at which damage initiated as well as the ultimate strength and the failure displacement of the composite T-joint.

Figure 5.1 shows a set of X-ray tomography images of the branch-trunk joint of *Pinus Radiata* [10]. The images highlight the key design features that give rise to the excellent mechanical properties of these branch-trunk joints. These features are embedded design, 3D fibre lay-up and variable density. Figure 5.1a illustrates the embedded design, which is comprised of a cone-shaped branch end embedded in the main trunk geometry. Such an embedded branch design has the advantages of increasing of the effective load transfer area at the joint load so as to reduce the average stress at the interface of the branch-trunk joint. Moreover, any interfacial cracks which initiate have to grow in a mode II shear mode than in a tensile mode I crack opening. This switch to shearing leads to an increased toughness. A second strengthening feature relates to the 3D fibre lay-up in which the fibres within the trunk extend forward and laterally within the joint. In this way the branch is fully enclosed in a “ball and socket” joint configuration (Fig. 5.1b). Finally there is a fibre density variation within the joint (see Fig. 5.1c) which leads to the creation of an iso-strain condition in the joint by reducing the elastic modulus mismatch between the fibres aligned along the branch and trunk directions.

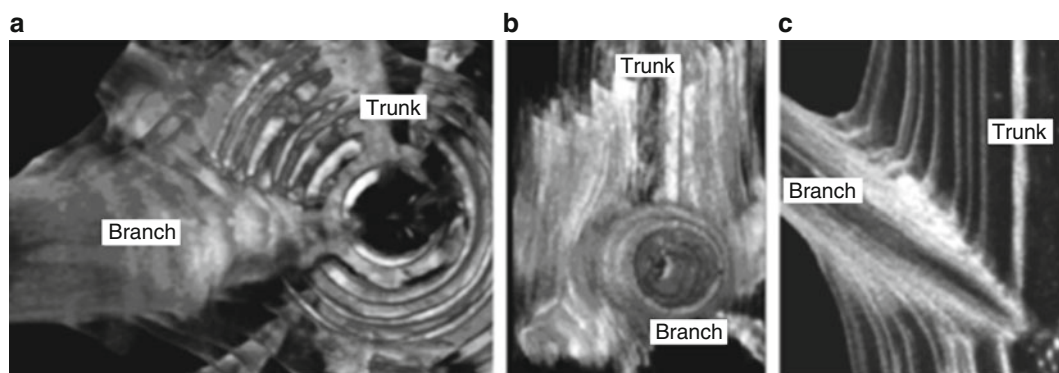


Fig. 5.1 (a) Internal cone-shaped branch structure embedded in the tree centre, (b) 3D fibre lay-up and (c) fibre density variation across the joint [10]

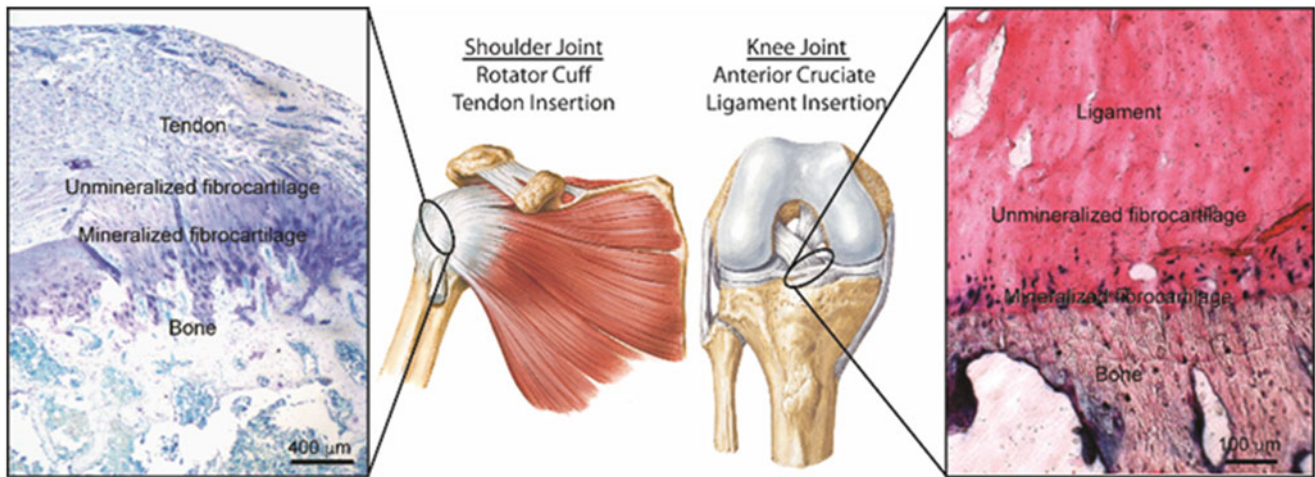


Fig. 5.2 Morphology of the supraspinatus tendon-to-bone insertion site [16]

5.2.2 Joining Method: Transitional Zone of Stiffness

Nature has a very effective way of joining flexible tendon to stiff bone. By introducing a complex transitional region at the interface, stress concentrations that could potentially arise at the joint are reduced or avoided. This is achieved by having a functionally-graded change in material properties at the tendon-to-bone insertion site, in which there are variations in mechanical properties, extracellular matrix composition (EMC), structural organization, and mineral content [13, 14]. Four different types of tissue can be identified in the tendon-to-bone insertion site when under an optical microscope [15]. These are tendon, fibrocartilage, mineralized fibrocartilage, and bone (see Fig. 5.2). There are two major factors which contribute to the increase in tissue stiffness from the tendon to the bone material. Firstly, the linearly increasing mineral concentration stiffens the partially mineralized collagen fibres [14]. Secondly, a decrease in the collagen fibre orientation distribution in the transition region going from the tendon to the bone gives rise to tissue stiffening. The combination of these two factors gives a variation in stiffness across the insertion site. In summary this tendon example demonstrates how nature is able to use a functionally-graded material transition region to provide an effective attachment mechanism between two mechanically different materials.

5.2.3 Options to Increase the Strength of Engineering Joining Systems

Joining of different materials with differing bulk properties is needed both in natural and man-made structures. In both cases the materials' mismatch leads to potential stress concentrations. So the issue in both cases is to ensure that the possibility of interfacial failure is reduced where such joints between different materials occur [17]. There are two options for engineering joints. The first option is to increase the interaction energy at the zone of contact between the two materials being joined. This can be effected by applying a surface treatment to the metal adherends prior to bonding (for example primers or a coupling agent) [18]. Although this procedure will not reduce the interfacial radial stresses, it will increase the failure stress. The second option is to avoid sharp boundaries between the different materials being joined by introducing functional gradients [19]. This method creates materials with graded mechanical properties such that they are able to resist damage more effectively than their homogeneous counterparts. In this novel procedure the radial stresses which are generated are spread over a larger surface area. This use of functional gradients in man-made structures has several advantages [19], such as reducing stress concentrations by eliminating stress singularities and by developing smooth stress distributions, increase fracture toughness and improve bonding strength.

5.3 Bio-Inspired CFRP to Perforated Steel Joints

This paper is inspired by the biomimetics approach, where nature uses a transitional zone of stiffness in the insertion site when joining dissimilar materials. One way to apply this design to engineering joints is to gradually decrease the stiffness of the joint metal part by perforating it. Figure 5.3 illustrates the proposed joint configurations, consisting of unidirectional CFRP and steel plates, which were perforated to create a transitional zone of stiffness between the steel and CFRP adherends. For comparison, reference specimens (REF) were tested with the same configuration but with a non-perforated steel part. A parametric finite element analysis was conducted to optimise the perforation patterns, while keeping all the other joint geometry the same. The analysis showed that two styles of perforation pattern performed well, a pattern with a maximum hole diameter of 4 mm (denoted “SH” for small hole), and a large hole (“LH”) pattern with a maximum hole diameter of 5 mm. In both cases there were seven rows of holes, with a change in diameter between rows of holes of 0.25 mm. The only difference between the two perforated configurations is the hole diameters in the steel plates. All the other geometric variables remained the same.

5.3.1 Numerical Modelling

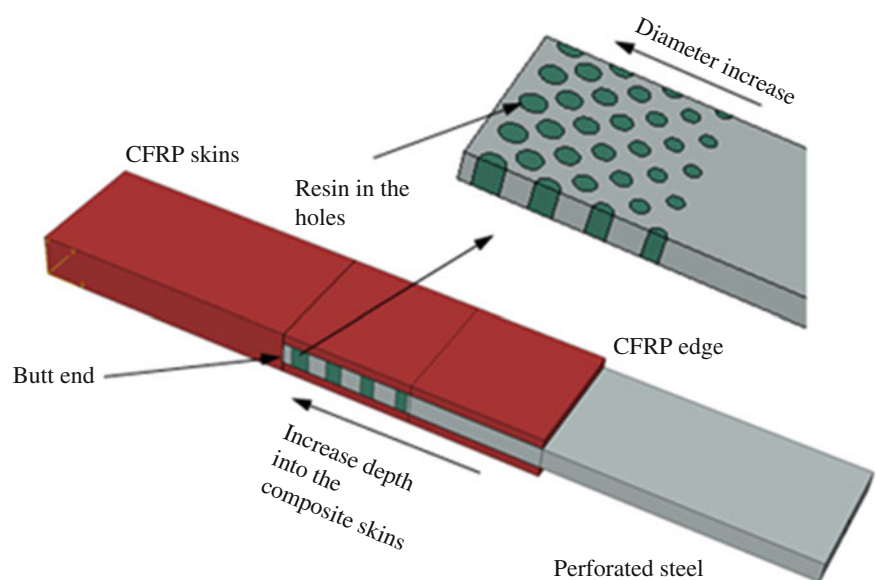
Three-dimensional finite-element models were developed with ABAQUS®. The overlap length and the free lengths of the steel and CFRP parts were all equal to 60 mm. The dimensions of the model can be seen in Fig. 5.4a. The CFRP and steel adherends were modelled with elastic orthotropic and isotropic material properties, respectively. Linear 8-node reduced integration brick elements (C3D8I) available in the ABAQUS® element library were used for both adherends.

The adhesive layer was modelled with a single layer of 8-node three-dimensional cohesive elements (COH3D8) with a thickness of 0.2 mm. A triangular cohesive zone degradation formulation was chosen because of its simplicity, widespread use for investigation purposes, especially for brittle adhesives [20], and availability in ABAQUS®. A geometrically non-linear static analysis was performed. Fixed boundary conditions were applied to the CFRP end of the joint to reproduce the testing machine gripping. A displacement u_x was applied to the steel end of the model together with a lateral restraint (Fig. 5.4b).

5.3.2 Specimen Manufacture and Tensile Testing

Resin transfer moulding was used to co-infuse and bond the CFRP/steel joint. The steel parts were perforated with a water-jet cutter, sand-blasted and cleaned before moulding. The panels were then cut into specimens with a nominal width of 30 mm. It was hypothesised that the mechanical interlocking effect of the resin ingress in the holes would enhance the joint

Fig. 5.3 CFRP to perforated steel model design configuration



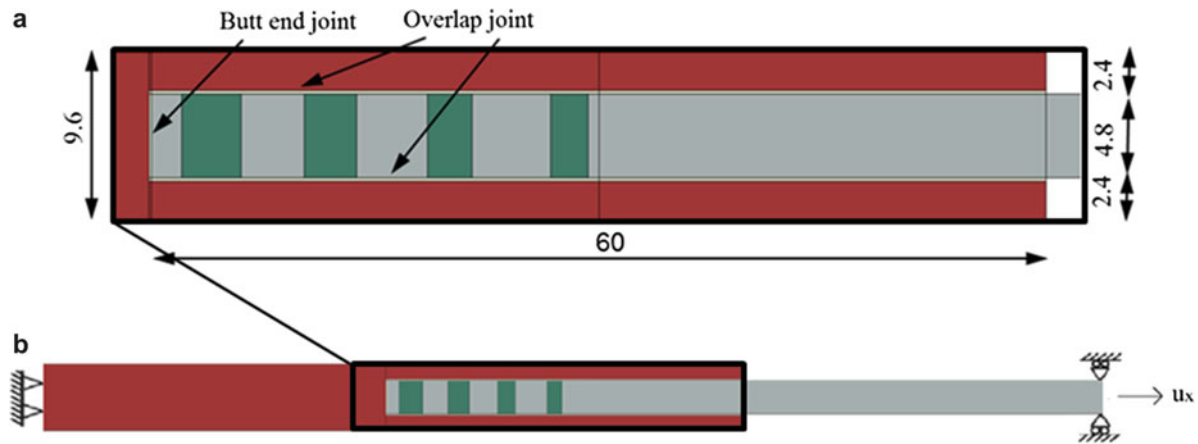


Fig. 5.4 (a) Joint geometry (dimensions in mm) and (b) loading and boundary conditions

mechanical properties. To test this all of the holes in some specimens were filled with PTFE plugs, preventing ingress of resin into the holes. Further details of the design and manufacturing can be found in [21]. Static tensile tests were performed with a fixed displacement rate of 0.2 mm/min. The load and displacement readings were obtained from the machine load cell and clip gauge extensometers, respectively. A high speed camera (16,000 frames per second) was used to image the initiation and propagation of the joint failure.

5.4 Results and Discussion of Bio-Inspired CFRP to Perforated Steel Joints

5.4.1 Load-Displacement Response

Figure 5.5 shows the load versus displacement results from experimental tests on a SH joint without PTFE inserts and on a reference joint configuration. The perforated joint has only a small drop in stiffness before it fails catastrophically. By contrast, the non-perforated reference joint failed prematurely at the butt end of the joint steel part, with a crack propagating away from there to give failure of one of the two laps. This gives the sharp change in the load–displacement curve (Fig. 5.5). After this failure, the remaining intact lap was able to carry a further increased load until final failure occurred. Included in Fig. 5.5 is a simulation for the standard reference configuration, and an additional calculation where one of the laps of the reference joint was assumed to fail at the load observed in the experimental test.

5.4.2 Maximum Load

Figure 5.6 summarises the average maximum loads obtained from the experiments. Compared to non-perforated joints, the perforated SH with PTFE configuration showed a 175% increase of joint strength. The difference in the average maximum load for perforated joints with and without PTFE in the SH specimens was negligible. Thus, the hypothesis that resin ingress into the holes gives an increase in joint strength associated with mechanical interlocking is not observed for this perforation case. Instead it is presumed that the dominant factor which contributed to the significantly higher strength of the perforated joints, comparing to the non-perforated ones, is the transitional zone of stiffness.

5.4.3 Failure Observation Using High Speed Camera

For all the perforated joints, high-speed camera images showed that the failure initiated at the CFRP end of the joint with a crack propagating rapidly towards the butt end. The crack propagated between the steel and composite interface. Figure 5.7 shows selected frames capturing the failure initiation and the catastrophic failure of a SH joint. On the other hand, the

Fig. 5.5 Comparison between the numerical predictions and measured experimental load-displacement response curves, comparing non-perforated (REF) and perforated (SH) steel joints

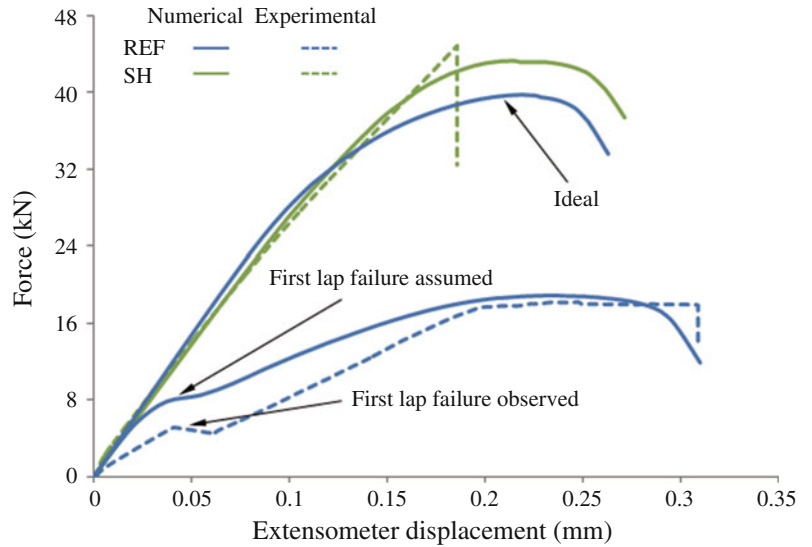


Fig. 5.6 Comparison of the average maximum load between non-perforated and perforated steel joints

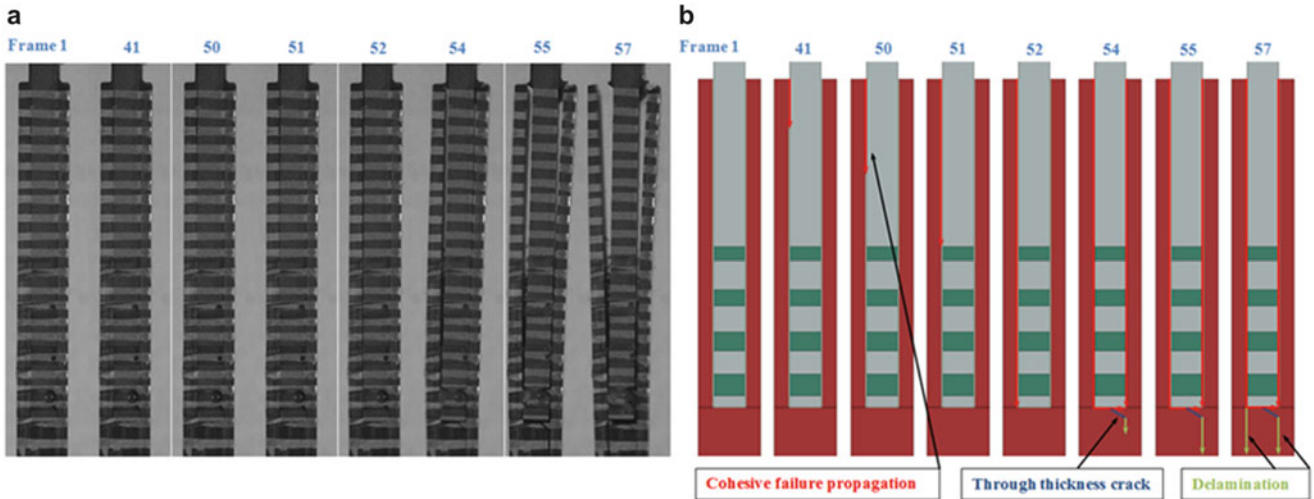
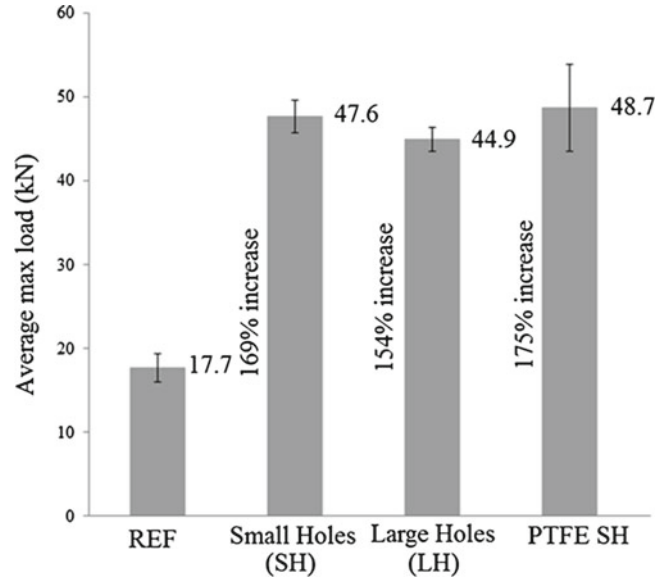


Fig. 5.7 (a) Catastrophic failure of a perforated SH specimen, showing selected frames from the high speed camera video (time proceeds from left to right as indicated by the frame number; the time between frames is 1/16,000 s), (b) schematic representation of the failure seen in the images

non-perforated joints indicated that the failure initiated at the butt end of the steel part of these joints, propagating towards the CFRP joint end until the first lap failed. From that point, the single intact lap carried a further increased load until final failure occurred. It is inferred that it is this change in failure mode associated with the change in steel stiffness which gives the observed increase in failure strength.

5.5 Conclusions

The biological principle of uniform strain found in branch-trunk joints has already inspired researchers to mimic this design to improve engineering joints. In nature, the tendon-to-bone attachment uses a gradual transition zone of stiffness to join flexible and stiff materials. One way to apply the idea of a transitional zone of stiffness to engineering joints is to gradually decrease the stiffness of the joint metal part by perforating it. A numerical and experimental investigation of bio-inspired CFRP to perforated steel joints has been presented. Compared to non-perforated joints, perforated joints showed a 175% increase of joint strength. High speed camera images showed that the failure initiated at the CFRP end with a crack propagating abruptly towards the butt end of the joint. By contrast, non-perforated joints failed prematurely at the butt end and a crack propagated away from there to give failure of the first lap. The factor that contributed to the significantly higher strength of the perforated joints was the transitional zone of stiffness that the perforated joints offer. The resin in the holes offered no additional increase of the joint strength in the SH specimens. The numerical and experimental results were in good agreement.

Acknowledgements The authors acknowledge the financial support provided by the Engineering and Physical Sciences Research Council (EPSRC) and Dowty Propellers (part of GE Aviation).

References

- Banea, M.D., da Silva, L.F.M.: Adhesively bonded joints in composite materials: an overview. *J. Mater. Des. Appl.* **223**, 1–18 (2009)
- Campilho, R.D.S.G., Banea, M.D., Neto, J.A.B.P., da Silva, L.F.M.: Modelling of single-lap joints using cohesive zone models: effect of the cohesive parameters on the output of the simulations. *J. Adhesion* **88**, 513–533 (2012)
- Anyfantis, K.N.: Finite element predictions of composite-to-metal bonded joints with ductile adhesive materials. *Compos. Struct.* **94**, 2632–2639 (2012)
- Anyfantis, K.N., Tsouvalis, N.G.: Loading and fracture response of CFRP-to-steel adhesively bonded joints with thick adherents—Part I: experiments. *Compos. Struct.* **96**, 850–857 (2013)
- Anyfantis, K.N., Tsouvalis, N.G.: Loading and fracture response of CFRP-to-steel adhesively bonded joints with thick adherents—Part II: numerical simulation. *Compos. Struct.* **96**, 858–868 (2013)
- Avgoulas, E.I., Sutcliffe, M.P.F.: Biomimetic-inspired joining of composite with metal structures: a survey of natural joints and application to single lap joints. In: *Proceedings of the SPIE Smart Structures and Materials: Bioinspiration, Biomimetics, and Bioreplication IV*, San Diego, CA, 9–13 March 2014
- Uden, H., Ridder, S.O.: Load-introducing armature as component part of a laminated structural element US Patent 4,673,606, 13 Feb 1985
- Melogranaa, D.J., Grenstedt, L.J.: Improving joints between composites and steel using perforations. *Compos. Part A: Appl. Sci. Manuf.* **33**, 1253–1261 (2002)
- Cao, J., Grenstedt, L.: Design and testing of joints for composite sandwich/steel hybridic ship hulls. *Compos. Part A: Appl. Sci. Manuf.* **35**, 1091–1105 (2004)
- Burns, L.A., Mouritz, A.P., Pook, D., Feih, S.: Bio-inspired design of aerospace composite joints for improved damage tolerance. *Compos. Struct.* **94**, 995–1004 (2012)
- Matthack, C., Bethge, K.: The structural optimisation of trees. *Naturwissenschaften* **85**, 1–10 (1998)
- Burns, L.A., Mouritz, A.P., Pook, D., Feih, S.: Strength improvement to composite T-joints under bending through bio-inspired design. *Compos. Part A: Appl. Sci. Manuf.* **43**, 1971–1980 (2012)
- Benjamin, M., Toumi, H., Ralphs, J.R., Bydder, G., Best, T.M., Milz, S.: Where tendons and ligaments meet bone: attachment sites ('entheses') in relation to exercise and/or mechanical load. *J. Anat.* **208**, 471–490 (2006)
- Thomopoulos, S., Genin, G.M., Galatz, L.M.: The development and morphogenesis of the tendon-to-bone insertion—What development can teach us about healing. *J. Musculoskelet. Neuronal Interact.* **10**(1), 35–45 (2010)
- Benjamin, M., Kumai, T., Milz, S., Boszczyk, B.M., Boszczyk, A.A., Ralphs, J.R.: The skeletal attachment of tendons-tendon 'entheses'. *Comp. Biochem. Physiol. A Mol. Integr. Physiol.* **133**(4), 931–945 (2002)
- Lu, H.H., Thomopoulos, S.: Functional attachment of soft tissues to bone: development, healing, and tissue engineering. *Annu. Rev. Biomed. Eng.* **15**, 201–226 (2013)
- Waite, J.H., Lichtenegger, H.C., Stucky, G.D., Hansma, P.: Exploring molecular and mechanical gradients in structural bioscaffolds. *Biochemistry* **43**(24), 7653–7662 (2004)
- Vincent, J.F.V.: *Structural Biomaterials*. Princeton University Press, Princeton, NJ (1990)
- Suresh, S.: Graded materials for resistance to contact deformation and damage. *Science* **292**, 2447–2451 (2001)

20. Campilho, R.D.S.G., Banea, M.D., Pinto, A.M.G., da Silva, L.F.M., de Jesus, A.M.P.: Strength prediction of single- and double-lap joints by standard and extended finite element modelling. *Int. J. Adhes. Adhes.* **31**, 363–372 (2011)
21. Avgoulas, E.I., Sutcliffe, M.P.F.: Numerical and experimental investigation of CFRP to perforated steel joints. In: *Proceedings of the 20th International Conference on Composite Materials*, Copenhagen, Denmark, 9–24 July 2015

Chapter 6

Fabrication of 3D Thermoplastic Sandwich Structures Utilizing Ultrasonic Spot Welding

Cassandra M. Degen and Navaraj Gurung

Abstract The ultimate goal of this work was to create 3D polycarbonate sandwich structures fabricated utilizing ultrasonic spot welding (USSW). First, a study of weld strength vs. weld time, frequency, amplitude of vibration and depth of penetration was carried out. Lap shear and peel tests were used to quantitatively characterize weld strength, and from these results, a set of parameters for USSW of polycarbonate was determined. To create the sandwich structures, three layers of 1.59 mm polycarbonate sheet were stacked together, and using an alternating pattern of USSW, the middle layer was joined to each of the outer layers. Post-weld processing of the stacked layers involving heat and pressurization of the structure with air generated a 3D open cell geometry sandwich structure of polycarbonate. 3-point bend and drop impact tests were conducted to study the stiffness and the impact properties of the sandwich structures, and the results suggest that the fabricated polycarbonate sandwich structures might be suitable for applications requiring high strength and energy absorption while maintaining low weight. Additionally, the ability to easily incorporate different geometries in the structure allows the possibility to design structures with tailored mechanical properties.

Keywords Sandwich structures • Ultrasonic spot welding • Thermoforming • Polycarbonate • Thermoplastic

6.1 Introduction

As industries across the globe move towards optimization of efficiency, lightweight structural components are becoming increasingly important. Large strides have been made in high strength-to-weight ratio structures, and manufacturing techniques are needed to match the expanding material technology and the applications in which they are used.

Ultrasonic welding is a widely used technique for joining polymeric materials, and in particular, thermoplastic polymers. This welding method uses high frequency, low amplitude vibrations applied through an ultrasonic horn to create frictional heat [1–3]. Localized melting occurs at the interface of the materials during the welding process, and upon solidification, a solid-state joint is produced between polymer sheets. Equipment for ultrasonic welding is available from a number of companies, small in physical size, and easy to operate. Most ultrasonic spot welders have a constant frequency, typically either 20 or 40 kHz for polymeric materials. Adjustable parameters include: amplitude of vibration, pressure applied to the material during welding, length of time of vibration applied during welding, and depth of penetration of the tip into the material, each of which has an effect on the strength of the ultrasonic weld [4]. The ultrasonic welding system used in this work is a 20 kHz instrument from the Dukane Corporation [5] shown in Fig. 6.1.

Advantages of ultrasonic welding over other joining methods include high production rates, design freedom, energy efficiency, and ease of assembly [6]. These advantages make ultrasonic welding attractive for automation and industrial use. Disadvantages of this joining method include sample size limitations, material limitations to mainly thermoplastic polymers, noise considerations, and expensive equipment [6]. Currently, ultrasonic welding is used in industry in the automotive arena, for medical applications [6], for packaging, and for sealing of MEMS devices [7]. Ultrasonic welding has also been used for applications such as the bonding of wood [8], and for application to recent technologies such as the bonding of thermoplastic microfluidics [9]. Modeling efforts have also been used to contribute to the understanding of ultrasonic welding, capturing deformation, vibration dissipation, material flow, and heat flow [10].

C.M. Degen (✉) • N. Gurung
Department of Mechanical Engineering, South Dakota School of Mines and Technology,
501 E. Saint Joseph St., Rapid City, SD 57701, USA
e-mail: cassandra.degen@sdsmt.edu

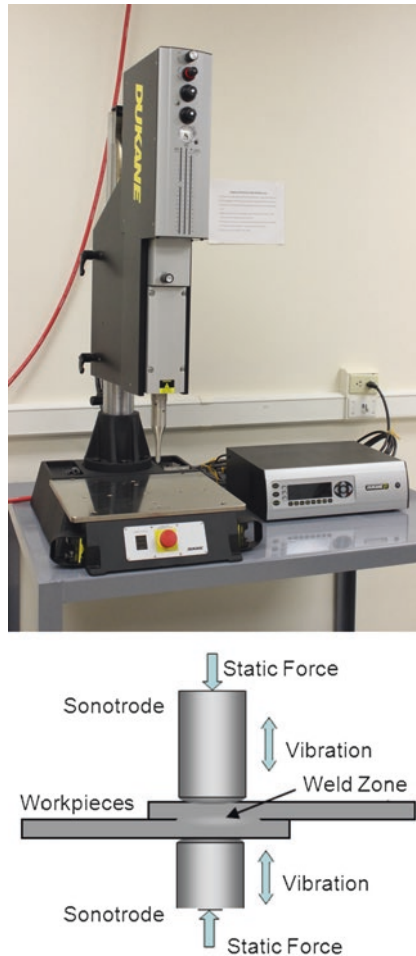


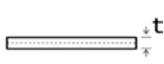
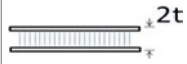

Fig. 6.1 Dukane ultrasonic welding system in PI's laboratory (*top*) and side-view schematic of ultrasonic spot welding process (*bottom*)

Polymers are extensively used for many consumer products. Low density, low electrical conductivity, high strength to weight ratio, good resistance to chemicals, wide choices of colors and transparencies, ease of manufacturing, and relatively low cost make polymers suitable for many applications [11]. The scope of applications of polymers ranges from common plastic bags to precision medical equipment. Polymers can contain a variety of additives and fillers to improve a particular property of the polymer such as processability, thermal or environmental stability, or the modulus of the final product [12]. Generally, for structural purposes, glass or carbon fibers are added to polymer resin to achieve superior strength. Carbon fiber reinforced plastic composites are one of the highly sought after materials for structural applications and the use of these composites has been growing steadily since the early 1950s [13]. Despite their superior structural efficiency, the complex processing techniques and high manufacturing cost of these reinforced plastics has restricted their use in general low budget applications.

The structural efficiency of any polymer component can be maximized by either using stronger materials or by optimizing the structure's geometry [13]. Therefore the limitation posed by the processing techniques and high manufacturing cost of reinforced polymers can be overcome by optimizing its structural geometry. One of the best methods to fabricate high strength-to-weight ratio structures is to use stiffeners, as in the cases of I-beams and T joints. These stiffeners can be used as an integral part of the component or may be attached through adhesive bonding [13].

Sandwich-structures are composite structures consisting of two face sheets and a preformed, lightweight core. In general, a sandwich layer consists of (1) a pair of thin stiff skins; (2) a thick, light weight core to separate the skins and carry the load from one skin to another; (3) an adhesive or some other form of attachment which transmits loads in between core and the skins. The separation created by the core increases moment of inertia of the skin plates, which makes them more efficient in resisting bending and buckling loads. Table 6.1 shows a comparison between the stiffness and strength of structures made out of the same thickness plate with varying thickness of core material, with the far left structure containing no core.

Table 6.1 An example of structural efficiency of sandwich panels in terms of weight [13]

			
Relative bending stiffness	1	7.0	37
Relative bending strength	1	3.5	9.2
Relative strength	1	1.03	1.06

Sandwich-structures have benefits of high strength-to-weight ratios [14] and enhanced resistance to impulsive loads [15], characteristics particularly important for aerospace or automotive applications, and have received significant attention in recent years. In addition, varying the geometry of sandwich-structures has been shown to affect their mechanical response [16, 17]. Sandwich-structures with a sinusoidal unit cell have been studied for their elastic properties analytically and experimentally [18]. Analytical models have been developed to predict the mechanical behavior of corrugated paperboard [18]. The dynamic shock cushioning of sandwich-structures is also an area of recent research, and has been explored experimentally with a drop shock tester to find that the structures have superior cushioning properties, particularly useful for the packaging industry [19, 20]. The adaptability of sandwich-structures as multifunctional materials has been explored with the incorporation of polymer resin and glass spheres into the structure to enhance the fire response [21], and the incorporation of shape memory materials into the structure to create sandwich-structures to detect damage [22]. Analytical and computational modeling of the mechanical [23–27] and thermal [28, 29] responses of sandwich-structures is also an area of interest. While the benefits of sandwich-structures are well-studied, cost- and time- effective manufacturing methods remain an active research area.

The goal of this work was to utilize ultrasonic spot welding to fabricate 3D polycarbonate sandwich structures and characterize the bending stiffness and impact properties of such structures. Experiments were carried out to determine the proper thermoforming parameters for the fabrication process. 3D sandwich structures designed and fabricated with two different grid sizes were analyzed to determine the possibilities of tailoring the mechanical properties of the structure. 3-point bend tests and impact tests were conducted to characterize the sandwich structures. While the work presented here focuses on using polycarbonate panels as both outer layers and core, the flexibility of the ultrasonic spot welding technique allows for the replacement of polycarbonate panels with fiber reinforced composite material, which broadens the scope of the work.

6.2 Characterization of Ultrasonic Spot Welds in Polycarbonate

The welding parameters that dictate the quality of ultrasonic spot welds are frequency, weld amplitude, weld time, weld pressure, and weld depth. The Dukane ultrasonic spot weld system has a fixed frequency of 20 kHz, a maximum amplitude of 120 μm adjustable from 20% (24 μm) to 100% (120 μm), variable weld time, pressure, and depth. The depth, to which the welding tip penetrates through the material, was kept constant for this work at 27% through the thickness of the bottom layer of material. The material used for this work was 1.59 mm thick Bayer MaterialScience Makrolon[®] polycarbonate sheet. To study the effect of varying parameters and determine effective parameters, welds were made with the parameters listed in Table 6.2 by varying one parameter while keeping the others constant, and the strength of those welds were measured by both lap shear and peel tests. During the welding process, the material at the welding interface melts and flows across the vicinity of spot weld. The area covered by this melted material can be visually traced from optical images of the spot weld. Image processing software (*ImageJ* 1.47 t) was used to measure each bond area.

To measure the tensile shear strength of the spot welds, lap shear tests were carried out according to ASTM D3164 [30]. Mode II failure of the welds was achieved by gluing tabs at both ends of the specimen to minimize the offsetting of uniaxial shear force. Peel tests designed to initiate Mode I failure were conducted according to ASTM D1876-08 [31], using metal hinges glued to this specimen to mount in the testing grips. A MTS 858 Mini Bionix II (Fig. 6.2) was used for both testing setups and the displacement rate used for all testing was 1.27 mm/min. During the lap shear and peel tests, the load was measured and the peak load was recorded. The peak load experienced by the sample before failure was divided by the previously measured bond area to calculate the peak stress.

Figure 6.3 shows the peak tensile shear stress achieved in ultrasonic spot welds with varying weld amplitude, weld time, and weld pressure during lap shear and peel testing. The Dukane ultrasonic welding system also measured the total energy input during the weld process by calculating the required power (voltage \times current) for each 0.5 ms and summing the power over the entire weld cycle to compute the input energy (power \times time). Figure 6.3 also shows the summary of weld strength measured by peak stress during lap shear and peel testing as a function of the energy input during the weld cycle. While the trend was weak and data was highly varied, the maximum weld strengths were seen when the energy input was near 100 J. The data suggests further optimization is needed for weld parameters as well as repeatability of ultrasonic spot welding to

Table 6.2 Ultrasonic spot welding parameters used for lap shear and peel samples

	Pressure (kPa)	Amplitude (um)	Time (s)	
Range of parameters	103, 172, 241	24, 30, 50.4	0.7, 1.4, 2.1,	2, 4, 6, 8
Number of samples (n)	12	9	12	3



Fig. 6.2 MTS Mini Bionix II with lap shear sample (left), and close up of the lap shear test (center) and peel test (right)

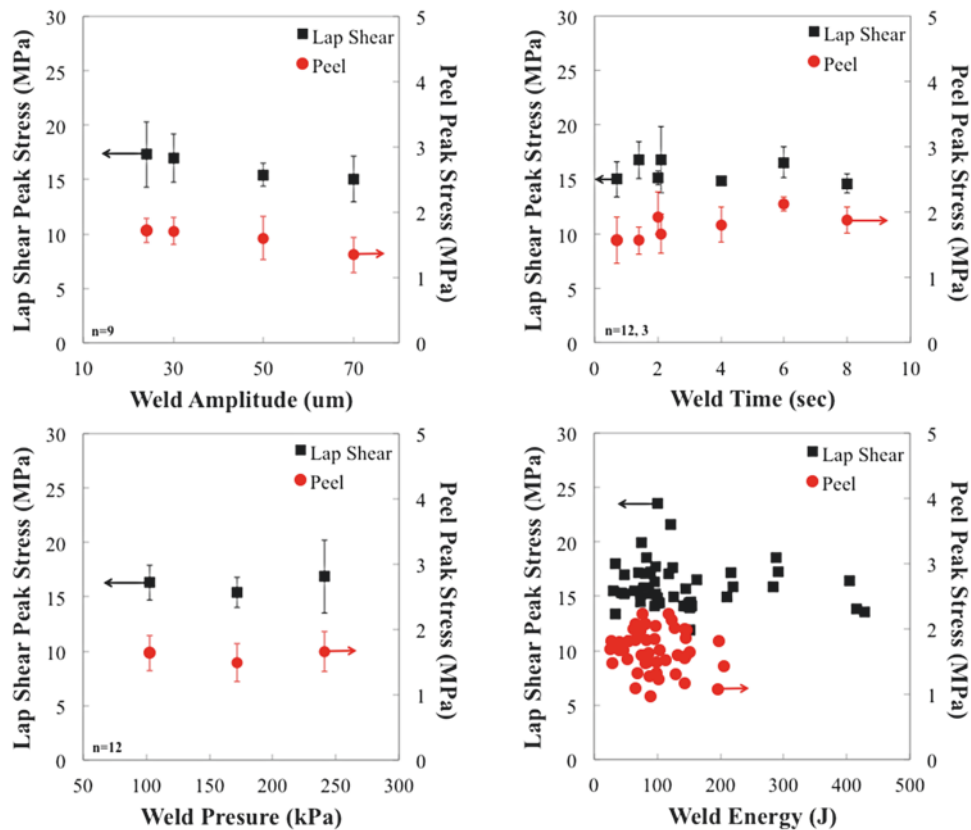


Fig. 6.3 Lap shear and peel test results for varying weld amplitude (top left), weld time (top right), weld pressure (bottom left), and weld energy (bottom right). Error bars represent one standard deviation

give clear trends for the ideal welding parameters to achieve maximum lap shear and peel strength. The results indicate the following as appropriate parameters for the ultrasonic spot welding of 1.59 mm thick polycarbonate sheet: welding amplitude of 24 μm , welding time of 6 s, and welding pressure of 241 psi. These parameters were used throughout the remainder of the work.

6.3 Fabrication of Sandwich Structures

To create sandwich structures, three stacked layers of polycarbonate sheets were prepared for ultrasonic spot welding by marking the grid size and spot weld location, drilling a hold on the corner of the lower layer and cutting a slot in the middle layer to serve as an air channel for later thermoforming, and spraying a thin layer of urethane mold release on the surfaces that come into contact with each other. Using the weld parameters discussed above (weld time=6 s, amplitude=24 μm (20%), weld pressure=241 kPa, depth of weld=1.89 mm), ultrasonic spot welds were placed in a weld pattern as shown in Fig. 6.4. The welding process involved creating ultrasonic spot welds in a grid pattern on one side of the polycarbonate stack, flipping the stack, and welding an alternate grid pattern of welds. The weld depth was changed by 0.6 mm when the stack was flipped over to account for the increased thickness of the stack due to the first set of welds. In Fig. 6.4, the dark black spots represent the spot welds between the top and middle layer, and the light grey spots represent the welds between middle and lower layer. Two structures with differing grid sizes were designed, and depending on the structure desired, the distance between the weld (x in Fig. 6.4) was either 50.8 or 76.2 mm.

A thermoforming process was used to expand the welded stack of polycarbonate sheets into a sandwich structure. A 6061 aluminum frame (Fig. 6.5) consisting of a base frame and a cover was fabricated to fit the polycarbonate stack. The protruded part of the cover fit in the cavity of the base frame but did not touch the bottom of the base frame. The welded polycarbonate stack sat in between the gaps so that all four edges were clamped evenly. An air inlet was drilled on one corner of the mold, which was later connected to a pressurized air supply. A 30 T CARVER hot press was used to heat the whole assembly (Fig. 6.5). From DMA results, the glass transition temperature was found to be 160 $^{\circ}\text{C}$ for the polycarbonate material used. Several experiments showed that forming the polycarbonate above 160 $^{\circ}\text{C}$ resulted in a degraded polycarbonate, while temperatures lower than 160 $^{\circ}\text{C}$ caused the ultrasonic spot welds to fail before thermoforming was complete.

The forming procedure was divided into five steps: (1) pre-drying, (2) clamping, (3) heating, (4) pressure forming, and (5) cooling. Because water vapor trapped in the polycarbonate sheets created bubbles and was detrimental to the thermoforming process, the polycarbonate sheets were pre-dried before thermoforming. As recommended by the material supplier, the polycarbonate was kept in a dehumidified air circulated oven at 120 $^{\circ}\text{C}$ for 4 h [32]. Within 10 h of pre-drying, the polycarbonate

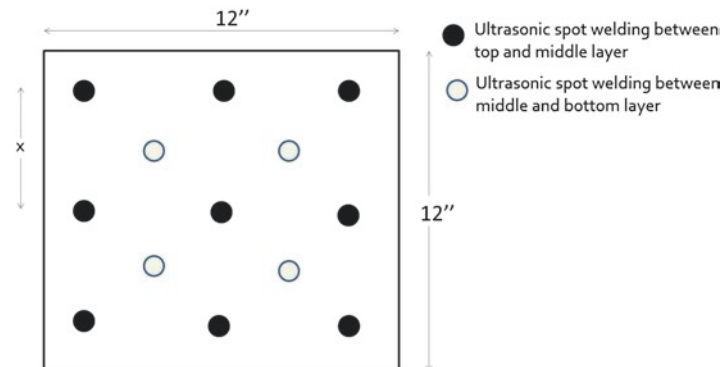


Fig. 6.4 Ultrasonic spot weld placement for sandwich structure fabrication



Fig. 6.5 Aluminum frame (left) to hold polycarbonate stack in hot press (center), and a side view schematic of the polycarbonate stack in the molds within the hot press (right)

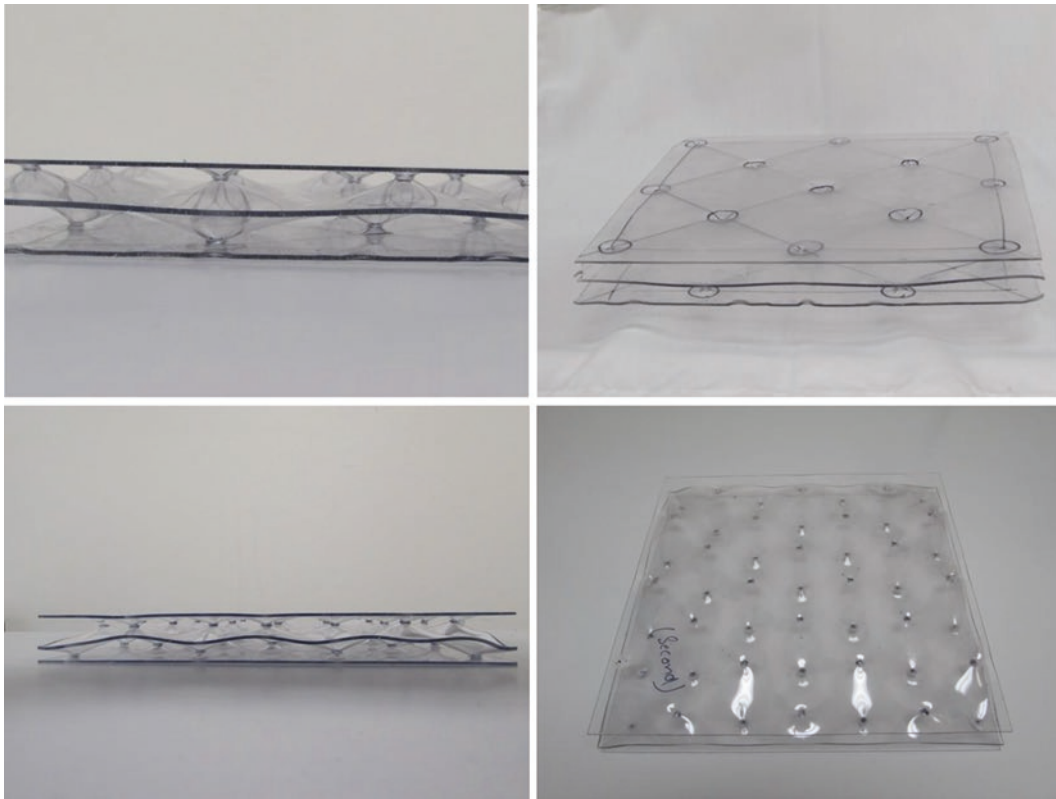


Fig. 6.6 Side (*left*) and top (*right*) views of the 50.8 mm (*top*) and 76.2 mm (*bottom*) grid size sandwich structures. The thickness of each structure is 25.4 mm

stack was placed in the aluminum mold with the air inlet port in the mold aligned with the hole drilled in the stack. The surface of the aluminum mold that came into contact with the polycarbonate sheet was packed with silicone gasket maker to ensure air tightness of the assembly. The molds were then clamped together and left to partially cure for about 30 min, so that any leaks would be further sealed when the assembly was clamped by the hydraulic press. A very low pressure was then applied to the assembly to check for air leaks. The entire assembly is shown schematically in Fig. 6.5.

A thin layer of urethane mold release was sprayed on the outer exposed surface of polycarbonate stack, which prevented the polycarbonate sheet from sticking to the surface of hot platens. The assembly was then pressed with a hydraulic pressure of 17.8 kN in between the hot platens, allowing the temperature of the polycarbonate to rise to the thermoforming temperature of 160 °C. Experiments showed that 96.5 kPa was a suitable pressure to properly form the structure without causing weld failure. When the assembly reached the desired forming temperature, the pressure was regulated to form the polycarbonate sheets into the designed shape. After forming for 30 min, the temperature of the hot press was turned off and the sandwich structure was cooled slowly in the hot press while the air pressure and clamping pressure were still applied. A representative fully formed 76.2 mm grid size sandwich structure and 50.8 mm grid size sandwich structure are shown in Fig. 6.6.

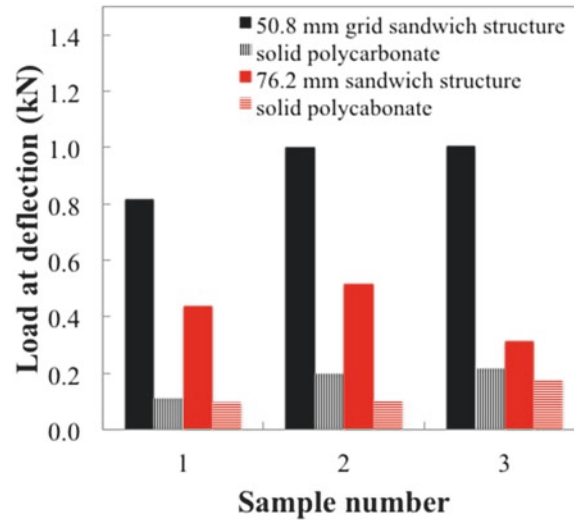
6.4 Mechanical Characterization of Sandwich Structures

6.4.1 3-Point Bend Testing

To investigate the bending behavior of the fabricated 3D structures, 3-point bend tests were carried out on both the 50.8 and 76.2 mm grid size polycarbonate sandwich structures. Under the 3-point bending loading scheme, each of the three layers of the sandwich structure experienced different loading stresses. The outer two layers acted as the flanges and carried the bending stress in response to the normal loading. The top layer was under compression while the bottom layer experienced expansion. The middle corrugated layer resisted the bending of the structure and held the outer layers apart such that the stiffness of the overall structure was increased. The ultrasonic spot welds, in between the outer and middle layer, held these layers together and allowed the structure to act as a single unit, providing bending rigidity.

Table 6.3 Welding parameters used for initial studies of ultrasonic spot welding of 1.59 mm thick polycarbonate

Specimen type	Sandwich structure peak load (kN)	Deflection of top surface (mm)	Deflection of bottom surface (mm)	Load required for solid polycarbonate sheet (kN)
50.8 mm grid sandwich structure	0.82	7.37	4.06	0.11
	1.0	10.9	7.62	0.20
	1.0	11.9	8.13	0.22
76.2 mm grid sandwich structure	0.44	11.2	3.56	0.10
	0.52	5.59	3.81	0.10
	0.32	11.2	6.60	0.18

**Fig. 6.7** Comparison of the 3-point bending load required to produce the same deflection in the 50.8 mm grid sandwich structure and solid polycarbonate of the same weight (*black*), and in the 76.2 mm grid sandwich structure and solid polycarbonate of the same weight (*red*)

ASTM D790-07 [33] was adapted to perform the 3-point bend test, and the rate of the cross-head motion was maintained at 14.4 mm/min. A MTS 810 was used as the test machine and special fixtures were designed and fabricated as recommended by the ASTM guidelines. Due to the compressible nature of the sandwich structures, the specimen was slightly compressed during the test. As a result, the top layer and the bottom layer did not experience the same strain. The deflection on the top layer is recorded by the machine itself and a dial gauge was used to measure the deflection of the lower layer. Three specimens of each 50.8 and 76.2 mm grid size sandwich structures were tested. The peak load is taken as the load that the structure can withstand before failing. For this work, failure of a weld is considered to be failure of the structure. These peak values occur just before the welds begin to fail. The peak load and the corresponding deflections of the top surface and bottom surface are listed below in Table 6.3.

To compare the bending properties of the sandwich structures to solid polycarbonate, the maximum deflection of the sandwich structures is used to calculate the load required to produce the same deflection in a solid polycarbonate material of the same weight. The thickness of polycarbonate sheet was taken as the combined thickness of all three layers, i.e. 4.76 mm, and the flexural modulus of polycarbonate was obtained from published values [34]. The required load to deflect a solid polycarbonate sheet of the same weight was calculated from ASTM guidelines using:

$$P = \frac{4EDbd^3}{L^3} \quad (6.1)$$

where, P = required load E = flexural modulus of polycarbonate (2380 MPa [34]), D = deflection of outer surface, b = width of the specimen (241 mm), d = thickness of specimen (25.4 mm), L = length of support span (210 mm). The results from the 3-point bend test of the sandwich structures and the calculated loads for solid polycarbonate are listed in Table 6.3 and compared graphically in Fig. 6.7.

The load bearing capacity of the sandwich structures averaged approximately five times that of plain polycarbonate sheets of the same weight when deflected by the same amount, indicating the effectiveness of sandwich structures for holding bending loads. This result shows that for applications where the weight of the structure plays a critical role, the sandwich structures can be a viable option for structural components.

6.4.2 Impact Testing

The behavior of the sandwich structures was also characterized with impact loading. Using an Instron CEAST 9350, a weight was vertically dropped along guide rails to strike the specimen. The 0.5" radius spherical head striker of the machine was fitted with a force transducer to measure the impact force during the test. The force-time data was used to extract information regarding each specimen. The energy of impact was determined by the mass of the falling weight (5.18 kg) and the initial height (75 mm). Three specimens of each of the 50.8 and 76.2 mm grid size structures as well as a solid polycarbonate sheet of the same thickness (25.4 mm) were tested under impact.

Figure 6.8 shows the force experienced by the striker for representative samples of the 50.8 mm grid size, 76.2 mm grid size, and the solid polycarbonate, and shows the peak force experienced by the striker with the 25.4 mm thick polycarbonate sheet was significantly higher than of with the sandwich structures and occurred over a shorter time.

The time over which the impact occurs indicates the cushioning ability of the material and the higher the time of impact, the better the material can mitigate the detrimental effects of impact loads. The results from the impact test showed the 76.2 mm grid size sandwich structure had a higher time of impact as compared to the 50.8 mm grid size sandwich structure. Similarly, the 50.8 mm grid size sandwich structure had a higher time of impact compared to the solid polycarbonate sheet. The impact properties of the 3D sandwich structures show their potential in impact and shock mitigation applications. The impact depth, associated with the compressible nature of the structure, was also measured. The results suggest that the 50.8 mm grid size sandwich structure is the most compressible among all three specimens.

Because energy absorption is a major criteria used to characterize many structural components, the amount of energy absorbed by each specimen during the impact test was calculated by a plate impact theory developed by Jang, Huang, Hsieh and Kowbel [35]. Here,

$$\Gamma(t) = \int_0^t P(t') \nu(t') dt' \quad (6.2)$$

where $\Gamma(t)$ is the total absorbed energy, $P(t')$ is the load as a function of time, $\nu(t')$ is the velocity as a function of time, and dt' is the size of the time interval. The calculated absorbed energy per weight for each sample is shown in Fig. 6.9, showing the advantage of the sandwich structures in energy absorption per weight over solid polycarbonate. The results of the impact tests suggest that the 3D polycarbonate sandwich structures might be suitable for applications where a large energy absorption and low weight are desired.

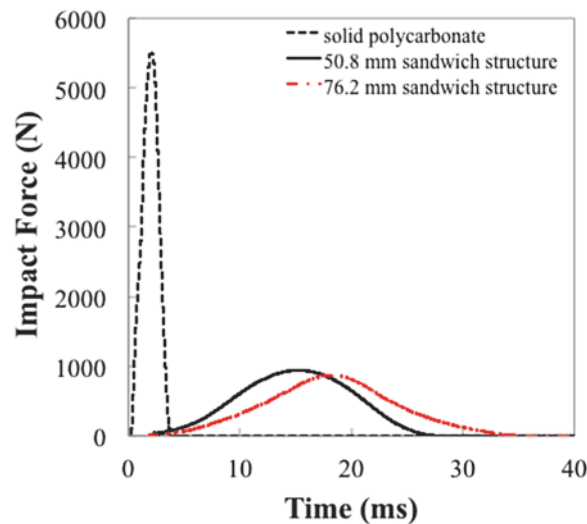


Fig. 6.8 Force read by the impact striker vs. time for a 50.8 mm grid sandwich structure, a 76.2 mm grid sandwich structure, and a solid polycarbonate of the same thickness

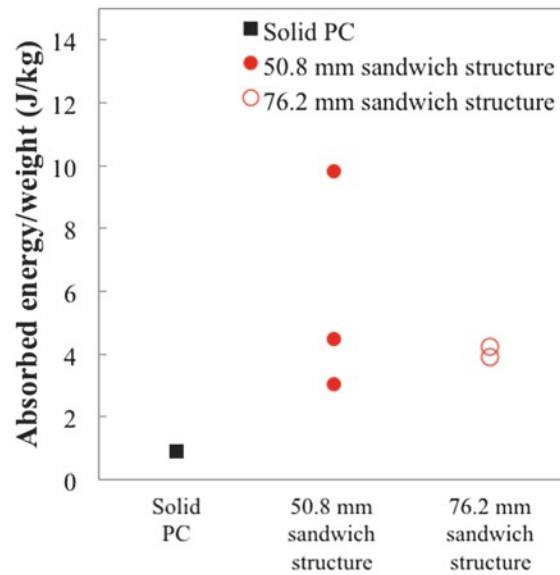


Fig. 6.9 The calculated absorbed energy per weight for a 50.8 mm grid sandwich structure, a 76.2 mm grid sandwich structure and a solid polycarbonate of the same thickness

6.5 Conclusions

The results of this work showed that 3D sandwich structures of polycarbonate could be fabricated using ultrasonic spot welding and demonstrated the flexibility in the fabrication technique. Tailoring of the mechanical properties of the sandwich structures was possible and was demonstrated with different grid size structures. Here, the ultrasonic spot welding process was used as the attachment method of different layers in a 3D sandwich structure. The strength of the ultrasonic spot welds was tested experimentally and was used to hold the layers of polycarbonate together while exposed to the thermoforming process. Both pressure and temperature proved to be important parameters of the thermoforming process. The 3D sandwich structures were tested for their structural properties in 3-point bend testing and impact testing. Experimental results revealed that the sandwich structures could withstand loads five times higher than solid polycarbonate of the same weight. Impact tests showed that the sandwich structures were superior in mitigating impact loads, making the sandwich structures appropriate for shock impact load resisting applications.

There are many aspects of the fabrication technique that could be improved in order to enhance the 3D sandwich structures, and the incorporation of other features to the polycarbonate sandwich structures is promising. The weld quality can be improved by investigations on the microscopic level regarding material interaction at the weld zone. Structures with desired properties can be designed and fabricated by altering not only the grid sizes, but also the thickness of the structure and the thickness of the individual layers. Moreover, the ultrasonic spot welding technique is compatible with dissimilar thermoplastic materials, which enables the use of different polymers for each layer of structure. This adaptability could help to integrate the properties of different materials into a single structure. Fiber reinforced composite materials are also a candidate for use on the outer layer of the structure to increase the stiffness and impact resistance of the overall structure.

References

1. Gutnik, V.G., Gorbach, N.V., Dashkov, A.V.: Some characteristics of ultrasonic welding polymers. *Fibre Chem.* **34**, 426–432 (2002)
2. Rani, M.R., Prakasan, K., Rudramoorthy, R.: Study of different joints for ultrasonic welding of semicrystalline polymers. *Exp. Tech.* **33**, 36–42 (2009)
3. Roopa Rani, M., Prakasan, K., Rudramoorthy, R.: Designing joints for ultrasonic welding of plastics. *Weld. J.* **84**, 50 (2005)
4. Liu, S.J., Chang, I.T., Hung, S.W.: Factors affecting the joint strength of ultrasonically welded polypropylene composites. *Polym. Compos.* **22**(1), 132–141 (2001)
5. Dukane iQ Series Ultrasonic Press System Specification Sheet, 2013
6. Amancip-Filho, S.T., Dos Santos, J.F.: Joining of polymers and polymer–metal hybrid structures: recent developments and trends. *Polym. Eng. Sci.* **49**, 1461–1476 (2009)
7. Kim, J.B., Jeong, B., Chiao, M., Lin, L.: Ultrasonic bonding for MEMS sealing and packaging. *IEEE Trans. Adv. Pack.* **32**, 461–467 (2009)

8. Gfeller, B., Zanetti, M., Properzi, M., Pizzi, A., Pichelin, F., Lehmann, M., Delmotte, L.: Wood bonding by vibrational welding. *J. Adhes. Sci. Technol.* **17**, 1573–1589 (2003)
9. Tsao, C.-W., DeVoe, D.L.: Bonding of thermoplastic polymer microfluidics. *Microfluid. Nanofluid.* **6**, 1–16 (2008)
10. Nonhof, C.J., Luiten, G.A.: Estimates for process conditions during the ultrasonic welding of thermoplastics. *Polym. Eng. Sci.* **36**, 1177–1183 (1996)
11. Singh, R., Mattoo, A., Saigal, A.: Optimizing the design and impact behavior of a polymeric enclosure. *Mater. Des.* **27**, 955–967 (2006)
12. Fried, J.R.: *Polymer Science & Technology*, 2nd edn. Prentice Hall, Upper Saddle River, NJ (2003).
13. Petras, A.: Design of sandwich structures (Doctoral dissertation), Cambridge University Engineering Department, Cambridge, England (1998)
14. Besse, C.: Development and optimization of a formable sandwich sheet (Doctoral dissertation), Ecole Polytechnique, Palaiseau, France (2012)
15. Rabczuk, T., Kim, J.Y., Samaniego, E., Belytschko, T.: A homogenization method is proposed for sandwich structures. *Int. J. Numer. Meth. Eng.* **61**, 1009–1027 (2004)
16. Kocher, C., Watson, W., Gomez, M., Gonzalez, I., Birman, V.: Integrity of sandwich panels and beams with truss-reinforced cores. *J. Aerospace Eng.* **15**, 111–117 (2002)
17. Xin, F.X., Lu, T.: Effects of core topology on sound insulation performance of lightweight all-metallic sandwich panels. *Mater. Manuf. Process.* **26**, 1213–1221 (2011)
18. Qiao, P., Wang, J.: Mechanics of composite sinusoidal honeycomb cores. *J. Aerospace Eng.* **18**, 42–50 (2005)
19. Krusper, A., Isaksson, P., Gradin, P.: Modeling of out-of-plane compression loading of corrugated paper board structures. *J. Eng. Mech.* **133**, 1171 (2007)
20. Guo, Y., Xu, W., Fu, Y., Wang, H.: Dynamic shock cushioning characteristics and vibration transmissibility of X-PLY corrugated paperboard. *Shock Vib.* **18**, 525–535 (2011)
21. Giancaspro, J., Balaguru, P.N., Lyon, R.E.: Use of inorganic polymer to improve the fire response of balsa sandwich structures. *J. Mater. Civil Eng.* **18**, 390–397 (2006)
22. Okabe, Y., Minakuchi, S., Shiraishi, N., Murakami, K., Takeda, N.: Smart honeycomb sandwich panels with damage detection and shape recovery functions. *Adv. Compos. Mater.* **17**, 41 (2008)
23. Doumanidis, C., Gao, Y.: Mechanical modeling of ultrasonic welding. *Weld. J.* **83**, 140–146 (2002)
24. Gao, Y., Doumanidis, C.: Mechanical analysis of ultrasonic bonding for rapid prototyping. *J. Manuf. Sci. Eng.* **124**, 426–434 (2002)
25. Besse, C.C., Mohr, D.: Optimization of the effective shear properties of a bidirectionally corrugated sandwich core structure. *J. Appl. Mech.* **80**, 011012 (2012)
26. Brauner, C., Block, T.B., Herrmann, A.S.: Meso-level manufacturing process simulation of sandwich structures to analyze viscoelastic-dependent residual stresses. *J. Compos. Mater.* **46**, 783–799 (2011)
27. Thomsen, O.T., Bozhevolnaya, E., Lyckegaard, A., Mortensen, F.: Characterisation and assessment of load response, failure and fatigue phenomena in sandwich structures induced by localized effects—a review. *Strain* **44**, 85–101 (2008)
28. Arao, Y., Koyanagi, J., Utsunomiya, S., Kawada, H.: Analysis of thermal deformation on a honeycomb sandwich CFRP mirror. *Mech. Adv. Mater. Struct.* **17**, 328–334 (2010)
29. Song, W., Ma, Z.: Behavior of honeycomb FRP sandwich structure under combined effects of service load and low temperatures. *J. Compos. Constr.* **15**, 985–991 (2011)
30. ASTM D3164. In: Standard Test Method for Strength Properties of Adhesively Bonded Plastic Lap-Shear Sandwich Joints in Shear by Tension Loading. ASTM International (2008)
31. ASTM D1876-08. In: Standard Test Method for Peel Resistance of Adhesives (T-Peel Test). ASTM International (2008)
32. Technology, B.S.: Bayer Guide on Thermoforming Makrolon
33. ASTM D790-07. In: Standard Test Methods for Flexural Properties of Unreinforced and Reinforced Plastics and Electrical Insulating Materials. ASTM International (2008)
34. LLC (BMS). Makrolon GP (Polycarbonate). Plastics International (2010)
35. Jang, B.P., Huang, C.T., Hsieh, C.Y., Kowbel, W., Jang, B.Z.: Repeated impact failure of continuous fiber reinforced thermoplastic and thermoset composites. *J. Compos. Mater.* **25**, 1171–1203 (1991)

Chapter 7

Impact and Lap Shear Properties of Ultrasonically Spot Welded Composite Lap Joints

Cassandra M. Degen, Lidvin Kjerengtroen, Eirik Valseth, and Joseph R. Newkirk

Abstract Ultrasonic spot welding (USSW) is a widely used technique for joining thermoplastics where high frequency, low amplitude vibrations are applied through an ultrasonic horn resting on the polymer surface to create frictional heat, producing a solid state joint between polymer sheets. Advantages such as short weld cycle time, fewer moving components and reproducibility make this technique attractive for automation and industrial use. The goal of this work was to evaluate the feasibility and analyze the lap shear and impact strength of a composite material joint created using ultrasonic spot welding. The base material used for the joints was a composite consisting of a polycarbonate matrix with chopped glass fibers. The strength of the lap joints was determined through experimental lap shear and impact testing. A finite element analysis was conducted for more thorough insight into the stress patterns in the lap joints. Experiments showed that the ultrasonically spot welded joints tested in tensile lap shear loading carried a load 2.3 times higher than adhesive joints and the impact tested joints had an impact strength 3.5 times higher than adhesive joints. The results of this work suggest ultrasonic spot welding as a viable joining method for thermoplastic composite materials.

Keywords Composite joining • Ultrasonic spot welding • Thermoplastic • Composites • Impact testing

7.1 Introduction

The use of composite materials has seen an explosive growth over the last 20 years as the need for lightweight materials pushes to the forefront of many industries [1]. While the design of a single-piece composite part is ideal, molding considerations and other mechanical limitations make joining of composite parts necessary to complete assembly and a critical step in the manufacture of composite parts [2]. In general, composite parts can be joined using mechanical fastening, adhesive bonding, or fusion welding processes. The main limitations of mechanical fastening include increased weight and the presence of large stress concentrations around the fastening locations. Adhesive bonding has material dependent limitations and requires proper mating of the material surface to the adherent [3, 4]. Composite fusion welding relies on the melting, intermolecular diffusion across the joint, and re-solidification of the matrix material. The molecular details of thermoplastic materials allows for melting due to applied heat. For this reason, thermoplastics matrix composites are candidate materials for fusion welding techniques.

Fiber-reinforced thermoplastic composites are one of the fastest growing material choices of the composites industry [5, 6]. Fueled largely by the automotive industry, composite materials with a thermoplastic matrix offer several advantages of traditional composites with a thermoset matrix, including: increased toughness, longer material lifespan, non-toxic and energy-saving production, recyclability, lower manufacturing cost, and the ability to reshape and reform [7]. As thermoplastic composite use increases, manufacturing techniques such as molding and joining for such materials must also progress, and these topics have been the focus of many recent investigations [5, 8–12].

Fusion welding may be achieved through a variety of welding techniques, and the technique studied here is ultrasonic spot welding (USSW). USSW is a mechanical welding process where low amplitude, high frequency vibrations are used to locally melt thermoplastic materials or metals thus creating a bond. This welding technique was developed in the 1940s, but was not patented or adapted in the US until the 1960s. The process of ultrasonically welding thermoplastics was started in 1963 by Sonics & Materials Inc [13]. USSW is now one of the most commonly used welding methods to join thermoplastic materials [14].

C.M. Degen (✉) • L. Kjerengtroen • E. Valseth • J.R. Newkirk
Department of Mechanical Engineering, South Dakota School of Mines and Technology,
501 E. Saint Joseph St., Rapid City, SD 57701, USA
e-mail: cassandra.degen@sdsmt.edu

The energy transferred to a thermoplastic material subjected to ultrasonic vibrations is dissipated through intermolecular friction, leading to heating of the material and localized melting [14]. An ultrasonic welder typically consists of six main components: a pneumatic press, generator, transducer, booster, welding horn and the base of the machine [15]. The ultrasonic spot welder used in this work is a 20 kHz Dukane iQ series Ultrasonic pneumatic press 43Q-220. The process of ultrasonic welding is typically separated into five steps [16]: (1) the two parts to be welded are fixed at the base in the fixture, (2) the welding horn is moved into contact with the upper part in the fixture, (3) a force (in the form of a pressure) is applied to hold the two parts to clamp the parts together during welding, (4) the ultrasonic vibrations are induced by vibrating the welding horn vertically at the desired frequency, thus melting the plastic material locally at the interface of the two pieces of material, (5) the ultrasonic vibrations are shut off after a preset time, and the horn is held in place by continuing to apply a force. The force is maintained until the melted material has solidified, and the horn is returned to its original position. USSW has several advantages over other welding techniques, such as fast cycle times, and is faster than other comparable welding or joining methods [14]. The process is energy efficient since the energy needed to induce local melting of the plastic material is modest, in the order of 2–3 kJ for this work. Minimal preparation of material before welding is required, compared to adhesive bonding or bonding using mechanical fasteners [14].

This work examines the feasibility of USSW of a composite consisting of a polycarbonate matrix with chopped glass fibers by analyzing the lap shear and impact strength joints created using ultrasonic spot welding. Experimental results coupled with a finite element analysis (FEA) give insight into the stress patterns of lap joints. Experiments showed that the ultrasonically spot welded joints tested in tensile lap shear loading carried a load 2.3 times higher than adhesive joints and the impact tested joints had an impact strength 3.5 times higher than adhesive joints. The results of this work suggest ultrasonic spot welding as a viable joining method for thermoplastic composite materials.

7.2 Ultrasonic Spot Welding of a Composite Material

Ultrasonic spot welding was used to join a thermoplastic fiber reinforced polymer (Tecanat GF20, produced by Ensinger Inc). This composite consists of a polycarbonate matrix and 20 wt% chopped glass fibers, and the mechanical properties are shown in Table 7.1. Tecanat GF20 is available in pre-compounded, extruded sheets, 6.35 mm thick, with 4.76 mm long fibers. The glass fibers are chopped and randomly oriented in three dimensions. However, the extrusion process in which the material is produced does align the fibers within the matrix, and thus the material is not fully isotropic due to this alignment of the fibers, and will have different properties in each direction. No data on the anisotropic properties of Tecanat GF20 was given by the supplier.

Since the welding parameters were expected to influence the strength of the welds, a study was carried out to determine the effect of changing amplitude, time, and pressure during the ultrasonic spot welding process. Because the Tecanat GF20 composite is 80 wt% polycarbonate, pure polycarbonate material was used to study and estimate appropriate ultrasonic spot welding parameters. Lap shear samples of 6.35 mm thick polycarbonate material were ultrasonically spot welded and subsequently analyzed by both optical observation and mechanical testing.

To find the acceptable amplitude, welding time, and welding pressure of polycarbonate, and to estimate the parameters to weld Tecanat GF20, a study of the effect of each of the three parameters was carried out, keeping the other parameters constant. The welding parameters studied are shown in Table 7.2. For each weld, the hold pressure and the hold time were kept constant at 276 kPa and 2.0 s, respectively.

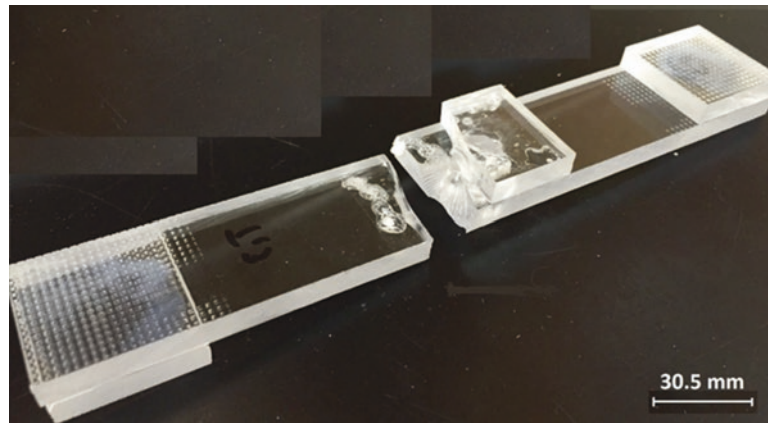
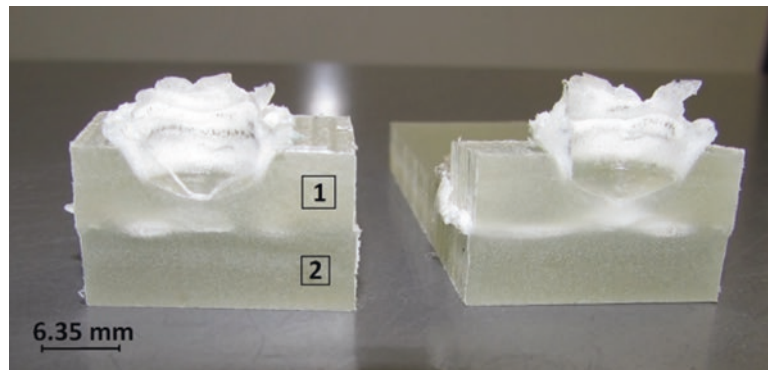
The criteria used to find the appropriate parameters were the total bonded area (shear area), the maximum load carried by the samples during a lap shear test, and the standard deviation (σ) of each set of sample set. The shear area was measured optically prior to lap shear testing. To measure the tensile lap shear strength of ultrasonic spot welds in polycarbonate, lap shear samples were prepared. Tabs on either end of the samples were glued to the lap shear specimen to reduce the offsetting of the applied force to reduce the bending moment acting on the joint. The lap shear samples were tested at a rate of 1.3 mm/min according to ASTM 3164 using an MTS 810 load frame. Four lap shear samples of each welding parameter combination were tested and the average maximum load and corresponding standard deviation are listed in Table 7.2. The failure type observed in most of the lap shear samples was almost immediate fracture after the peak load was reached. The fracture took

Table 7.1 Mechanical properties of Tecanat GF20 [17]

Property	Metric units
Young's modulus	4826 MPa
Ultimate tensile strength	110 MPa
Elongation at break	4 %
Impact strength (IZOD, unnotched)	1.01 J/mm
Poisson's ratio	0.37
Compressive strength	76 MPa

Table 7.2 Welding parameter combinations and results of lap shear testing of 6.35 mm thick pure polycarbonate ultrasonic spot welds

Sample number	Welding amplitude [μm]	Weld pressure [kPa]	Weld time [s]	Average maximum load [N]	Standard deviation of maximum load [N]
A1	46.5	207	12.5	3075	2038
A2	46.95			4057	1014
A3	47.4			3703	418
A4	47.85			6192	1301
T1	47.4	207	12.2	5457	1473
T2			12.5	3816	1206
T3			12.7	6213	1493
T4			13.0	3612	1243
P1	47.4	172	13.0	2739	413
P2		207		2642	1091
P3		241		3099	2412

**Fig. 7.1** Failed polycarbonate lap shear sample after tensile testing**Fig. 7.2** Sectioned view of an ultrasonically spot welded composite material

place close to the point where the welded area begins, indicating a bending moment and a large stress concentration in this area. A failed sample can be seen in Fig. 7.1. This fracture was likely due to bending stresses and stress concentrations at the interface between the weld and polycarbonate similar to those observed by Hart-Smith [18].

It was clear that varying welding parameters influenced the strength of the joints and it was noted that a more thorough analysis is required for full optimization. For this study, the following parameters produced welds that carry high loads in polycarbonate, and were used when ultrasonically spot welding the composite material, Tecanat GF20: amplitude of 47.85 μm , weld time of 12.7 s, and weld pressure of 241 kPa. The other adjustable parameters of hold time and hold pressure were kept constant at 2.0 s and 276 kPa, respectively. A sectioned view of an ultrasonically spot welded Tecanat GF 20 composite welded with these parameters is shown in Fig. 7.2. In this weld, the tip did not penetrate all the way through the top layer of the composite labeled 1 in Fig. 7.2, but the ultrasonic vibrations still induced melting at the interface between the top and bottom layer, labeled 2 in Fig. 7.2 to create a bond.

7.3 Characterization of Ultrasonically Spot Welded Tecnat GF 20

7.3.1 Ultrasonically Spot Welded Lap Joints

The ultrasonically spot welded lap joints of Tecnat GF20 were characterized experimentally with a tensile lap shear test (based on ASTM 3164) and an impact test (based on ASTM 950) to assess their load bearing capacity. For impact testing, the lap joints used were unconventional without notches or other modifications to create stress concentrations to reduce the amount of material for each sample (Fig. 7.3).

Lap shear samples were tested according to the procedure described for pure polycarbonate above. To impact test unconventional lap joints, a test rig, shown in Fig. 7.4a, was designed and built to hold the lap joints in the correct position such that they were impacted in a repetitive fashion to yield useful results. The design of the test rig was based on the design specified in ASTM D950 to impact test adhesively bonded lap joints. The impact tester used was an Instron SI-1D3 (Fig. 7.4b), and had the ability to impact samples with an energy of up to 407.6 J.

The absorbed energy was recorded from the impact tests and was analyzed by normalizing to both the shear area of the weld and the shear length of the weld. The fibers in Tecnat GF20 cause the material to be opaque, and the weld area and weld length could not be determined before the experiments using optical techniques, therefore, the area and length were found optically after the welds were tested to failure. The impact test was set up as seen in Fig. 7.4 where the lap joints were loaded in the test rig and mounted to the test machine. A total of seven lap shear and six impact samples were tested, with results shown in Tables 7.3 and 7.4, respectively. Representative failed samples are shown in Fig. 7.5.

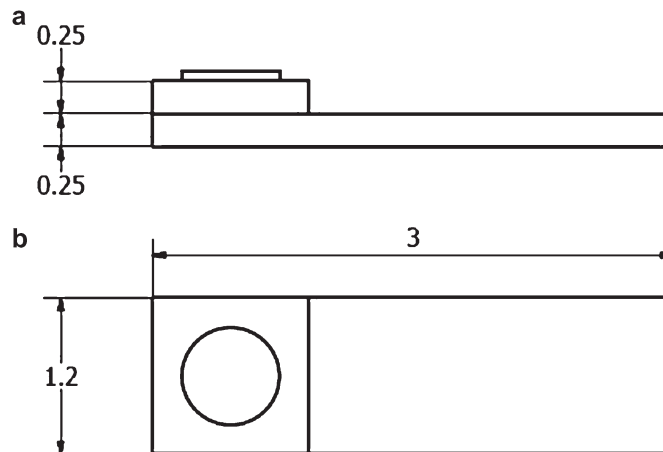


Fig. 7.3 Unconventional lap joint, (a) side view (b) top view



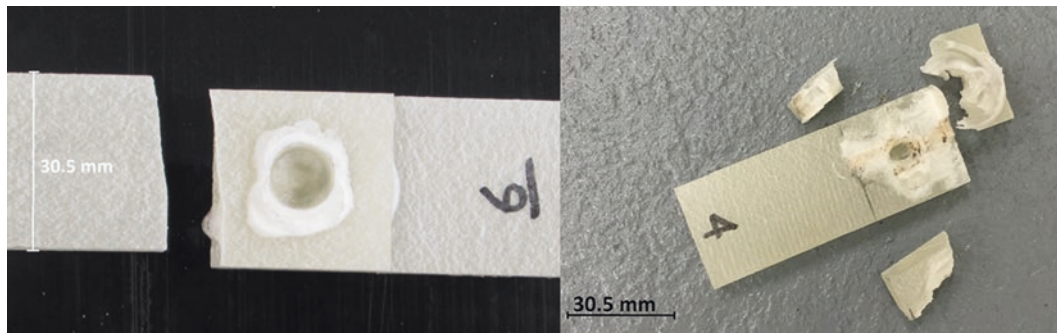
Fig. 7.4 CAD model of impact test rig, isometric view (left), the thickness of side walls are 3.175 mm, the Instron SI-1D3 impact tester (center), and test rig with mounted impact sample (right). The direction of the striker is shown by the arrow

Table 7.3 Results from lap shear test, maximum load, and elongation at maximum load

Sample	Maximum load [N]	Elongation at maximum load [mm]
LS-1	5552	1.2
LS-2	4745	1.0
LS-3	5703	1.1
LS-4	6169	1.2
LS-5	5352	1.0
LS-6	6039	1.2
LS-7	5589	1.2
Average	5593	1.1

Table 7.4 Results from impact tests, measured weld width, weld area, calculated joint strength in terms of weld area and weld length

Sample	Absorbed energy [J]	Weld length [mm]	Weld area [mm ²]	Impact strength [J/mm]	Impact strength [J/mm ²]
I-1	51	30	722	1.7	0.07
I-2	66	29	775	2.2	0.08
I-3	88	28	789	3.1	0.11
I-4	44	29	641	1.5	0.07
I-5	66	29	596	2.2	0.11
I-6	65	30	794	2.2	0.08
Average	63	29	719	2.2	0.09

**Fig. 7.5** Representative failed lap shear sample (*left*) and failed impact sample (*right*)

All seven lap shear samples failed in a similar manner to that shown in Fig. 7.5(left). The samples failed in a near linear region of the load-deformation profile and not undergo significant plastic deformation, suggesting the presence of bending stresses and stress concentrations contributing to the failure of the joint. Additionally, the thickness of the welds induced a bending moment in the joints observed in videos of the tests. Lap joints subjected to a load that is not perfectly aligned, as in these experiments, tend to fail in the base material due to the bending moment and stress concentrations that arise due to the offsetting of the force as observed by Hart-Smith [18]. The stresses in the lap joints were further investigated by conducting a finite element analysis (FEA). All impact samples failed in a consistently brittle manner, as shown in Fig. 7.5(right), attributed to the high strain rate of the impact test. This type of behavior under impact loading was also observed by Barlow et al. [19].

For each lap shear sample, the normal stresses in the base material and the shear stresses in the weld were calculated and used to determine a stress concentration factor to compare with the finite element model. The nominal normal stress in the material was calculated using:

$$\sigma_{x_0} = \frac{P}{A} \quad (7.1)$$

In Eq. (7.1), P is the peak load of the applied tensile force and will be defined as such for the remainder of the calculations, and A is the area of the base material. The average shear stress in the weld was defined as the applied tensile force divided by the shear area:

$$\tau_{x_1x_2} = \frac{P}{A_s} \quad (7.2)$$

In Eq. (7.2), A_s is the shear area. This definition of average shear stress assumes that the shear stresses are uniform throughout the shear area. It was shown by Goland and Reissner [20], and Hart-Smith [18] that the shear stress distribution in adhesive lap joints has a significant distribution and that shear stress increases near the edges of the adhesive area. However, the experiments showed that the lap joints did not fail due to the shear stresses in the welds, and as such the average shear stress definition was used. The calculated average shear stresses are all lower than the published shear strength of Tecanat GF20, and as expected none of the lap joints failed in the welds. The bending stresses in the base material were calculated using:

$$\sigma_{bending} = \frac{My}{I} \quad (7.3)$$

In Eq. (7.3), M is the bending moment at the root of the weld, y is the distance from the neutral axis, equal to one half of the thickness of the base material, and I is the area moment of inertia of the base material. The values of y and I were calculated for each sample. The bending moment M was calculated using:

$$M = Pk \frac{t_{weld} + t_{base\ material}}{2} \quad (7.4)$$

In Eq. (7.4), t_{weld} is the thickness of the welds, $t_{base\ material}$ is the thickness of the base material, equal to 3.4 mm, and k is the bending moment factor defined by Hart-Smith [23]. The sum of the bending stress and normal stress was also calculated and this total stress in the x_j direction at the experimental peak load were all lower than the published ultimate tensile stress for Tecanat GF20 of 110 MPa, suggesting the presence of a stress concentration at the root of the weld. The stress concentration factor at the weld was defined as:

$$K_f = \frac{\sigma_f}{\sigma_{total}} \quad (7.5)$$

where σ_f is the ultimate tensile stress of Tecanat GF20, and σ_{total} is the total stress in Table 7.5.

7.3.2 Adhesively Joined Lap Joints

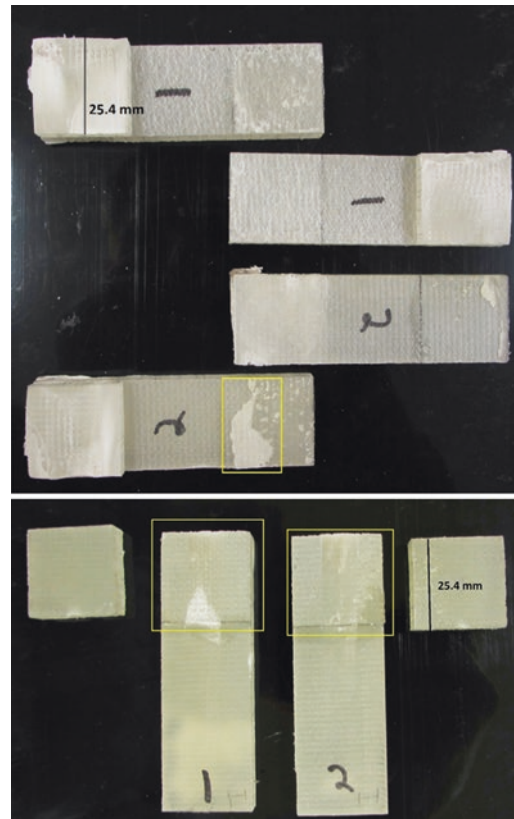
To compare ultrasonically spot welded lap joints to adhesively joined lap joints, Pace Technologies ultrathin 2 low viscosity epoxy resin [21] was used to join Tecanat GF20. Here, the surfaces were wiped clean to remove large surface contaminations, the joints were clamped together to ensure the correct geometry, and cured for 24 h minimum. The published tensile strength of the adhesive is 55.1 MPa [21]. The lap joints failed in the adhesive, as expected since Tecanat GF20 has a significantly higher failure load than the epoxy. Two lap shear and two impact samples were tested using the same methods as described above, and the results are shown in Table 7.6. The load–displacement curves for the lap shear tests showed that the adhesive underwent significant plastic deformation as compared to the curves for ultrasonic spot welds. The adhesive samples failed in a mixed type of fracture between adhesive failure and cohesive failure, highlighted in Fig. 7.6(top). The absorbed energy from the impact tests and the areas measured optically after testing are also listed in Table 7.6, along with the calculated impact strength per area and per length. The impact tested samples failed cohesively as shown by the outlined epoxy on one side of the joints in Fig. 7.6 (bottom), suggesting less than ideal bonding [22].

Table 7.5 Average shear stress at peak load, nominal stress, bending stress, total stress, and stress concentration factor for all seven lap shear tested samples

Sample	Average shear stress [MPa]	Nominal stress [MPa]	Bending stress [MPa]	Total stress [MPa]	K_f
LS-1	13.2	27.5	16.6	44.1	2.5
LS-2	10.2	23.5	19.1	42.6	2.6
LS-3	12.1	28.1	17.3	45.4	2.4
LS-4	11.8	30.8	18.1	48.9	2.3
LS-5	12.8	26.6	23.8	50.4	2.2
LS-6	14.0	29.3	18.7	48.0	2.3
LS-7	11.4	27.7	17.2	44.9	2.5
Average	12.2	27.6	18.7	46.3	2.4

Table 7.6 Results from adhesive lap shear and impact tests

Sample	Maximum load [N]	Elongation at maximum load [mm]	Absorbed energy [J]	Adhesive width [mm]	Adhesive area [mm ²]	Impact strength [J/mm]	Impact strength [J/mm ²]
LS-A-1	2242	0.6					
LS-A-2	2445	0.7					
LS-A-Average	2343	0.65					
I-A-1			13.6	24	579	0.6	0.02
I-A-2			15.6	24	582	0.6	0.03
I-A-Average			14.6	24	581	0.6	0.025

**Fig. 7.6** Failed adhesive lap shear (*top*) and impact samples (*bottom*) with remaining epoxy highlighted

7.3.3 Comparison of Adhesively Joined and USSW Joints

In Fig. 7.7, LS-USSW and LS-Adhesive are the results from the lap shear tested USSW and adhesively joined Tecanat GF20, respectively, and I-USSW and I-Adhesive are the impact tested USSW and adhesively joined Tecanat GF20, respectively. The results show that the USSW joints tested in lap shear has a maximum load 2.3 times higher than adhesively joined samples (Fig. 7.7). The adhesive failure mode suggests that the Tecanat GF20 would benefit from a surface treatment before adhesion, and the cohesive mode suggests that the epoxy resin used was not sufficiently strong to bond Tecanat GF20 in lap shear loading conditions [23]. Increasing the thickness of the adhesive layer could reduce the normal stresses in the adhesive and increase the strength of the adhesive joints. The experimental impact results had an average impact strength 3.5 times higher than the adhesively joined samples (Fig. 7.7). This may be due to the low impact strength of epoxy resins as suggested by LeGrand [24].

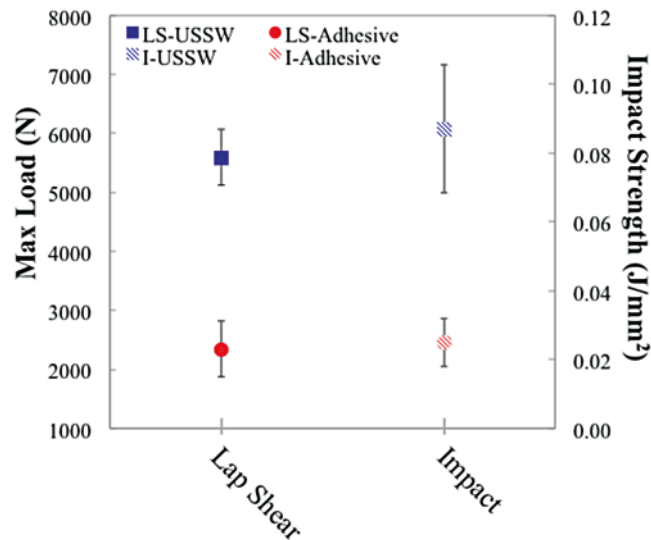


Fig. 7.7 Comparison of ultrasonically spot welded and adhesively joined Tecanat GF20 in both loading scenarios

7.4 Finite Element Analysis

A finite element analysis (FEA) of a lap joint in a loading situation comparable to the lap shear test was conducted using the commercial software ABAQUS CAE. The lap joint was modeled in the software with geometric simplifications where the weld was modeled as perfectly circular while the hole left by the pilot tip was omitted. The load was applied as a prescribed displacement of tabbed ends of 1.1 mm (the average experimental displacement at the maximum load). The goal of the FEA analysis was to investigate the distribution of stresses in the lap joints and assess how they affect the failure of the lap joints. Tecanat GF20 was assumed to be isotropic and linearly elastic as the material has very little plastic deformation before failure. Generalized Hooke's law was used as the constitutive relationship and Young's Modulus and Poisson's ratio were assumed to be 4826 MPa and 0.366, respectively.

The mesh used consisted of two types of elements from the ABAQUS three-dimensional solid element library, the C3D8R element and C3D6 element. In this case, the C3D6 element, was used to ease meshing around the spot weld which was modeled as perfectly circular. The number of these elements in the mesh was low compared to the number of hexahedral elements (<0.4% of the total number of elements in the mesh used), and it was assumed that their effect on the results was negligible. To ensure that the error in the finite element model was as low as possible, a convergence study was conducted. The maximum Von Mises stress and the maximum displacement magnitude were calculated for a varying number of nodes. The mesh used had a change in maximum stress of less than 10%, which was deemed sufficient for this application.

Figure 7.8 shows the relative stresses throughout the entire sample, the normal stresses in the z direction for half of the model, and a side view of the stress distributions. In Fig. 7.8 (center), high stresses are present at the transition between weld and base material. To calculate the stress concentration created by the weld, the ratio between the maximum stress at the root of the weld and the stresses far away from the weld were used. A stress concentration of 2.6 was found using this method.

The FEA also showed that the shear stresses in the weld were low. From the analysis, the maximum shear stress in the sample was 24.7 MPa, which is well below the shear strength of Tecanat GF20. This results was expected as the experiments showed that the lap joints did not fail due to shear forces. To analyze the bending stresses, a small portion of the base material was investigated and the stresses in the z direction were plotted through a cross section of the y-z plane (Fig. 7.9). The stress distribution in Fig. 7.9 shows that bending stresses are present in the z direction, as the stresses change from tensile to compressive over the cross section.

The results from the finite element analysis confirmed that the presence of bending in the base material, and the presence of a stress concentration of 2.6 at the root of the weld. The stress concentration factor of 2.6 found in the finite element model agrees with the calculated results for each sample. The error in the calculated K_f and the K_f from FEA may be attributed to the geometric simplifications, the boundary conditions used, and the linear assumptions.

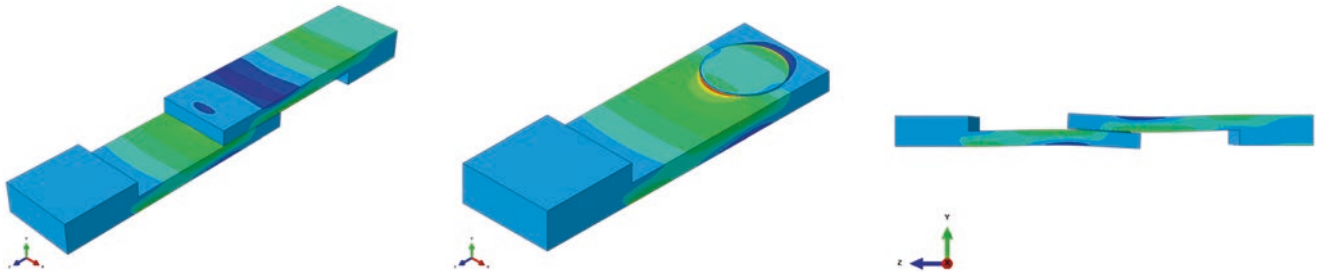


Fig. 7.8 Isometric view of lap joint (*left*), isometric view of half of the joint (*center*), and side view (*right*) of the joint showing plot of normal stress in the z direction. *Dark colors* indicate compressive stress, *light colors* indicate tensile stress, *red colored areas* are subjected to the highest tensile stress, and the thickness of material is 6.35 mm



Fig. 7.9 Stresses in z direction plotted on the y - z cross section. *Arrows* in the negative z -direction are tensile stresses, *arrows* in the positive z -direction are compressive stresses, and the thickness of material is 6.35 mm

7.5 Microscopy of Welds

To optically assess the fractures in the lap shear samples, scanning electron microscopy of the fracture was conducted with a Zeiss Supra 40 scanning electron microscope. This was done to compare with the results of Suzuki et al. [24], who investigated the fracture surface of a composite material subjected to bending stresses. A stitched image of the fracture surface of sample LS-1 at $\times 60$ magnification can be seen in Fig. 7.10.

The highlighted areas indicated in Fig. 7.10 show areas that have been studied more closely. The top area is close to where the highest tensile stresses were due to the bending and stress concentration from the results of the FEA. The lower area is near an area with the lowest stresses due to the bending stress distribution.

In Fig. 7.10 (top), the dark spots (circled) are voids left after fiber pullout, which is expected in high tensile stress regions [25]. In Fig. 7.10 (bottom), a region near lower stresses is shown, where fewer fiber pullout areas are present, suggesting that this region failed due to crack propagation through this region of the composite [25].

The scanning electron microscopy of the fracture surface supports the results from the FEA, showing a region of high tensile stresses close to the weld due to the bending stresses and stress concentration. These stresses were the driving force of the failure of the lap joints [18].

7.6 Conclusions

The results of this work have successfully shown the use of ultrasonic spot welding to join chopped fiber thermoplastic composite materials. The results from the experiments showed that welding composite materials are similar to welding the thermoplastic material of the composite matrix, and welding parameters used to join thermoplastics may be used to join composites with the same thermoplastic matrix.

Lap joints were manufactured by ultrasonically spot welding 6.35 mm thick Tecanat GF20 and characterized by lap shear and impact testing to determine their mechanical strength. A high repeatability suggests that the ultrasonic spot welding process may be well suited for high volume production. The lap shear samples all failed in a consistent manner, due to bending stress and a stress concentration at the interface between the weld and the base material. This theory was further confirmed by conducting FEA and scanning electron microscopy of the fracture surfaces. The stresses in the experimentally tested lap joints were calculated, and agreed with the results from the finite element model.

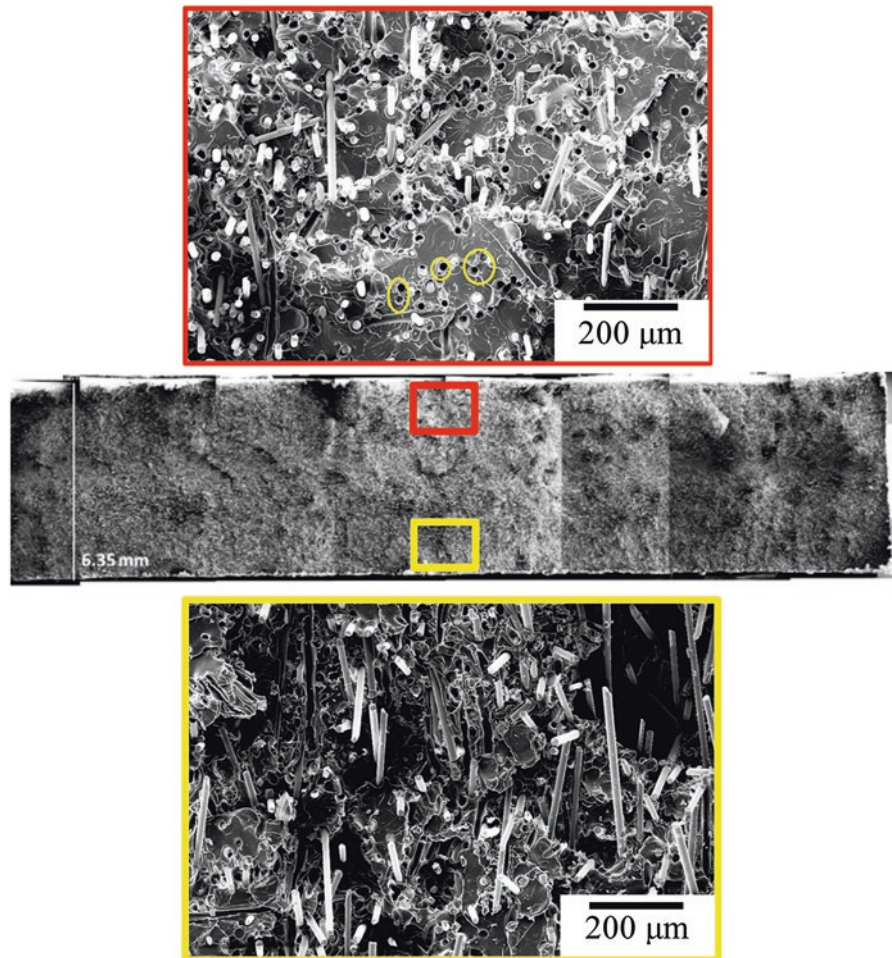


Fig. 7.10 Fracture surface of a lap shear sample (*center*) and enlarged region subjected to lowest tensile stresses (*top*) and region subjected to highest tensile stresses (*bottom*)

To compare the performance of ultrasonic spot welds to adhesives, lap joints joined using an epoxy resin were fabricated. These adhesively bonded joints were subjected to the same tests as the ultrasonically spot welded joints. The ultrasonically spot welded samples outperformed the adhesively joined samples in both lap shear and impact tests. The adhesively joined samples required 24 h to fabricate due to the curing time of epoxy resin, while the ultrasonically spot welded samples took 14.7 s to weld plus time taken to fix the samples correctly in the spot welder, typically less than one minute total. The significantly shorter fabrication time, in addition to the high strength of the ultrasonically spot welded joints are the benefits of ultrasonic spot welding when used to join thermoplastic composite materials. Future work includes further assessment of the strength of ultrasonic spot welds, manufacturing and testing of double lap joints to reduce the bending stresses, and a more detailed study of the microscopic details of the joint.

References

1. Hull, D., Clyne, T.W.: An Introduction to Composite Materials. Cambridge University Press, Cambridge (1996)
2. Yousefpour, A., Hojjati, M., Immarigeon, J.P.: Fusion bonding/welding of thermoplastic composites. *J. Thermoplast. Compos. Mater.* **17**(4), 303–341 (2004)
3. Vinson, J.R.: Adhesive bonding of polymer composites. *Polym. Eng. Sci.* **29**(19), 1325–1331 (1989)
4. Banea, M.D., da Silva, L.F.: Adhesively bonded joints in composite materials: an overview. *Proc. Inst. Mech. Eng. Part L: J. Mater. Des. Appl.* **223**(1), 1–18 (2009)

5. Ageorges, C., Ye, L., Hou, M.: Advances in fusion bonding techniques for joining thermoplastic matrix composites: a review. *Compos. A: Appl. Sci. Manuf.* **32**(6), 839–857 (2001)
6. Ageorges, C., Ye, L.: *Fusion Bonding of Polymer Composites: From Basic Mechanisms to Process Optimization*. Springer, London (2002)
7. Friedrich, K., Almajid, A.A.: Manufacturing aspects of advanced polymer composites for automotive applications. *Appl. Compos. Mater.* **20**(2), 107–128 (2013)
8. Stavrov, D., Bersee, H.E.N.: Resistance welding of thermoplastic composites—an overview. *Compos. A: Appl. Sci. Manuf.* **36**(1), 39–54 (2005)
9. Ahmed, T.J., Stavrov, D., Bersee, H.E.N., Beukers, A.: Induction welding of thermoplastic composites—an overview. *Compos. A: Appl. Sci. Manuf.* **37**(10), 1638–1651 (2006)
10. Benatar, A.: Ultrasonic welding of advanced thermoplastic composites. Doctoral dissertation, Massachusetts Institute of Technology (1987)
11. Bates, P., Couzens, D., Kendall, J.: Vibration welding of continuously reinforced thermoplastic composites. *J. Thermoplast. Compos. Mater.* **14**(4), 344–354 (2001)
12. Stokes, V.K.: Joining methods for plastics and plastic composites: an overview. *Polym. Eng. Sci.* **29**(19), 1310–1324 (1989)
13. Weber, A.: *Welding Still Ensures High-Strength Joints* (2007, November)
14. Troughton, M.J.: *Handbook of Plastics Joining: A Practical Guide*, 2nd edn. William Andrew, Norwich (2008)
15. The Welding Institute. “Ultrasonic welding of injection moulded components.” TWI. <http://www.twi-global.com/technical-knowledge/job-knowledge/ultrasonic-welding-of-injection-moulded-components-part-1-process-and-equipment-061/>. Accessed 21 Jul 2016.
16. Dukane Intelligent Assembly Solutions. “What is Ultrasonic Welding?” Dukane. http://www.dukane.com/us/PPL_whatIsUPA.htm. Accessed 21 Jul 2016.
17. Ensinger Inc. “TECANAT GF20 glass filled PC.” Ensinger. Accessed 21 July 2016. <http://www.ensingerinc.com/products.cfm?page=product&product=tecanat+gf20+glass+filled+pc>. Accessed 21 Jul 2016.
18. Hart-Smith, L.: Adhesive-bonded single-lap joints. Technical Report NASA CR 112236 (1973)
19. Barlow, C., Kumar, V., Flinn, B., Bordia, R., Weller, J.: Impact strength of high density solid-state microcellular polycarbonate foams. *J. Eng. Mater. Technol.* **123**, 229–233 (2001)
20. Goland, M., Reissner, E.: The stresses in cemented joints. *J. Appl. Mech.* **11**, A17–A27 (1944)
21. Pace Technologies. “Metallographic Castable Mounting.” Pace Technologies. <http://www.metallographic.com/Technical/Castable%20Mount.htm>. Accessed 21 Jul 2016.
22. LeGrand, D.: *Handbook of Polycarbonate Science and Technology*. Marcel Dekker, New York (2000)
23. Davis, M.J., Bond, D.A.: The importance of failure mode identification in adhesive bonded aircraft structures and repairs. In: ICCM 12, Paris, France (1999)
24. Suzuki, K., Ohsawa, I., Uzawa, K., Nagata, K., Matsuo, T., Yamane, M., Takahashi, J. (2012): Joint Efficiency of Ultrasonic Welding of CFRTP (Carbon Fiber Reinforced Thermoplastics) for Structural Applications
25. Srinivasa, V., Shivakumar, V., Nayaka, V., Jagadeeshaiih, S., Seethram, M., Shenoy, R., Nafidi, A.: Fracture morphology of carbon fiber reinforced plastic composite laminates. *Mater. Res.* **13**(3), 417–424 (2010)

Chapter 8

Numerical and Experimental Characterization of Hybrid Fastening System in Composite Joints

Ermias G. Koricho, Mahmoodul Haq, and Gary L. Cloud

Abstract Drilling of holes in continuous fiber composites for fastening reduces the load carrying capacities, introduces delamination and creates sites for failure initiation and progression. Recent work on a novel hybrid fastening system, which introduces a structural resin insert through a channel in the bolt shaft, overcomes the effects of drilling, eliminates slip, reduces delamination and increases the load-carrying capacities. While the benefits of this system are experimentally observed, the phenomena that govern these improvements are not fully understood. In this work, numerical simulations and experimental tests of hybrid fastening systems comprised of glass fiber reinforced polymer (GFRP) composite substrates fastened using a 1/2" Grade 5 bolt, and with a preload torque of 35 N-m were performed. The results were compared one to the other for stiffness and strength. The simulations captured the damage initiation and progress around the hole, and showed the reduction in bolt tilt ascribed to the incorporation of the adhesive insert. Overall, numerical simulations show promise in providing quantitative information about these complex phenomena, and such post-experimental validations can be used as powerful design tools.

Keywords Hybrid bolted joint • Bolt • Composite • FEM • Damage

8.1 Introduction

The use of composite materials is getting significant attention in the transport industries such as in automotive, aerospace, and naval applications in order to achieve lightweight structures. Bolted joints are one of the most frequently used methods of fastening in composite structures where there is a desire for repairing/replacing structural components or increasing the reliability of the adhesively bonded joints.

However, composite bolted joints have their own disadvantages, since composite substrates need to be drilled to insert the bolt. Drilling and machining of holes in composites cause stress concentrations and delamination that reduce the resistance of the joint construction to applied loads, and thus its efficiency. Besides, gaps usually occur at wearing surfaces during assembly of large scale structures. This problem can be exacerbated for composite structures as it is comparably more difficult to control dimensional tolerances of composite components than those of conventional materials such as steel and aluminum. Consequently, pre-stresses could be developed by these gaps and the assembly forces, which could result in initiation of cracks and delaminations that would adversely affect the performance of the structures [1–3]. To overcome these problems, inserts, such as shims, have often been used to fill the clearance to avoid possible structural damage caused by pre-stress and delamination [4–7]. Huhne et al. [5] carried out quasi-static tests to investigate the influence of liquid–shim thickness on the strength and structural behavior of carbon fiber laminate single-lap bolted joints, and they found that the joint stiffness reduced with shim thickness but ultimate joint load was unaffected up to a liquid–shim thickness of 1.5 mm. However, the Mil-Handbook [6] holds a different point of view: it states the usage of shims will cause reduction of bearing strength in bolted composite joints even if the shim is very thin, and, as the thickness of the shim increases, the reduction will be greater. To clearly understand the effect of shims on the mechanical behavior of bolted joints, Liu et al. [7] investigated both experimentally and numerically the performance of composite-to-titanium bolted joints with liquid shims. Results showed that both the failure load and stiffness decrease with the thickness of the shim, however, the effect of the shim becomes negligible as the thickness is diminished between 0.5 and 1 mm.

E.G. Koricho (✉) • G.L. Cloud

Composite Vehicle Research Center, Michigan State University, 2727 Alliance Drive, Lansing, MI 48910, USA
e-mail: koricho@msu.edu

M. Haq

Composite Vehicle Research Center, Michigan State University, 2727 Alliance Drive, Lansing, MI 48910, USA

Department of Civil and Environmental Engineering, Michigan State University, Engineering Building, East Lansing, MI 48824, USA

On the other hand, Haq et al. [8, 9] have studied the effects on the quasi-static behavior of hybrid bolted joints of resin inserts with various reinforcements (nano-fillers and glass/carbon sleeves) that are similar to the joints studied in this work. They have observed zero slip, considerable improvements in static load carrying capacities, increased strengths, and delayed onset of delamination in the resulting joints. However, no numerical study on the mechanical behavior of such novel hybrid bolted joints is presented in their works.

In this work, numerical simulations and experimental tensile tests of conventional and hybrid fastening systems comprised of glass fiber reinforced polymer (GFRP) composite substrates fastened using a 1/2" Grade 5 bolt, and with a preload torque of 35 N-m were performed. The results were compared one to the other for stiffness and strength. The damage initiation and evolution were also predicted at particular points of interest using the Hashin failure criteria available in ABAQUS® and compared with the experimental results.

8.2 Materials

In this study, the vacuum-assisted resin transfer molding (VARTM) technique was used to manufacture the glass fiber reinforced plastic (GFRP) composite laminates used for the single-lap composite bolted joints. The reinforcement was S2-glass plain weave fabric (Owens Corning ShieldStrand S) with a real weight of 818 g/m². The resin used was a two part toughened epoxy, namely SC-15 (Applied Poleramics Inc., CA). The SC-15/glass-fiber laminates were cured in a convection oven at 60 °C for 2 h followed by a post cure of 4 h at 94 °C. Sixteen layers of plain-weave glass reinforcement were used for each adherend in this study. The thickness of the cured laminate was found to be 9.6 mm. The laminate coupons for the bolted joints were cut by a water-cooled, diamond-coated-disc cutting machine to achieve final dimensions of 100 mm width by 150 mm length.

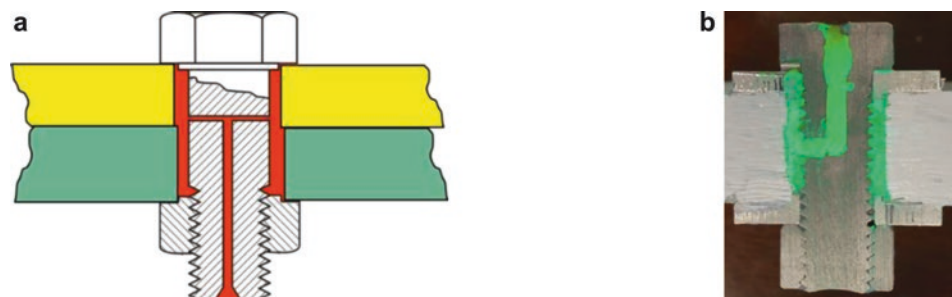
The bolt was a nominal 1/2 in. grade five, medium-strength steel hex head (head width: 19.05 mm or 3/4 in.; head height 7.94 mm or 5/16 in.) bolt with a right-hand thread having a length of 38.1 mm (1.5 in.), fully threaded with a 12.7 mm-13 (1/2 in.-13) thread. The bolts were drilled with 2 mm diameter passageways for resin injection.

8.3 Fabrication of Bolted Joints

Two approaches were used to develop the composite single lap bolted joints: conventional and hybrid. The schematic diagram of the hybrid joint bolt (see Fig. 8.1a) shows that, in its simplest form, it basically consists of a bolt that has a channel through the shank that allows the injection of an insert that fills the clearance space between the bolt and work-pieces and acts as a structural component [10, 11]. One of major advantages of this invention is that the presence of the adhesive/insert compensates for the variation of hole clearance that typically occurs during conventional machining processes. Additionally, in layered composites, the delaminations and irregularities that are introduced by hole-drilling become filled with the resin insert, thereby repairing any damage and creating a monolithic part. Finish reaming of the holes is thereby eliminated at considerable reduction of fabrication cost. Many variations of the insert concept exist, but only the simplest form was treated in this study.

The GFRP substrates were joined using the bolts described above and flanged sleeve washers. A 15.7 mm diameter hole was drilled in the work pieces 50.5 mm away from three edges. The sleeve washer has the following dimensions: flange diameter 25.4 mm, ID of 13.46 mm, sleeve OD of 15.88 mm, flange thickness of 3.18 mm, overall height of 4.75 mm. The radial clearance between the bolt shank and the hole was ~1.5 mm. This gap, which probably exceeds the optimum, was to be filled with resin to create the hybrid joints. The control specimens that lacked the resin insert were manufactured to the

Fig. 8.1 (a) Schematic of basic hybrid composite joint, (b) Cross section of hybrid joint with resin insert exaggerated



same specifications, and the resulting clearance is not consistent with typical manufacturing practice for critical structures although it is not unusually high for non-critical factory or field assembly. The tightening torque of 35 N-m was applied by a digital torque wrench.

After assembly, the samples that were selected for the hybrid joint were injected with SC-15 resin through the channels in the bolts so as to fill the clearance space between the threaded bolt shank and the work pieces. The injected inserts were cured by a convection oven at 60 °C for 2 h followed by post curing at 94 °C for 4 h. Figure 8.1b shows a cross-section of the bolted joint, wherein the channels are exaggerated for better visibility. As can be seen, the resin fills all the intricate areas including the threads of the bolts and, upon curing, creates a monolithic structure.

8.4 Experimental Setup

All quasi-static testing was performed using a 100 kN load cell servo-hydraulic testing machine (MTS 810), and a typical test setup is shown in Fig. 8.2. The machine is equipped with a standard load cell and an internal crosshead displacement measuring extensometer. An external laser extensometer was also used to measure the joint longitudinal displacement, as shown in the figure.

The tests were performed according to ASTM STP1455-EB. In this work, five tests were carried out for statistical significance. The average shear strength of the joint was calculated by dividing the maximum load reached in each test divided by the cross-sectional area of the bolt.

8.5 FEM Modeling

8.5.1 Modeling and Meshing

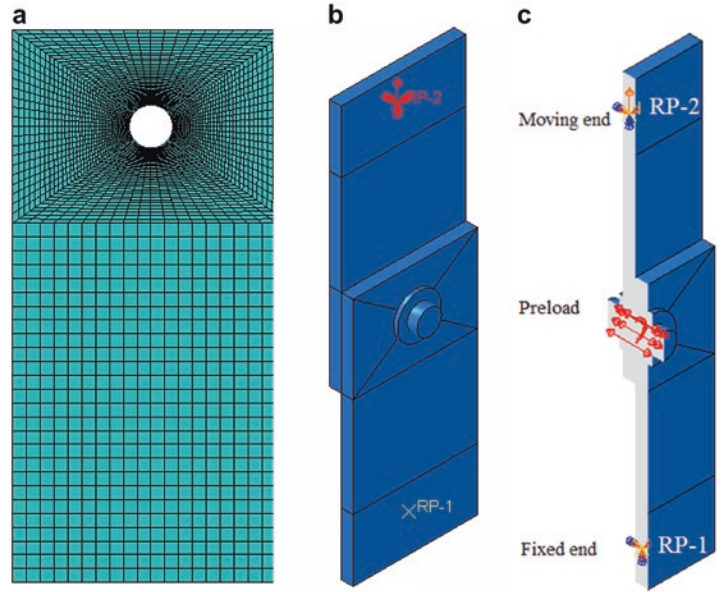
In this study, the commercially available finite element software ABAQUS® was used to obtain the stress distribution and damage initiation near the holes in the bolted composite coupons. The overall dimensions for modeling of the GFRP with a drilled hole were obtained from the specimens used for the experimental tests.

Eight-node quadrilateral in-plane general-purpose continuum shell elements with reduced integration and hourglass control were used to model the 16 ply plain-weave composite plates, $[0]_{16}$. A minimum of three integration points using the Simpson integration rule were assigned at each layer of continuum shell elements. As is shown in Fig. 8.3a, the specimen was partitioned at specific sections to apply boundary conditions and localized meshes, especially around the hole, where they need to be refined to capture more accurately the steep stress gradients there. During the meshing process, the bias method was implemented to allow the element size to be varied with respect to the areas near the holes: the nearest element to the hole has the smallest element size, as shown in Fig. 8.3a. Figure 8.3b shows the completely assembled lap joint as modeled.

Fig. 8.2 Experimental setup



Fig. 8.3 FEM model: (a) mesh, (b) assembled joint, (c) sectional view of loading and boundary conditions



The bolt and the nut, which were made of a steel, were considered to be a single part in order to reduce computational time by avoiding modeling the contact between the bolt and nut. A ten-node quadratic tetrahedron three-dimensional element was used to model the bolt and the resin insert. The “surface-surface contact” model was incorporated to define the interaction in the joint. The tangential and normal contact properties were defined using the “penalty” friction formulation and “hard” contact pressure overclosure methods, respectively. For the hybrid bolted joint, the resin insert was placed between the bolt and the composite hole wall and constrained using the “Tie option” available in ABAQUS®.

The joint was subjected to tensile loading by constraining all degrees of freedom at the fixed end (RP-1 in Fig. 8.3c) of the joint and allow a constant displacement rate of 2 mm/min at the moving end (RP-2 in Fig. 8.3c). The preload, which was developed by the bolt tightening torque, was incorporated in the bolt shank through the “Bolt load” module in ABAQUS CAE, as shown in Fig. 8.3c. It was set to be 10 kN, which is the preload that corresponds to 35 N-m tightening torque according to the usual empirical formula.

8.5.2 Material Modeling

The damage initiation and evolution model used in this work was based on the Hashin failure criteria in ABAQUS®. In this model, four different modes of failure were considered, namely, fiber rupture in tension, fiber buckling and kinking in compression, matrix cracking under transverse tension and shearing, and matrix crushing under transverse compression and shear.

The Hashin failure initiation metrics for the above modes of failures take the following general forms, and failure is predicted to occur when any one of these metrics attains a value of one:

$$F_f^t = \left(\frac{\sigma_{11}}{X^T} \right)^2 + \alpha \left(\frac{\tau_{12}}{S^T} \right)^2, \text{ for fiber tension } (\sigma_{11} \geq 0) \quad (\text{HSNFTCRT}) \quad (8.1)$$

$$F_f^c = \left(\frac{\sigma_{11}}{X^C} \right)^2, \text{ for fiber compression } (\sigma_{11} < 0) \quad (\text{HSNFCCRT}) \quad (8.2)$$

$$F_m^t = \left(\frac{\sigma_{22}}{Y^T} \right)^2 + \alpha \left(\frac{\tau_{12}}{S^L} \right)^2, \text{ for matrix tension } (\sigma_{22} \geq 0) \quad (\text{HSNMTCRT}) \quad (8.3)$$

$$F_m^c = \left(\frac{\sigma_{22}}{2S^T} \right)^2 + \left[\left(\frac{Y^C}{2S^T} \right)^2 - 1 \right] \frac{\sigma_{22}}{Y^C} + \left(\frac{\tau_{12}}{S^L} \right)^2, \text{ for matrix compression } (\sigma_{11} < 0) \quad (\text{HSNMCCRT}) \quad (8.4)$$

Table 8.1 Laminate strength data

Composite	Weave type	Fiber fraction (wt%)	Tensile strength (MPa)	E_x (Gpa)	G_{xy} (Gpa)	ν_{xy}
0/90 S-glass/epoxy	Plain	0.61	476.264	23.18	4.0	0.08

where: X^T and X^C are longitudinal tensile and compressive strengths, respectively;

Y^T and Y^C are transverse tensile and compressive strengths, respectively;

S^L and S^T are longitudinal and transverse shear strengths, respectively;

α is a coefficient that determines the contribution of the shear stress to the fiber tensile failure initiation criterion; and

σ_{11} , σ_{22} , and τ_{12} are components of the effective stress tensor, σ , that is used to evaluate the initiation criteria.

The response of the material during the post-damage initiation phase is computed as,

$$\sigma = S\varepsilon \quad (8.5)$$

where ε is strain and S is the damaged elastic matrix

$$S = \frac{1}{D} \begin{bmatrix} (1-d_f)E_1 & (1-d_f)\nu_{21}E_1 & 0 \\ (1-d_f)(1-d_m)\nu_{12}E_2 & (1-d_m)E_1 & 0 \\ 0 & 0 & (1-d_s)GD \end{bmatrix} \quad (8.6)$$

$$D = 1 - (1-d_f)(1-d_f)\nu_{12}\nu_{21} \quad (8.7)$$

The three scalar parameters, d_f , d_m , and d_s represent the current state of fiber damage, matrix damage, and shear damage, respectively. The damage parameters have $0 \leq d_i \leq 1$ values, with monotonically increasing values up to $d_i = 1$, where complete failure occurs.

Some of the materials properties that were used to model the GFRP were experimentally found and are summarized in Table 8.1 [12]. To incorporate the damage evolution parameters in ABAQUS®, additional experimental data was obtained from the literature [13]. An elastic–plastic multi-linear isotropic hardening material model was used to represent the stress–strain relationship of the resin insert material that was used as the interface in the hybrid bolted joint. The resin material properties were taken from [14].

8.6 Results and Discussion

Figure 8.4 shows the load vs. deformation characteristics of conventional and basic hybrid bolted joints that have been reported earlier and were used for comparisons with the FEM study [8, 9, 12]. Unlike the conventional bolted joint, the hybrid joint exhibits a monotonic increase of load without slippage. Onset of delamination occurs at approximately 32 kN for the hybrid, while the conventional joint begins to delaminate at approximately 12 kN. Once delamination initiates, the stiffness of the hybrid joint reduces gradually until it reaches its maximum load carrying capacity, ~ 51.5 kN. If the stiffness of the conventional bolted joint is calculated between points 1 and 2, the hybrid bolted joint improves the stiffness of the joint by ~62% prior to the onset of delamination. Furthermore, if slip is critical, then the hybrid bolt can be considered infinitely better than the conventional one. If failure is defined as the onset of delamination, then the hybrid bolt is roughly three times better than the conventional one.

Figure 8.5 compares the force-displacement curves from the experimental and numerical studies of the hybrid joint. The stiffness of the numerical model is seen to be in good agreement with the experimental one within a range of 0–7 kN. However, as the load increases further, the slope (joint stiffness) of the experimental curve decreases more quickly than does that of the analytical model. As mentioned above, the onset of delamination from the experiments, labeled as point *a* in Fig. 8.5, occurs at 32 kN. The FEM curve shows delamination onset, identified by the slight plateau labeled as point *b* in Fig. 8.5, occurring at about 30 kN. These findings agree to within 6%, which seems very good considering the complexities of the problem and the unknown factors.

Practically, the experimental results could be influenced by several factors including the quality of the infusion process, geometry variations, joint assembly issues, distribution of the resin insert around the bolt, gripping pressure, and alignment of the specimen with the loading direction. The cumulative effect of all those factors could adversely or favorably affect the stiffness of the joint, first damage initiation point, maximum failure load, and mode of failure. None of these factors could be taken into account in the idealized FEM model. In summary, it seems that the model is quite well validated by the experiments.

Fig. 8.4 Tensile tests of bolted lap joint with conventional and hybrid bolts

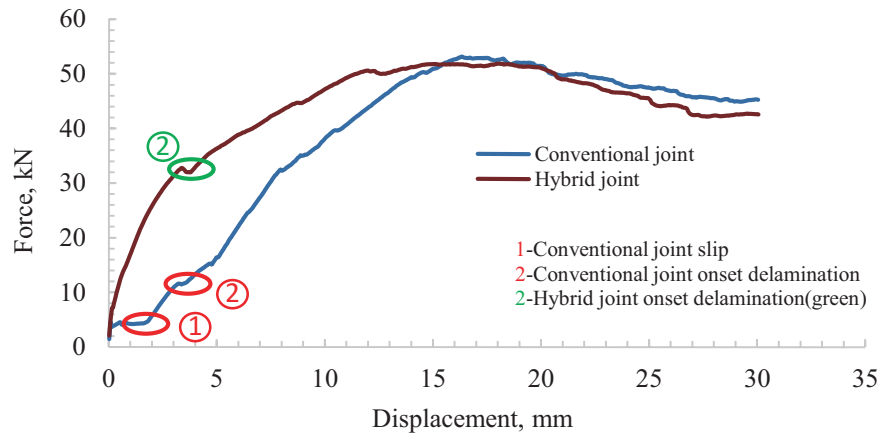
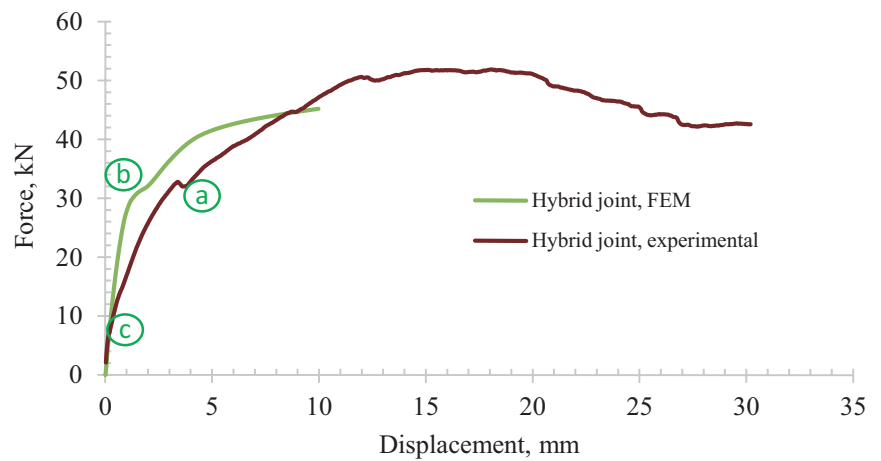


Fig. 8.5 Comparison of results of experimental and FEM modeled tensile test of hybrid bolted lap joint



One of the critical aspects in the design of composite structures and joining is understanding damage initiation and evolution at critical locations such as at hole, near abrupt change in cross-section, and at interfaces. Those kinds of features affect directly or indirectly the performance of a joint designed for a particular application. Investigation in depth of the interactions of the materials as well as in-plane and through-thickness stress distributions could help in the design of robust structural composite bolted joints. The main failure modes in a hybrid bolted joint can be categorized into three groups, namely: yielding of the bolt, deformation and fracture of the washers, and excessive damage of composite substrates characterized by matrix and/or fiber failure. Figure 8.6a shows a hybrid bolted joint that has been tested to failure and then exposed to UV light after dye penetration. For qualitative comparison, Fig. 8.6b shows the Von Mises stress distribution predicted by FEM at failure. Notice that the experimentally tested composite substrate is severely damaged around the hole due to tensile loading, bearing pressure, and localized compressive load beneath the washer. The FEM predicts well the fractured surface beneath the washer. A further interesting comparison is presented by the figure following. Figure 8.7a is a photograph of the hybrid composite bolted joint at failure under tensile loading. Figure 8.7b shows the Von Mises stress distribution in the bolt and washer from the FEM model. These results show that the tensile shear loading and secondary bending effects cause the bolt to become noticeably tilted and to develop plastic zones at points 1 and 2 of the washer, which ultimately leads to deformation and fracture. As expected, the maximum stress in the bolt shank is developed at the shear plane of the joint, that is, at its intersection with the interface of the joined components.

Reference is made to two points in the force-displacement curve obtained from the FEM model and shown in Fig. 8.5 to interpret their significances and to aid in visualizing the corresponding stress distributions and damage initiations in composite substrates. The first of these is point *c*, where, evidently, initial matrix failure occurs; and the second is point *b*, which demonstrates significant stiffness reduction at, evidently, delamination. Figure 8.8a–d show the four failure metrics at damage initiation. As shown in these figures (look inside the hole), out of the four Hashin failure criteria, the first onset of damage

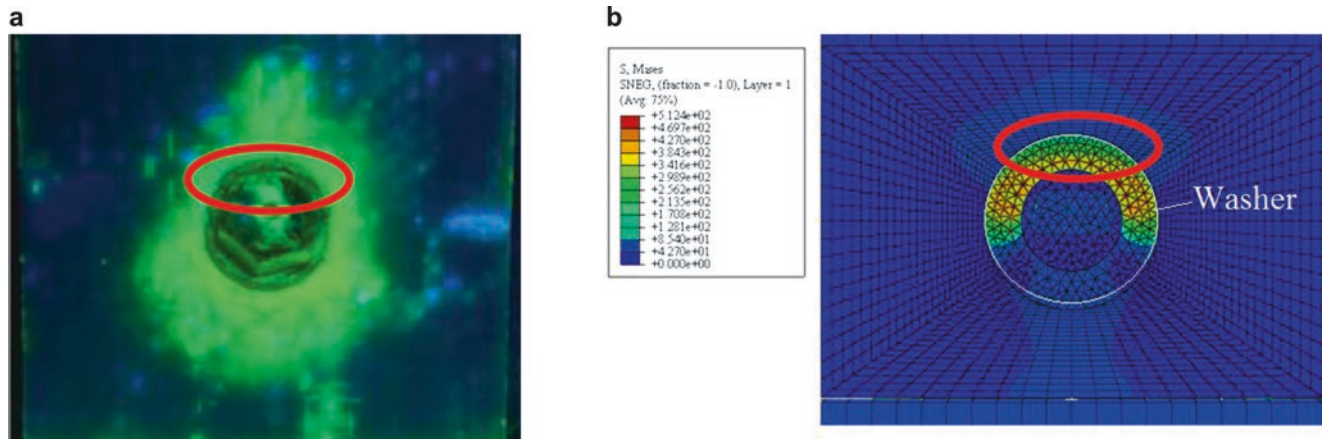


Fig. 8.6 Qualitative comparison of experimental and FEM results. (a) Photo from dye penetrant test of surface of hybrid joint tested to failure. (b) FEM prediction of Von Mises stress beneath the washer

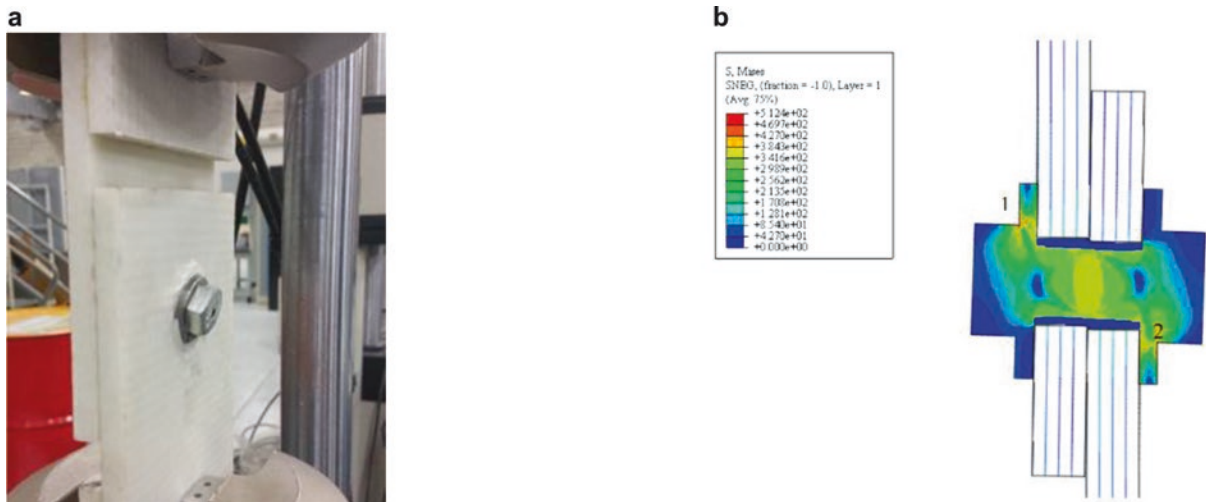


Fig. 8.7 Hybrid joint: (a) photograph of a hybrid composite bolted joint at failure under tensile loading, (b) FEM prediction of Von Mises stress in the bolt and washer

initiation due to matrix failure was observed when the failure index, R , that is based on matrix tension (see Fig. 8.8d and Eq. 8.3) is equal to one $\left(R \equiv F_m^t = \left(\frac{\sigma_{22}}{Y^T} \right)^2 + \alpha \left(\frac{\tau_{12}}{S^L} \right)^2 = 1 \right)$. The remaining failure metrics from Eqs. 8.1, 8.2, and 8.4 show

low values at this stage, which implies that their influences are minimal in causing any considerable damage within the composite specimen. The maximum principal stress field was also captured in order to observe the stress gradient around the hole, and this is shown in Fig. 8.8e. At this stage, the stress field indicates that the load tends to develop a significant bearing stress in the composite substrate.

Fiber failure is a usually considered to be the critical failure mode in composite structures as compared with matrix failure. In the absence of fiber failure, the loading of the joint can be increased even though some matrix failure has occurred. However, as matrix failure becomes more dominant, it will detrimentally affect the stiffness of the joint.

Figure 8.9 shows the FEM damage predictions according to each of the four Hashin criteria for the composite substrate of the hybrid bolted joint at the onset of delamination, which corresponds to point b of Fig. 8.5. Figure 8.9a, b show that the predicted failure begins with the near-simultaneous compressive and tensile matrix failures at separate locations and progresses with broadening damage areas when the corresponding failure indexes $R \geq 1$. At this point, the stiffness of the

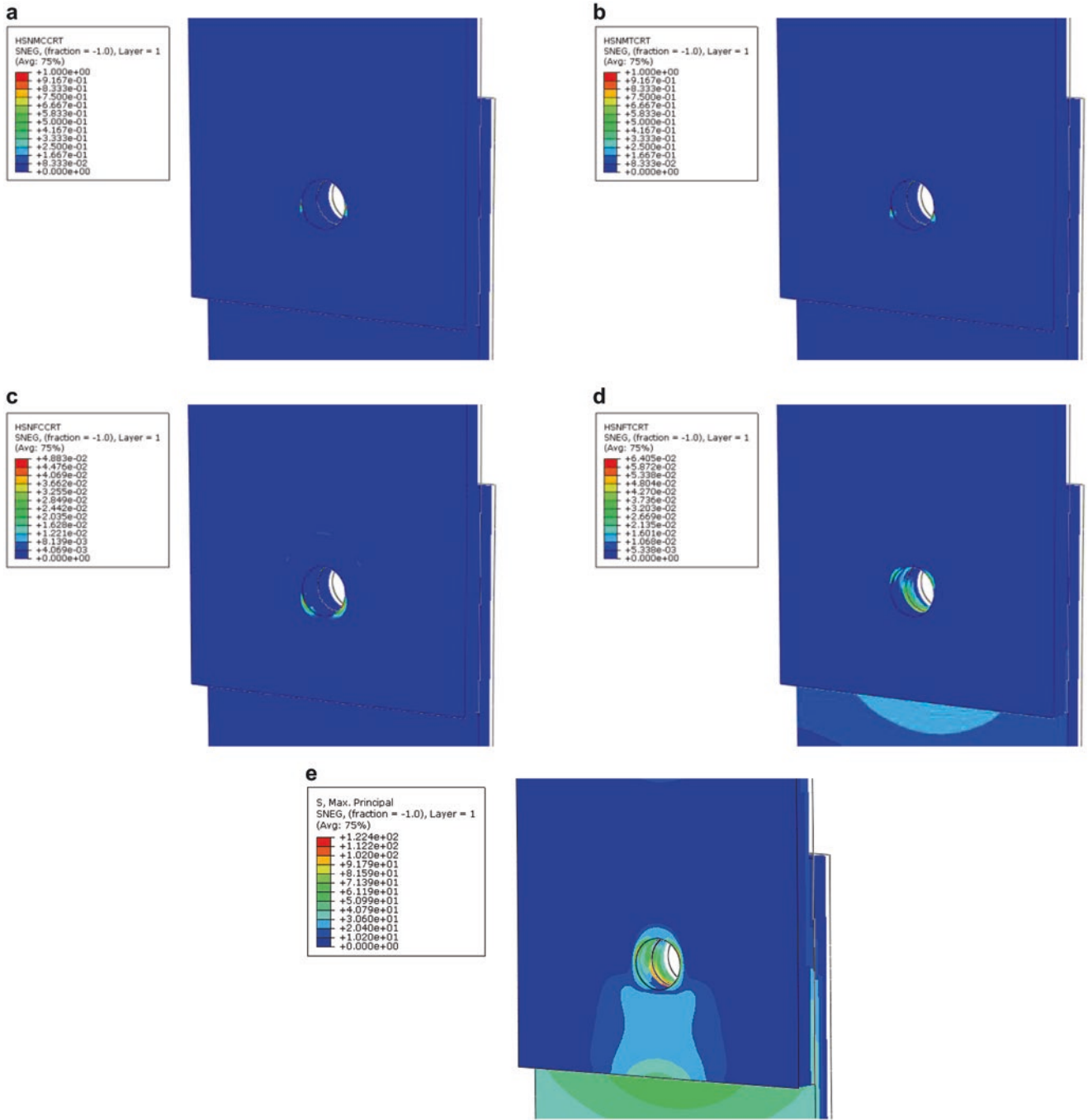


Fig. 8.8 Hashin damage metrics and stress prediction from FEM model of hybrid bolted joint at first onset of matrix failure: (a) Hashin matrix compression metric; (b) Hashin matrix tension metric; (c) Hashin fiber compression metric; (d) Hashin fiber tension metric; (e) Maximum principal stress distribution

joint declines to its lowest value prior to ultimate load. On the other hand, the tensile fiber failure [HSNFTCRT] and compressive fiber failure [HSNFCCRT] metrics, represented in Fig. 8.9c, d respectively, show values that are less than one,

specifically, $R \equiv F_f' = \left(\frac{\sigma_{11}}{X^T} \right)^2 + \alpha \left(\frac{\tau_{12}}{S^T} \right)^2 = 0.7244$, $R \equiv F_f^c = \left(\frac{\sigma_{11}}{X^C} \right)^2 + \alpha \left(\frac{\tau_{12}}{S^T} \right)^2 = 0.799$. These results confirm that in

composite bolted joints, even though the fibers might remain intact at elevated load, the performance of the joint is degraded owing to the presence of matrix failure. Matrix failure is one of the main factors driving delamination between the layers. Usually, delamination can also be caused by interlaminar stresses, which are developed due to mismatches in material properties, discontinuities in the structure (e.g. holes), and high deformation gradients [15].

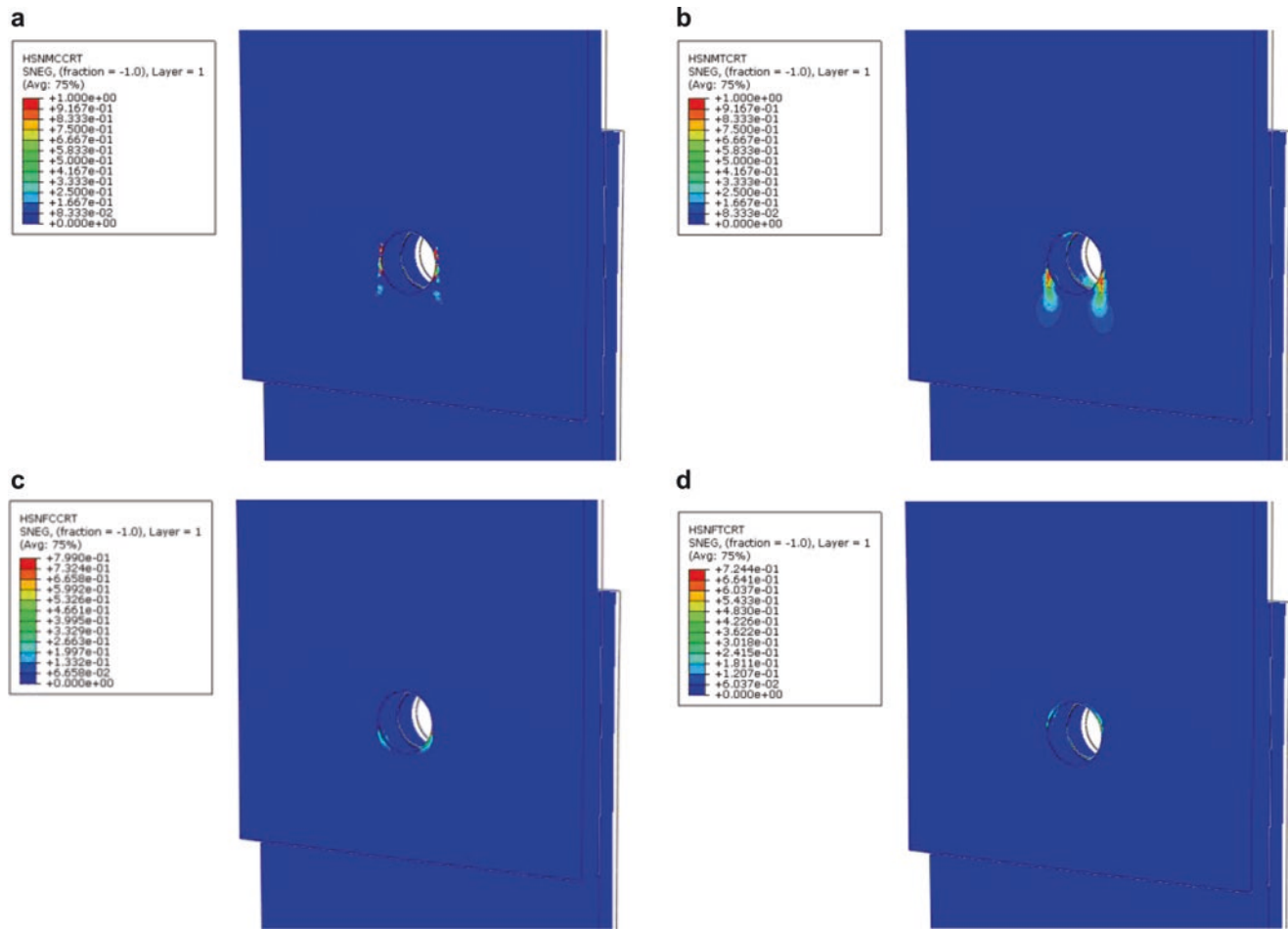


Fig. 8.9 Hashin damage metrics from FEM model of hybrid bolted joint at first onset of delamination: (a) matrix compression metric; (b) matrix tension metric; (c) fiber compression metric; (d) fiber tension metric

8.7 Conclusions

In this work, experimental and numerical methods were adopted to investigate the mechanical properties of hybrid composite bolted joints. The numerical model was developed in Abaqus/Standard. By comparing the numerical results with the experimental results, the validity of the numerical model was verified in terms of load–displacement and damage patterns. The observed results can be summarized as follow:

- Generally, this study targets the development of a numerical model of a single-lap hybrid bolted composite joint that was extensively studied experimentally by the same group in the past.
- As reported in the previous works, the hybrid joint eliminates the presence of slippage and delays the onset of delamination from occurring at low load level.
- The stiffness of the hybrid joint predicted by the numerical method is shown to be in a good agreement with the experimental result, particularly at the initial stage of the load–displacement curve.
- Major phenomenon, such as onset of delamination and maximum load carrying capacity of the hybrid joint, are also predicted well using the numerical model along with the Hashin failure criteria.
- The damage of the composite beneath the washer is well predicted.
- The deformation of the bolt and washer was predicted, and the results agree qualitatively with experimental results.
- Significant stiffness variations and absences of detailed load fluctuations are observed as the applied load increases. These behaviors can be explained by the fact that, in the current numerical model, the interfaces between the individual plies within the laminate were assumed to be ideal.

- A delamination model, which is usually represented by cohesive elements between the plies, was intentionally excluded in order to minimize computational time.
- Future work includes detailed modeling of the hybrid bolted joint including a delamination model within the interface, tailored inserts that contain particulates and fibers, and multi-material joints.

References

1. Dhôte, J.X., Comer, A.J., Stanley, W.F., Young, T.M.: Investigation into compressive properties of liquid shim for aerospace bolted joints. *Compos. Struct.* **109**, 224–230 (2014)
2. Walker, T.H., Minguet, P.J., Flynn, W.F., Cargery, D.J., Swanson, G.D., Ilcewicz, L.B.: Advanced technology composite fuselage-structural performance. NASA Contractor report 4732 (1997)
3. Lu, X., Kim, K.Y., Sachse, W.: In situ determination of elastic stiffness constants of thick composites. *Compos. Sci. Technol.* **57**, 753–762 (1997)
4. Goering, J., Bohlmann, R.E., Wanthal, S., Kautz, E., Neri, L.: Assembly induced de-laminations in composite structures. In: Proceedings of Ninth DoD/NASA/FAA Conference on Fibrous Composites in Structural Design, Lake Tahoe (1991)
5. Hühne, C., Zerbst, A.K., Kuhlmann, G.: Progressive damage analysis of composite bolted joints with liquid shim layers using constant and continuous degradation models. *Compos. Struct.* **92**, 189–200 (2010)
6. Military Handbook - MIL-HDBK-17-1F: Composite Materials Handbook, Volume 1 - Polymer Matrix Composites Guidelines for Characterization of Structural Materials. U.S. Department of Defense, ELECTRONIC ISBN 978-1-59124-509-4, (2002)
7. Liu, L., Zhang, J., Chena, K., Wanga, H., Liub, M.: Experimental and numerical analysis of the mechanical behavior of composite-to-titanium bolted joints with liquid shim. *Aerosp. Sci. Technol.* **49**, 167–172 (2016)
8. Haq, M., Khomenko, A., Cloud, G.: Novel hybrid fastening system with nano-additive reinforced adhesive inserts. In: SEM 2014 Annual Conference & Exposition on Experimental and Applied Mechanics, Greenville, 2–5 June 2014
9. Haq, M., Cloud, G.: Flexible hybrid fastening system. In: SEM 2013 Annual Conference & Exposition on Experimental and Applied Mechanics, Chicago, 3–5 June 2013
10. Cloud, G.: 2012 William M. Murray Lecture: some curious unresolved problems, speculations and advances in mechanical fastening. *Exp. Mech.* **53**(7), 1073–1104 (2013). doi:[10.1007/s11340-013-9736-3](https://doi.org/10.1007/s11340-013-9736-3)
11. Cloud, G.L.: Hybrid fastener. Provisional Patent 6550-000226-US-PS1-1 (2012). General patent application filed (2013)
12. Koricho, E.G., Khomenko, A., Haq, M., Cloud, G.L.: Fatigue behavior of novel hybrid fastening system with adhesive inserts. In: Proceeding of SEM 2015 Annual Conference & Exposition on Experimental and Applied Mechanics, Costa Mesa, 7–11 June 2015
13. Belingardi, G., Koricho, G.K., Beyene, A.T.: Characterization and failure modeling of notched cross-ply and angle-ply fabric GFRP composite material. *J. Compos. Struct.* **112**, 237–2049 (2013)
14. Khomenko, A., Koricho, E.G., Haq, M.: Fiber Bragg-grating sensors for SHM and FEM of in service bonded multi-material Pi-joints. In: Proceeding of American Society for Composites 29th Technical Conference, La Jolla, 8–11 Sept 2014
15. Gara, A.C.: Delamination—a damage mode in composite structures. *Eng. Fract. Mech.* **29**, 557–587 (1988)

Chapter 9

Application of Digital Image Correlation to the Thick Adherend Shear Test

Jared Van Blitterswyk, David Backman, Jeremy Laliberté, and Richard Cole

Abstract The purpose of this study was to develop and validate a novel method for measuring shear deformation during the Thick Adherend Shear Test (TAST), to determine *in situ* mechanical properties of an adhesive under tensile shear loading, using two-dimensional (2D) Digital Image Correlation (DIC). Shear strains were optically measured using DIC from the bond line and also from adherend deformations; both were compared against measurements made using the ASTM D5656 standard (KGR-1 extensometers). The results from 17 TAST specimens showed that all techniques were in good agreement, however, both DIC techniques had significantly lower variance on measured mechanical properties compared to the KGR-1 extensometers. The use of correlated adherend deformations was the preferred technique for deriving plastic shear strains, and overall produced the lowest scatter on mechanical properties. This study demonstrates the potential for the use of 2D DIC as a more precise, and time-efficient alternative to the KGR-1 extensometers for room temperature *in situ* characterization of adhesives in shear.

Keywords Adhesives • Mechanical properties • Single-lap joint • Digital image correlation (DIC) • KGR-1 extensometer • Experimental test methods

1 Introduction

Bonded joints are seeing increasing application in the aircraft industry for their many advantages over mechanically fastened joints. One of the main challenges facing aircraft designers relates to demonstrating compliance with certification requirements. Certification of highly-loaded adhesive bonded joints typically requires a detailed characterization of the stress-strain response of the adhesive and a statistically-based set of material strength allowables. The large volume of testing required to develop such bases for material design allowables necessitates an experimental methodology that is credible, precise, repeatable, and time and cost efficient.

The thick adherend single-lap joint specimen specified in the ASTM D5656 standard [1], is the accepted methodology for measuring *in situ* adhesive shear properties. The use of thick aluminum adherends is most effective for measuring the response of an adhesive in shear due to enhanced bending rigidity along the bonded overlap, which reduces peel stresses and joint rotation. These considerations restrict the use of other thin adherend single-lap joint test methods, such as ASTM D1002 [2] and ASTM D3165 [3], to “apparent” strength tests of bonded joints, as peel stresses having significant influence on the overall joint strength [2–5]. ASTM D5656 [1] requires the use of the KGR-1 extensometer system to measure relative adherend deformation across the bond line of Thick Adherend Shear Test (TAST) specimens that are subjected to a tensile shear load. The KGR-1 extensometer is a specialized mechanical device, tailored for the TAST specimen, which can resolve sub-micron, relative, uniaxial displacements. The KGR-1 mounting pins span the bond line and measure relative shear displacements of the adjacent adherends. The measured displacements consist of both adhesive shear and adherend elongation. To isolate the strain in the adhesive, the adherend deformations are approximated based on KGR-1-measured displacements on a solid aluminum specimen of the same geometry as the bonded joint, commonly referred to as a “dummy specimen”.

J. Van Blitterswyk • J. Laliberté

Department of Mechanical and Aerospace Engineering, Carleton University, 1125 Colonel By Drive, Ottawa, ON, Canada K1S 5B6

D. Backman (✉) • R. Cole

National Research Council Canada, Aerospace Portfolio, 1200 Montreal Road, Ottawa, ON, Canada, K1A 0R6

e-mail: david.backman@nrc.gc.ca

The KGR-1 system is tedious and time consuming to operate, and is susceptible to numerous experimental errors which can significantly affect the level of data scatter. Furthermore, the quality of measurements is heavily dependent on placement repeatability and operator skill, and the resulting experimental errors are difficult to quantify. Some of the experimental errors include: mounting pin slippage, rotation, and poor placement repeatability both across the bond line, and along the joint overlap [6–8]. Quantifying the experimental errors associated with the KGR-1 and the ASTM D5656 test method has received much attention over the past 20 years [4, 6–9]. In addition, a small number of studies have explored modifications to the KGR-1 device and other experimental techniques for characterizing structural adhesives including pilot holes and additional mounting pins [4, 7], clip gauge extensometers and digital video microscopy [10, 11], and stacked strain gauge rosettes [12].

Since none of the proposed techniques have been properly developed, have limited working ranges, require correction factors, or are time consuming or expensive, the KGR-1 remains the accepted instrument for measuring adhesive properties in shear. With the development of full-field optical techniques, several researchers have considered the use of Digital Image Correlation (DIC) as an alternative technique for characterizing adhesives using single lap-joint specimens.

Lemmen *et al.* [13] characterized the shear stress-shear strain behaviour of an adhesive using a TAST specimen and an optical high magnification digital grid deformation technique. This allowed strains to be extracted using bond line deformations, thus eliminating the need for correction factors to compensate for adherend deformations. Unfortunately, the high magnification created issues with image focusing and field of view, as the camera required repositioning mid-test to capture the non-linear adhesive deformations. The combination of the two problems created large scatter in the data. Moreover, only two specimens were tested and no comparison was provided to a reference standard methodology, thus leaving the repeatability and credibility of this technique in question. Several other studies have been conducted using two-dimensional (2D) and three-dimensional (3D) DIC on single and double lap-joints [14–20], however these efforts used thin adherend specimens, which do not create the proper stress field for adhesive characterization [2–5]. In the case where material properties were estimated [14], a comparison was not provided to a reference standard and several assumptions were required, which limited the technique to linear strains.

To the authors' knowledge there has yet to be a rigorous comparison of DIC to the accepted ASTM D5656 methodology in terms of measurement precision, repeatability, cost and testing time. The purpose of this research is to validate 2D DIC as a new, faster, more precise and cost effective method for characterizing the *in situ* properties of adhesives in shear using the ASTM D5656 test specimen and procedure. This study compares the KGR-1 in ASTM D 5656, to two DIC data extraction approaches, using 17 ($n=17$) TAST specimens bonded with aerospace-grade AF 163-2K epoxy structural film adhesive.

2 Experimental

2.1 KGR-1 Extensometer

The KGR-1 extensometer, from Cytec Engineered Materials, is a mechanical instrument for precisely measuring relative uniaxial deformation. The KGR-1 extensometer system consists of two Linear Variable Differential Transformers (LVDTs), each housed in a two-piece (front/back) rigid frame, which span the bonded joint as shown in Fig. 9.1. Each front frame has one steel mounting pin while the back frame has two. The front and rear frame mounting pins are held in plane, parallel to the specimen surface, using an extension arm attached to the back side of the frame. This configuration allows the two sets of mounting pins to displace independently from one another, causing the LVDT core to move with respect to the LVDT coils, which outputs a voltage from the transformer. The instrument is mounted on the specimen using a self-supporting spring-clamp mechanism (Fig. 9.2) and suspends itself on the specimen via the mounting pins, mechanically restraining the assembly to displace with the adherends. The mounting pins have sharp points that indent into the adherends to minimize slippage.

Calibration of the KGR-1 output voltage was performed using an extensometer calibrator (MTS Calibrator Model 650.03). The calibrator has two aluminum mounting blocks that are spanned by the KGR-1 mounting pins and a micrometer dial that enables precise relative displacements to be applied to the aluminum blocks, which was then correlated to the output voltage.

2.2 Digital Image Correlation

Digital Image Correlation (DIC) is a non-contact optical method for measuring surface deformation and strain. The technique requires at least two images of the surface of interest; one in a state with no applied load (reference), and one under applied load. A computer algorithm discretizes the images into regions referred to as “subsets”, and characterizes the transformation of each subset, between images, using shape functions based on optimizing a cross-correlation coefficient of

Fig. 9.1 KGR-1 extensometer schematic layout (based on [21])

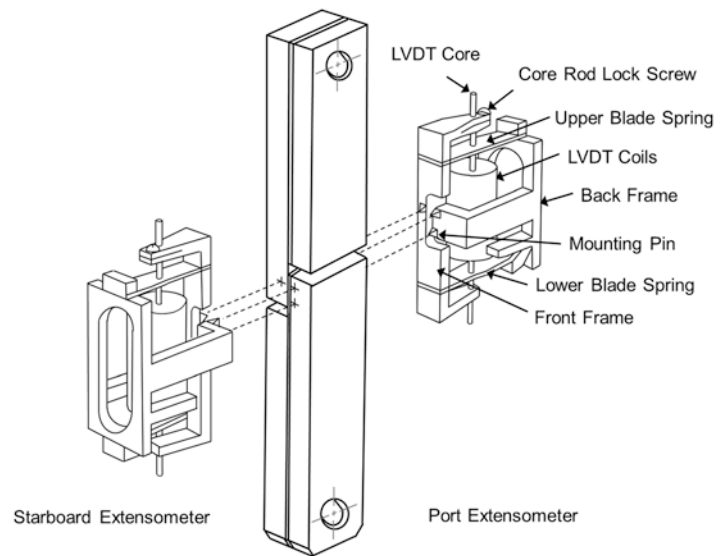
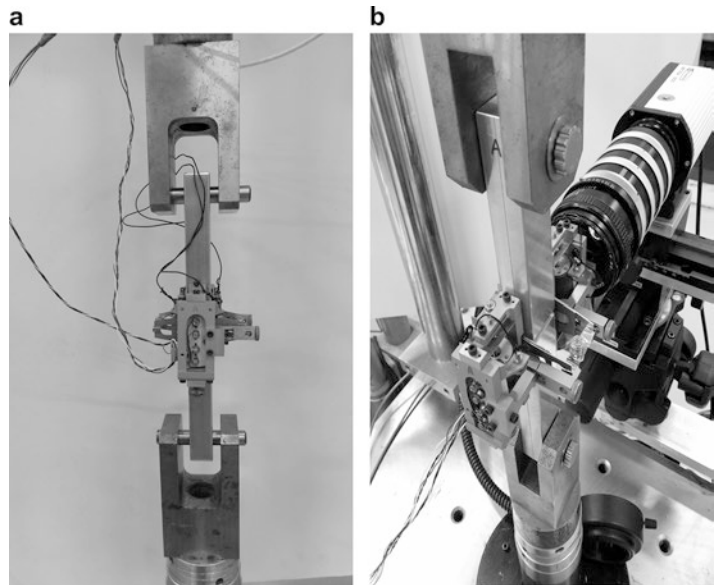


Fig. 9.2 Experimental setup for (a) KGR-1 and (b) DIC with KGR-1 in place to show stand-off distance



subset pixel intensities. The 2D DIC camera system consisted of a 1.3 M pixel QImaging Retiga 1300i CCD monochrome video camera, outfitted with a Canon 50 mm macro zoom lens with three extension tubes. The system had a field of view of approximately $6.5 \text{ mm} \times 5.5 \text{ mm}$ with a corresponding spatial resolution of $5.30 \text{ } \mu\text{m}/\text{pixel}$ (189 pixels/mm). The camera was mounted on a set of high precision vernier cross-stages and fixed to a tripod head. The entire assembly was fixed to a custom frame, supported on the upright supports of the load frame, as shown in Fig. 9.2b. The tripod enabled three degrees of freedom for the camera orientation, with fine focal adjustments achieved via the linear vernier stages.

A ring light was mounted on the lens to uniformly illuminate the bonded overlap region. Images of the gauge region and synchronized recordings of applied load and displacement from the load frame were acquired using the VicSnap software (v. 2010) from Correlated Solutions Inc. The image processing and data extractions were performed via post-processing with Vic2D (v. 2009 1.0) from Correlated Solutions Inc. The strain and displacement resolution was estimated using a series of correlated images of the stationary specimen surface under no applied load. The corresponding maximum strain and maximum displacement provides an indication of the level of Gaussian camera noise, lighting noise, and lack of contrast or focus. For the current setup, the strain and displacement noise levels did not exceed 100 microstrain and $35 \text{ } \mu\text{m}$, respectively. For the purposes of this comparative study, image correlation was only performed on the port side of the specimens, rather than both sides, as was done with the KGR-1 extensometer system.

2.3 Manufacturing

Eighteen single-lap shear joints were prepared from two sets of two 254 mm × 305 mm × 9.5 mm (10 in. × 12 in. × 0.375 in.) MIC-6 aluminum plates bonded together with AF 163-2K-0.06 epoxy film adhesive. Plate flatness was determined to be within 0.025 mm (0.001 in.) as measured with a dial gauge prior to bonding. The plates were prepared by cleaning with Methyl-Ethyl-Keytone followed by grit blasting, and a surface pre-treatment with Sol-gel AC130-2. The bond line thickness was regulated using four 0.203 mm (0.008 in.) spacer wires. The panels were vacuum bagged and cured in an autoclave according to the adhesive suppliers' suggested cure cycle (100 min at 121 °C (250 °F) and 674 kPa (83 psig) with a temperature ramp rate of 1 °C (3.5 °F) per minute). The bond line temperature was monitored by embedding a thermocouple at the plate-to-edge dam interface. An ultrasonic C-scan was performed on each bonded plate to verify acceptable bond quality and uniformity. One bonded plate was labeled 'J' and the other 'K'. The specimens were rough cut from the bonded plates and finished to the dimensions specified by ASTM D5656 [1] (25.4 mm in width and 228.6 mm in length) with an end mill. The notches were cut with a slitting saw; however, the adhesive was not removed from the notches to avoid any possibility of damaging the bond line at the ends of the gauge region. Only 17 specimens were tested as one was damaged during manufacturing. Prior to tests utilizing either of the DIC techniques, the port side of the gauge region was lightly abraded to generate a random surface texture.

Bond line metrology was performed using an optical microscope and an in-house program which extracted the coordinates of the microscope crosshairs. A calibrated stage was used to align the specimen bond line with the microscope crosshairs and the bond line thickness was manually calculated using extracted coordinates from each side of the bond line. The overall bond line thickness was calculated using an average of five measurements, equally spaced along the overlap. All of the specimens were measured to have the same bond line thickness on either side to within 0.013 mm (0.0005 in.). For the KGR-1 extensometers, strain was calculated using the average bond line thickness between both sides of the specimen, whereas DIC strains were calculated using the bond line thickness measured on the port side of each specimen.

2.4 Testing

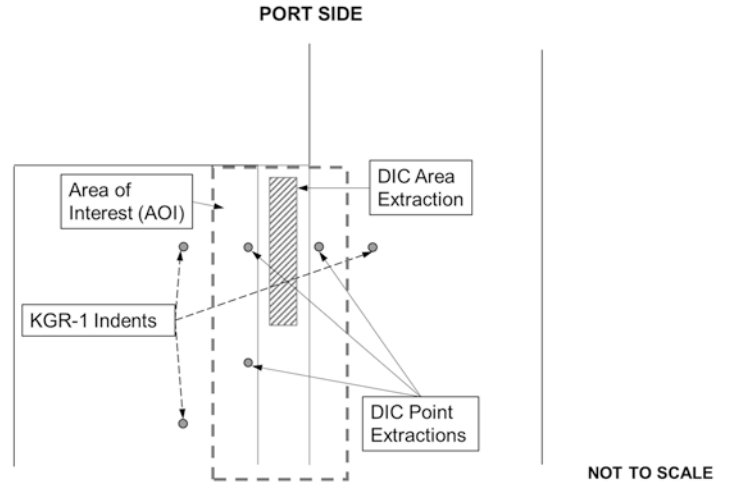
Since simultaneous measurements with the KGR-1 extensometers and DIC was not possible, an alternative testing approach was developed, with measurements taken with DIC and the KGR-1 on the same specimen, in separate loading sequences up to 4482 N (1000 lbf) (within adhesive linear range). This permits direct comparisons of the measured shear modulus between the techniques. Following these measurements, and without removing the specimen from the load frame, each specimen was loaded to failure. Randomly selected specimens were allocated to the DIC (n=8) and to the KGR-1 (n=9) systems, respectively for tests to failure.

3 Data Processing

The images, along with the file containing synchronized analog outputs from the test frame's load and displacement sensors, were uploaded into the Vic2D software. A reference image was captured with the specimen subjected to a small tensile load of 222 N (50 lbf) to ensure proper self-alignment of the universal joint and the bushings within the mounting holes. The Vic2D software correlates the deformed images to the reference image within a user-defined Area of Interest (AOI). The selected AOI enclosed the entire bond line within the available field of view, and outwards on the adherends to the locations of the KGR-1 mounting pin indents (Fig. 9.3). The images were processed using a correlation algorithm based upon the normalized squared differences criterion, with sub-pixel interpolations performed using an optimized eight-tap spline; the most efficient interpolation method in terms of minimizing Gaussian noise [22]. To achieve maximum strain and displacement resolution, a smoothing window of 5 pixels (step=1 pixel, filter=5) or 27 μm was selected. During large plastic deformations, the image correlation algorithm could not correlate the deformed images to the reference image. Therefore, beyond the onset of plasticity incremental correlation was applied, which correlates each successive image with the previous image.

Two data extraction techniques were explored for the DIC measurements. The first used three small area extractions of adherend displacement (here forth referred to as 'point' extractions), in the same general arrangement as the KGR-1 mounting pins, but much closer to the bond line, and the second technique utilized a shear-strain extraction directly from the bond line (see Fig. 9.3). Adherend displacement was extracted from a small area, rather than a point, to minimize measurement noise. For consistent DIC displacement extractions, in line with the KGR-1 mounting pins, the KGR-1 was mounted on the speci-

Fig. 9.3 Locations of DIC data extractions on the port side of a TAST specimen



men prior to DIC measurements to indent the adherends. A custom mounting fixture was used to place the KGR-1 mounting pins in the same position on each specimen to within 0.5 mm. The two upper DIC points were taken in-line with the upper KGR-1 indents with each extraction centered 50 pixels (265 μm) away from the bond line. The bond line area extraction covered the centerline of the bond and was positioned such that it extended equal distances on either side of the upper KGR-1 indents (Fig. 9.3). The area extraction did not extend to the edge of the overlap to avoid bias from the strain concentration.

The ability to place the DIC data extraction points closer to the bond interface than the KGR-1 mounting pins greatly reduced the influence of adherend deformation on the measured relative displacements. To simplify the analysis, corrections for adherend deformation were neglected for DIC measurements as they were estimated to account for a mere 0.3% of the shear strain at 4482 N (1000 lbf).

3.1 Correcting DIC Displacement Measurements for Rigid Body Rotation

Although the TAST specimen is designed to mitigate adherend bending effects and thus, gauge region rotation, this cannot be completely eliminated due to the inherent loading eccentricity across the bond line. The three contact points force the extensometers to rotate with the specimen and resolve only relative shear displacements in a local reference frame, whereas DIC measures deformation of the specimen in a global reference frame. Therefore, DIC-measured displacements capture aggregate motion of rigid body rotation and relative shear displacement (Fig. 9.4a), with rigid body rotation increasing with increasing tensile load. In much of the same way as the KGR-1 mounting pins, three extractions of displacement allow one to resolve the rigid-body rotation, effectively characterizing the transformation between an equivalent local reference frame and the global reference frame. This process will be described next.

Let the original position of the three points be denoted l_0, r_0 and b_0 . As the specimen deforms, the gauge region rotates by an angle θ and the extraction points move to their respective deformed positions denoted as l', r', b' . This motion is captured through displacements in the x-direction (u_r, u_l, u_b) and y-direction (v_l, v_r, v_b). Embedded in this motion is relative shear displacements, which when added to the rotation, results in the final deformed positions at l'', r'', b'' . Therefore, with the relative orientation of the points known, the reference frame rotation angle can be calculated for each image using Eq. (9.1).

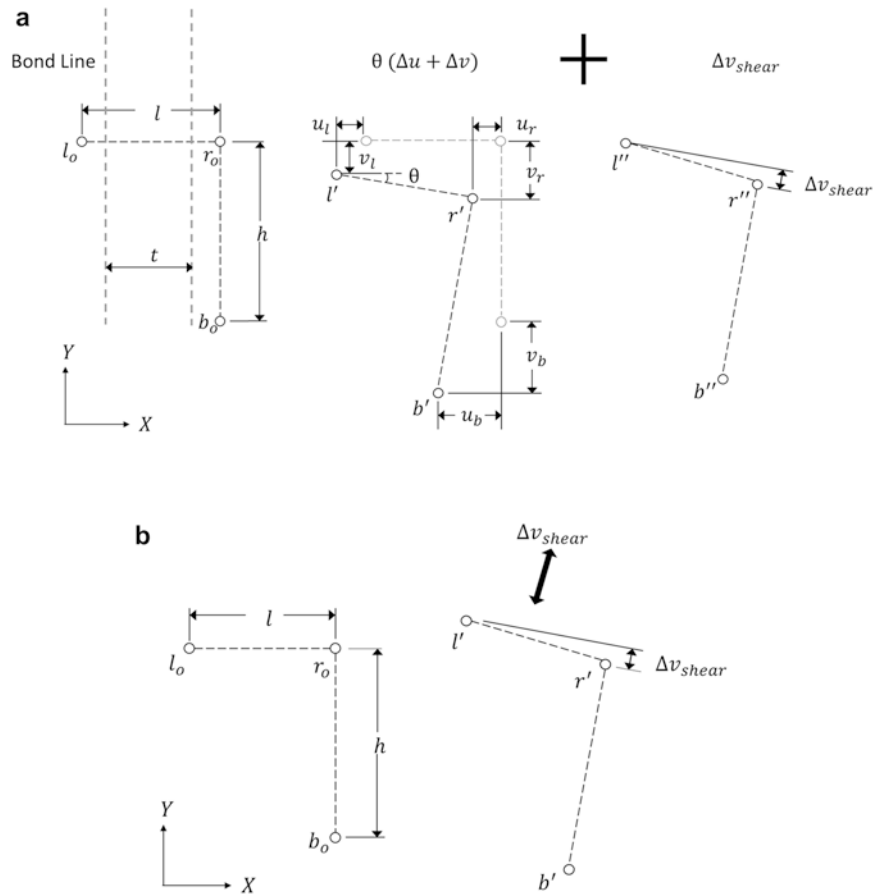
$$\theta = \tan^{-1}(u_b - u_r / h) \quad (9.1)$$

Neglecting relative displacements in the x-direction between point l and r , the relative shear displacement (Δv) can then be found by transforming the deformed coordinate frame back to the reference orientation. This is equivalent to subtracting the vertical displacement due to pure rotation from the relative vertical displacements between the two points spanning the bond line, as measured by DIC (Δv_{DIC}) (Eq. (9.2)). The resulting relative displacement is that caused by pure shear deformation in the adhesive (Eq. (9.3)).

$$v_{DIC} = v_r - v_l \quad (9.2)$$

$$v_{resultant} = v_{DIC} - l \tan \theta \quad (9.3)$$

Fig. 9.4 Effect of reference frame on measurements of relative shear displacements using (a) a DIC global frame, consisting of rigid body rotation and shear deformation and, (b) the KGR-1 in a body-fixed frame of reference which measures only relative shear deformations



Shear strain is then calculated by dividing $\Delta v_{resultant}$ by the bond line thickness, t . This correction was not required for the strain measurements directly from the bond line as the Vic 2D software accounts for rigid-body motion between subsets. The KGR-1 data was corrected for adherend deformation using measurements from the solid ‘dummy’ specimen, as per ASTM D5656 [1]. The *in situ* shear stress–shear strain curves and mechanical properties were then computed for all data sets using the graphical process outlined in ASTM D5656 [1].

4 Results

4.1 Shear Stress–Shear Strain Curves

The upper and lower bounds of all shear stress–strain curves measured with the KGR-1 system, DIC three point extractions of adherend displacement, and DIC area extractions of bond line strains, are shown in Fig. 9.5a–c, respectively, with a comparison of the three measurement methods shown in Fig. 9.5d.

4.2 Statistical Testing

A statistical analysis (student’s T -test) was performed to detect significant differences in average measured mechanical properties on a per-plate, and overall (or ‘aggregate’) basis. The average mechanical properties, \bar{x} , and standard deviation, σ , along with results from the statistical analysis are detailed in Table 9.1. In Table 9.1, ‘SD’ and ‘NSD’, denote that a significant difference between techniques exists, or does not exist, respectively. Furthermore, ‘DIC-P’ denotes the DIC technique using three extractions of adherend displacement, and ‘DIC-A’ denotes DIC area extractions of strain from the bond line.

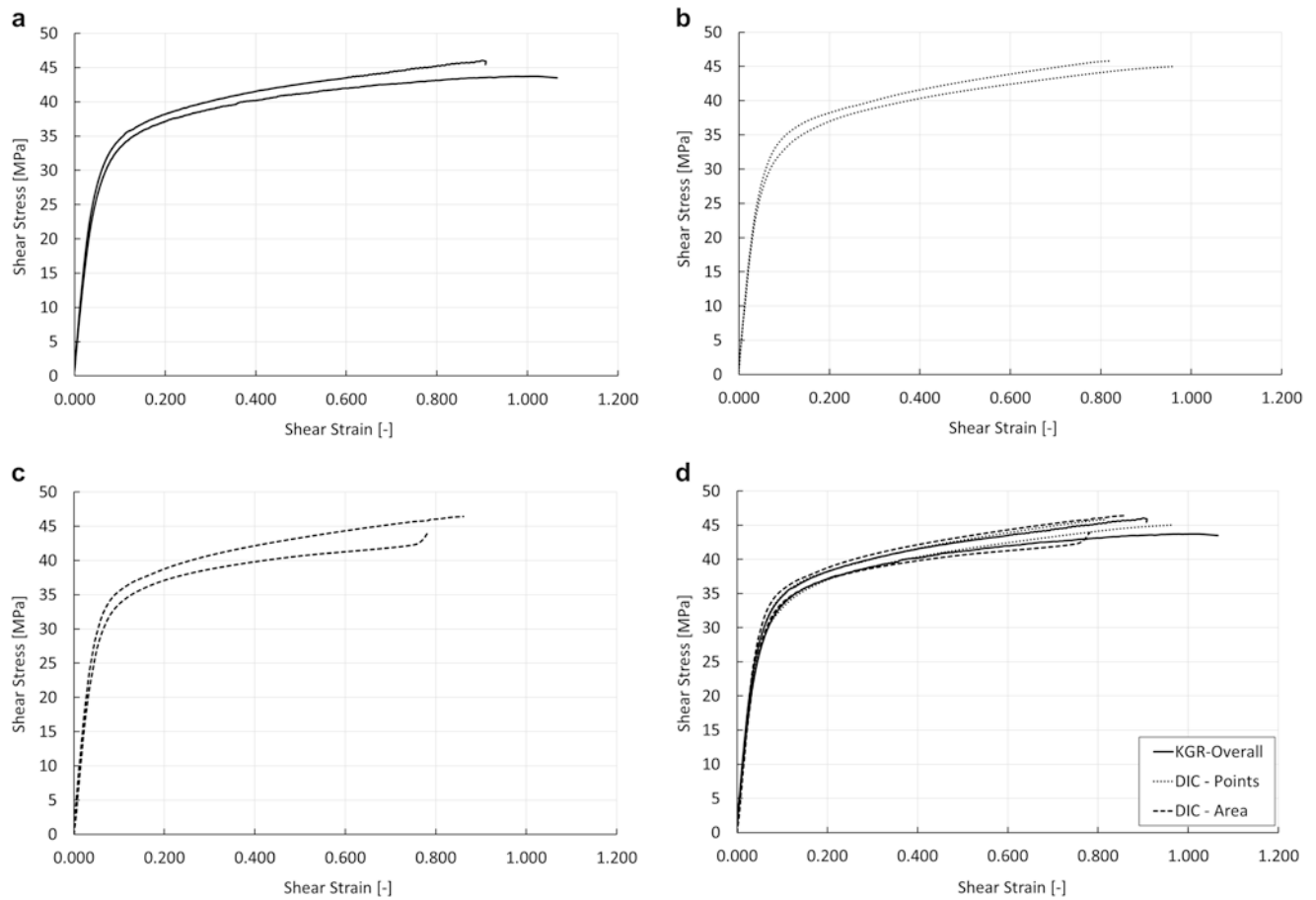


Fig. 9.5 Upper and lower bound shear stress-shear strain curves for AF 163-2K film adhesive measured using: (a) the KGR-1 extensometers, (b) DIC-measured displacements on the adherends, (c) DIC-measured strains extracted directly from the bond line, and (d) an overall comparison of three methods

Table 9.1 Statistical significance testing for differences in average measured properties between the KGR-1 and DIC data sets

Mech. property		Shear modulus, MPa	Prop. limit stress, MPa	Prop. limit strain	Knee stress, MPa	Knee strain	Ultimate strain
<i>Plate J</i>							
KGR-1	$\bar{x}(\sigma)$	696.8 (35.4)	11.5 (2.6)	0.014 (0.004)	35.5 (0.5)	0.147 (0.008)	0.998 (0.066)
DIC-P	$\bar{x}(\sigma)$	669.6 (7.7)	17.3 (1.2)	0.024 (0.001)	35.4 (0.2)	0.124 (0.013)	0.888 (0.043)
DIC-A	$\bar{x}(\sigma)$	720.0 (12.5)	16.5 (0.6)	0.022 (0.003)	35.1 (1.3)	0.115 (0.013)	0.840 (0.052)
KGR-1 vs. DIC-P		NSD	SD	SD	NSD	SD	NSD
KGR-1 vs. DIC-A		NSD	SD	SD	NSD	SD	NSD
DIC-P vs. DIC-A		SD	NSD	NSD	NSD	NSD	NSD
<i>Plate K</i>							
KGR-1	$\bar{x}(\sigma)$	685.4 (90.7)	13.9 (2.1)	0.018 (0.005)	35.6 (0.3)	0.140 (0.015)	1.021 (0.075)
DIC-P	$\bar{x}(\sigma)$	653.6 (21.1)	17.2 (0.7)	0.024 (0.001)	35.4 (0.5)	0.127 (0.012)	0.925 (0.061)
DIC-A	$\bar{x}(\sigma)$	713.7 (22.7)	16.8 (1.0)	0.023 (0.001)	35.4 (0.6)	0.110 (0.003)	0.842 (0.054)
KGR-1 vs. DIC-P		NSD	SD	NSD	NSD	NSD	NSD
KGR-1 vs. DIC-A		NSD	SD	SD	NSD	SD	SD
DIC-P vs. DIC-A		SD	NSD	NSD	NSD	SD	NSD

(continued)

Table 9.1 (continued)

Mech. property		Shear modulus, MPa	Prop. limit stress, MPa	Prop. limit strain	Knee stress, MPa	Knee strain	Ultimate strain
<i>Aggregate</i>							
KGR-1	$\bar{x}(\sigma)$	690.8 (68.5)	12.6 (2.6)	0.016 (0.005)	35.5 (0.4)	0.144 (0.011)	1.008 (0.067)
DIC-P	$\bar{x}(\sigma)$	661.1 (22.9)	17.2 (0.8)	0.024 (0.001)	35.4 (0.4)	0.126 (0.011)	0.911 (0.055)
DIC-A	$\bar{x}(\sigma)$	716.7 (29.8)	16.7 (0.8)	0.023 (0.002)	35.3 (0.8)	0.112 (0.007)	0.842 (0.050)
KGR-1 vs. DIC-P		NSD	SD	SD	NSD	SD	SD
KGR-1 vs. DIC-A		NSD	SD	SD	NSD	SD	SD
DIC-P vs. DIC-A		SD	SD	NSD	NSD	SD	SD

5 Discussion

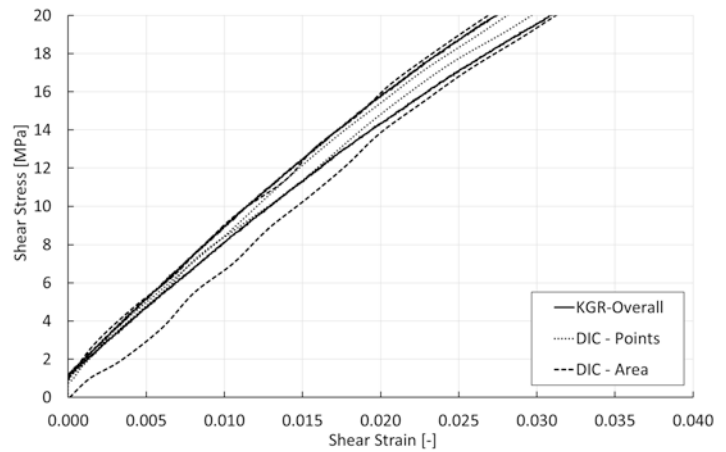
Despite having a small sample size, several useful observations were made from the comparisons between DIC and the KGR-1 regarding the influence of instrumentation on the degree of data scatter and mechanical properties derived from the measured adhesive response.

Generally speaking, the shear stress–strain curves obtained with the KGR-1 system and DIC, shown in Fig. 9.5, are in excellent agreement and have low scatter. With this experimental test, some scatter can always be expected due to the inherent variability in the epoxy adhesive, degree of cure within the bond, bond line thickness between specimens, residual stresses within the specimens, and defects within the bond line [23]. However, any biases imposed by these variations were mitigated through random assignment of the specimens and repeated measurements of the shear modulus with different measurement techniques on each specimen. DIC measurements have lower variance compared the KGR-1 measurements for all mechanical properties, with exception to knee stress and knee strain. In the case of the shear modulus, the aggregate statistics show that the variance associated with the KGR-1 is up to 300% greater than DIC. This may be caused by progressive pin slippage or rotation, which was observed in almost all post-test inspections. The significant difference detected for measured knee strain, and proportional limit stress and strain between all techniques suggests that the shape of the stress–strain curve may have an appreciable dependence on strain measurement technique.

A closer examination of the elastic region (Fig. 9.6) shows that, in addition to measuring lower strains, the DIC-area extractions had higher noise levels compared to the point extractions of adherend displacement. This is a result of reduced contrast in the bond line, strain resolution limits imposed by system noise (100 microstrain) and spatial resolution within the bond line. The issue of spatial resolution, within and along the bond line, is an inherent compromise when using DIC on this specimen due to the large aspect ratio of the gauge region. The resolution chosen for this work (5.30 $\mu\text{m}/\text{pixel}$) was such that one half of the overlap region was captured, from which strain extractions were likely to be more representative of the average response of the whole overlap, compared to a setup with higher resolution across the bond line. Further studies are required to investigate the sensitivity to spatial resolution within the bond line. A separate test with a high contrast, fine speckle pattern applied to the surface resulted in a slight reduction in measurement noise, but had no appreciable effect on measured mechanical properties. The strains resolved using the DIC point extraction technique were not affected by the speckle pattern. The minimal improvements from the speckle pattern do not justify the time required to paint each specimen, especially in the context of adhesive characterization for certification due to the extensive amount of testing required. However, this requires further study before definitive claims regarding the effects of surface contrast can be made.

With increasing shear strain, all techniques show larger scatter, likely due to inter-specimen variations (varying bond line thickness, bond line imperfections, etc.). The KGR-1 measured slightly higher ultimate strains compared to either DIC technique, however the validity of these ultimate strains was brought into question as post-test inspection showed substantial pin slippage on four of the nine specimens tested to failure. Similar issues were encountered when collecting data from the dummy specimen, as 16 tests were required to capture 10 quality data sets. The ultimate shear strains measured within the bond line were consistently lower due to large relative displacements within the bond line, which caused problems for the correlation algorithm. This problem was first observed just beyond the onset of plasticity, and incremental correlation of images was required to capture the response. However, near failure the surface features changed so drastically that correlation was not possible. The omission of these regions of large deformation from the average shear strain measurement, causes the strain attenuation. This issue was not resolved using a speckled pattern as the paint did not adhere well to the surface under such large plastic deformations.

Fig. 9.6 Comparison of the bounds on the initial linear response region as measured using KGR-1 and DIC techniques



The KGR-1 does offer some advantages over DIC, especially in regards to measuring material allowables in less favourable environmental conditions. Adhesives prescribed for aerospace applications must be capable of sustaining ultimate design loads in the most adverse conditions, i.e. hot and wet environments. The KGR-1 can be mounted to the specimen in an environmental chamber, whereas these tests become far more difficult with DIC as the cameras may require specialized enclosures and heating can cause mirage effects and artificial strains. Further, the onset of poor quality data (i.e. due to pin slippage) is typically easier to detect with the KGR-1 by comparing the output voltages from the two extensometers. The results also suggest that the adherend correction from the dummy specimen, the validity of which has disputed in the literature [6, 7], should not necessarily be discredited as the KGR-1 measurements are in good agreement with DIC. This is surprising given the inherent assumption that the adherend deformation is insensitive to adhesive compliance and bond line thickness. That said, any errors in this correction are difficult to resolve with the current data set since the true mechanical properties for a given specimen are not known.

This study has shown that the most reliable and repeatable DIC technique is that which uses measured deformations in the adherends adjacent to the bond line. The lower relative adherend displacements are optimal for correlation right up to failure and the rotation correction is simple to apply. Further, the ability to perform correlations on the bare specimen surface offers significant time savings. Additional time savings are offered in pre-test setup time as the KGR-1 requires consistent recalibration to ensure that the shock loading at failure does not create bias or error in subsequent measurements. Frequent pin slippage can also double or triple specimen testing times [24]. The post-processing time was slightly higher for DIC as the image correlation routine had to be first performed before extracting the data, however this expense could be mitigated with the use of more powerful computing resources. As a final point, an additional advantage of DIC is the availability of formalized calibration procedures, such as that developed by Patterson et al. [25], whereas no such procedures exist for the KGR-1 extensometers.

6 Conclusions

From this study of 17 thick adherend shear tests, it was found that DIC measurements, using both adherend point displacements adjacent to the bond line, and direct strain extractions from the bond line, were in good agreement with the KGR-1 measurements. However, material properties measured using DIC measurements had up to 300% lower variance than those from the KGR-1, and the failure strains recorded by the KGR-1 system were brought into question due to frequent pin slippage at large plastic strains.

Correlating images based solely on surface texture was found to be a viable technique for strain measurement. Of the two DIC techniques trialed, the most reliable technique in this study was that using DIC-measured relative adherend displacements (three-point technique), since the adherends undergo much smaller and more controlled relative displacement, and can be reliably correlated right up to failure. DIC also offers significant time savings in pre-test setup and regular calibrations. The statistical analysis performed on the KGR-1 and DIC measurements found significant differences in the knee strain, and proportional limit stress and strain values, suggesting that the shape of the shear stress-shear strain curve may have an appreciable dependence on measurement technique.

Future work includes further testing to develop a larger statistical data base to compare DIC to the KGR-1 extensometers, and detailed studies on the sensitivity of material properties to the location of data extraction and spatial resolution within the bond line.

Acknowledgement The technical support of Richard Desnoyers and Matthieu Harrison of NRC-Aerospace and Dr. Steven Philips of McGill University are gratefully acknowledged.

References

1. ASTM D5656-10: Standard Test Method for Thick-Adherend Metal Lap-Shear Joints for Determination of the Stress-Strain Behaviour of Adhesives in Shear by Tension Loading. ASTM International, West Conshohocken (2010). doi:10.1520/D5656-10. <http://www.astm.org>
2. ASTM D1002-10: Standard Test Method for Apparent Shear Strength of Single-Lap-Joint Adhesively Bonded Metal Specimens by Tension Loading (Metal-to-Metal). ASTM International, West Conshohocken (2010). doi:10.1520/D1002-10. <http://www.astm.org>
3. ASTM D3165-07: Standard Test Method for Strength Properties of Adhesives in Shear by Tension Loading of Single-Lap-Joint Laminated Assemblies. ASTM International, West Conshohocken (2007). doi:10.1520/D3165-07. <http://www.astm.org>
4. Tomblin, J.S., Yang, C., Harter, P.: Investigation of thick bondline adhesive joints. U.S. Department of Transportation Federal Aviation Administration, Report: DOT/FAA/AR-01/33 (2001)
5. Vijaya Kumar, R.L., Bhat, M.R., Murthy, C.R.L.: Experimental analysis of composite single-lap joints using digital image correlation and comparison with theoretical models. *J. Reinf. Plast. Compos.* **32**(23), 1858–1876 (2013)
6. Kassapogluo, C., Adelman, J.: KGR-1 thick adherend specimen evaluation for the determination of adhesive mechanical properties. In: 23rd International SAMPE Technical Conference, Society for the Advancement of Material and Process Engineering, pp. 162–176 (1991)
7. Yang, C., Huang, H., Tomblin, J.S., Oplinger, D.W.: Evaluation and adjustments for ASTM D5656 standard test method for thick-adherend metal lap-shear joints for determination of the stress-strain behaviour of adhesives in shear by tension loading. *J. Test. Eval.* **29**(1), 36–43 (2001)
8. Tsai, M.Y., Morton, J., Krieger, R.B., Oplinger, D.W.: Experimental investigation of the thick-adherend lap shear test. *J. Adv. Mater.* **27**(3), 28–36 (1996)
9. Tomblin, J.S., Seneviratne, W., Escobar, P., Yoon-Khian, Y.: Shear stress-strain data for structural adhesives. U.S. Department of Transportation Federal Aviation Administration, Report: DOT/FAA/AR-02/97 (2002)
10. da Silva, L.F.M., da Silva, R.A.M., Chousal, J.A.G., Pinto, A.M.G.: Alternative methods to measure the adhesive shear displacement in the thick adherend shear test. *J. Adhes. Sci. Technol.* **22**(1), 15–29 (2008)
11. da Silva, L.F.M., Adams, R.D.: Measurement of the mechanical properties of structural adhesives in tension and shear over a wide range of temperatures. *J. Adhes. Sci. Technol.* **19**(2), 109–141 (2005)
12. Tsai, M.Y., Morton, J., Oplinger, D.W.: In situ determination of adhesive shear moduli using strain gages. *Exp. Mech.* **36**(4), 297–304 (1996)
13. Lemmen, H.J.K., Alderliesten, R.C., Benedictus, R., Hofstede, J.C.J., Rodi, R.: The power of Digital Image Correlation for detailed elastic-plastic strain measurements. In: WSEAS International Conference on Engineering Mechanics, Structures, Engineering Geology, Creta, 22–24 July 2008
14. Nunes, L.C.S.: Shear modulus estimation of the polymer polydimethylsiloxane (PDMS) using digital image correlation. *Mater. Des.* **31**(1), 583–588 (2009)
15. Comer, A.J., Katnam, K.B., Stanley, W.F., Young, T.M.: Characterising the behaviour of composite single lap bonded joints using digital image correlation. *Int. J. Adhes. Adhes.* **40**, 215–223 (2013)
16. Moutrille, M.P., Derrien, K., Baptiste, D., Balandraud, X., Grediac, M.: Through-thickness strain field measurement in a composite/aluminum adhesive joint. *Compos. Part A* **40**(8), 985–996 (2008)
17. Adams, R.D., Wake, W.C.: *Structural Adhesive Joints in Engineering*. Elsevier Applied Science, New York (1984)
18. Colavito, K.W., Gorman, J., Madenci, E.: Refinements in digital image correlation technique to extract adhesive strains in lap joints. In: Proceedings of the 50th AIAA/ASME/ASCE/AHS/ASC Structures, Structural Dynamics, and Materials Conference, American Institute of Aeronautics and Astronautics, Palm Springs, 4–7 May 2009
19. Cognard, J.Y., Davies, P., Sohler, L.: Design and evaluation of bonded composite assemblies. In: European Congress of Computational Methods in Applied Sciences and Engineering (ECCOMAS), Jyväskylä, 24–28 July 2004
20. Wang, Z.Y., Wang, L., Guo, W., Deng, H., Tong, J.W., Aymerich, F.: An investigation on strain/stress distribution around the overlap end of laminated composite single-lap joints. *Compos. Struct.* **89**(4), 589–595 (2008)
21. Cytec Engineered Materials, Extensometer Operating Manual (2000)
22. Sutton, M., Orteu, J., Schreier, H.: *Image Correlation for Shape, Motion and Deformation Measurements*. Springer, New York (2009)
23. Baker, A., Dutton, S., Kelly, D.: *Composite Materials for Aircraft Structures*, 2nd Edition. AIAA Education Series (2004). ISBN 978-1-56347-540-5
24. Seneviratne, W.P., Tomblin, J.S.: Adhesive characterization using NIAR-modified KGR extensometer. *Soc. Adv. Mater. Process Eng.* **47**(5), 37–44 (2011)
25. Patterson, E.A., Hack, E., Brailly, P., Burguete, R., Saleem, Q., Siebert, T., Tomlinson, R., Whelan, M.: Calibration and evaluation of optical systems for full-field strain measurement. *Opt. Laser Eng.* **45**, 550–564 (2007)

Chapter 10

Interfacial Strength of Thin Film Measurement by Laser-Spallation

Leila Seyed Faraji, Dale Teeters, and Michel W. Keller

Abstract Improving adhesion properties and strength of thin films used in wide range of important application is the key factor in successfully manufacturing micro-electro-mechanical devices, multilayer micro-electronic and optical devices. Mechanical performance and reliability of thin film on a substrate depends on strength of interfacial adhesion. Understanding the role of process parameters like deposition condition and design parameters such as substrate thickness and film thickness, on mechanical performance of the layer is essential in optimizing manufacturing. However, there are limited techniques for characterizing intrinsic interfacial strength of thin films. The use of laser-generated stress pulses has shown the ability to provide quantitative evaluation of the adhesion strength of thin films. In the current work, we use the laser-spallation approach for the investigation of the adhesion strength of thin tin oxide films to alumina substrates.

Keywords Laser-spallation • Interfacial strength • Aluminum thin film • Tin oxide thin film • X-ray diffraction

10.1 Introduction

The mechanical strength of thin films used in electronic component such as electrodes for batteries, solar cells, or batteries is dependent on many factors. Critical issues include deposition technique and the chemical and electrical environment in which the films exist. Probing the mechanical strength of thin films and their interfaces is challenging and frequently requires complex micromachining and processing to produce samples. In order to reduce the time required for iterative designs that may eventually result in an acceptable structure, fundamental investigations of the thin film properties and interfaces are essential. These studies are expected to improve the efficiency of the design process and speed the optimization of the thin film process conditions. A critical point in any multi-layer structure is the interface region between two dissimilar materials. This interface is commonly a location for mechanical stress concentration, which can lead to failure of the interface and eventually the device [1, 2]. Due to lattice mismatch or thermal expansion differences between the layers, there are also residual stresses at interface. Depending on the magnitude and sign of the residual stress at the interface, this location may become a preferred site of the film debonding. Many approaches have been adopted to probe these interfaces, such as scratching by sharp tip [3, 4], AFM nano indentation [5], and laser spallation [6, 7]. All mentioned interfacial strength measurement methods are destructive tests. For example in scratching method, spalling and buckling failure modes occur as a result of the compressive stress field preceding the moving tip scratching the surface [8]. There are many other failure modes of films that depend on the measurement method. Debonding, spallation, cracking, channeling are some of these failure modes that could be used for attachment strength of a film [9].

One application for this technique is in the understanding of adhesion in solid state battery systems. There is high demand for advanced rechargeable lithium-ion batteries with high energy densities, small dimensions and ultra-light weight for portable electronic devices. Fabrication of small-scale solid state batteries requires optimization of fabrication method, microstructure, crystal structure and electrochemical properties of both anode and cathode thin films. The interfaces in a solid state battery system consisting of the current collector/anode/solid electrolyte/cathode/current collector system are all susceptible to severe stress during charge/discharge cycles. One promising anode material for these batteries is tin oxide, SnO₂ [10, 11].

L.S. Faraji • M.W. Keller (✉)
Department of Mechanical Engineering, The University of Tulsa, Tulsa, OK, USA
e-mail: michael-keller@utulsa.edu

D. Teeters
College of Engineering & Natural Sciences, Chemistry and Biochemistry, The University of Tulsa, Tulsa, OK, USA

SnO_2 has a theoretical capacity of more than twice that of graphite, the commonly used anode material in commercial batteries [12] hence batteries using this material as an anode would have very high energy densities that is very desirable for the heavy demand placed on batteries today. However, when lithium is intercalated into SnO_2 during the charging process, SnO_2 can swell almost 300%, [13, 14] which cause stresses that can debond the attached current collector or separate the anode from a solid electrolyte. Nam et al., reported on enhancing electrochemical properties of thin film tin oxide negative electrodes for lithium batteries [15] and nano-structuring of the SnO_2 anode thin films can help in the management of interfacial stresses [16]. Yet interfacial strength is still an issue and gaining an understanding of interface properties by measuring the adhesion strength at battery interfaces would be invaluable in designing battery systems. Battery electrode systems such as SnO_2 and other electrode materials that have excellent capacities, but adhesion problems could be better understood and processing conditions changed to enhance adhesion mechanisms in these new, high capacity battery systems.

This paper presents the experimental results for spallation of tin oxide layer from Alumina substrate [17]. Back side of the alumina substrate was coated by Aluminum thin film and spalled by laser. After propagation of the pressure pulse throughout the sample thickness, it reaches to the thin layer and either forms the second spallation on tin oxide side or delamination of tin oxide happens. The primary goal of the current work is to optimize the power of the laser to preferentially detach the tin oxide layer instead of bulk substrate spallation. The residual stresses in the heat-affected zone of laser spalled Aluminum layer deposited on alumina are also measured.

10.2 Material and Experimental Setup

10.2.1 SnO_2 Thin Film Deposition

To model a battery anode, a thin film of SnO_2 was coated on surface with an RF magnetron sputter coater. Film thicknesses of approximately 100 nm were deposited. A quartz crystal deposition monitor was used to determine deposition thickness. The sputtering chamber was evacuated and refilled with pure argon gas three times to remove reactive gases. Sputtering plasma was maintained by adjusting the power supply tune and load and maximized power to improve deposition. The substrate was 99.6% purity Alumina with 1 mm \pm 0.05 mm thickness. The Alumina was lapped both sides and was polished to optical degree.

10.2.2 Aluminum Thin Film Back Layer

Aluminum thin films were deposited by a DC off axis magnetron sputtering system (AJA Orion) onto polished alumina substrates. The metallic target (purity 99.99%) was 2 in. in diameter and 0.25 in. thick. The working distance between the cathode and the substrate holder was \sim 100 mm and the base pressure of 5×10^{-6} Torr was achieved by a turbo molecular pump prior to the introduction of argon into the deposition chamber. The final film thickness was measured using a surface profiler (Alpha Step 500). The process parameters for thin film deposition are given in Table 10.1.

10.2.3 Laser Spallation

A 1064 nm wavelength Litron Nano S 130 mJ YAG Pulsed laser with focusing lens was used for laser spallation. The laser produces a Gaussian laser energy pulse with a rise time of 4.4 ns. The peak laser energy could be adjusted between 1 and 130 mJ. A confining layer of waterglass was deposited on an absorbing layer of aluminum as described in [18].

Table 10.1 Process parameters used for Aluminum deposition

	DC power	Process pressure	Ar flow rate	Deposition rate	Final thickness
Al	350 W	3 mT	12 sccm	\sim 8.3 nm/min	500 nm

10.2.4 Thin Film Characterization

The surface topography of the spallation sites were studied by scanning electron microscopy with an FEI Helios Nanolab 600 Scanning Electron-Focused Ion dual-beam microscope (SEM/FIB). Due to the micro-scale diameter sizes (500–900 μm) of the damage, the SEM images were captured at relatively low magnification ($\times 54$) and relatively high ($\sim 10\text{--}14$ mm) working distance. However, the sufficiently high energy of the electron beam, at 5.0 kV accelerating voltage and 43 pA electron beam current, produced very fine, detailed images of the topography of the substrate.

X-ray diffraction was performed a Bruker's D8 Discover XRD² micro-Diffractometer equipped with Pilot software and VANTEC-500 area detector. Tube parameters of 40 kV/40 mA using Cu-K α radiation at the detector distance of 30 cm which covers approximately the area of 20° in 2θ and 20° in γ with 0.02° resolution was used. For sample positioning, a motorized five axis (X, Y, Z (translation), ψ (tilt), ϕ (rotation)) stage was used for positioning which can move the measurement spot to the instrument center within 12.5 μm position accuracy and 5 μm repeatability. A photograph of experimental set up is shown in Fig. 10.1a, b.

Figure 10.2 shows the laser-camera focusing method used for sample alignment. 2D XRD frames from center of spallation sites and the surface that is coated with aluminum were collected using 800 μm pinhole collimator while oscillating the sample 1 mm in both x and y direction. Sample was also rotated during exposure more grains. X-ray exposure time per frame was 120 s.

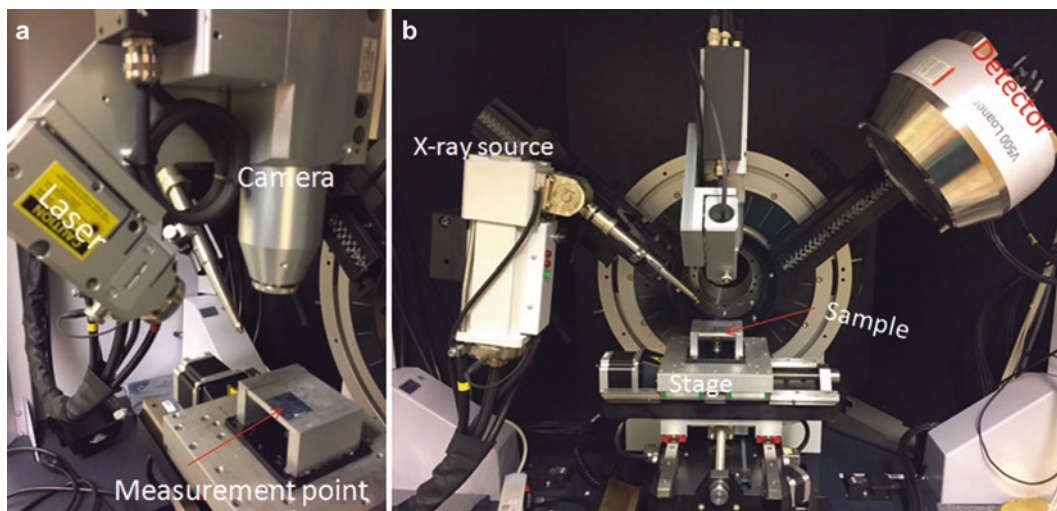
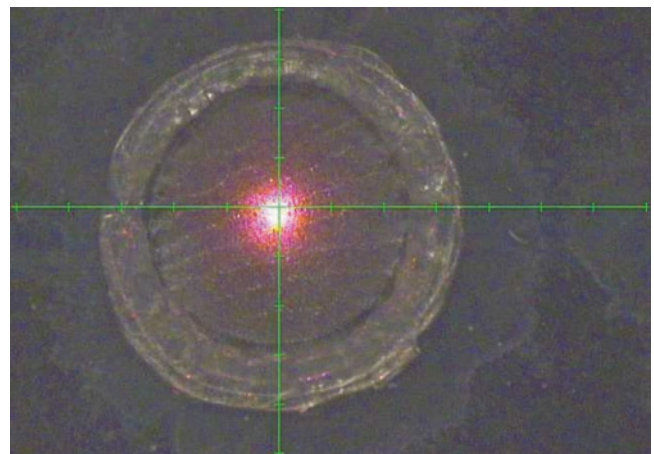


Fig. 10.1 (a) Sample orientation on the XRD stage (b) Photograph of the experimental setup

Fig. 10.2 Top view optical microscopy image of Aluminum sample, superimposed with a target points. Camera cross hair and laser point and X-ray are coincide at measurement points which is the laser spallation site



10.3 Result and Discussion

In laser spallation, a YAG laser pulse is incident on a thin aluminum layer which vaporizes and induces a large localized temperature increase due to the dissipation within the shock front [19]. In practice, spallation happens in very short time and material goes back to ambient in order of approximately a nano second.

Figure 10.3 shows SEM micrograph of spallation point on the Aluminum side for four different laser powers. For 15 and 20 mJ laser energy large circumferential ring cracks were observed around spallation point. When a short and intense laser pulse irradiated on the Aluminum thin film, high pressure plasma is formed on the surface [20]. An elastic-plastic wave propagates through the Alumina substrate and hits the tin oxide layer. This shock wave has created a plastic strains behind on the surface of alumina. Most of the Aluminum layer has been evaporated but very thin layer aluminum left behind is solidified with wave marks on the surface as labeled with arrows on Fig. 10.3b.

The YAG laser beam energy causes the aluminum absorbing layer to vaporize. The thermal expansion of the aluminum causes a compressive stress wave to form that travels longitudinally towards the film/substrate interface. When this compression wave reflects off the free surface of the test film, the wave is reflected back towards the substrate and becomes a tensile wave that loads the film/substrate interface in tension. The tensile stress wave pulls the test film from the substrate. If the tensile stress is stronger than the film/substrate adhesion strength, the film is spalled from the substrate.

In order to determine if spallation occurred at a lower power, the test film spots on SnO₂ were then viewed with a Scanning Electron Microscope as shown in Fig. 10.4. The power increases as we move from top left to bottom right. The lowest power level at which the film spalled is the point at which the test film to substrate adhesion fails. For the current tests we see that at all powers investigated that some substrate spallation occurred for this SnO₂ system. In ongoing studies we are modifying the test specimen to include a metal layer that will simulate the current-collector that is present in these battery systems.

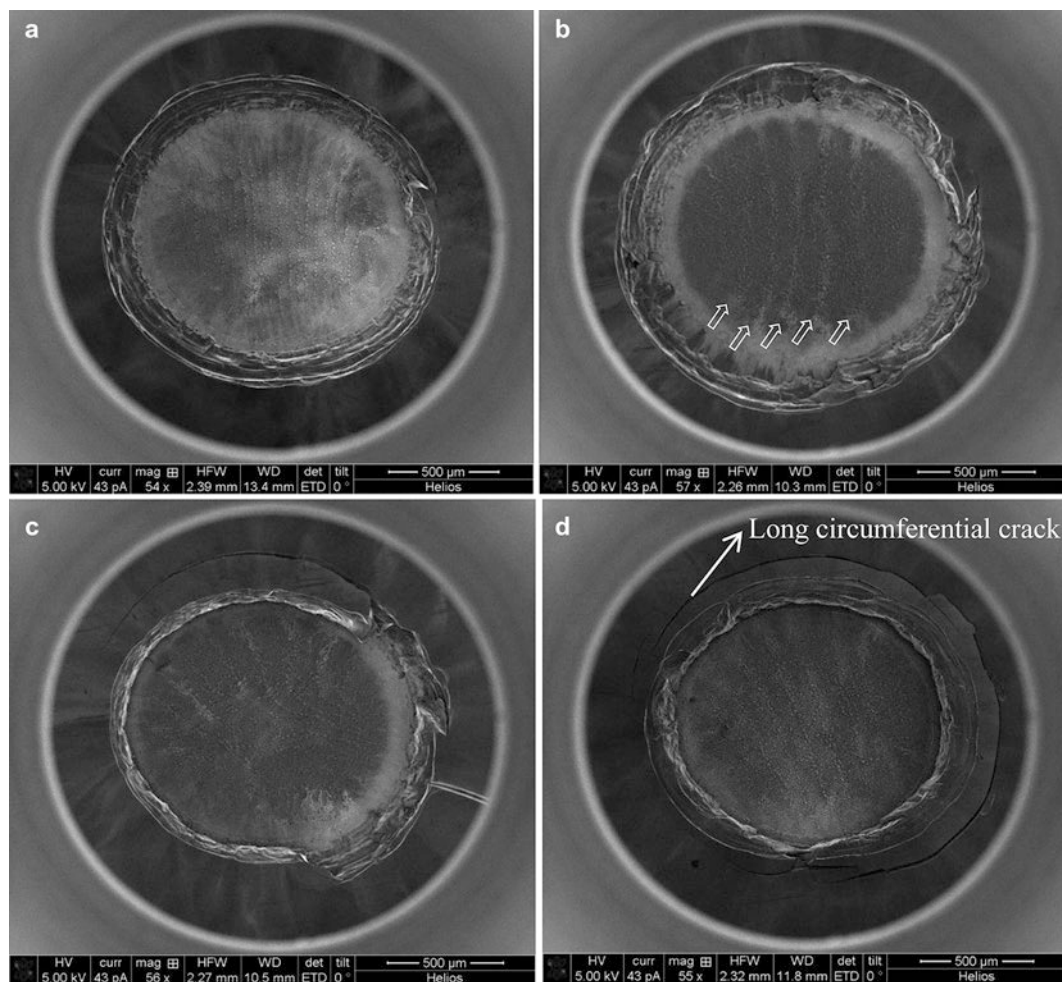


Fig. 10.3 Spalled spot of Aluminum coating from an Alumina Substrate (a) 5 mJ, (b) 10 mJ, (c) 15 mJ, (d) 20 mJ

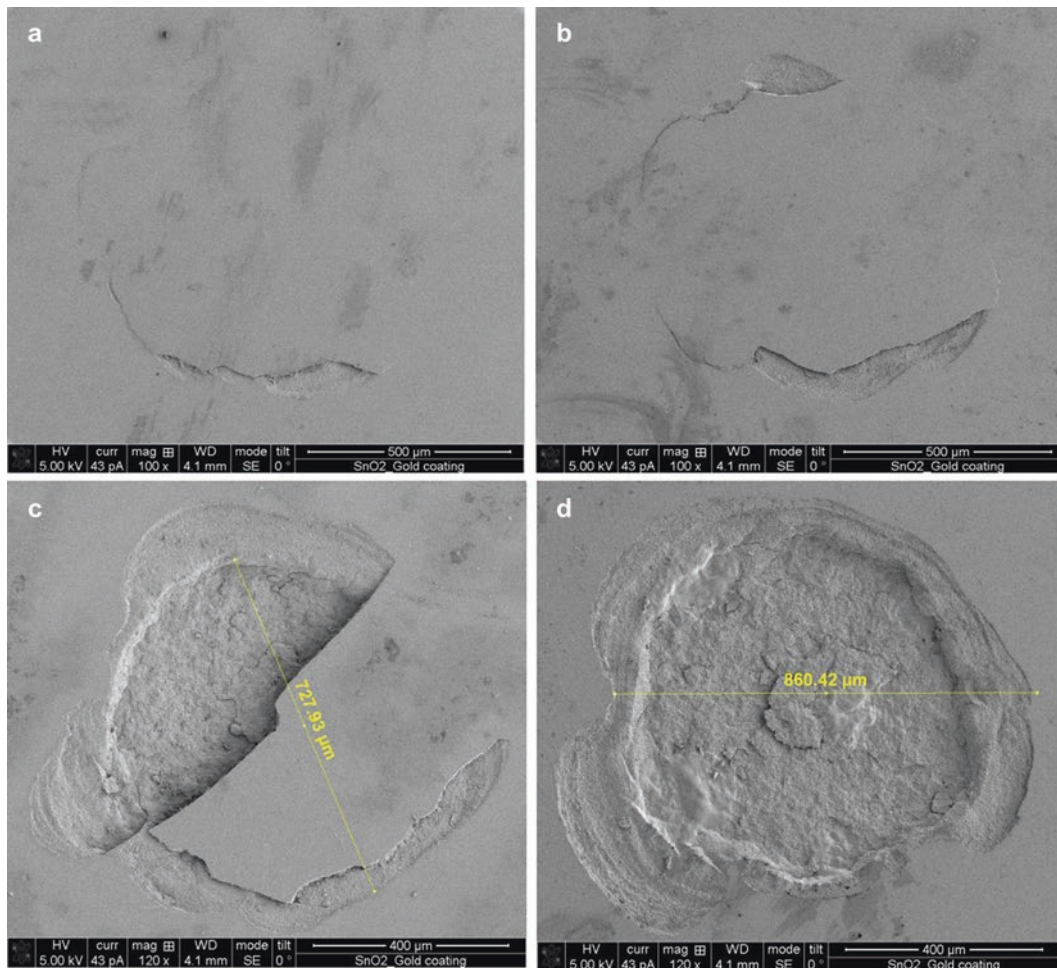


Fig. 10.4 SEM micrograph of delaminated SnO₂ (a) 5 mJ, (b) 10 mJ, (c) 15 mJ, (d) 20 mJ

10.4 Residual Stress Measurement After Laser Spallation Using Two Dimensional μ XRD Data

Laser spallation can generate heterogeneous plastic deformation and microstructure modifications, leading to high residual stresses appearance. $\text{Sin}2\psi$ method was used to measure the residual stress state induced by the laser interaction with surface with Bruker's LEPTOS software [21]. Laser spallation spots on alumina substrate with four different values of the laser intensity 5, 10, 15 and 20 (mJ) were used for X-ray diffraction measurement.

Figure 10.5 shows indexed rings on frames for Alumina substrate only and Aluminum coating on Alumina. Diffraction rings are indexed according to 01-081-2266 PDF card for AL₂O₃ and 03-065-2869 PDF card for Aluminum. The aluminum layer is very thin and while exposing the Aluminum layer, X-ray penetrates all the way through the Aluminum layer and diffracted beam contains information from both Aluminum layer and surface of Alumina substrate. Using low angle incident beam 5° we were able to see aluminum related rings. Aluminum (111), (220) and (311) rings at 38.47, 44.719, and 78.225 and 2 θ degrees respectively are shown in Figs. 10.5 and 10.6.

10.5 Peak Selection for Residual Stress Measurement

Diffraction rings at high 2 θ angles are appropriate for residual stress measurement. There is a larger peak shift $\Delta 2\theta^\circ$, and less effect from sample displacement error for high 2 θ rings. The selected peak for residual stress measurement is better to have sufficient intensity and preferentially not in vicinity of other diffraction peaks. Therefore, the (311) ring could be the best

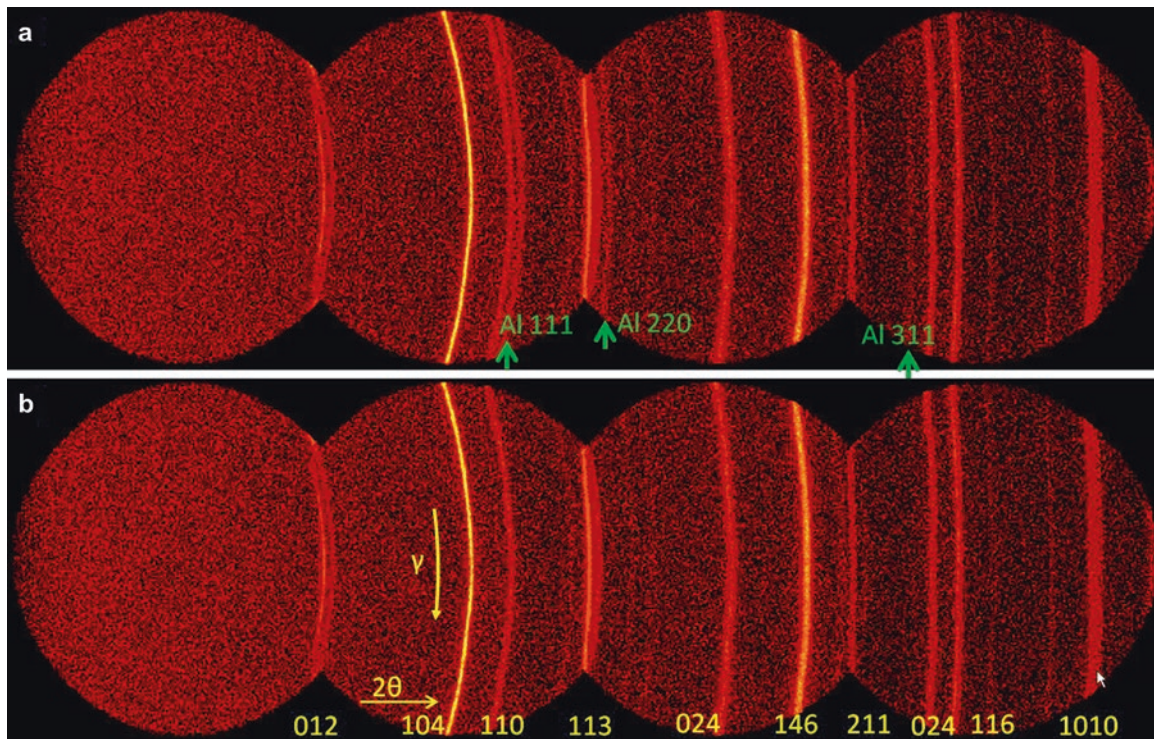


Fig. 10.5 (a) 2D X-ray diffraction pattern of Aluminum coating on Alumina (b) Alumina surface without coating

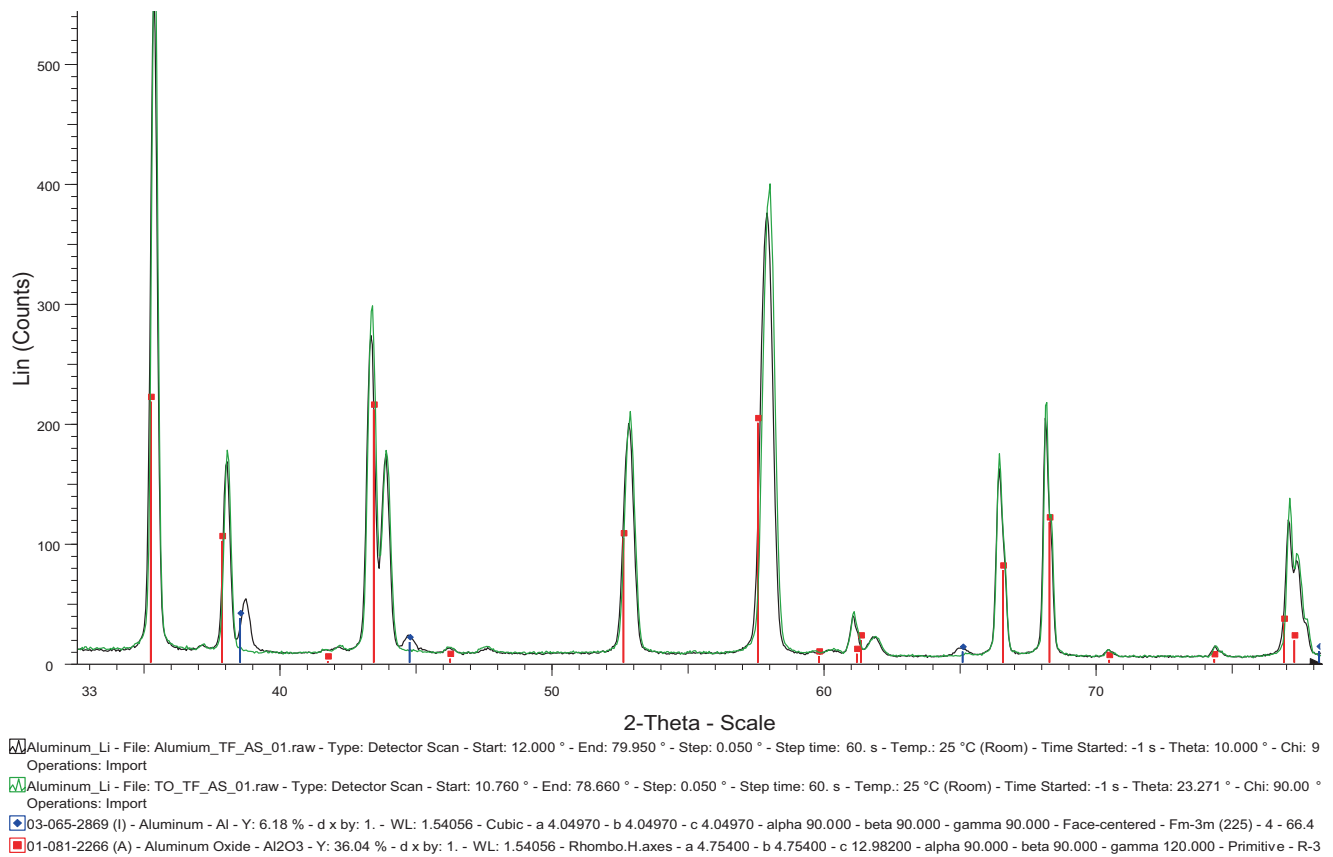


Fig. 10.6 1D X-ray diffraction pattern of Aluminum coating on Alumina compared with Alumina sample before coating

option which could be selected for our residual stress measurements in order to include material isotropy and the possibility of obtaining high angle measurements with higher stress sensitivity [22, 23]. But only 111 peak at $2\theta=34.4$ has acceptable intensity for peak fitting.

Using Bragg's law for $\lambda = 1.54178\text{\AA}$ and given $\theta_0 = 38.47$ and 111 ring,

$$\frac{1}{d_{hkl}^2} = \frac{h^2 + k^2 + l^2}{a^2} \rightarrow \frac{1}{d_{111}^2} = \frac{1^2 + 1^2 + 1^2}{(4.04970)^2} \rightarrow d_{111} = 2.33814 \quad (10.1)$$

The peak shift is expressed in degrees [24],

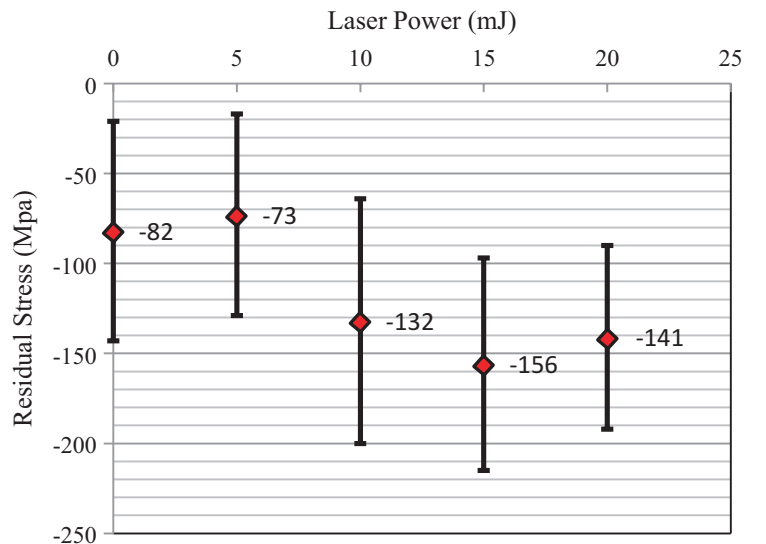
$$\Delta(2\theta)^\circ = -2 \frac{180}{\pi} \frac{1+\nu}{E} \sigma_\phi \tan\theta \sin^2(\psi) \Rightarrow \sigma_\phi = \frac{\Delta(2\theta)^\circ \pi}{-360 \tan\theta \sin^2(\psi)} \frac{E}{1+\nu} \quad (10.2)$$

For given resolution of 0.01° , $E=69$ MPa, $\nu=0.33$, minimum σ_ϕ as a function of 2θ and ψ can be obtained. For a typical $2\theta=34.4^\circ$ and $\psi=12^\circ$, a residual stress with magnitude of ± 23.34 MPa is measurable.

Residual stress was measured on four laser exposed points and one point on a sample without spallation as reference for zero residual stress sample. Two dimensional frame data were imported to Bruker's LEPTOS software for residual stress evaluation. Each frame was divided to sub regions and locally integrated along the γ direction to obtain 1D diffraction pattern for each sub region. Correction on polarization, background, $K_{\alpha 2}$ was performed. The peak positions were determined by fitting Pearson VII type peak. Due to the related large number of points available of a diffraction peak, the Pearson VII function was statistically reliable. The stress was calculated assuming the stress is measured as uniform averaged value and stress has a scalar nature.

We would like to control the energy of laser to create laser spallation on aluminum surface, transfer energy through alumina substrate and delaminate the tin oxide layer. When the energy is high (10–20 mJ) the second spallation also happens in SnO_2 layer. Aluminum grains around the spallation region act like strain gauges recording plastic deformation due to laser shock wave around the spallation point. Residual stresses were obtained at each exposure location on the sample are shown in Fig. 10.7. Location in which low energy laser is used (1–5 mJ) has smaller residual stress values (around –80 Mpa). On this sample SnO_2 layer has started to delaminate from the substrate. But higher energy laser (10–20 mJ) used for laser spallation in addition to laser spallation on Aluminum side have created a second spallation on the SnO_2 layer. An interesting observation is spallation from high energy laser beam have left more residual stress (around –145 Mpa) in the Aluminum layer.

Fig. 10.7 Residual stress vs. spallation power



10.6 Conclusion

Tin oxide and Aluminum thin films were deposited on both sides of optically polished alumina substrate with an RF magnetron sputter coater and a DC off axis magnetron sputtering system. A pulsed YAG laser (wavelength of 1064 nm) was used for laser spallation technique in order to determine threshold of energy of laser beam required to study adhesion properties of tin oxide thin film on Alumina substrate. It was found that if the energy of laser pulse is less than 10 mJ the thin oxide thin film starts to delaminate. Higher energy up to 20 mJ was tested and found to create spallation in the SnO₂ layer as well. Laser spallation implies heterogeneous plastic deformation and microstructure modifications, leading to high residual stresses appearance. Sin²ψ method was used to measure the residual stress. For the first time residual stresses of (−80 to −145 MPa) was recorded in laser spalled samples caused by individual laser interaction with film and substrate surface. Spallation from high energy laser beam generates large residual stresses (around −145Mpa) in the Aluminum layer while low energy laser pulse (1–5 mJ) creates smaller residual stress values.

References

- Kilinc, Y., Unal, U., Alaca, B.E.: Residual stress gradients in electroplated nickel thin films. *Microelectron. Eng.* **134**(20), 60–67 (2015)
- Allahkarami, M., Bale, H.A., Hanan, J.C.: Analytical model for prediction of residual stress in zirconia porcelain bi-layer. In: Narayan, R., Colombo, P. (eds.) *Advances in Bioceramics and Porous Ceramics III: Ceramic Engineering and Science Proceedings*, vol. 31, pp. 19–26 (2010)
- Larsson, M., Olsson, M., Hedenqvist, P., Hogmark, S.: Mechanisms of coating failure as demonstrated by scratch and indentation testing of TiN coated HSS on the influence of coating thickness, substrate hardness and surface topography. *Surf. Eng.* **16**, 436–444 (2000)
- Beake, B.D., Harris, A.J., Liskiewicz, T.W.: Review of recent progress in nanoscratch testing. *Tribol. Mater. Surf. Interfaces* **7**(2), 87–96 (2013)
- Seyed Faraji, L.: *Nanoscale carbon fiber-matrix interphase characterization with atomic force microscopy indentation*. Oklahoma State University, ProQuest Dissertations Publishing (2014)
- Gupta, V., Yuan, J., Pronin, A.: Recent developments in the laser spallation technique to measure the interface strength and its relationship to interface toughness with applications to metal/ceramic, ceramic/ceramic and ceramic/polymer interfaces. *J. Adhes. Sci. Technol.* **8**(6), 713–747 (1994)
- Gupta, V., Yuan, J.: Measurement of interface strength by the modified laser spallation technique II Applications to metal/ceramic interfaces. *J. Appl. Phys.* **74**(4), 2397–2399 (1993)
- Rats, D., Hajek, V., Martinu, L.: Micro-scratch analysis and mechanical properties of plasma-deposited silicon-based coatings on polymer substrates. *Thin Solid Films* **340**(1–2), 33–39 (1999)
- Hutchinson, J.W.: *Stresses and Failure Modes in Thin Films and Multilayers*. Notes for Academic Course. Technical University of Denmark, Lyngby (1996)
- Idota, Y., Matsufuji, A., Maekawa, Y., Miyasaki, T.: Tin-based amorphous oxide: a high-capacity lithium-ion-storage material. *Science* **276**, 1395 (1997)
- Courtney, I.A., Dahn, J.R.: Electrochemical and in situ X-ray diffraction studies of the reaction of lithium with tin oxide composites. *J. Electrochem. Soc.* **144**, 2045 (1997)
- Kim, T.J., Son, D., Cho, J., Park, B., Yang, H.: Enhanced electrochemical properties of SnO₂ anode by AlPO₄ coating. *Electrochim. Acta* **49**, 4405–4410 (2004)
- Beaulieu, L.Y., Eberman, K.W., Turner, R.L., Krause, L.J., Dahna, J.R.: Colossal reversible volume changes in lithium alloys. *Electrochem. Solid-State Lett.* **4**, A137–A140 (2001)
- Robert, F., Lippens, P.E., Olivier Fourcade, J., Jumas, J.C., Gillot, F., Morcrette, M., Tarascon, J.M.: Mössbauer spectra as a fingerprint in tin-lithium compounds: applications to Li-ion batteries. *J. Solid State Chem.* **180**, 339–348 (2007)
- Nam, S.C., Yoon, Y.S., Cho, W.I., Cho, B.W., Chun, H.S., Yun, K.S.: Enhancement of thin film tin oxide negative electrodes for lithium batteries. *Electrochem. Commun.* **3**(1), 6–10 (2001)
- Smith, M.R., Johnson, P.L., Teeters, D.: Interfacial storage of lithium in the nanostructure of SnO₂ nanobaskets for capacities exceeding theoretical values. *Solid State Ion.* **225**, 680–684 (2012)
- Wang, J., Sottos, N.R., Weaver, R.L.: Mixed-mode failure of thin films using laser-generated shear waves. *J. Mech. Phys. Solids* **57**, 51–66 (2009)
- Wang, J.: *Thin-film adhesion measurement by laser-induced stress waves*. Ph.D. thesis, Theoretical and Applied Mechanics, University of Illinois at Urbana Champaign (2002)
- De Ressaiguier, T., Loison, D., Dragon, A., Lescoute, E.: Laser driven compression to investigate shock-induced melting of metals. *Metals* **4**(4), 490–502 (2014)
- Ballard, P., Fournier, J., Fabbro, R.: Study of residual stresses induced by laser-shocks. *J. Phys. IV* **01**(C7), 132 (1991)
- He, B.B.: *Two-Dimensional X-Ray Diffraction*. Wiley, Hoboken (2009)
- Allahkarami, M., Jayakumar, B., Hanan, J.C.: Residual stress of individual aluminum grains from three dimensional X-ray diffraction. *Exp. Appl. Mech* **6**, 123–130 (2015)
- Benedetti, M., Fontanari, V., Allahkarami, M., Hanan, J.C.: Notch fatigue behavior of shot peened high-strength aluminium alloys: role of the residual stress field ahead of the notch root. In: *Experimental and Applied Mechanics*, vol. 6, pp. 113–121. Springer (2015)
- Krawitz, A.D.: *Introduction to Diffraction in Materials, Science, and Engineering*. Wiley, New York (2001)

Chapter 11

Joining of UHTC Composites Using Metallic Interlayer

Noritaka Saito, Laura Esposito, Toshio Yoneima, Koichi Hayashi, and Kunihiko Nakashima

Abstract Ultra-high temperature ceramics (UHTCs) are the subject of intense worldwide research effort, and their stability in severe environments makes them candidates for aerospace, nuclear and solar energy applications. Widespread usage UHTCs requires the development of effective and reliable joining methods that facilitate the fabrication of large, complex-shaped, and potentially multimaterial components and devices. Joining of HfB_2 and ZrB_2 , UHTC diborides, which exhibit outstanding thermo-mechanical and thermochemical properties and good erosion and corrosion resistance, was the focus of the present study. MoSi_2 is an effective sintering aid and a composite component for both HfB_2 and ZrB_2 , resulting in dense bulk materials with excellent mechanical properties. HfB_2 -10 vol.% MoSi_2 composites were joined at 1500 °C with a Ni/Nb/Ni interlayer that forms a thin liquid film. Joint-region characterization revealed well-bonded interfaces with interfacial reaction products with the MoSi_2 . Well-bonded interfaces were also obtained for a ZrB_2 -10 vol.% MoSi_2 composite bonded at 1500 °C with both Ti and Zr interlayers. It was found that the Ti interlayer exhibited more intensive interfacial reaction with ZrB_2 composite than the Zr interlayer. Additionally, well-bonded interfaces were also found for a ZrB_2 -10 vol.% MoSi_2 composite bonded at 1500 °C with ZrB_2 -X vol.% Ni (X=20, and 40) powder-based interlayer. Joint-region characterization revealed well-bonded interfaces with microstructures strongly dependent on the Ni content.

Keywords Ultra-high temperature ceramics • Joining • Transient liquid phase • Interfacial reaction • Four-point bending test

11.1 Introduction

The attractive and unusual properties that can be exhibited by ultrahigh temperature ceramics (UHTCs) have made them appealing candidate materials for a wide range of applications, including ones in the nuclear, solar, and aerospace sectors. The ultrarefractory borides, (e.g., ZrB_2 , TiB_2 and HfB_2), like the ultrarefractory carbides, are difficult to sinter in undoped form, and for both types of UHTCs, the use of modest amounts of an appropriate sintering aid has played a key role in facilitating densification (even in the absence of an applied pressure), refining the microstructure, and improving properties. For the specific case of ZrB_2 , additions of MoSi_2 have produced the desired processing and microstructural benefits, and thereby, have drastically improved the mechanical performance [1–4].

Applications often require that components be joined. This has many practical advantages. It allows the fabrication of complex-shaped structures, and for multimaterial structures, can allow costly high-performance materials to be used selectively and judiciously, where they are most needed. Prior work [5–7] has demonstrated the feasibility of a transient-liquid-phase (TLP) inspired approach to joining undoped ZrC , HfC , and TaC . The introduction of sintering aids, while beneficial to the properties of the material, may create additional challenges when joining is required. When joining undoped carbide UHTCs with a multilayer Ni/Nb/Ni interlayer, a Ni-Nb alloy liquid forms at reduced temperature that wets and partially penetrates some of the undoped carbides examined. Well-bonded, crack-free joints were produced. The dissolution and incorporation of the sintering aid into the liquid will affect its composition, likely change its total volume, and may alter the

N. Saito (✉) • K. Hayashi • K. Nakashima
Kyushu University,
744, Motoooka, Nishi, Fukuoka 819-0395, Japan
e-mail: saito@zaiko.kyushu-u.ac.jp

L. Esposito
CNR ISTEC National Research Council of Italy–Institute of Science and Technology for Ceramics,
via Granarolo, 64, Faenza RA 48018, Italy

T. Yoneima
Shoei Chemical Inc.,
5-3, Aza Wakasakura, Fujinoki-machi, Tosu 841-0048, Japan

wetting behavior, potentially deleteriously. In addition, as a result of the change in composition and volume, both new and increased amounts of phases can develop either due to reactions occurring at the bonding temperature or during cooling (especially if residual liquid is present at the onset of cooling). The potential duality in the role of sintering aids is explored in the present work.

We have examined the bonding of HfB_2 - and ZrB_2 -based composite with MoSi_2 , by employing three joining techniques, which are transient liquid phase (TLP) bonding using a Nb-dominated Ni/Nb/Ni interlayer, reactive bonding using group IV transition metal monolayer, and TLP bonding using ZrB_2 -Ni powder-based interlayer, to assess the potential for making reliable bonds using the more easily fabricated MoSi_2 -containing UHTC boride materials. A thorough microstructural characterization of the bond region has been performed intended to identify the nature of the phases formed, and the extent of the reaction/interaction zone. The four-point bending strength of the joints has also been measured.

11.2 Materials and Experimental Procedures

11.2.1 HfB_2 - and ZrB_2 -Based Composites

Powders of HfB_2 (99.5%, -325 mesh, Materion, Mayfield Heights, OH, USA) and ZrB_2 (98.0%, 1.5–2.5 microns, Japan New Metals Co., Ltd., Toyonaka, Osaka, Japan) as principal material and MoSi_2 (99.0%, Sigma-Aldrich Japan, Tokyo, Japan) as a sintering aid were employed. $\text{HfB}_2 + 10 \text{ vol.}\% \text{ MoSi}_2$ and $\text{ZrB}_2 + 10 \text{ vol.}\% \text{ MoSi}_2$ mixture powders were ball milled for 24 h using zirconia milling media (2 mm in diameter) in ethanol as dispersion medium, dried in a rotary evaporator, and passed through a -50×47 mesh polyethylene sieve. The resulting powders were uniaxially pressed into 12 mm diameter pellets, and then cold isostatically pressed (CPA50-300, Sansho Industry, Osaka, Japan) under 300 MPa for 3 min. The pellets were placed in a BN crucible (N1, Denki Kagaku Kogyo, Tokyo, Japan), sintered under 0.1 MPa argon atmosphere at 1950 °C for 60 min for HfB_2 - MoSi_2 composite, and sintered under 0.1 MPa argon atmosphere at 2000 °C for 60 min for ZrB_2 - MoSi_2 , using a graphite element furnace (FVPHP-R-3, Fuji Dempa Kogyo, Osaka, Japan) with a heating rate of 5 °C/min, and furnace cooled by shutting off the power.

The cross-section of the sintered bodies was polished and investigated using a typical field emission scanning electron microscope (FESEM, Ultra55, Carl Zeiss, Oberkochen, Germany) with energy dispersive spectroscopy (EDS). Mean relative density of the HfB_2 and ZrB_2 composite was measured by Archimedeian method. Mean bending strength was measured by four-point bending test explained in later Sect. 11.2.5. One surface of each composite pellet was polished with 9, 6, 1, and 0.25 μm diamond suspension solutions by using an automatic polisher (Automet250, Buehler, Lake Bluff, IL, USA). The polished pellets were ultrasonically cleansed in mixed solution of ultrapure water and soap, ultrapure water, acetone, and 2-propanol in the order listed before the bonding process.

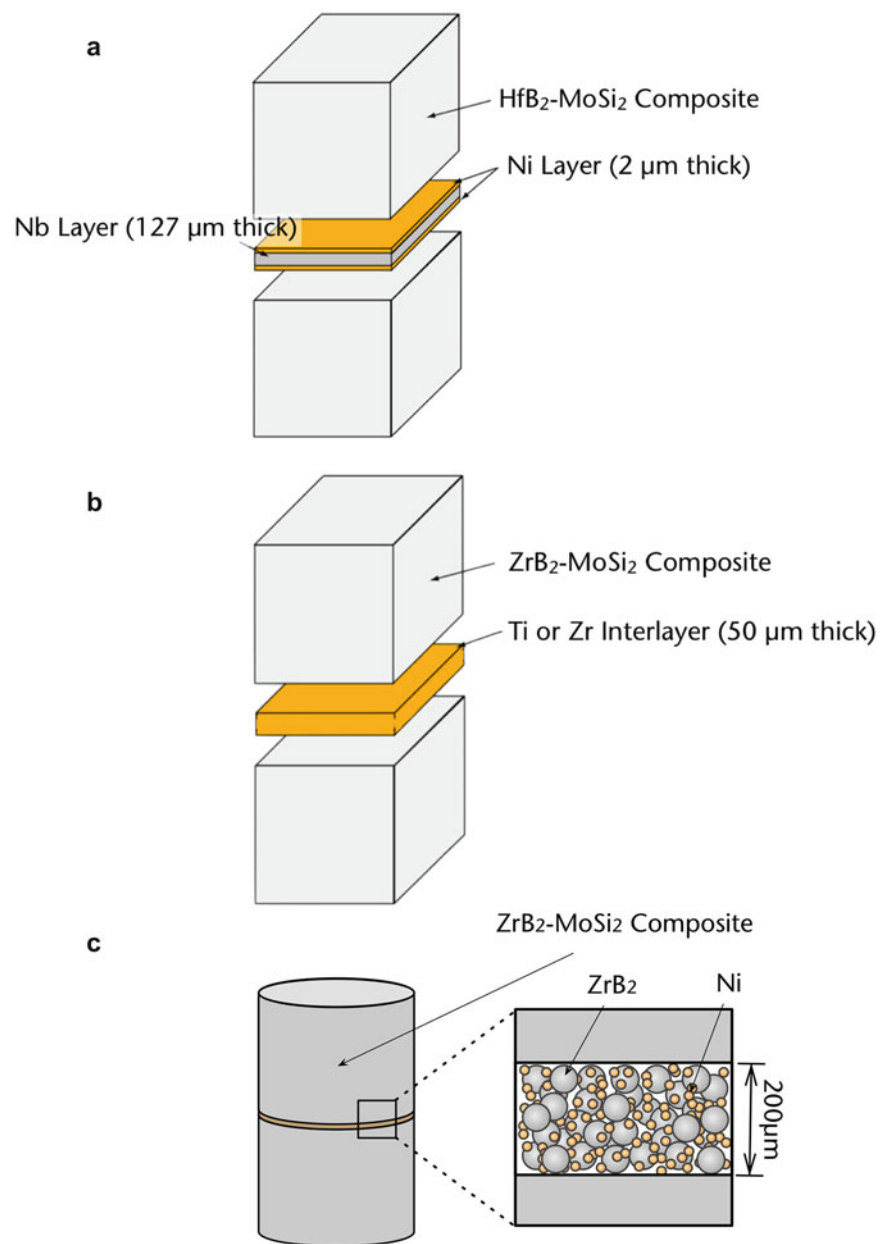
11.2.2 Transient Liquid Phase (TLP) Bonding Using Ni–Nb–Ni Interlayer

In principle, TLP bonding of ceramics has the potential to join high-temperature, high-performance materials at significantly reduced temperatures relative to brazing and solid-state diffusion bonding, in processing cycles that are short in duration (comparable to those in brazing). The extension of TLP bonding to ceramics employs a multilayer (A/B/A) interlayer. A minor portion of the interlayer (A) generates the TLP, and the major portion (B) remains solid during joining, and provides the sink for the liquid former. By choosing a major component, the core layer, with a high melting point and a good thermal expansion match with the ceramic, a refractory alloy that minimizes residual stresses is expected to evolve during processing and use. In order for the approach to be successful, there needs to be a synergistic interaction between several features or characteristics of the interlayer system. The outer cladding layer material must promote the formation of a liquid at reduced temperature. Phase diagrams can provide guidance on this issue. The liquid that forms will generally include some of the core layer due to dissolution, and can similarly interact with the ceramic being joined. The resulting liquid is thus at least a binary and can include additional components. Ideally the wetting characteristics and volume of the liquid are such that all of the interfacial gaps are completely filled, producing a well-bonded interface. Extensive reaction with the ceramic or sintering aids therein is not necessarily desirable, particularly if it leads to the formation of brittle intermetallics or substantially increases the amount of liquid. Ideally, once the liquid has formed and filled interfacial gaps, the liquid former (A) diffuses rapidly into the core layer (and/or adjoining ceramic) causing a progressive decrease in liquid volume at the joining temperature, and ultimately complete isothermal solidification of the joint. As a result, and particularly if extensive redistribution and

dilution of the melting point depressant occurs, the remelt temperature of the joint can be several 100° above the original joining temperature, which is obviously advantageous for high-temperature applications. Creating an interlayer that meets all of these criteria simultaneously is challenging, and experiments that are intended to examine individual aspects of the process can often be difficult.

Here, a schematic illustration of HfB_2 composite TLPB joint is shown in Fig. 11.1a. The interlayer sandwiched between being joined composites was consisted of core Nb layer of $127\ \mu\text{m}$ (99.9%, Nilaco, Tokyo, Japan) with cladding Ni layer of $2\ \mu\text{m}$ (99.9%, Goodfellow). The Ni and Nb foils were cleaned in the same manner as the HfB_2 composites and immersed in 1:1 $\text{H}_2\text{O}:\text{HNO}_3$ aqueous solution for 10 s to remove any oxide layer. The Ni/Nb/Ni interlayer was placed between the HfB_2 composites as shown in Fig. 11.1a. The joining assembly was heat-treated using a graphite element hot press furnace (FVPHP-R-3, Fuji Dempa Kogyo, Osaka, Japan) under 20 Pa vacuum at 1500°C with holding time of 30 min and a constant 8.5 MPa applied pressure. The furnace was heated at a constant heating rate of $15^\circ\text{C}/\text{min}$ and cooled by cutting the furnace power off. The joining samples were embedded in epoxy and sectioned across the interfacial region using a diamond saw (Isomet4000, Buehler, Lake Bluff, IL, USA). The sectioned samples were then polished and cleaned in the same manner as mentioned in Sect. 11.2.1. The interfacial regions of the samples were examined using FESEM with EDS and an electron probe microanalysis (EPMA-1610, Shimadzu, Kyoto, Japan) with a wavelength-dispersive X-ray spectrometer (WDS).

Fig. 11.1 Schematic illustrations of joining assemblies, (a) Transient liquid phase (TLP) bonding using Ni-Nb interlayer, (b) Reactive bonding using Ti or Zr interlayer, and (c) Transient liquid phase (TLP) bonding using ZrB_2 -Ni powder-based interlayer



11.2.3 Reactive Bonding Using Ti or Zr Interlayer

A schematic of ZrB₂ composite reactive bonding joint is shown in Fig. 11.1b. The interlayer was consisted of monolayer of 50 μm thick Ti (99.9%, Nilaco, Tokyo, Japan) or Zr (99.9%, Nilaco, Tokyo, Japan). The Ti and Zr foils were cleaned in the same manner as the ZrB₂ composites and immersed in 1:1 H₂O:HNO₃ aqueous solution for 10 s to remove any oxide layer. The Ti or Zr interlayer was placed between the ZrB₂ composites as shown in Fig. 11.1b. The joining assembly was heat-treated using a graphite element hot press furnace (FVPHP-R-3, Fuji Dempa Kogyo, Osaka, Japan) under 20 Pa vacuum at 1500 °C with holding time of 30 min and a constant 13 MPa applied pressure. The furnace was heated at a constant heating rate of 15 °C/min and cooled by cutting the furnace power off. The interfacial regions of the samples were examined in the same manner as mentioned above.

11.2.4 Transient Liquid Phase (TLP) Bonding Using ZrB₂-Ni Powder-Based Interlayer

A schematic of ZrB₂ composite TLPB is shown in Fig. 11.1c. The interlayer was consisted of powder mixture of ZrB₂ (98.0%, 1.5–2.5 microns, Japan New Metals Co., Ltd., Toyonaka, Osaka, Japan) and Ni (99.9%, 0.2 microns, Shoei Chemical Inc., Tosu, Saga, Japan). ZrB₂+20 vol.% Ni and ZrB₂+40 vol.% Ni mixture powders were ball milled for 24 h using zirconia milling media (2 mm in diameter) in ethanol as dispersion medium, dried in a rotary evaporator, and passed through a –50×47 mesh polyethylene sieve. The resulting powders were uniaxially pressed into 12 mm diameter pellets, and then cold isostatically pressed (CPA50-300, Sansho Industry, Osaka, Japan) under 300 MPa for 3 min, to form 200 micron thick interlayer of the mixed powder compact. The interlayer was placed between the ZrB₂ composites as shown in Fig. 11.1b. The joining assembly was heat-treated using a graphite element hot press furnace (FVPHP-R-3, Fuji Dempa Kogyo, Osaka, Japan) under 20 Pa vacuum at 1500 °C with holding time of 30 min and a constant 8.5 MPa applied pressure. The furnace was heated at a constant heating rate of 15 °C/min and cooled by cutting the furnace power off. The interfacial regions of the samples were examined in the same manner as mentioned in Sect. 11.2.2.

11.2.5 Four-Point Bending Test of the Joints

Following bonding, the joining samples were sectioned into 25 mm×2.5 mm×2 mm (length×width×thickness) beams using a electrical discharge machine (ROBOCUTα-400iC, Fanuc, Yamanashi, Japan). The beams were beveled and then polished in the same manner as mentioned in Sect. 11.2.1. 10 bending beams were tested at room temperature. In addition, HfB₂ and ZrB₂ composite beams were processed in the same manner and tested for 12 times at room temperature to compare the strength of the joints.

11.3 Results and Discussion

The relative densities of composites were found to be 97.6% for HfB₂ composite and 98.2% for ZrB₂ composite, respectively. Both composites revealed nearly full-dense sintering characteristics by utilizing MoSi₂ addition as the sintering aid and composite component.

11.3.1 Transient Liquid Phase (TLP) Bonding Using Ni-Nb Interlayer

Back-scattered electron (BSE) micrographs of transient liquid phase (TLP) bonding joint of HfB₂-MoSi₂ composite using Ni-Nb interlayer with the results of WDS chemical analyses are shown in Fig. 11.2. As can be seen at the lower magnification, it was found that no macroscopic void and crack, and the original Ni/Nb interlayer structure has evolved into a multilayer structure with each layer exhibiting distinct contrast at each interface as a result of melting, dissolution, and interfacial interaction with HfB₂ composite. The thick layer that has the brightest contrast was identified as Nb using the WDS analysis.

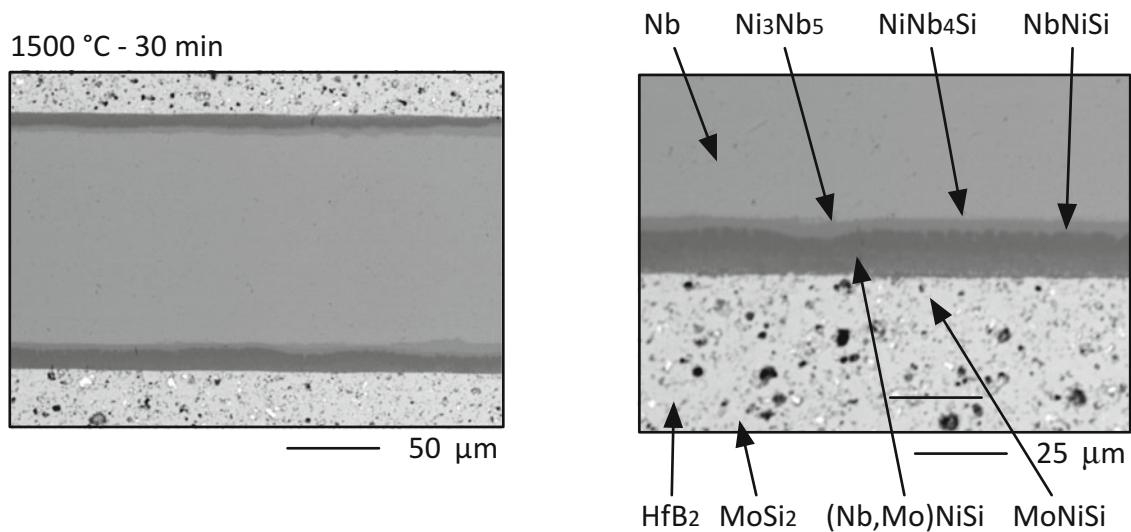


Fig. 11.2 Microstructural and microchemical analyses results of the polished images of the reaction layer and related phases identified on the basis cross section of HfB_2 - MoSi_2 composite joint

The total “Nb” thickness decreased from 125 μm to ≈ 110 μm . The decrease in the thickness of the Nb layer indicates enhanced dissolution of Nb because, at the bonding temperature, 1500 $^\circ\text{C}$, the solubility limit of Nb into molten Ni is expected to ≈ 55 at.%. Since the Ni layer is only 2 μm thick, one would only expect a comparable thickness of Nb to dissolve on each side in the absence of an effect of HfB_2 dissolution.

The thicker reaction layer, ≈ 10 –20 μm depending on the position measured, is a consequence of the enhanced dissolution of both the core layer and the HfB_2 composite, and is made up of multiple layers. From the HfB_2 side of the reaction layer, $(\text{Nb},\text{Mo})\text{NiSi}$, NbNiSi , NiNb_4Si , and Ni_3Nb_5 inter metallic phases were identified by WDS analysis. The Mo and Si found in these intermetallics are originally from the MoSi_2 sintering aid. Although reaction between the Ni/Nb/Ni interlayer and the HfB_2 composite was extensive, the interface was relatively flat, suggesting that the dissolution of HfB_2 composite was uniform along the interface. Furthermore, the HfB_2 composite well maintained the microstructure of the as-processed composite, which is a good indication for less degradation of the bulk properties during the TLP joining process. The four-point bending test on the joints revealed 412 ± 53.9 MPa of fracture strength at the room temperature, besides 462 ± 45.7 MPa for the HfB_2 composite itself, which suggests the TLP joints of HfB_2 composite with Ni-Nb interlayer well-maintains the strength of the composite.

11.3.2 Reactive Bonding Using Ti or Zr Interlayer

As described in the Sect. 11.3.1, UHTC boride was found to be reactive against metallic phase. In the current section, we would like to utilize interfacial reaction between UHTC boride composite and metallic interlayer for the bonding. Back-scattered electron (BSE) micrographs of reactive bonding joint of ZrB_2 - MoSi_2 composite using (a) Ti or (b) Zr interlayer with the results of WDS chemical analyses are shown in Fig. 11.3. As can be seen in Fig. 11.3a, b, no void and crack were observed in the current magnification, which indicates the reactive bonding of ZrB_2 composite have successfully done. However, the interfacial microstructures of ZrB_2 composite joints were found to significantly differ from each other. In the case of using Ti interlayer, cf. Fig. 11.3a, the interfacial reaction between the ZrB_2 composite and Ti interlayer was tremendously intensive, and resulted in the formation of reaction products as needle like TiB grains, $(\text{Ti},\text{Zr},\text{Mo})\text{B}$, $(\text{Ti},\text{Zr},\text{Mo})$ and $(\text{Ti}-\text{Zr}-\text{Si})$ solid solutions. These reactions were attributed to accelerated diffusion via Ti-Zr-Si liquid phase at the bonding temperature of 1500 $^\circ\text{C}$. By contrast, shown in Fig. 11.3b, the ZrB_2 composite joint with Zr interlayer revealed modest interfacial reaction against the ZrB_2 composite, and ended up to generate (Zr,Mo) solid solution, Zr_4Si and Zr_2Si silicides, because of the solid phase bonding. The four-point bending test on the joints revealed 477.7 ± 88 MPa for the Ti interlayer and 439.3 ± 70 MPa for the Zr interlayer, respectively at the room temperature, besides 376.8 ± 77.0 MPa for the ZrB_2 composite itself, which suggests the RB joints of ZrB_2 composite with Ni-Nb interlayer do not degrade the strength of the composite.

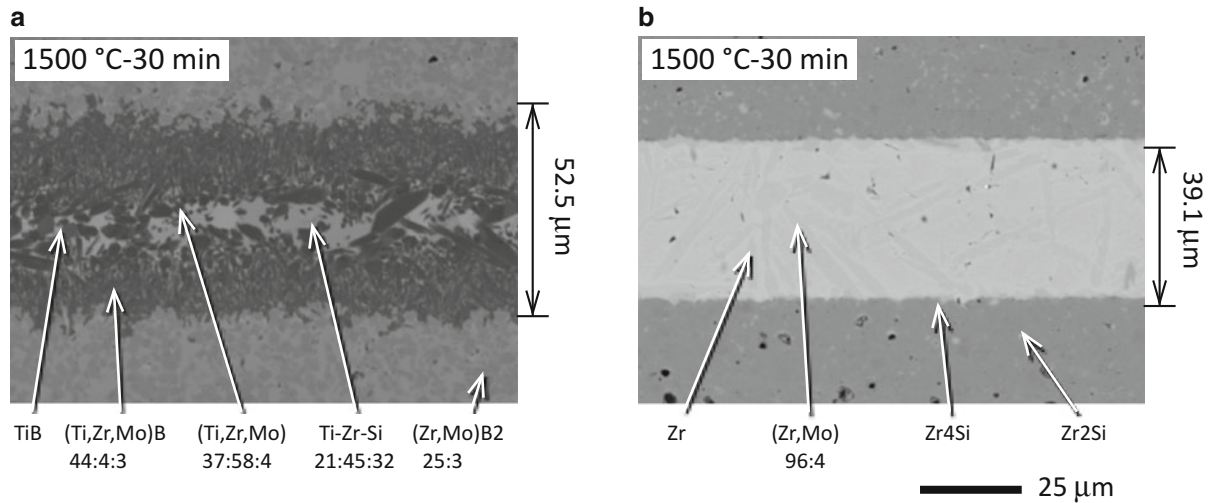


Fig. 11.3 Microstructural and microchemical analyses results of the polished images of the reaction layer and related phases identified on the basis cross section of ZrB₂-MoSi₂ composite joints, (a) with Ti interlayer, and (b) with Zr interlayer

11.3.3 Transient Liquid Phase (TLP) Bonding Using ZrB₂-Ni Powder-Based Interlayer

Here, the other effort on TLP bonding of ZrB₂ composite employing ZrB₂-Ni powder-based interlayer, which can provide us more rapid interfacial reaction of TLP interlayer because of larger surface area that could be involved into the intensive reaction. Back-scattered electron (BSE) micrographs of reactive bonding joint of ZrB₂-MoSi₂ composite utilizing (a) ZrB₂-20 vol.% Ni (ZN20) interlayer and (b) ZrB₂-40 vol.% Ni (ZN40) interlayer with the results of WDS chemical analyses are shown in Fig. 11.4. As can be seen in Fig. 11.4a, b, no void and crack were observed, which indicates the joining of ZrB₂ composite have successfully done by using ZrB₂-Ni powder-based interlayer. Similar interfacial microstructures were found in both joints, however, the porosity in the ZN40 interlayer seemed to be slightly smaller than that in the ZN20 interlayer. Additionally, B-Ni-Si-Zr phases with the different compositions were identified in both the composite and interlayer side. The four-point bending test on the joints revealed 423.0 ± 83.2 MPa for the ZN20 interlayer and 512.5 ± 54.7 MPa for the ZN40 interlayer, respectively at the room temperature, besides 376.8 ± 77.0 MPa for the ZrB₂ composite itself, which suggests the TLP joints of ZrB₂ composite with ZrB₂-Ni interlayer enhances the strength of the composite.

11.4 Summary

The bonding of HfB₂- and ZrB₂-based composite with MoSi₂, by employing three joining techniques have been explored, which were transient liquid phase (TLP) bonding using a Nb-dominated Ni/Nb/Ni interlayer, reactive bonding using group IV transition metal monolayer, and TLP bonding using ZrB₂-Ni powder-based interlayer. Major findings were as follows.

1. HfB₂-10 vol.% MoSi₂ and ZrB₂-10 vol.% MoSi₂ composites were successfully processed with 97.6% and 98.2% in relative densities, and 462 ± 45.7 MPa and 376.8 ± 77.0 MPa in four-point bending strength.
2. Micro-structural and -chemical analyses at the joining interface region of the joints fabricated in the present study revealed well-bonded features without any voids and cracks along the interface.
3. For TLP bonding of HfB₂ composite using Ni-Nb-Ni interlayer, the interlayer showed interfacial reaction against the composite at the bonding temperature, and resulted in the formation of intermetallic silicides. The four-point bending test on the joints revealed 412 ± 53.9 MPa of fracture strength at the room temperature, besides 462 ± 45.7 MPa for the HfB₂ composite itself, which suggests the TLP joints of HfB₂ composite with Ni-Nb interlayer well-maintains the strength of the composite.
4. For reactive bonding of ZrB₂ composite using Ti or Zr interlayer, the interfacial reactions were found to be significantly dependent on the formation of liquid phase. The Ti interlayer indicated more intensive and active interfacial reaction against ZrB₂ composite than the Zr interlayer. The four-point bending test on the joints revealed 477.7 ± 88 MPa for the Ti interlayer and 439.3 ± 70 MPa for the Zr interlayer, respectively at the room temperature, besides 376.8 ± 77.0 MPa for

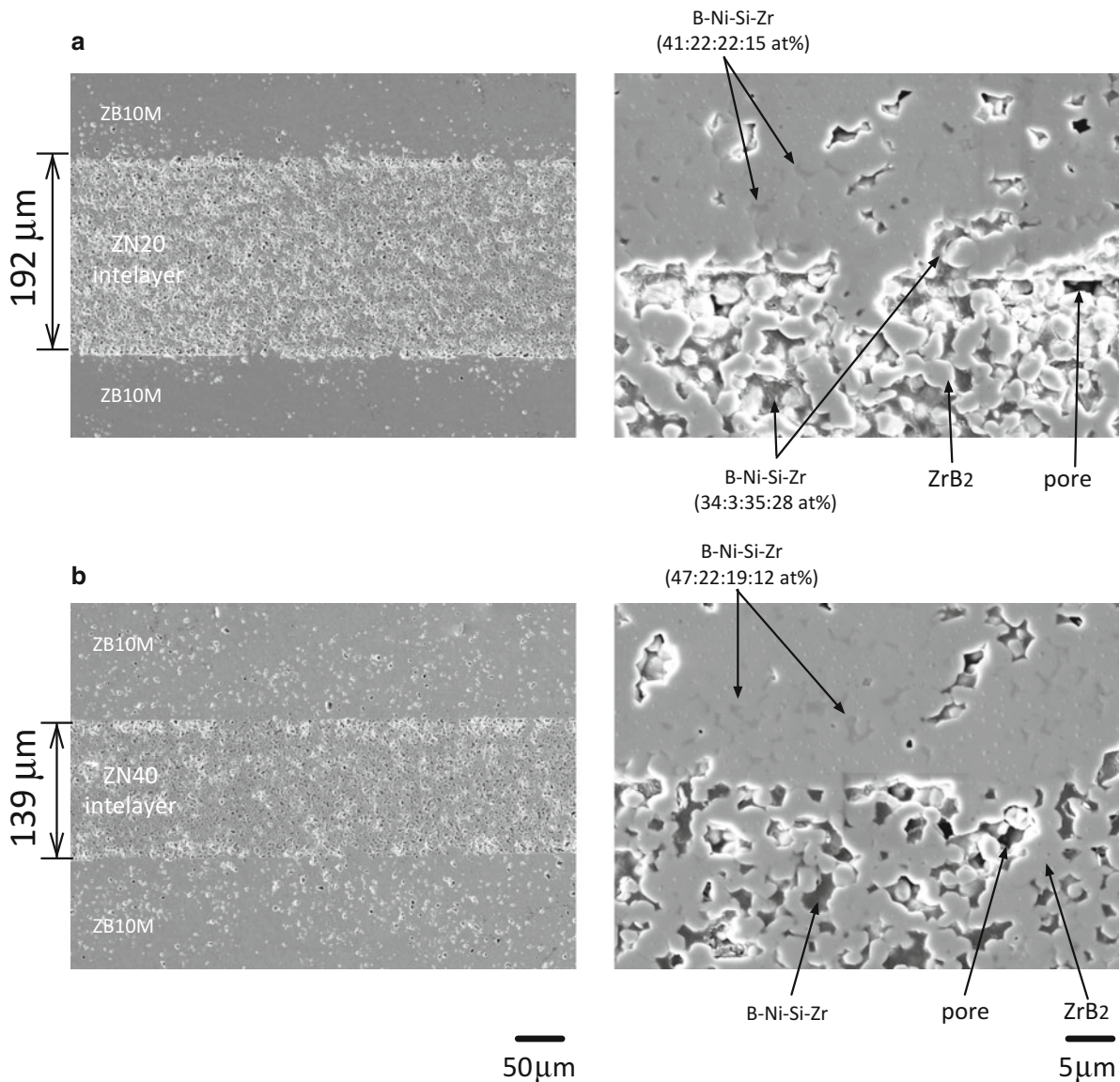


Fig. 11.4 Microstructural and microchemical analyses results of the polished images of the reaction layer and related phases identified on the basis cross section of $\text{ZrB}_2\text{-MoSi}_2$ composite joints, (a) with $\text{ZrB}_2\text{-20 vol.}\%$ Ni interlayer, and (b) with $\text{ZrB}_2\text{-40 vol.}\%$ Ni interlayer

the ZrB_2 composite itself, which suggests the RB joints of ZrB_2 composite with Ni-Nb interlayer do not degrade the strength of the composite.

- For TLP bonding of ZrB_2 composite using $\text{ZrB}_2\text{-Ni}$ powder-based interlayer, the similar interfacial microstructures were observed except thickness of the interlayer and porosity along the joining interface. The four-point bending test on the joints revealed 423.0 ± 83.2 MPa for the $\text{ZrB}_2\text{-20 vol.}\%$ Ni interlayer and 512.5 ± 54.7 MPa for the $\text{ZrB}_2\text{-40 vol.}\%$ Ni interlayer, respectively at the room temperature, besides 376.8 ± 77.0 MPa for the ZrB_2 composite itself, which suggests the TLP joints of ZrB_2 composite with $\text{ZrB}_2\text{-Ni}$ interlayer enhances the strength of the composite.

References

- Sciti, D., Brach, M., Bellosi, A.: Oxidation behavior of a pressureless sintered $\text{ZrB}_2\text{-MoSi}_2$ ceramic composite. *J. Mater. Res.* **56**(3), 149–158 (2005)
- Sciti, D., Brach, M., Bellosi, A.: Long-term oxidation behavior and mechanical strength degradation of a pressurelessly sintered $\text{ZrB}_2\text{-MoSi}_2$ ceramic. *Scr. Mater.* **53**(11), 1297–1302 (2005)

3. Sciti, D., Guicciardi, S., Bellosi, A., Pezzotti, G.: Properties of a pressureless-sintered ZrB_2 - $MoSi_2$ ceramic composite. *J. Am. Ceram. Soc.* **89**(7), 2320–2322 (2006)
4. Silvestroni, L., Kleebe, H.J., Lauterbach, S., Muller, M., Sciti, D.: Transmission electron microscopy on Zr- and Hf-borides with $MoSi_2$ addition: densification mechanisms. *J. Mater. Res.* **25**(5), 828–834 (2010)
5. Saito, N., Ikeda, H., Yamaoka, Y., Glaeser, A.M., Nakashima, K.: Wettability and transient liquid phase bonding of hafnium diboride composite with Ni-Nb alloys. *J. Mater. Sci.* **47**(24), 8454–8463 (2012)
6. Silvestroni, L., Sciti, D., Esposito, L., Glaeser, A.M.: Joining of ultra-refractory carbides. *J. Eur. Ceram. Soc.* **32**(16), 4469–4479 (2012)
7. Esposito, L., Sciti, D., Silvestroni, L., Melandri, C., Guicciardi, S., Saito, N., Nakashima, K., Glaeser, A.M.: Transient liquid phase bonding of HfC-based ceramics. *J. Mater. Sci.* **49**(2), 654–664 (2014)

Chapter 12

Metal-to-Composite Structural Joining for Drivetrain Applications

Peter J. Fritz, Kelly A. Williams, and Javed A. Mapkar

Abstract Dissimilar material components in structural applications require advanced joining geometries and processes that permit the interface of these components to have mechanical behavior equivalent to the lesser of the base metal material behavior and the base composite material behavior. In volume-constrained applications, such as drivetrain parts, the interface must have the strength of the base materials, and the envelope of space of the current drivetrain componentry. The interface surfaces of the composite and metal are demonstrated here to achieve base material capability for the thickness, width, and length directions, resulting in conservation of mechanical properties throughout the interfaces, for all loading and deformation at material transitions. The method of material forming, modification, combining, and product operation is explained here, for optimization of materials usage and for processing equipment.

In designs to date, the metal to composite interface has been the weak link of the assembly, and product performance has been limited to this characteristic. This new method of interface build, and theory of base-to-joint equivalent strength, results in a new capability for drivetrain component design, and will start a new era of dissimilar materials combinations to offer the consumer improved product functionality with enhanced interface design, manufacture, envelope, and operational improvements.

Keywords Drivetrain • Joining • Dissimilar • Structural • Composite

12.1 Introduction

Metal parts in vehicle drivetrains dominate the materials selection for cars and trucks. The mostly steel, cast iron, and aluminum parts of the drivetrain are reliable, and are low-cost, but these metal parts result in drivetrain components that are heavy. As drivetrain components are generally very heavily loaded, composite material substitutions require the higher-strength composite selections, and joining between metal and composite must be sufficient to equal the strength of the base materials. To achieve such high interfacial strength capabilities, metal-to-composite interfaces need to be tailored by composite-fiber orientation, loading, geometry, and metal surface preparation.

Basic research has been completed here, to characterize joining between dissimilar materials, such as metal and composite, to determine the capability of standard joining within the framework of application requirements, and the special geometries necessary to attach metals to composites in drivetrains. Fundamental interfacial shear strengths for rotational component interfaces will be demonstrated here, and compared to the minimal necessary shear strengths of the base materials. Basic information on metal surface preparation, cylindrical interfaces, classical analysis, and thermal limitations will be verified here, so that the metal-to-composite interface capability of drivetrain applications can be compared to the base material of component metal shear capability and component composite interlaminar capability, leading to the design of joints that are stronger than the base materials.

The Eaton Vehicle Group provides automotive, aerospace, and commercial vehicle manufacturers worldwide with products and systems that are designed to improve vehicle efficiency, performance and power—such as emission control components, engine valves, valve-train systems and superchargers—as well as offering driveline expertise through its transmission, clutch and torque management products and systems. The testing and verification in this report was done for Eaton on driveline parts including transmission, differential, supercharger, and clutch.

P.J. Fritz (✉) • K.A. Williams • J.A. Mapkar
Eaton Corporate Research and Technology, 26201 Northwestern Highway, Southfield, MI 48076, USA
e-mail: peterfritz@eaton.com

12.2 Shear Strength

12.2.1 Shear Strength Samples

To determine the effect of the metal surface preparation, the metal surface of coupon parts for bonding attachment were prepared as plain, textured (grit blasted), dimpled, and holes (penetrated). These preparations were all cleaned by acetone wipe, and then adhesively bonded or overmolded to a polymer, such as a thermoplastic, and cooled to strength. In tensile testing, the shear coupons were subjected to the highest loading to lead to failure, and that load was divided by the contact area, such as both sides summed, leading to the average shear stress of the interface at failure. In general, these coupons were loaded with an increasing load until debond occurred. At coupon debond, the peak load was recorded, and the interface area with the thermoplastic polymer was recorded, to calculate the peak shear stress. The schematic of Fig. 12.1 shows a standard lap-shear coupon indicating two green areas where the composite base material (d_1) on the left is bonded by overmolding to the metal component on the right (d_0). The bond area A_b then, is

$$A_b = 4l/z_0 \quad (12.1)$$

where z_0 is the width of the metal specimen near the green area, but in a direction z that is not shown, but is the direction perpendicular to both directions x and y . This geometry is useful for symmetrical loading of the bonded area so that the shear strength can be measured with reduced peeling of the bond area.

The specimens used a composite thermoplastic, as shown on the left in Fig. 12.2, where the reinforced thermoplastic was overmolded on steel half-dogbone-shaped base material. Unlike Fig. 12.1, the reinforced thermoplastic was bonded on five sides of the steel. As the “end” of the steel was small and the end area offered only tensile bonding in all specimens, its area was ignored. But the other four sides did provide shear strength so all were utilized in the measurement of the shear area A_s as

$$A_s = 4l(z_0 + d_0) \quad (12.2)$$

This geometry of testing follows the method of ASTM D3528 [1], and uses symmetrical loading to prevent wrenches (force couples) in the interlaminar bond area. This deviates from the method of Watson in AFWAL-TR-82-4013 where steel plates are used on both ends of the coupon [2], but allows for symmetrical overmolding of the composite component.

Fig. 12.1 Schematic of composite material surrounding metal sheet specimens for shear loading

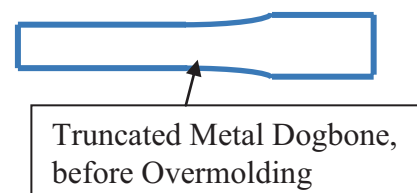
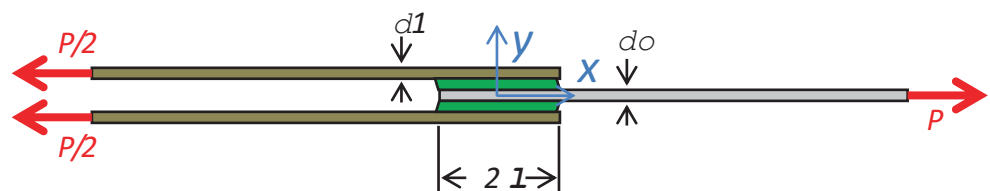
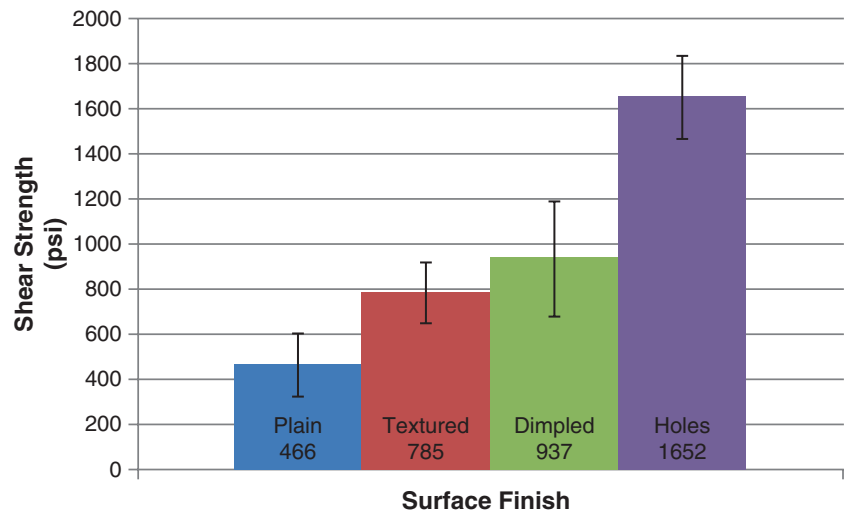


Fig. 12.2 Photograph of composite material bonded to truncated metal dogbone specimens for shear loading

Fig. 12.3 Shear strength of metal-to-composite interfaces with application of metal surface preparation, and overmolding of the composite coupons, with the metal as an insert



12.2.2 Shear Strength Verification

The base metal surface preparation, per the test plan, resulted in significant variations in interfacial shear strength. For these samples, all of the composite was overmolded onto the metal extended half-dogbones, so that results would only indicate the relative performance of the surface preparation. The weakest was the metal with flat faces, and no preparation. When texturing (grit blasted) was added, the interfacial shear strength increased with the additional geometry and increase in surface area, because of the texturing. The dimpling was a more severe case of geometry alteration, so more surface area was generated, and more shear strength was measured. Finally, with “holes,” an additional material interlock of the metal and composite was introduced, so significant additional shear strength was obtained, because all of the bonded surface was loaded and the composite material that extruded into the holes formed a base material mechanical “interlock,” increasing the maximum strength of the interface. The interlock was independently about as strong as the overmold (flat surfaces van der Waals) bond, so that strength of the “holes” samples was about double that of the other textured and dimpled attachment methods. Unfortunately, the holes interface strength also only achieve under 10% of that of the shear-strength of the steel base material (Fig. 12.3).

12.2.3 Shear Strength with Metal Surface Preparation

For metal preparation, the more severe the treatment is, and as the additional surface area is created by disturbing the metal surface, the higher the apparent shear-bond strength is attained. Where mechanical interlocks (holes) are used in the preparation of the base material, strength, beyond that of the chemical bonding, whether van der Waals or covalent, can be readily achieved.

12.3 Adhesive Bonding

12.3.1 Adhesive Bond Samples

To determine the interfacial strength of a rotational-part subassembly-interface, a set of two metal components were made with a cylindrical interface. The components were fitted to allow a 0.25 mm gap, as recommended by the adhesive manufacturer, between the metal parts for the joining. The bonding surfaces were all cleaned with an acetone wipe to remove grease and oil residue. Two-part epoxy adhesive was mixed by hand and applied to all surfaces on both the metal parts where adhesion was desired, as shown in Fig. 12.4, on a cylindrical interface. The parts were slid together on a fixture that assured concentricity. Excess adhesive flowed on both sides of the cylindrical interface during assembly, assuring complete coverage. After green strength was achieved in an hour, the bonded part was removed from the fixture. The adhesively bonded parts were cured by manufacturer specification, and then inspected for tolerance stack. All parts were found to be within 0.025-mm of

Fig. 12.4 Rotational parts slathered with cyan-colored adhesive, before assembly



Fig. 12.5 Rotational parts assembled together with cylinder-shaped adhesive dollops



circumferential and radial dimensioned positions, well within tolerance of rotational equipment. One assembled part is shown in Fig. 12.5, where the cyan-colored band is the thermoset adhesive.

12.3.2 Adhesive Bond Verification

The bonded parts were subjected to rotational loading as pure torsion, and torqued to failure. The smooth surface adhesive-bonded area failed by a combination of cohesive and adhesive failure. All of the 57 square centimeters of adhesive bond failed simultaneously, and the failure occurred at a load of 2400 Nm. For design purposes, this corresponds to a shear load on the specimen of 15 MPa, that is average for a structural epoxy adhesive. Compared to a flat interface, such as with a symmetrical shear-load coupon, this cylindrical shaped strength is slightly more than can be achieved by the same adhesive in a flat area. This shear strength of the adhesive bond is less than 10% of that of the base material steel, so is significantly low for joining.

12.3.3 *Adhesive Bond of Rotational Parts*

In the situation of a cylindrical shaped adhesive bond interface (rotational part), the shear loading is uniform, and not dependent on a symmetrical and flat surface (e.g. lap-shear coupon), that has stress concentrations at the ends of the bonded intervals. For a symmetrical shear flat-adhesive coupon, the ends are subject to stress concentration, lowering the measured strength of the complete adhesive dollop. So, although the strength of the adhesive may be the same at all sites, in practice, the stresses will appear higher where there are starts and ends to the bond area, as is the situation for a lap-shear coupon. For the situation of a cylindrical bond shape, the strength will be slightly higher, as the load is distributed evenly.

12.4 Thermal Range

12.4.1 *Thermal Range Samples*

Rotational components need to operate at high and low temperatures. To determine the range of temperature that interface joining can survive, samples were constructed with cylindrical interfaces to represent rotational machinery. The samples were built with metal and composite parts, and these parts were attached by adhesive and by interference fit. To create a mechanical load, the subassemblies were shaken with an acceleration of up to 50 g's to represent a 10,000 N load, as rotational components encounter as their highest known loading. Simultaneously, the assemblies were subjected through a 24-h cycle to achieve a high dwell temperature of 175 °C and a low dwell temperature of -45 °C, repeatedly. Various combinations of base materials were tested, but all had a 0.25 mm adhesive gap, and were assembled with coaxial alignment. The temperatures and accelerations were ramped up with a slow gradient, so that if an intermediate failure occurred, the maximum achievable temperature and acceleration could be recorded as the joint capability. The shake was applied in the radial direction of the rotational component, the component was constrained to a central axis, and to prevent circumferential movement, the component was further constrained at a line near the outer radius. The shake was applied at a rate lower than one cycle per second, and hundreds of cycles were conducted at each temperature extreme, as traced in Fig. 12.7. To establish capability, these parts were disassembled from the fixture, visually inspected for cracks and disassembly, at every temperature extreme shown in Fig. 12.7. If no cracks or disassembly could be observed by visual, tactile, CMM, thermography, and NDE, then the assembly was labeled to be structurally intact, and capable of that loading at temperature.

12.4.2 *Thermal Range Verification*

The rotational components were subjected to ramped-up temperature extremes for exposed automotive driveline components, and ramped-up accelerations. All samples were inspected after shaking, for each temperature low extreme and each temperature high extreme, for microcracking, relative movement between parts, and catastrophic separation of parts. All parts passed this testing, showing no deterioration, during all of the temperature extremes, to the last cycle, with no microcracking, relative movement, or part separation. This is a significant observation, as both the base materials and the interfaces survived readily within the temperature bounds.

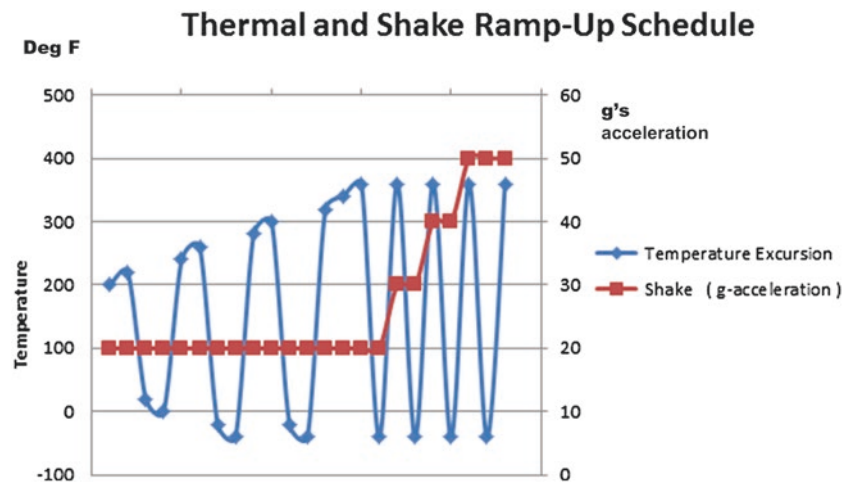
In Fig. 12.6, three drivetrain components (samples) that are each rotationally symmetric were tested simultaneously in the thermal chamber. At each temperature extreme, the components were disassembled from the fixture and inspected for survivability. All bonded components passed completely, with no visible damage. These parts were subjected to additional fatigue testing to indicate that there was no operational damage to all of these components.

In other testing of rotational components, a reinforced thermoplastic part was overmolded onto a metal part, and subjected to the thermal excursions of Fig. 12.7, without external loading. All of the adhesively-bonded parts passed this test, and when inspected by ultrasonic, tactile, and thermography methods, indicated that no opening occurred, and the bonding by van der Waals force of overmolding had no gapping.

Fig. 12.6 The hydraulic actuator is behind the step-ladder and the rotational components to be tested are in the thermal chamber. The rotational components are shaken in the stationary thermal chamber



Fig. 12.7 Ramped loading and thermal excursions for the shake testing of the metal-to-composite interfaces

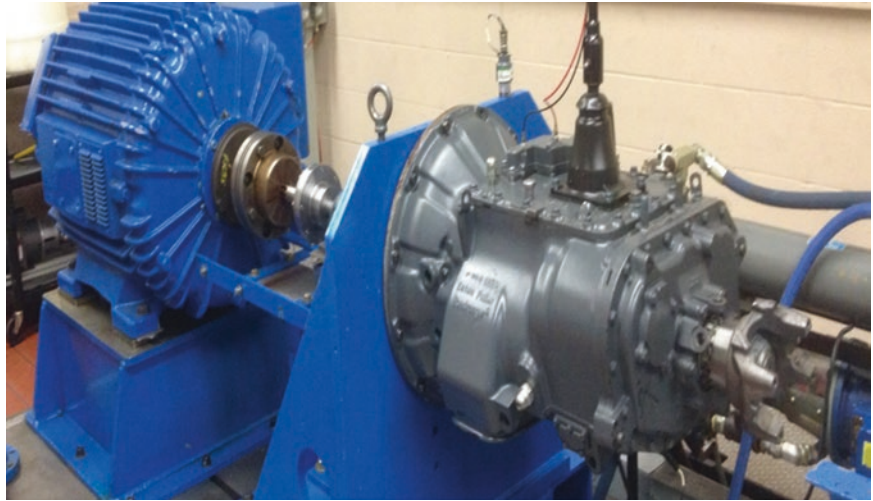


12.4.3 Thermal Capability of Composite to Metal Interfaces

Rotational parts bonded with thermoset adhesive were subjected to forces of over 1000 N. No damage (microcracking or disassembly) was observed by visual, tactile, CMM, or NDE. Multiple “baseline” rotational components that were interference-fit assembled (no van der Waals or covalent bond) failed by disassembly in this testing procedure as shown in Fig. 12.6, indicating that the thermoset adhesive and overmold bond did have a significant role. Although this testing indicates significant capability for thermoset adhesive interfaces, it is well known that both the base composite material, and the thermoset adhesive material can be weaker at temperatures at our use of 175 °C (350 F), compared to room temperature structural performance [3].

In another situation, with a thermoplastic composite overmolded to metal, the van der Waals (polymer to metal) bond was sufficient for the component to survive multiple cycles of extreme hot and cold with no exterior structural loading, successfully, as proven by ultrasonic and thermographic testing to assure metal-to-composite bonding without gapping.

Fig. 12.8 Metal-and-composite components are prototyped full-scale and tested inside existing subassemblies as shown in the dynamometer test cell here



12.5 Structural Behavior

12.5.1 Structural Behavior Samples

Samples of rotational equipment were prototyped and loaded into drivetrain assemblies to test duty cycles to failure. The metal-to-composite interfaces had mechanical interlocks, and were attached by overmolding in some parts, interference-fit in some parts, and adhesive bonding in some parts. The rotational components were tested for noise, torsional strength, and fatigue life in dynamometers. The rotational parts were made of metal components and composite components. The composite components were attached to the metal by van der Waals forces (overmolding), friction (interference fit), and by covalent bonds (two-component adhesive bonding), depending on how these were assembled. All were built to current standards for such equipment, and tested in existing housings that are readily available in the marketplace.

12.5.2 Structural Behavior Verification

The components were prototyped to full scale, assembled into a drivetrain subassembly, and mounted on dynamometers that were customized to perform the duty cycles of vehicles, in a stationary test cell. For the rotational components that were overmolded, as reinforced thermoplastic on textured metal, the parts failed after conventional all-metal subassembly components failed and were replaced, but before the duty cycle was completed, for verification testing. The metal-and-composite rotational part assembled by overmolding failed just before achieving 20% of the duty cycle, where the baseline is an all-cast-iron part that achieves five-times more cycling to failure. This metal-and-composite rotational part assembled by overmolding showed in testing that it was significantly weaker than the all-metal current production part.

In other verification testing, for significantly different rotational components made with thermoset adhesive to bond the composite to the textured metal, all of the components survived the entire duty cycle for that component, as did the current all-steel part. This thermoset adhesive method of assembly was fully successful, and indicates a significant method for successful joining of metal and composite. A dynamometer test cell for rotational equipment is shown in Fig. 12.8, with the dissimilar material component inside the blue housing.

12.5.3 Full Prototype Dynamometer Duty Cycles

For full-scale testing, on various drivetrain components, the material choice, processing, surface preparation, and component loading for the duty cycle, influence the outcome of the verification testing. Although there were mixed reports in the described results, the outcome is dependent on multiple inputs, making broad conclusions difficult. But it is clear that certain designs and materials in drivetrains, with cylindrical geometries, can be made successfully, by use of large interface-areas with mechanical-interlocks, with the appropriate choices of materials, process, and interface bonding method.

12.6 Conclusion: Utility of Composite-and-Metal Components for Use in Drivetrains

Drivetrains represent the highest demand of performance for materials used in the Eaton vehicle and aerospace group, with regard to structural and thermal capability, and indicate potential capabilities of primary-structural components, such as control arms, for vehicles. Verification testing here for metal and composite two-component parts have shown that metal-to-reinforced-thermoplastic and metal-to-reinforced-thermoset driveline components are achievable in current vehicle configurations and envelopes. Metal-to-composite components have the capability for base-material-attachment, cylindrical interfaces, thermal excursions, and full duty-cycle durability. Furthermore, the interfaces can be enhanced by any metal surface preparation that leads to additional surface area and mechanical interlock of base materials. Driveline applications for lightweighting can greatly influence vehicle dynamics, as rotational components tend to be unsprung components, components that add to the rotational inertia of the vehicle, components that add to the translational inertia of the vehicle, and components that generate undesired vibration, harshness, or noises. Metal-and-composite components have now been built, analyzed and verification tested, so are available for new designs where lightweighting, and NVH need to be enhanced.

References

1. ASTM D3528-96(2008): Standard Test Method for Strength Properties of Double Lap Shear Adhesive Joints by Tension Loading, p. 249. ASTM International, West Conshohocken (2008)
2. Watson, D.C.: Mechanical Properties of E293/1581 Fiberglass-Epoxy Composite and of Several Adhesive Systems, p. 30. Final Report, May 1982, AFWAL-TR-82-4013
3. Ruggles-Wrenn, M.B.: Effects of Temperature and Environment on Mechanical Properties of Two Continuous Carbon-Fiber Automotive Structural Composites. DOE DE-AC05-00OR22725, Oak Ridge National Laboratory, Oak Ridge, TN (2003)

Chapter 13

Short-Term Preload Relaxation in Composite Bolted Joints Monitored with Reusable Optical Sensors

Anton Khomenko, Ermias G. Koricho, Mahmoodul Haq, and Gary L. Cloud

Abstract Bolted fastening is one of the oldest joining techniques, and it is widely used in vast number of applications. Although such fasteners provide many advantages, bolted joint assemblies and in-service behaviors demonstrate complex phenomena and stress distributions. Among these factors, bolt tension affects joint reliability and residual lifetime most significantly. One of the major concerns in bolted joints with composite panels is the effect of creep in the through-the-thickness direction of the material, which leads to preload reduction and premature failure of the loosened bolted joint. Thus, it is essential to monitor the preload after joint assembly. In this work, a previously developed bolt tension monitor that is instrumented with a reusable optical sensor was used to evaluate the short-term relaxation of preload in similar and dissimilar composite bolted joints. A single-parameter model was used to fit experimental data and obtain a relaxation parameter, which was assumed to be an extensive property. Preload reductions in lap joints with steel and glass fiber reinforced plastic (GFRP), and GFRP with GFRP were measured for ca. 9 min after the application of two levels of initial preloads. It was found that, depending on the joint configuration, the preload reduction varied considerably; and an increase in initial preload tends to reduce the preload relaxation. Overall, this technique provides robust and cost-efficient health monitoring in composite bolted joints.

Keywords Bolt tension monitor • FBG sensor • Preload relaxation • Bolted joint • Composite creep

1 Introduction

Bolted fastening is one of the most-used joining techniques in vast numbers of applications including manufacturing, construction, machine design, transport and aerospace sectors, etc. While these fasteners exhibit many advantages such as ease of assembly and repair, in-service behavior is defined by many complex phenomena that depend on various parameters affecting serviceability and durability. One of the major reasons for failure of bolted joints is the preload relaxation that can be caused by rotational self-loosening or creep in the through-the-thickness direction of one or both of the joined components. This issue is especially acute in structures containing plastics or composites that are increasingly being used to reach mandated strength/weight goals. In service self-loosening of components have been reported frequently; and a survey of automobile service managers in the United States reported that one-quarter of all service problems were traced back to

A. Khomenko (✉)

General Photonics Corporation, 5228 Edison Avenue, Chino, CA 91710, USA

Composite Vehicle Research Center, Michigan State University, 2727 Alliance Drive, Lansing, MI 48910, USA

e-mail: khomenka@msu.edu

E.G. Koricho • G.L. Cloud

Composite Vehicle Research Center, Michigan State University, 2727 Alliance Drive, Lansing, MI 48910, USA

M. Haq

Composite Vehicle Research Center, Michigan State University, 2727 Alliance Drive, Lansing, MI 48910, USA

Department of Civil and Environmental Engineering, Michigan State University,
Engineering Building, East Lansing, MI 48824, USA

lose fasteners [1]. Hence, bolt loosening has become an important research area as ways are sought to prevent failures in a variety of applications, particularly in similar and dissimilar composite joining [2]. The loss of preload induced by creep has a detrimental effect on the strength and the residual lifetime of the connection. Thus, it is essential to monitor the bolt preload in service conditions to prevent catastrophic failure of the bolted joint. Many studies on composite creep have been performed, but in all of these investigations the clamp-up forces were randomly selected and neither the influences of different clamp-up forces nor the effects of external static and dynamic loads on relaxation were investigated in detail [3]. In most of the previous studies, the tools for preload measurements were used ‘as is’ without any systematic evaluation of instrumentation errors on the preload measurements, a critical omission for long-term measurements. Moreover, since there is not any standard or single procedure, monitoring times have been randomly selected and the results have been presented in different formats, meaning that the various results cannot be compared directly. Lastly, the results for initial preload effect on composite creep display some contradictions [3, 4]. Comprehensive research on the creep of similar and dissimilar composite joints, including proper selection of the NDE technique employed, is badly needed in order that designers and manufacturers might meet weight and performance criteria.

Numerous techniques for bolt tightening control and structural health monitoring exist and can be classified into several categories as follows: external miniature load cells [2], acoustic inspection [5, 6], optical inspection [7], internally embedded strain gages and fiber Bragg grating (FBG) sensors [8, 9], and techniques based on other physical principles. Each of these techniques has its own merits and limitations. Optical inspection is complex and is not suitable for continuous monitoring under field conditions [1]. Acoustic inspection is sensitive to external vibrations [5]. Sensing washers have to be incorporated into the structure, and the load cells are quite expensive [10]. Moreover, sensing washers and load cells add weight to the structure. Installation of electrical resistance strain gages (RSGs) in the bolt shaft is cumbersome, they are temperature sensitive, and the drilled channel has to be several mm in diameter, which is detrimental to the integrity of the bolt. Moreover, RSGs are not compatible with some types of bolts. FBG sensors are very small in diameter (up to 100 μm) and easy to install in any type of the bolt, but permanent embedding is not practical because the cost of the sensor is much higher than that of traditional RSG’s. Previously, we developed a novel technique to monitor bolt clamping force utilizing removable and reusable embedded FBG sensors, and we validated the technique for static preload measurements in multi-material bolted joint configurations [11]. The “bolt tension monitor” uses a temporary adhesive for embedding an FBG sensor into the bolt shaft, thereby converting the bolt into a tension measuring device that is a reliable tool for evaluating the behavior of the bolted joint. The FBG sensor can be embedded at any given time into any type of bolt, then be removed and reused later in the same or another bolt. The bolt tension monitor provides real-time precise clamping force measurements and does not require complicated manufacturing or setup preparation. Significantly, the bolt tension monitor is resistant to most external environmental effects, the major exception being changes in gross temperature of the bolt.

In this work, bolt tension monitors utilizing hot melt adhesive or polylactide (PLA) plastic as the medium for embedding FBG sensors were compared and used for the monitoring of preload relaxation caused by creep in similar and dissimilar composite bolted joints. Initially, instrumented bolts were calibrated using an external load cell, and the creep in the embedding thermoplastic was evaluated using a single steel plate. Afterwards, short-term preload reductions that occurred within the first 9 min after bolt tightening in lap joints with two material combinations, i.e., steel with glass fiber reinforced plastic (GFRP) and GFRP with GFRP, were studied for two levels of initial preload. A single-parameter model was used to fit experimental data and obtain a relaxation parameter, which was assumed to be an extensive property. This means that the value of the relaxation parameter for the system would be the sum of the relaxation parameters for each subsystem. Finally, the thru-hole load cell used for bolt tension monitor calibration was evaluated for preload relaxation measurements in a composite material.

2 Specimen Preparation

2.1 Bolt Tension Monitor Fabrication

Two bolt tension monitors were manufactured as is described in [9]. The bolts were grade five medium-strength steel hex head (head width: 19.05 mm or 3/4"; head height 7.94 mm or 5/16") bolts with a right-hand thread having a length of 38.1 mm (1.5"), threaded with a 12.7 mm-13 (0.5"-13) thread. A 1.8 mm diameter hole was drilled along the axis of each bolt through one-half of its length (23 mm). A conventional heat gun was employed to embed an FBG sensor inside each bolt using in one case 3M™ Scotch-Weld™ Hot Melt Adhesive 3779 PG Amber and in the second case polylactide (PLA) plastic. The embedded FBG sensors used were Micron Optics os1100 with a gage length of 10 mm. The spectral responses of the FBG sensors were acquired using a Micron Optics sm125 700 Optical Sensing Interrogator. Both bolt tension monitors are illustrated in Fig. 13.1.

Fig. 13.1 Bolt tension monitors: (a) with hot melt adhesive embedding medium, (b) with PLA plastic embedding medium

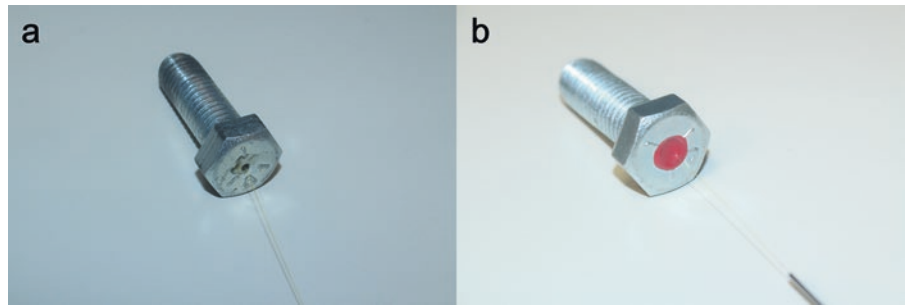
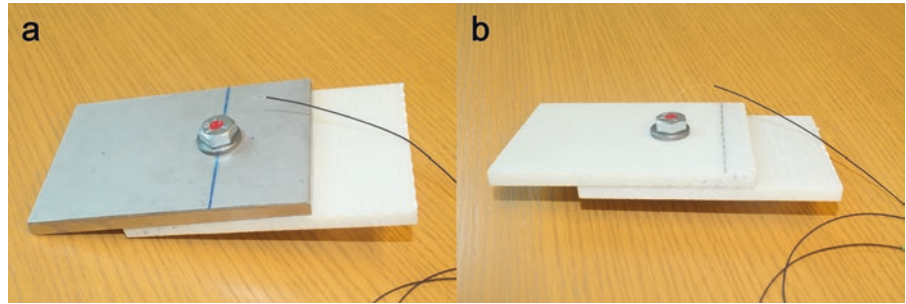


Fig. 13.2 Assembled bolted joints: (a) steel-GFRP configuration, (b) GFRP-GFRP configuration



The operating principle of the bolt tension monitor is based on the spectrum monitoring of the embedded FBG sensor. Such a sensor acts as an optical filter that transmits the entire spectrum of the light source and reflects back the resonant Bragg wavelength [11]. Any perturbation of the Bragg grating period results in a shift of Bragg wavelength. The strain response arises from both the physical elongation of the sensor and the change in fiber effective refractive index caused by stress-birefringence, whereas a thermal response arises from the inherent thermal expansion of the fiber material and the temperature dependence of the refractive index. Because FBG sensors require only very small stresses to induce appreciable strains, temporary adhesives (e.g., thermoplastics) suffice for attachment of these sensors well enough so that, within certain limits, they accurately indicate strain in the bolt body. Within the linear elastic regime, the axial tension load in the bolt is directly proportional to the measured elongation strains and can be easily calculated if the bolt material properties are known. However, as with all load transducers, direct calibration with known loads is the only truly valid way to accurately establish the relationship between force and system output for each transducer.

2.2 Bolted Joints Assembly

GFRP composite panels for the bolted joints were manufactured using a liquid molding process. The reinforcement used was Owens Corning ShieldStrand® S, S2-glass plain weave fabric with areal weight of 818 g/m². Sixteen layers of fabric were used. The distribution medium was Airtech Advanced Materials Group Resinflow 60 LDPE/HDPE blend fabric. The resin used was a two-part toughened epoxy, namely SC-15, obtained from Applied Poleramic. A steel mold having dimension of 609.6 mm × 914.4 mm with point injection and point venting was used to fabricate 508.0 mm × 609.6 mm plates. After the materials were placed, the mold was sealed using a vacuum bag and sealant tape. The mold was then infused under vacuum at 29 in Hg. The resin-infused panel was cured in a convection oven at 60 °C for 2 h and post-cured at 94 °C for 4 h.

The steel and GFRP coupons used in the joint assembly had dimensions of 152 mm × 101 mm × 9.5 mm and 152 mm × 101 mm × 9 mm, respectively. A 15.7 mm diameter hole was drilled in the plates 50.5 mm away from three edges, and a steel sleeve washer was inserted. The sleeve washer had the following dimensions: flange diameter 25.4 mm, sleeve ID of 13.46 mm, sleeve OD of 15.88 mm, flange thickness of 3.18 mm, overall height of 4.75 mm. The resulting assemblies for steel-GFRP and GFRP-GFRP configurations with the PLA-based bolt tension monitor are illustrated in Fig. 13.2.

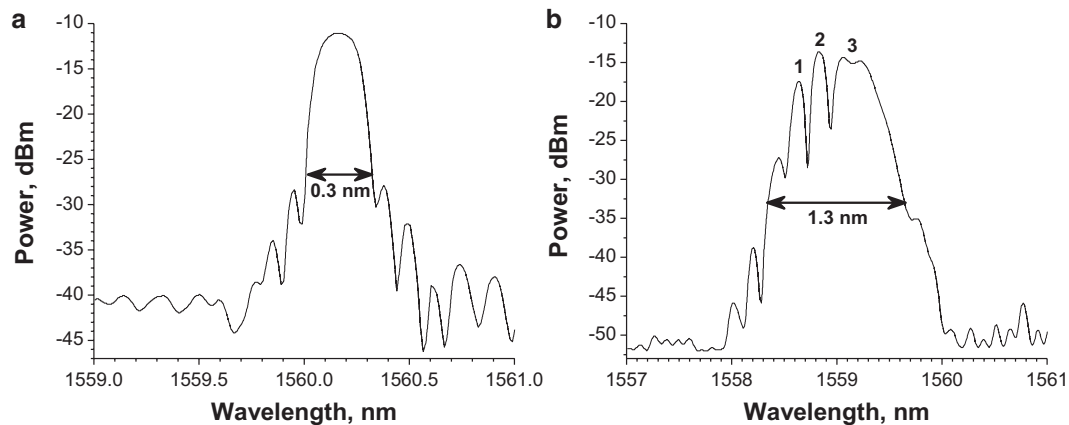


Fig. 13.3 Spectral response of FBG sensor in PLA-based bolt tension monitor: (a) before installation, (b) after installation

3 Experimental Results and Discussion

3.1 Bolt Tension Monitor Features and Calibration

Spectral responses of FBG sensors embedded in hot melt adhesive and PLA plastic were compared before and after FBG sensor installation. The spectral changes were not pronounced for the sensor that was embedded in hot melt adhesive; however, in the case of PLA as the embedding medium, the spectral response the FBG sensor was distorted and exhibited multi-peaks, as shown in Fig. 13.3.

The spectrum broadening from ~ 0.3 to ~ 1.3 nm and the significant distortion were probably caused by non-uniform shrinkage of the PLA thermoplastic during cooling. Although it would seem to be detrimental to the FBG sensor, this multi-peak feature can be considered as beneficial. Indeed, instead of a single gage, the various peaks serve as several randomly distributed gages, each of which can be used to monitor strains [12]. This system then provides redundant measurements and the ability to monitor strain uniformity along the bolt shaft [11]. In this work, peaks 1, 2, and 3 shown in Fig. 13.3b were used to measure the preload with the PLA-based bolt tension monitor.

Both bolt tension monitors were calibrated using a thru-hole load cell model THC-1K-T manufactured by Transducer Techniques[®] with a maximum load capacity of 4448 N (1000 lb). During the manual tightening of the bolt, the spectral responses of the FBG sensor embedded into the bolt were acquired using the interrogator and synchronized with the load cell data. The calibration curves, showing typical dependences of Bragg wavelength shift of the sensors on the applied preload as measured by the load cell, are reproduced in Fig. 13.4. The relationship between applied load and wavelength shift was found to be linear and the calibration coefficient was found to be 37.1 ± 0.8 N/pm for the hot melt adhesive-based bolt tension monitor. For the PLA-based bolt tension monitor, the calibration factors are and 23.7 ± 0.8 N/pm, 22.8 ± 0.6 N/pm, and 21.7 ± 0.6 N/pm for peak 1, peak 2, and peak 3, respectively. The differences in calibration factors indicate that sensor installation has a notable effect on calibration factor, thus each transducer has to be calibrated prior to actual measurements.

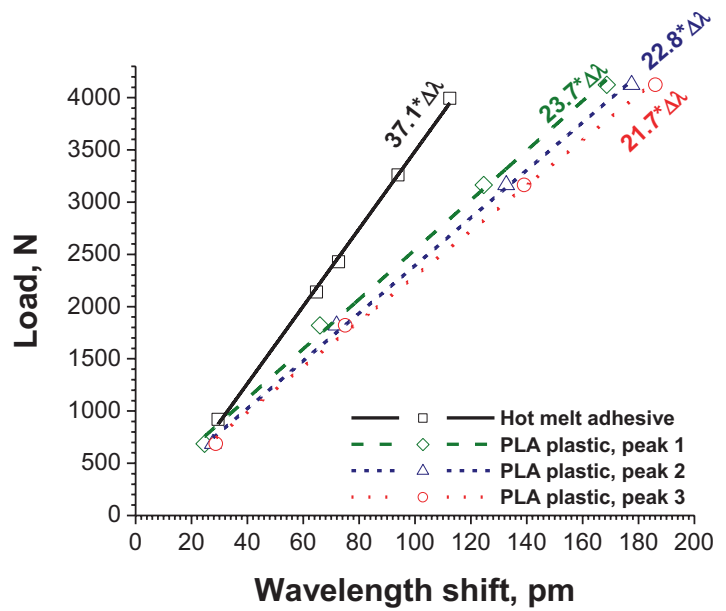
3.2 Data Analysis Using a Single-Parameter Model for Preload Relaxation

After the measurements were completed for each case, the preload reduction was approximated using a modified version of the equation according to Caccese et al. [2]:

$$\frac{P_t}{P_0} = p(t + t_0 + 1)^{-\alpha}, \quad (13.1)$$

where P_t is the measured preload, P_0 is the initial preload, $p \sim 1$ is the coefficient that takes into account the continually changing load value at the start of the tests which is affected by the primary creep response [2], t is time in seconds, $t_0 = 2$ is the time interval between the maximum preload and the first fitted data point, and α is the relaxation parameter. Coefficient

Fig. 13.4 Calibration curves for hot melt adhesive- and PLA-based bolt tension monitors



t_0 was introduced for proper data fitting, since the measurements were taken 2 s after the maximum preload. An important hypothesis was adopted, namely that the relaxation parameter is an extensive property. Thus, the relaxation parameter of the selected configuration can be represented as the sum of the relaxation parameters of individual components. For example, if a transducer has its own relaxation parameter α_T , the relaxation parameter of studied configuration α_C can be found by a simple subtraction of α_T from measured relaxation parameter α , i.e., $\alpha_C = \alpha - \alpha_T$. Hence, Eq. (13.1) can be rewritten as:

$$\frac{P_t(t+t_0+1)^{\alpha_T}}{P_0} = p(t+t_0+1)^{-\alpha_C}, \quad (13.2)$$

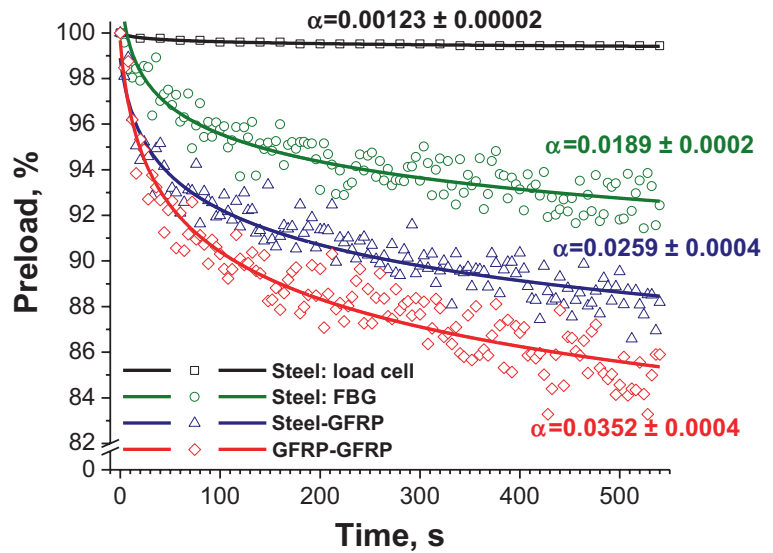
A singular beneficial characteristic of this approach is that the preload relaxation contributed by the transducer itself is eliminated by scaling of the measured preload to the value which would be expected in the absence of the transducer. The results are thereby caused to be relatively independent of test conditions so that they become physical rather than phenomenological, and, if properly interpreted, they have broad application.

The use of the single parameter α allows simple case-by-case comparison, whereas a two-parameter model is not quite practical and suitable for this purpose [2, 4, 13]. The value of α may depend upon such variables as material creep properties, temperature, humidity, moisture content, stress and thickness. Preload reduction in a bolted joint is a complex phenomenon, which is caused by continuously changing material creep and stress relaxation. After initial preload, the material begins to creep causing a small reduction in material thickness which in turn leads to contraction of the bolt and decrease of reaction force. Thus, the more the creep in the material the faster the preload decreases (relaxation parameter increases).

3.3 Short-Term Preload Relaxation Measurements by Hot Melt Adhesive-Based Bolt Tension Monitor for 4500 N Initial Preload

In the first set of experiments, short-term preload relaxation measurements using the bolt tension monitor that incorporated the hot melt adhesive as the embedding medium were performed on the steel-GFRP and GFRP-GFRP bolted joint configurations for an initial preload of 4500 N and for periods of ca. 9 min after bolt tightening. At least three tests were performed at $45 \pm 5\%$ humidity and room temperature, which was $24 \pm 2^\circ$, for each case; and approximately 2700 measurement data points were obtained during each test. Before every test run, the system (bolted joint and bolt tension monitor) was verified to be in its initial state. In order to achieve that, the system was kept untightened for at least 15 min so it could achieve temperature equilibrium and return to its initial state with no residual creep in the embedding thermoplastic or the GFRP plate(s). After the manual tightening, the short-term preload relaxation was monitored for about 9 min. Preload measurements were

Fig. 13.5 Typical preload relaxation measured (every 20th point plotted) in steel-GFRP and GFRP-GFRP bolted joint configurations with hot melt adhesive-based bolt tension monitor and in steel plate measured by thru-hole load cell and monitored with FBG sensor embedded with hot melt adhesive for 4500 N initial preload



begun 2 s after the bolt was tightened to eliminate the effect of tightening rate. Typical preload relaxation measurements from one test are presented in Fig. 13.5.

When a single steel plate was used, the average relaxation parameters α from the series of tests were found to be 0.0013 ± 0.0002 and 0.0158 ± 0.0029 measured by the thru-hole load cell and the embedded FBG, respectively. In other words, assuming that the steel did not creep, the hot melt adhesive-based bolt tension monitor had a creep in the embedding thermoplastic itself, which is not desired for long-term measurements. The average relaxation parameters for a steel-GFRP and GFRP-GFRP bolted joint configurations measured using the hot melt adhesive-based bolt tension monitor were found to be 0.0268 ± 0.0024 and 0.0346 ± 0.0046 , respectively. These values, however, are contaminated by the creep-induced relaxation in the embedding thermoplastic mentioned above. Since the relaxation parameter was assumed to be an extensive property, the relaxation parameter for the studied configuration can be easily obtained by simple subtraction of the thermoplastic relaxation parameter from the measured configuration relaxation parameter, as described above. Thus, the average relaxation parameters were 0.0110 ± 0.0038 and 0.0188 ± 0.0054 for the steel-GFRP and GFRP-GFRP configurations.

3.4 Short-Term Preload Relaxation Measurements by PLA-Based Bolt Tension Monitor for 4500 N Initial Preload

Following the procedure described previously but using the bolt tension monitor with the PLA thermoplastic embedding medium, short-term preload relaxation was measured again for 9 min in steel-GFRP and GFRP-GFRP bolted joint combinations for an initial preload of 4500 N. Typical preload relaxation measurements are shown in Fig. 13.6.

When a single steel plate was used, the average relaxation parameter α was found to be 0.0013 ± 0.0001 and 0.0021 ± 0.0008 measured by the thru-hole load cell and the PLA-embedded FBG, respectively. The average relaxation parameters for a steel-GFRP and GFRP-GFRP bolted joint configurations measured by the PLA-based bolt tension monitor were found to be 0.0123 ± 0.0025 and 0.0241 ± 0.0023 , respectively. The measured relaxation in the PLA thermoplastic was much lower than that obtained for the hot melt adhesive, which means that PLA is a better candidate for embedment of the FBG in the bolt tension monitor. Subtracting the previously obtained relaxation parameter found for PLA plastic, the average relaxation parameters for steel-GFRP and GFRP-GFRP bolted joint configurations are found to be 0.0102 ± 0.0026 and 0.0220 ± 0.0024 , respectively. Since the creep-induced relaxation of the PLA plastic was insignificant, preload relaxation measurements would seem to yield higher precision. The measured relaxation parameter for a bolted joint with two composite panels was approximately twice as great as that for a bolted joint with a single composite plate. This observation can serve as an indication that the relaxation parameter is, indeed, an extensive property.

Fig. 13.6 Typical preload relaxation measured (every 20th point plotted) in steel-GFRP and GFRP-GFRP bolted joint configurations with PLA-based bolt tension monitor and in steel plate measured by both the thru-hole load cell and by FBG sensor embedded with PLA plastic for 4500 N initial preload

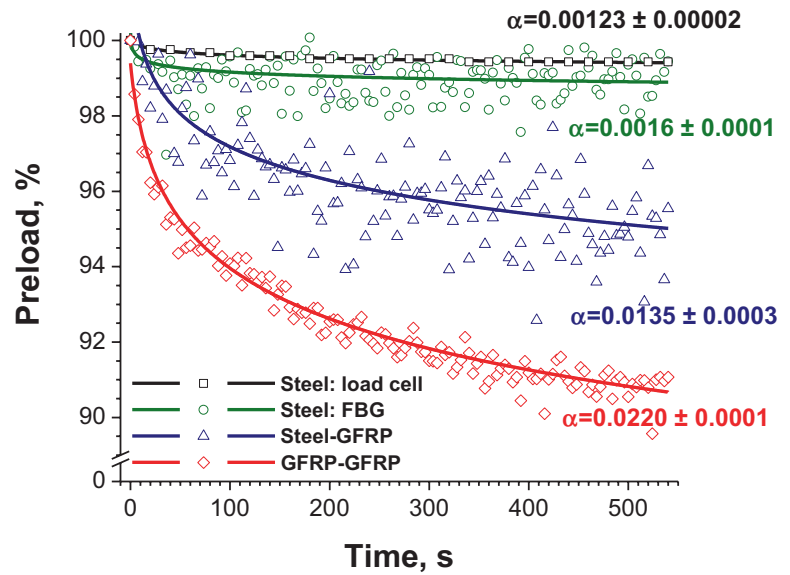
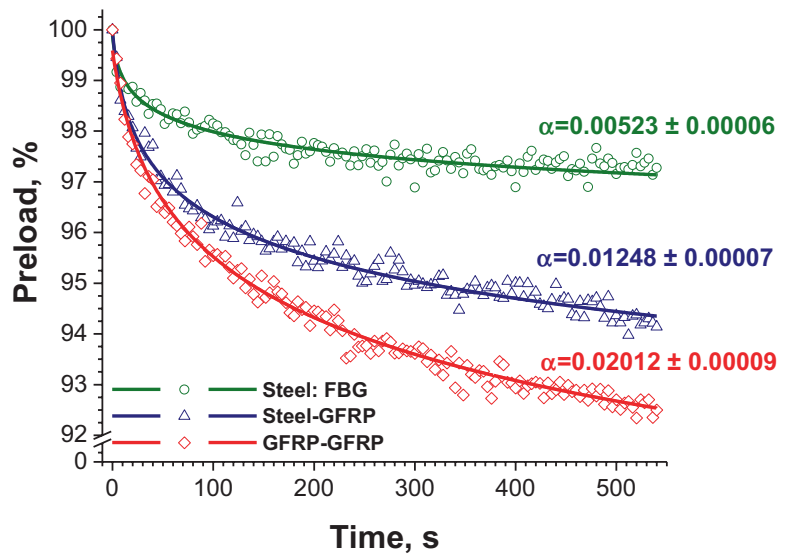


Fig. 13.7 Typical preload relaxation measured (every 20th point plotted) in steel-GFRP and GFRP-GFRP bolted joint configurations and in steel plate measured with PLA-based bolt tension monitor for 8000 N initial preload

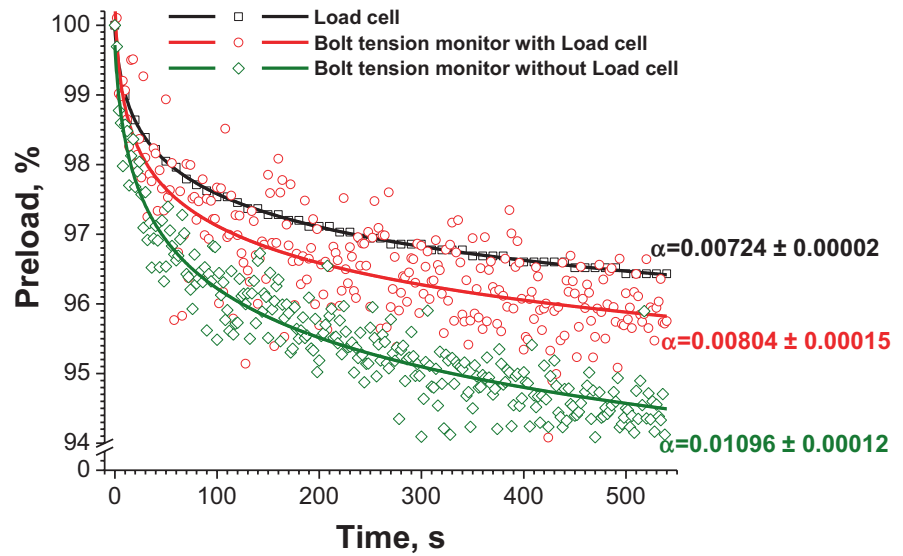


3.5 Short-Term Preload Relaxation Measurements by PLA-Based Bolt Tension Monitor for 8000 N Initial Preload

Short-term preload relaxation measurements in the PLA thermoplastic embedding medium, the steel-GFRP and the GFRP-GFRP bolted joint configurations were performed for 9 min using an initial preload of 8000 N. The procedures were the same as those outlined above. Typical preload reduction measurements are reported in Fig. 13.7.

The average relaxation parameter α for the PLA plastic measured by testing the embedded FBG sensor with the steel plate was found to be 0.0050 ± 0.0007 , which was higher than that for the 4500 N preload. The average relaxation parameter for the steel-GFRP and GFRP-GFRP bolted joint configurations measured by the PLA-based bolt tension monitor for this higher initial preload was found to be 0.0127 ± 0.0005 and 0.0204 ± 0.0003 , respectively. Taking into account the previously obtained relaxation parameter in PLA plastic, the average relaxation parameters for the steel-GFRP and GFRP-GFRP bolted joint configurations can be found to be 0.0077 ± 0.0008 and 0.0154 ± 0.0008 , respectively. As with the 4500 N initial preload case, the bolted joint with two composite panels had a relaxation parameter nearly twice that of a bolted joint with a single composite plate. This agreement can be taken as further validation of the single parameter approximation and proposed hypothesis. Although the average values showed a reduction of the relaxation parameter with increased preload, more experiments with higher preloads and longer monitoring times are required to confirm this dependency.

Fig. 13.8 Typical reload relaxation measured (every tenth point plotted) in GFRP plate by thru-hole load cell and by PLA-based bolt tension monitor with and without thru-hole load cell in the assembly for 4500 N initial preload



3.6 Evaluation of Thru-Hole Load Cell for Preload Relaxation Measurements

In the final set of experiments the thru-hole load cell was evaluated for use in composite creep/preload relaxation measurements. For this purpose a single GFRP plate in combination with the PLA-based bolt tension monitor and the thru-hole load cell was tightened to 4500 N, and the preload reduction was monitored. In the first case, the system consisted of a GFRP panel with a steel washer, the PLA-based bolt tension monitor, the thru-hole load cell, and a nut. In the second case, the thru-hole load cell was replaced by a steel block of similar thickness and size. All performed measurements followed the procedure described previously. Typical preload reduction measurements are illustrated in Fig. 13.8.

The average relaxation parameters α measured by the thru-hole load cell, the PLA-based bolt tension monitor with and without the load cell present in the assembly were found to be 0.0077 ± 0.0007 , 0.0081 ± 0.0009 , and 0.0108 ± 0.0005 , respectively. If the PLA relaxation parameter obtained previously is taken into account, the average relaxation parameter for the GFRP plate can be obtained, giving values of 0.0060 ± 0.0012 and 0.0087 ± 0.0009 for the GFRP plate and PLA-based bolt tension monitor assembly with and without the thru-hole load cell, respectively. The average GFRP plate relaxation parameter measured in the assembly without the load cell shows good agreement with the steel-GFRP bolted joint relaxation parameter obtained earlier. This indicates that the majority of the preload relaxation in the steel-GFRP bolted joint combination was caused by the GFRP plate, as expected. Note also that the presence of the thru-hole load cell in the assembly tends to reduce the measured relaxation parameter of the GFRP plate. Such behavior can be explained if the thru-hole load cell acts as a spring washer, which partially offsets the reduction of the preload, hence artificially decreasing the actual preload relaxation. This example demonstrates that any tool for preload measurements cannot simply be used ‘as is’; and more rigorous study is required to fully evaluate the use of such a tool for creep monitoring.

4 Conclusions

In this work, bolt tension monitors utilizing hot melt adhesive and PLA plastic as an embedding medium were compared and used for the monitoring of short-term preload relaxation in similar and dissimilar GFRP composite bolted joints. It was found that if the sensor is embedded in hot melt adhesive, the spectral changes in the FBG output were not pronounced; while, in the case of PLA as the embedding medium, the spectral response of the FBG sensor was distorted and exhibited multiple peaks, which were caused by non-uniform shrinkage of the PLA thermoplastic as it cooled and solidified. Although it would seem to be detrimental to the proper functioning of the FBG sensor, this multipeak feature can be viewed as beneficial and afforded the opportunity to obtain several redundant preload measurements. The relationship between applied load and wavelength shift (or calibration curve) was found to be linear for both hot melt adhesive- and PLA-based bolt tension monitors.

The results demonstrated that for a 4500 N initial bolt preload the hot melt adhesive-based bolt tension monitor exhibited the creep in the embedding thermoplastic itself, which is not desirable for long-term measurements. However, if a single-parameter approximation (see Eq. 13.1) is used and the relaxation parameter is assumed to be extensive property, the relaxation parameter of the studied configuration can be obtained by subtraction of the embedding thermoplastic relaxation parameter from the measured one.

It was found that for the PLA-based bolt tension monitor, the PLA relaxation parameter slightly increased for higher initial preload. An important finding is that the PLA relaxation parameter was considerably lower than that of hot melt adhesive. This allowed more precise evaluation of the relaxation parameters for steel-GFRP and GFRP-GFRP bolted joint configurations. It was demonstrated that for both the 4500 N and the 8000 N initial preload cases, the relaxation parameter for the bolted joint with two composite panels was nearly twice as large as the relaxation parameter compared with a bolted joint with a single composite plate. This observation can serve as an indication that the relaxation parameter is an extensive property. Although the average values showed reduction of the relaxation parameter with increased preload, more experiments with higher preloads and longer monitoring times are required to confirm this trend.

Finally, it was demonstrated that the presence of the thru-hole load cell in the assembly tends to reduce the measured relaxation parameter of the GFRP composite. This can be explained if the thru-hole load cell acts as a spring washer, which partially offsets the reduction of the preload, hence artificially decreasing the actual relaxation parameter.

The results of these tests demonstrate that the single-parameter approximation used in the study provided good fitting of the experimental data and allowed simple case-by-case comparison, provided the relaxation parameter is proven to be an extensive property. The comparison of relaxation parameters for various configurations further confirms that the chosen approximation was valid. The next step is further validation of the proposed hypothesis for multi-material configurations under various conditions, and more detailed research on the limits of the chosen approximation.

Overall, this study aims to assist in the development of a single procedure for simple, robust and cost-efficient characterization of preload relaxation that is caused by creep in bolted joints. Future work includes the use of distributed fiber optic sensors and long-term strain measurements, which can be accomplished if temperature and strain effects are discriminated. This step can be achieved in several ways, e.g., use of temperature insensitive fiber optic sensors, temperature compensation with secondary fiber optic sensors, and the use of a fiber optic sensor which provide separate measurements for strain and temperature.

References

1. Li, C., Xu, C.-N., Adachi, Y., Ueno, N.: Real-time detection of axial force for reliable tightening control. *Proc. SPIE* **7522**, 75223G (2010)
2. Caccese, V., Berube, K.A., Fernandez, M., Melo, J.D., Kabche, J.P.: Influence of stress relaxation on clamp-up force in hybrid composite-to-metal bolted joints. *Compos. Struct.* **89**, 285–293 (2009)
3. Thoppul, S.D., Finegan, J., Gibson, R.F.: Mechanics of mechanically fastened joints in polymer-matrix composite structures—a review. *Compos. Sci. Technol.* **69**(3–4), 301–329 (2009)
4. Thoppul, S.D., Gibson, R.F., Ibrahim, R.A.: Phenomenological modeling and numerical simulation of relaxation in bolted composite joints. *J. Compos. Mater.* **42**(17), 1709–1729 (2008)
5. Coelho, C.K., Das, S., Chattopadhyay, A., Papandreou-Suppappola, A., Peralta, P.: Detection of fatigue cracks and torque loss in bolted joints. *Proc. SPIE* **6532**, 653204 (2007)
6. Amerini, F., Meo, M.: Structural health monitoring of bolted joints using linear and nonlinear acoustic/ultrasound methods. *Struct. Health Monit.* **10**(6), 659–672 (2011)
7. Huang, Y.H., Liu, L., Yeung, T.W., Hung, Y.Y.: Real-time monitoring of clamping force of a bolted joint by use of automatic digital image correlation. *Opt. Laser Technol.* **41**(4), 408–414 (2009)
8. Industrial and research news: miniature load cells. *Strain* **23**, 196 (1987)
9. Hay, A.D.: Bolt, stud or fastener having an embedded fiber optic Bragg grating sensor for sensing tensioning strain. US Patent 5,945,665, 31 Aug 1999
10. Jiang, Y., Zhang, M., Park, T.-W., Lee, C.-H.: An experimental study of self-loosening of bolted joints. *J. Mech. Des.* **126**(5), 925–931 (2004)
11. Khomenko, A., Koricho, E.G., Haq, M., Cloud, G.L.: Bolt tension monitoring with reusable fiber Bragg-grating sensors. *J. Strain Anal. Eng. Des.* (2015). doi:[10.1177/0309324715598265](https://doi.org/10.1177/0309324715598265)
12. Haq, M., Khomenko, A., Udpa, L., Udpa, S.: Fiber Bragg-grating sensor array for health monitoring of bonded composite lap-joints. In: Proceedings of the 2013 Annual Conference on Experimental and Applied Mechanics: Experimental Mechanics of Composite, Hybrid, and Multifunctional Materials, vol. 6, pp. 189–195 (2014)
13. Shivakumar, K.N., Crews, J.H.: Bolt clampup relaxation in a graphite/epoxy laminate. In: O'Brien, T.K. (ed.) Long-Term Behavior of Composites, ASTM STP, vol. 813, pp. 5–22. American Society for Testing and Materials, Philadelphia (1983)